System Identification of the Delfly Nimble:

Modeling of the Lateral Body Dynamics

K.V. Bains

Faculty of Aerospace Engineering

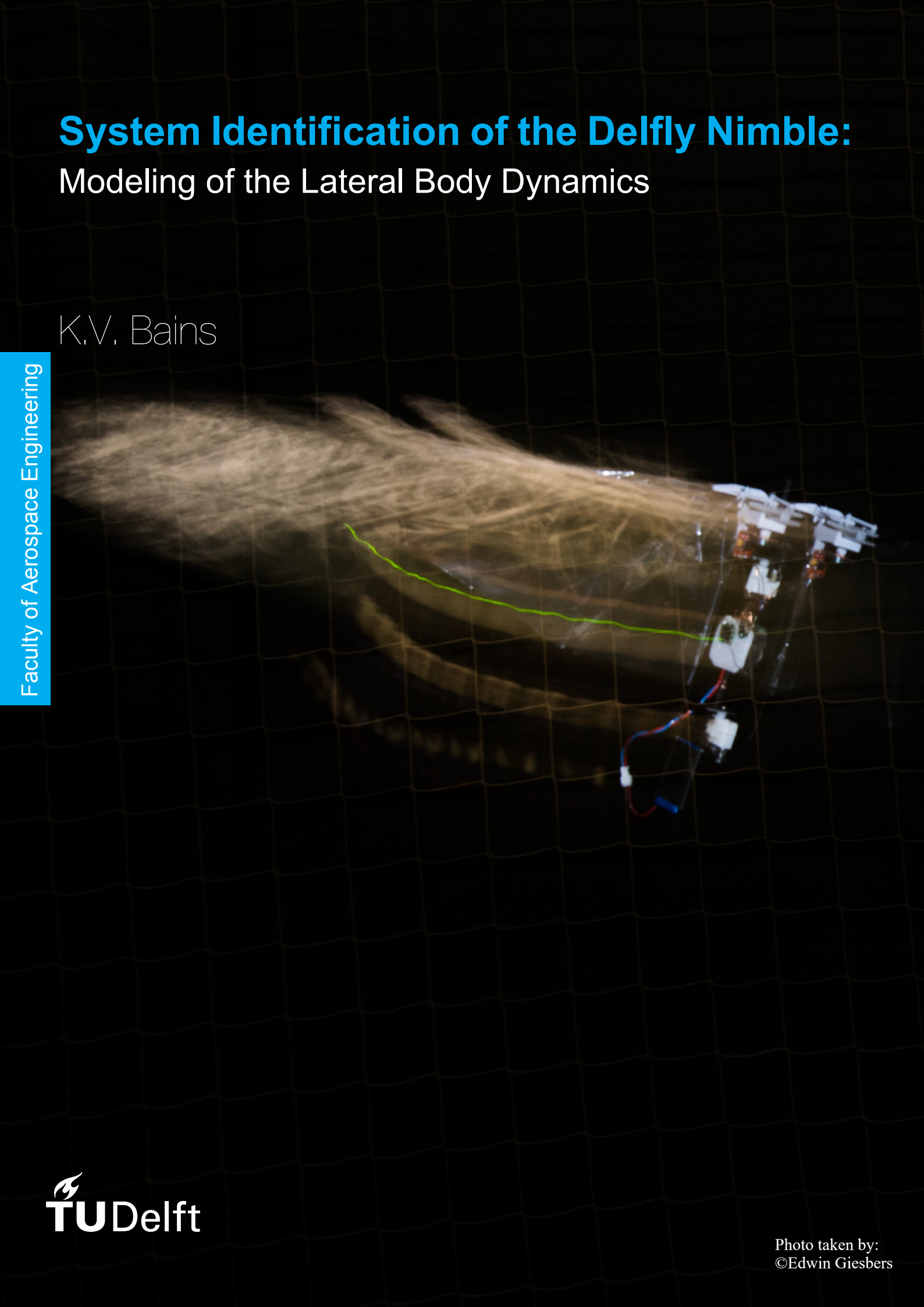

TU Delft

Photo taken by:
©Edwin Giesbers

System Identification of the Delfly Nimble:

Modeling of the Lateral Body Dynamics

by

K.V. Bains

to obtain the degree of Master of Science
at the Delft University of Technology,
to be defended publicly on Friday December 11, 2020 at 2:00 PM.

Student number:	4296117	
Project duration:	May 21, 2019 – December 11, 2020	
Thesis committee:	Prof. dr. ir. G.C.H.E de Croon,	TU Delft
	Dr. ir. C.C. de Visser,	TU Delft, main supervisor
	D.A. Olejnik MSc,	TU Delft, daily supervisor
	Dr. ir. E. Mooij,	TU Delft, Examiner

An electronic version of this thesis is available at `http://repository.tudelft.nl/`.

TU Delft Delft University of Technology

Contents

List of Figures

List of Tables

Nomenclature

Latin letters

A, B, C, D	Matrices in the state-space system
A_w	Wing area, m^2
a_x, a_y, a_z	Linear body accelerations, ms^{-2}
B_{lon}	Input matrix for the longitudinal state-space system
B_{lat}	Input matrix for the lateral state-space system
b	Wing span, m
b_{a_x}, b_{a_y}, b_{a_z}	Bias terms accelerometers
$b_{\dot{p}}$, $b_{\dot{r}}$, $b_{\dot{v}}$, $b_{\dot{\phi}}$	Bias terms
b_p, b_q, b_r	Bias terms gyroscope
$\mathscr{B}(i), COV, Cov, \mathbf{R}$	Covariance matrix
$\bar{c}$	Mean chord length, m
$C(\tau)$	Autocorrelation matrix
f	Flapping frequency, Hz
f_1, f_2, f_3	Natural frequencies, Hz
f_L, f_R	Flapping frequency of the left and right wing, Hz
F_x, F_y, F_z	Forces along the body axes. N
g	Earth's gravitational constant, ms^{-2}
G	Controller
$H, \hat{H}$	Aircraft dynamic system, Estimate of aircraft dynamic system
I_{xx}, I_{yy}, I_{zz}	Mass moment of inertias, kgm^2
I_{xy}, I_{yz}, I_{xz}	Products of inertias, kgm^2
I_c	$I_{xx} \cdot I_{zz} - I_{xz}^2$, kg^2m^4
$J(\mathbf{x}, \bar{\theta})$	Cost function
K	Kalman gain
L, M, N	Aerodynamic moments along the body axes, Nm
l_x, l_z	Fixed linear displacements of the COP with respect to the COM
l_d	Adjustable linear displacements of the COP with respect to the COM
$L_{ext}, M_{ext}, N_{ext}$	External moments along the body axes, Nm
L_p, L_r, L_v	Dimensional stability derivatives of the moment L
$L_{\delta_d}, L_{\delta_f}, L_{\delta_w}$	Control derivatives of the moment L
L_p^+, L_r^+, L_v^+	Non-dimensional stability derivatives of the moment L
$L_{\delta_d}^+, L_{\delta_f}^+, L_{\delta_w}^+$	Non-dimensional control derivatives of the moment L
M_x, M_y, M_z	Moments about the body axes. N
M_q, M_u, M_w	Dimensional stability derivatives of the moment M
$M_{\delta_d}, M_{\delta_f}, M_{\delta_w}$	Control derivatives of the moment M
N_p, N_r, N_v	Dimensional stability derivatives of the moment N
$N_{\delta_d}, N_{\delta_f}, N_{\delta_w}$	Control derivatives of the moment N
N_p^+, N_r^+, N_v^+	Non-dimensional stability derivatives of the moment N
$N_{\delta_d}^+, N_{\delta_f}^+, N_{\delta_w}^+$	Non-dimensional control derivatives of the moment N
N	Total number of datapoints
m	Mass. kg
P	Number of parameters
$p(\mathbf{x}, \bar{\theta})$	Polynomial function
p, q, r	Angular rates, $rads^{-1}$
$\dot{p}, \dot{q}, \dot{r}$	Angular accelerations, $rads^{-2}$
q_0, q_1, q_2, q_3	Attitude quaternions
$\hat{r}$	Radius of the second moment of inertia, m

$\hat{\mathbf{R}}$	Estimate of the covariance matrix
R^2	Goodness of fit
$S_{pp}, S_{vv}, S_{rr}, S_{\phi\phi}$	Power spectral densities of the states
T	Wing beat period, s
THR_F	Throttle factor
t	Time, s
u, v, w	Body velocities, ms^{-1}
u_b, v_b, w_b	Body velocities, ms^{-1}
u_b^*, v_b^*, w_b^*	Measured body velocities, ms^{-1}
u_0, v_0, w_0	Initial body velocities, ms^{-1}
$\dot{u}, \dot{v}, \dot{w}$	Body accelerations, ms^{-1}
U	Average center of pressure velocity, ms^{-1}
$\mathbf{u}(t)$	Input vector
$\underline{u}_{lon}$	Input vector for the longitudinal dynamics
$\underline{u}_{lat}$	Input vector for the lateral dynamics
$v, \bar{v}$	Residual, mean of all residual
V_0	Initial forward velocity, ms^{-1}
$v(t), w(t)$	Sensor and process noise vector
W	Weight matrix
$W_1, W_2, W_3, W4$	Wing bodies
$\underline{x}_{est}, \underline{x}_{pred}$	Estimated and predicted state
$\mathbf{x}(t), \mathbf{y}(t), \mathbf{z}(t)$	State, output and measurement vector
X, Y, Z	Aerodynamic forces along the body axes, N
$X_{ext}, Y_{ext}, Z_{ext}$	External forces along the body axes, N
x, y, z	Position in the inertial reference frame, m
$x_b, X_{body}, y_b, z_b, Z_{body}$	Body axes
X_q, X_u, X_w	Dimensional stability derivatives of the force X
$X_{\delta_d}, X_{\delta_f}, X_{\delta_w}$	Control derivatives of the force X
Y_p, Y_r, Y_v	Dimensional stability derivatives of the force Y
$Y_{\delta_d}, Y_{\delta_f}, Y_{\delta_w}$	Control derivatives of the force Y
Y_p^+, Y_r^+, Y_v^+	Non-dimensional stability derivatives of the force Y
$Y_{\delta_d}^+, Y_{\delta_f}^+, Y_{\delta_w}^+$	Non-dimensional control derivatives of the force Y
$y_i, \hat{y}_i$	measurement point, model predicted measurement
$\bar{y}$	Mean of all measurements
Z_q, Z_u, Z_w	Dimensional stability derivatives of the force Z
$Z_{\delta_d}, Z_{\delta_f}, Z_{\delta_w}$	Control derivatives of the force Z
Y_v^+	Non-dimensional stability derivative
$\underline{z}_{meas}, \underline{z}_{pred}$	Measured and predicted measurement

Greek letters

α_0	Initial angle of attack, rad
α^*	Inclination angle, rad
δ_d	Dihedral deflection, rad
δ_e	Elevator deflection, rad
δ_f	Difference in flapping frequency between the wings , Hz
δ_r	Rudder input, rad
δ_w	Wing root angle, rad
ε	Residual
ζ_0	Dihedral angle, rad
$\hat{\theta}$	Parameter estimate
$\ddot{\theta}$	Pitch acceleration, $rads^{-2}$
$\bar{\theta}, \mathbf{\Theta}$	Parameter vector
$\theta_0, \theta_1, \theta_2, \theta_3$	Parameter terms
Θ_0	Initial pitch angle

ρ	Air density, kgm^{-3}
Σ	Covariance matrix
τ	Lag
$\boldsymbol{v}(i)$	Sensor noise vector
ϕ_m, ζ, ϕ_f	Wing sweep angle, rad
ϕ_{sp}	Setpoint roll angle, rad
ϕ, θ, ψ	Attitude angles, rad
Φ, Θ, Ψ	Attitude angles, rad
Φ_m, Θ_m, Ψ_m	Measured attitude angles, rad
$\dot{\phi}, \dot{\theta}, \dot{\psi}$	Attitude angular rates, $rads^{-1}$

Acronyms

COM	Center of mass
COP	Center of pressure
DARPA	Defence Advanced Research Projects Agency
EKF	Extended Kalman filter
FWMAV	Flapping-wing micro air vehicle
GLS	General least-squares
IEKF	Iterated extended Kalman filter
IMU	Inertial measurement unit
IV	Instrument Variable
LEV	Leading Edge Vortex
LPV	Linear parameter-varying
LTI	Linear time-invariant
MAV	Micro air vehicle
OLS	Ordinary least-squares
PD	Proportional differential (controller)
RMSE	Root mean-squared error
UAV	Unmanned aerial vehicles
WLS	Weighted least-squares

1

Introduction Thesis

Unmanned aerial vehicles (UAV's), and their smaller counterpart micro air vehicles (MAV's), have been found to be useful for a large variety of civil and military applications [14, 15, 17, 19, 75, 84]. A subcategory of UAV's are flapping wing micro air vehicles (FWMAV's). These FWMAV's have favorable properties such as: being able to fly at low velocities, having high agility and maneuverability and some even have the ability to hover[3, 36]. In general, FWMAV's are bio-inspired, either using the basic principles of the flapping motions for the thrust generation or trying to mimic the flapping mechanism of the animal as closely as possible. Inspirations for the design of the FWMAV's have been birds, such as the Nano Hummingbird [37], insects, as is the case for the Delfly family [17] and the KU Beetle [58], and bats, such as the Bat Bot B2 [59]. FWMAV's have also been used for the analysis of the control strategies of flying insects during various maneuvers, as was done in the research of Karásek et al. using the Delfly Nimble [36], in which it was shown that fruitflies use yaw and roll torque coupling during rapid bank turns. This was verified using an automated evasive roll maneuver. This complex and quick maneuver was possible due to the tailless design of the Delfly Nimble, although this did make the Delfly Nimble inherently unstable, as is the case for tailless FWMAV's [36, 37, 45, 58].

The Delfly Nimble is a member of the Delfly Family, a group of FWMAV's which has been developed at the Delft University of Technology. The development of the first Delfly dates back to 2005 [17]. The first versions of the Delfly have a tail, which passively stabilize the drone, as has been shown in research of Caetano et al. [9] and Armanini et al. [5]. The first tailless member of this family is the Delfly Nimble, which has a wingspan of 33 cm and a weight of approximately 27 $grams$. Due to the inherent instability of the Delfly Nimble, a PD-controller is used for control of the attitude of the Delfly Nimble, ensuring that the FWMAV remains airborne. The gains of the PD-controller were determined by trial and error, first analyzing the response of the Delfly Nimble while holding it in the hand and then in a later stage analyzing the response during flight. For the automated evasive roll maneuver used in the research of Karásak et al. [36] an open-loop program was developed, also tuned by trial and error. The probability of the Delfly Nimble crashing during such rapid maneuvers is high. Since this tailless FWMAV is fragile in nature, repairs would often be required after such a crash. In order to develop more automated rapid movements with fewer crashes, a simulation of the response of the Delfly Nimble could be used before implementing the maneuver or a new controller on the actual FWMAV. However, this would require a mathematical model of the dynamics of the Delfly Nimble. Several models have been identified for the **longitudinal** body dynamics using free-flight data [32, 33, 51, 52]. For the **lateral** body dynamics of the Delfly Nimble, such a model did not exist yet.

This thesis addresses the absence of a mathematical model of the **lateral** body dynamics of the Delfly Nimble. The main deliverable of this research is a such a model which has sufficient accuracy to be used for stability analysis and controller design. When only the body dynamics are considered, the identified dynamics are time-averaged, i.e. neglecting the influence of the wings. This assumption is valid when the flapping frequency is higher than the bandwidth of the system, i.e. the flapping frequency is larger than the highest natural frequency of the body dynamics [34]. This model will be developed using free-flight data and system identification approach, which consists of three phases: the experiment phase, the model identification phase, and the model validation phase. A similar approach had been taken in previous research, where models had been identified for the Delfly II [5, 9], and for the longitudinal body dynamics of the Delfly Nimble.

Various maneuvers were used during the experiments, such as roll doublets, 112-maneuvers in the roll direction, coupled maneuvers where inputs are given to multiple mechanisms, and roll doublets while the Delfly Nimble is flying sideways. Two types of model structures were used in this research: grey-box model structures, where the parameters are the stability and control derivatives, and black-box ones. The parameters were estimated using linear regression techniques, specifically the ordinary least-squares and the weighted least-squares. The accuracy of the identified models was analyzed using residual analysis and analysis of the statistical properties of the estimated parameters.

This thesis consists of three parts. In Part I, the main results of this research are shown in a scientific paper. This is followed by Part II, where the literature study is shown which consists of four chapters. In Chapter 2, the introduction of the literature study is given, in which the working principle of the Delfly Nimble and other FWMAV's is explained, the System Identification Cycle is elaborated on, and the research objective and the research questions are formulated. There are three sub-questions, each covering a phase of the System Identification Cycle. In Chapter 3, the development of the Equations of Motion is shown, and an overview is given of the maneuvers considered for this research. Chapter 4 gives an overview of the various model structures and parameter estimation techniques which were considered for this research. The final chapter of Part II is Chapter 5, where background information is given about the validation techniques used in this thesis. The final part of this Thesis is Part III, which also consists of four chapters. Chapter 6 is an introduction to this part, showing the lay-out of it. In Chapter 7, an overview is given of the maneuvers used during the experiments, the influence of the controller is analyzed, and the identifiability of the data is verified. This is followed by Chapter 8, where the results of the state estimation, the parameter estimation, and the analysis of the natural motions are shown. The final chapter of this part is Chapter 9, where the validation results of the identified models are discussed. The conclusions of this research, along with recommendations for future work are elaborated on in Chapter 10.

I

Scientific Paper

Model Identification of the lateral body dynamics near hover of a tailless four-winged flapping wing MAV using flight data

K.V.Bains *, C.C. de Visser †, and D.A. Olejnik ‡
Delft University of Technology, Delft, Zuid-Holland, 2629 HS

M. Karásek §
Flapper Drones, Delft, Zuid-Holland, 2629 HS

S.F.Armanini ¶
Imperial College London, London, South Kensington, SW7 2AZ

Flapping wing micro air vehicles (FWMAV's) are a subcategory of unmanned aerial vehicle which use flapping wings for thrust generation. The high agility and maneuverability of FWMAV's are very favorable attributes, making them more applicable in cluttered spaces. A tailless FWMAV called the Delfly Nimble has been developed at the Delft University of Technology. Due to the inherent instability of the tailless design an active controller is required to ensure safe and stable flight of the drone. In previous research, models have been developed for the longitudinal dynamics of the Delfly Nimble. In this paper, a grey-box state-space model of the lateral body dynamics in hover conditions is identified using system identification techniques. The parameters which needed to be estimated were stability and control derivatives, and they were obtained with a least-squares approach. Free-flight experiments were performed to generate the identification and validation data. A doublet train was used in the identification experiments, with the gains of the controller adjusted in such a way that maximum excitation was acquired. The identified model has been validated with various maneuvers. These included doublets, 112-maneuvers, maneuvers using coupled inputs, and maneuvers with sideways flight. The resulting model is able to predict the state derivatives of most maneuver accurately, reaching accuracies of over 90% for maneuvers close to hover. Moreover in closed-loop configuration it is able to simulate the state response accurately, with accuracies of over 85 % for maneuvers close to hover, and remains stable, making it applicable for controller design and stability analysis. Finally, based on the model the inherent instability of the lateral body dynamics was also confirmed, for there are eigenvalues with positive real parts.

*MSc Graduate Student, Faculty of Aerospace Engineering, Department of Control & Simulation, karan.vir.bains@gmail.com
†Assistant Professor, Faculty of Aerospace Engineering, Department of Control & Simulation, c.c.devisser@tudelft.nl
‡PhD student, Faculty of Aerospace Engineering, Department of Control & Simulation, d.a.olejnik@tudelft.nl
§CEO and Co-Founder Flapper Drones, matej@flapper-drones.nl
¶Research Associate, Department of Aeronautics, s.f.armanini@imperial.ac.uk

Nomenclature

$A_{ss}, B_{ss}, C_{ss}, D_{ss}$	=	Matrices in the state-space system
a_x, a_y, a_z	=	Linear body accelerations, ms^{-2}
f	=	Flapping frequency, Hz
f_L, f_R	=	Flapping frequency of the left and right wing, Hz
F_x, F_y, F_z	=	Forces along the body axes. N
g	=	Earth's gravitational constant, ms^{-2}
I_{xx}, I_{yy}, I_{zz}	=	Mass moment of inertias, kgm^2
I_{xy}, I_{yz}, I_{xz}	=	Products of inertias, kgm^2
$J(\mathbf{x}, \bar{\theta})$	=	Cost function
L, M, N	=	Aerodynamic moments along the body axes, Nm
L_p, L_v	=	Stability derivatives of the moment L
$L_{\delta_f}, L_{\delta_t}$	=	Control derivatives of the moment L
m	=	Mass. kg
p, q, r	=	Body angular rates, $rads^{-1}$
$\dot{p}, \dot{q}, \dot{r}$	=	Body angular accelerations, $rads^{-2}$
q_0, q_1, q_2, q_3	=	Attitude quaternions
$\mathbf{R}^2$	=	Goodness of fit
$\mathbf{r}_{xy}$	=	Output Correlation
RMSE	=	Root mean-squared error
$\hat{r}$	=	Radius of the second moment of inertia, m
$S_{pp}, S_{vv}, S_{\phi\phi}$	=	Power spectral densities of the states
t	=	Time, s
u, v, w	=	Body velocities, ms^{-1}
u_0, v_0, w_0	=	Initial body velocities, ms^{-1}
$\dot{u}, \dot{v}, \dot{w}$	=	Body accelerations, ms^{-1}
W	=	Weight matrix
$\mathbf{x}, \mathbf{x}_{ss}$	=	State vector
X, Y, Z	=	Aerodynamic forces along the body axes, N
x, y, z	=	Position in the inertial reference frame, m
$x_b, X_{body}, y_b, z_b, Z_{body}$	=	Body axes
$\mathbf{y}_{ss}$	=	Output vector

y_i	=	measurement point
Y_p, Y_v	=	Stability derivatives of the force Y
$Y_{\delta_f}, Y_{\delta_t}$	=	Control derivatives of the force Y
δ_d	=	Dihedral deflection, rad
δ_f	=	Difference in flapping frequency between the wings , $rads^{-1}$
δ_w	=	Wing root angle, rad
ε	=	Residual
$\hat{\theta}, \bar{\theta}$	=	Parameter estimate, parameter vector
$\hat{\mathbf{\Theta}}$	=	Estimated parameter
θ_0	=	Initial pitch angle, rad
$\lvert\hat{\sigma}\rvert$	=	Standard deviation of the parameter
ϕ_0	=	Initial roll angle, rad
ϕ_f	=	Wing flapping amplitude, rad
ϕ, θ, ψ	=	Attitude angles, rad
$\dot{\phi}, \dot{\theta}, \dot{\psi}$	=	Attitude angular rates, $rads^{-1}$

I. Introduction

Unmanned aerial vehicles (UAV's), and their smaller counterpart micro air vehicles (MAV's), have been found to be useful for a large variety of civil and military applications [1–6]. A subcategory of UAV's are flapping wing micro air vehicles (FWMAV's). These FWMAV's have favorable properties such as: being able to fly at low velocities, having high agility and maneuverability and some even have the ability to hover[7, 8]. In general, FWMAV's are bio-inspired, either using the basic principles of the flapping motions for the thrust generation or trying to mimic the flapping mechanism of the animal as closely as possible. Inspirations for the design of the FWMAV's have been birds, such as the Nano Hummingbird [9], insects, as is the case for the Delfly family [6] and the KU Beetle [10], and bats, such as the Bat Bot B2 [11]. FWMAV's have also been used for the analysis of the control strategies of flying insects during various maneuvers, as was done in the research of Karásek et al.[8] using the Delfly Nimble, in which it was shown that fruitflies use yaw and roll torque coupling during rapid bank turns. This was verified using an automated evasive roll maneuver. This complex and quick maneuver was possible due to the tailless design of the Delfly Nimble, although this did make the Delfly Nimble inherently unstable, as is the case for tailless FWMAV's [8–10, 12].

The Delfly Nimble is a member of the Delfly Family, a group of FWMAV's which has been developed at the Delft University of Technology. The development of the first Delfly dates back to 2005 [6]. The first versions of the Delfly have a tail, which passively stabilize the drone, as has been shown in research of Caetano et al. [13] and Armanini et al.

[14]. The first tailless member of this family is the Delfly Nimble, which has a wingspan of 33 cm and a weight of approximately 27 $grams$. Due to the inherent instability of the Delfly Nimble, a PD-controller is used for control of the attitude of the Delfly Nimble, ensuring that the FWMAV remains airborne. The gains of the PD-controller were determined experimentally, first analyzing the response of the Delfly Nimble while holding it in the hand and then in a later stage analyzing the response during flight. For the automated evasive roll maneuver used in the research of Karásak et al. [8] an open-loop program was developed, also tuned using trial and error. The probability of the Delfly Nimble crashing during such rapid maneuvers is high. Since this tailless FWMAV is fragile in nature, repairs would often be required after such a crash. In order to develop more automated rapid movements with fewer crashes, a simulation of the response of the Delfly Nimble could be used before implementing the maneuver or a new controller on the actual FWMAV. However, this would require a mathematical model of the dynamics of the Delfly Nimble. Several models have been identified for the ***longitudinal*** body dynamics using free-flight data [15–18]. For the ***lateral*** body dynamics of the Delfly Nimble, such a model did not exist yet.

The main contribution of this paper is a mathematical model of the ***lateral*** body dynamics of the Delfly Nimble. The resulting model in this research is the first one which focuses on the lateral part of the body dynamics, instead of the longitudinal part. When only the body dynamics are considered, the identified dynamics are time-averaged, i.e. neglecting the high frequency components. This assumption is valid when the flapping frequency is higher than the bandwidth of the system, i.e. the flapping frequency is larger than the highest natural frequency of the body dynamics [19]. Due to the focus on only the body dynamics, the rigid body approximation can be used, as has been done in previous research for the stability analysis of hovering insects and the modeling of flapping flight [14, 17, 19–26]. The parameters of the mathematical model are determined using linear regression techniques.

The remainder of this paper consists of six more sections. In Section II, the experimental setup is outlined. Section III shows the model structure which has been used for the development of the mathematical model. The paper continues with Section IV, in which the parameter estimation is elaborated on. This is followed by Section V, which describes the various maneuvers used during the experiments. The modeling results are clarified in Section VI. The conclusion and recommendations for future work are written in Section VII.

II. Experimental Setup

A. The Delfly Nimble

The FWMAV used in this research, the Delfly Nimbe is inherently unstable due to its tailless design. Therefore, an active controller is required for stable flight, and uses different control mechanisms compared to the tailed versions of the Delfly, which had most of the control surfaces built in the tail. The control mechanisms used in the Delfly Nimble are shown in Figure 1.

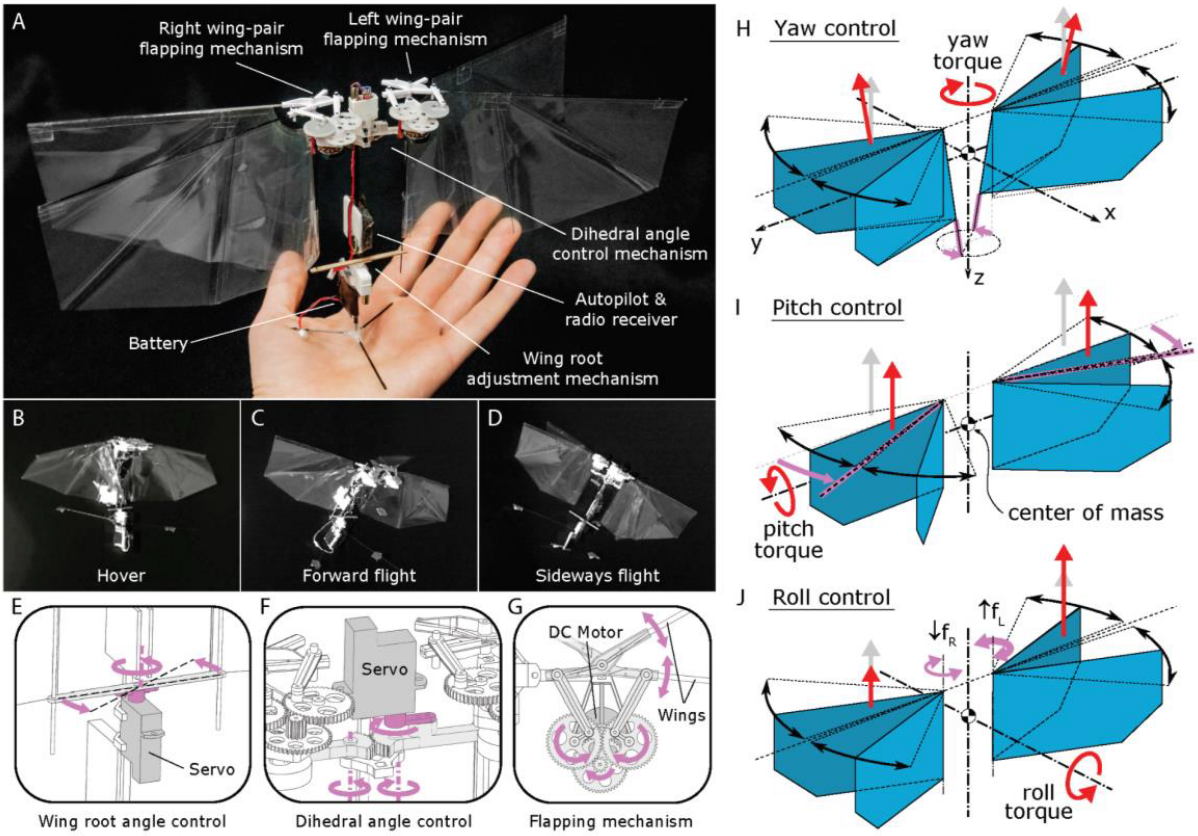

Fig. 1 Explanation of the working principle of the Nimble. In A an overview of the various components. In B to D, three different flights are shown, hover, forward and sideways. E to G show the working principle of the servos and flapping mechanism. H to J explain the control of the yaw, pitch and roll attitude.[8]

It can be seen that the Delfly Nimble uses wing modulation techniques for the control of its attitude. Wing twist modulation is used to control the yaw attitude. A servo is used in order to change the wing root angle angle, shown in **H** of Figure 1. For the control of the pitch attitude, it changes the dihedral angle using a servo, shown in **I** of Figure 1. For control of the roll attitude it does not use wing modulation. Instead, the roll attitude is controlled by generating a difference in the flapping frequencies of both wings, shown in **J** of Figure 1. This difference in flapping frequency generates a roll torque. The side with the lower frequency is the one where the Delfly Nimble rolls towards. The amount of torque required for stable flight is determined by a controller. The controller for the pitch and roll attitude is shown in **A** and **B** of Figure 2 [8]. A reference generator is used to determine the input to the proportional and derivative controller. The controller for the yaw angle is show in **C** of Figure 2. This controller uses a proportional gain and also an additional feed-forward loop. The gains have been determined by trial and error, first by observing the stability of the Delfly Nimble while holding it in hand, and then by observing the stability in flight. For more complex maneuvers, such as rapid bank turns and pitch and roll flips, an open-loop program can be switched to. The autopilot is then in the open-loop configuration, switching back to the closed-loop one in order to recover the Delfly Nimble after the maneuver

and preventing crashing [8].

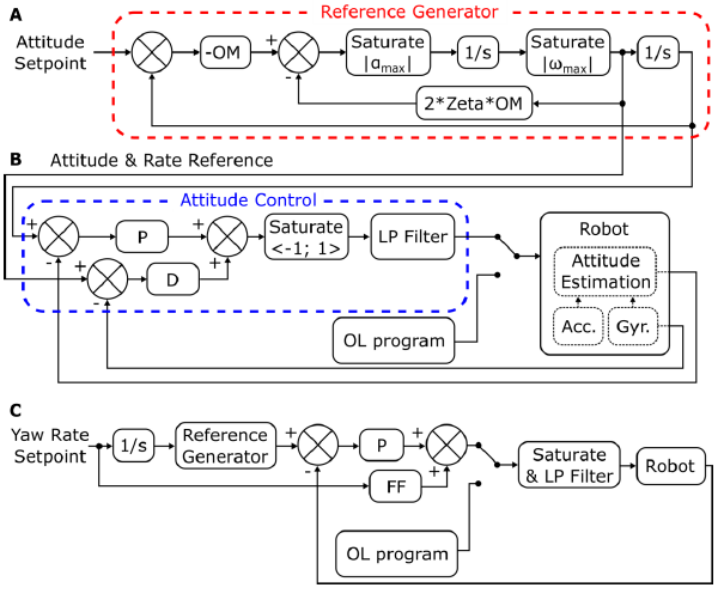

Fig. 2 Schematics of the on-board controller [8]. The controller for the roll and pitch attitude is shown in A and B. In A the reference generator is shown. In B the attitude controller is shown which has proportional and derivative terms. The open-loop program is used for more rapid maneuvers. In C the yaw loop is shown, which only uses a proportional controller and an additional feedforward term.

B. Sensors and processing of the data

The flight data experiments were done in the flight arena called the "Cyberzoo" in the faculty of Aerospace Engineering at the Delft University of Technology. This arena has a size of $10 \times 10 \times 7$ m, and uses 12 Prime 17W OptiTrack Motion tracking cameras. Gathered data from the motion tracking system was complemented by the on-board sensory output, for which a Lisa/MXS autopilot was used. An overview of the obtained measurements is shown in Table 1.

Table 1 Overview of the data obtained from the Optitrack Motion tracking system and the on-board systems.

Source	Obtained measurements	Sampling frequency (Hz)
OptiTrack	Position (x,y,z)	200
	Attitude Quaternions (q_0, q_1, q_2, q_3)	200
On-board	Angular Velocities (p, q, r)	512
	Linear Accelerations (a_x, a_y, a_z)	512
	Flapping frequency right (f_R)	100
	Flapping frequency left (f_L)	100
	Dihedral servo deflection (δ_d)	100
	Wing root servo deflection (δ_w)	100
	Throttle value (δ_t)	5

The OptiTrack (OT) data consisted of the position of the Delfly Nimble and the attitude quaternions, which were converted to the attitude angle ϕ, θ, and ψ. In order to capture the data, four reflective markers with a diameter of approximately 20 mm were mounted on the Delfly Nimble. The marker setup is illustrated in Figure 3.

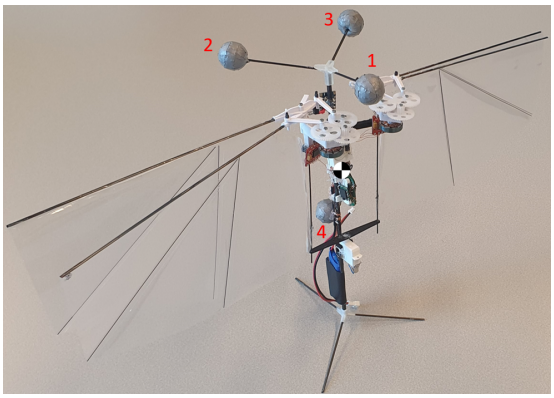

Fig. 3 Marker setup of the Delfy Nimble used for capturing the positions and attitude quaternions in the OptiTrack Motion tracking system. Three markers are on the 'crown', and one is just below the autopilot.

The mean error of the position of the markers was 0.85 mm. The on-board data consisted of measurements from the MPU-6000 inertial measurement unit, which recorded the angular velocities and the linear accelerations, and also of deflections of control mechanisms, such as the flapping frequencies of both wings, servo deflections, and throttle values. The gyroscopes had an accuracy of 0.05 $^\circ/s$, and the accelerometers had an accuracy of 0.05 g in the X and Y direction, and 0.08 g in the Z direction. The two sources of data were synchronized by the same procedure developed by Armanini et al.[27], and was used for the model identification of the Delfly II. Sensor fusion was applied to assure high accuracy of the data, using an Extended Kalman Filter. For the data fusion, all the data was upsampled to 512 Hz. The fused data was then filtered using a zero-phase Butterworth filter in order to reduce the noise in the data.

III. Model Structure Definition

In many existing studies, the stability analysis of hovering insects and the modeling of flapping flight dynamics was done using the rigid body approximation [14, 17, 19–26]. The following assumptions are made for the determination of the nonlinear equations of motion (EOM's) [28, 29]: the body of the vehicle is rigid, the mass of the vehicle is constant, the Earth is flat and non-rotating, and X_bZ_b is a symmetry plane, so I_{xy} and I_{yz} are assumed to be zero. The rigid body assumption can be made if only the body dynamics of the Delfly Nimble are analysed, i.e. if the flapping dynamics and the body dynamics of the Delfly Nimble can be treated separately. This is the case when the flapping frequency is higher than the bandwidth of the system [19]. For the Delfly Nimble the estimated natural frequencies for the lateral body dynamics are around the 1 to 2 Hz in the roll direction, while the mean flapping frequency is 17 Hz. The natural frequencies were estimated using analytic models of flapping flight. Based on the assumptions and the defined axis

system of Figure 4, the nonlinear equations for the aerodynamic forces and moments, defined in Equation (1) to (6), and the kinematic equations, shown in Equations (7) to (9) are determined.

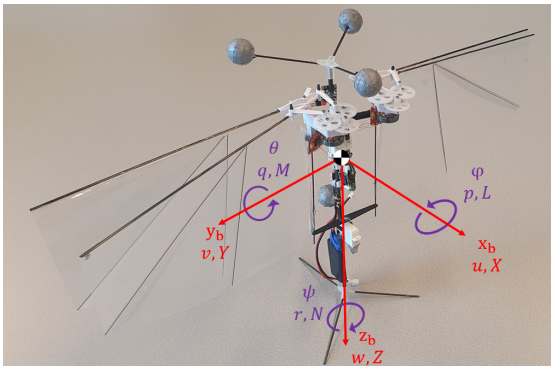

Fig. 4 Axis system used on the Delfly Nimble.

$$F_x = X - mg \cdot \sin(\theta) \qquad = \overbrace{m \cdot (\dot{u} + qw - rv)}^{states} \tag{1}$$

$$F_y = Y + mg \cdot \cos(\theta) \cdot \sin(\phi) \qquad = m \cdot (\dot{v} + ru - pw) \tag{2}$$

$$F_z = \underbrace{Z + mg \cdot \cos(\theta) \cdot \cos(\phi)}_{forces} \qquad = m \cdot (\dot{w} + pv - qu) \tag{3}$$

$$M_x = \quad L \quad = \overbrace{I_{xx} \cdot \dot{p} + (I_{zz} - I_{yy}) \cdot qr - I_{xz} \cdot (\dot{r} + pq)}^{states} \tag{4}$$

$$M_y = \quad M \quad = I_{yy} \cdot \dot{q} + (I_{xx} - I_{zz}) \cdot rp - I_{xz} \cdot (p^2 + r^2) \tag{5}$$

$$M_z = \underbrace{N}_{moments} = I_{zz} \cdot \dot{r} + (I_{yy} - I_{xx}) \cdot pq - I_{xz} \cdot (\dot{p} - qr) \tag{6}$$

$$\dot{\phi} = p + q \cdot \sin(\phi) \cdot \tan(\theta) + r \cdot \cos(\phi) \cdot \tan(\theta) \tag{7}$$

$$\dot{\theta} = q \cdot \cos(\phi) - r \cdot \sin(\phi) \tag{8}$$

$$\dot{\psi} = q \cdot \frac{\sin(\phi)}{\cos(\theta)} + r \cdot \frac{\cos(\phi)}{\cos(\theta)} \tag{9}$$

Here F_x, F_y, F_z are the forces, and M_x, M_y, M_z are the external moments about the x, y, z axes. The m is the mass of the Delfly Nimble and the g is the gravitational constant. Furthermore, u, v, w are the body velocities, $\dot{u}$, $\dot{v}$, $\dot{w}$ are the body accelerations, p, q, r are the angular rates, $\dot{p}$, $\dot{q}$, $\dot{r}$ are the angular accelerations, X, Y, Z are the aerodynamic

forces, L, M, N are the aerodynamic moments, I_{xx} etc. are the inertia terms, ϕ, θ, ψ are the attitude angles, and $\dot{\phi}$, $\dot{\theta}$, $\dot{\psi}$ are the attitude angular rates. For the analysis of the dynamics, the linearized EOM's will be used, as is done often for aircraft systems [28, 30]. The linearization is done using two techniques, the Taylor series expansion and the small perturbation theorem [28, 31]. The EOM's are further simplified by use of the additional assumption that the longitudinal and lateral dynamics are decoupled. For the lateral dynamics it is then assumed that only the aerodynamic force Y, the aerodynamic moments L and N, and the states p, r, v, and ϕ are included. The EOM's are further simplified by assuming that the roll and yaw dynamics are decoupled, omitting N and r from the EOM's of the lateral dynamics. This assumption was made because there was little excitation seen in the yaw dynamics in the data gathered during the identification experiments, explained in more detail in Appendix D. For the control inputs, only the inputs δ_f and δ_t are included in the EOM's, for only these inputs are actively given during the maneuvers. Leaving out the inputs δ_d and δ_w did not greatly influence the model accuracy. The resulting linearized EOM's are defined in Equations (10) to (12).

$$L_p \Delta p + L_v \Delta v + L_{\delta_f} \Delta \delta_f + L_{\delta_t} \Delta \delta_t = I_{xx} \cdot \Delta \dot{p} \tag{10}$$

$$Y_p \Delta p + Y_v \Delta v + Y_{\delta_f} \Delta \delta_f + Y_{\delta_t} \Delta \delta_t + mg \cdot cos(\theta_0) \cdot cos(\phi_0) \cdot \Delta \phi = m \cdot (\Delta \dot{v} - w_0 \cdot \Delta p) \tag{11}$$

$$\Delta \dot{\phi} = \Delta p \tag{12}$$

Where L_p, L_v, Y_p, and Y_v are the stability derivatives and L_{δ_f}, L_{δ_t}, Y_{δ_f}, and Y_{δ_t} are the control derivatives. The stability and control derivatives are the parameters to be estimated. For given initial conditions w_0, θ_0 and ϕ_0, these EOM's can then be formulated in a linear time-invariant state-space system, the general form of which consists of the state equation shown in Equation (13), and the output equation shown in Equation (14).

$$\dot{\mathbf{x}}_{ss}(t) = A_{ss} \cdot \mathbf{x}_{ss}(t) + B_{ss} \cdot \mathbf{u}_{ss}(t) \tag{13}$$

$$\mathbf{y}_{ss}(t) = C_{ss} \cdot \mathbf{x}_{ss}(t) + D_{ss} \cdot \mathbf{u}_{ss}(t) \tag{14}$$

Substituting the linearized EOM's of Equations (10) to (12), into Equation (13) results in Equation (15).

$$\begin{bmatrix} \dot{p} \\ \dot{v} \\ \dot{\phi} \end{bmatrix} = \begin{bmatrix} \frac{I_{zz}}{I_c} \cdot L_p & \frac{I_{zz}}{I_c} \cdot L_v & 0 \\ \frac{Y_p}{m} + w_0 & \frac{Y_v}{m} & g \cdot \cos(\theta_0) \cdot \cos(\phi_0) \\ 1 & 0 & 0 \end{bmatrix} \cdot \begin{bmatrix} p \\ v \\ \phi \end{bmatrix} + \begin{bmatrix} \frac{I_{zz}}{I_c} \cdot L_{\delta_f} & \frac{I_{zz}}{I_c} \cdot L_{\delta_t} \\ \frac{Y_{\delta_f}}{m} & \frac{Y_{\delta_t}}{m} \\ 0 & 0 \end{bmatrix} \cdot \begin{bmatrix} \delta_f \\ \delta_t \end{bmatrix} \tag{15}$$

Where I_c is as defined by Equation (16).

$$I_c = I_{xx} \cdot I_{zz} - I_{xz}^2 \tag{16}$$

In the output equation shown in Equation (14) the matrix C_{ss} is set to an identity matrix, and the matrix D_{ss} to a zero matrix, resulting in Equation (17).

$$\mathbf{y}_{ss}(t) = \mathbf{x}_{ss}(t) \tag{17}$$

IV. Parameter Estimation

The parameters to be estimated are the stability and control derivatives shown in the state-space system of Equation (15). These were estimated using a least-squares approach, a variant of linear regression techniques. In this approach the sum of squares of the residuals are minimized, which is done by optimizing the cost function shown in Equation (18) [32].

$$J(\mathbf{x}, \bar{\theta}) = \sum_{i=1}^{N} \varepsilon_i^2 = \sum_{i=1}^{N} (y_i - A(x_i) \cdot \bar{\theta})^2 \tag{18}$$

The main goal is to find a set of parameters $\bar{\theta}$ which minimizes the cost function J. In the state-space system shown in Equation (15) only the state derivatives $\dot{p}$ and $\dot{v}$ are calculated using the stability and control derivatives. The least-squares approach is then applied to each of the equations of the state derivatives $\dot{p}$ and $\dot{v}$. The output equations of the state derivatives are defined in Equations (19) and (20).

$$\frac{I_c}{I_{zz}} \cdot \begin{bmatrix} \dot{p}_1 \\ \dot{p}_2 \\ \vdots \\ \dot{p}_N \end{bmatrix} = \begin{bmatrix} p_1 & v_1 & \delta_{f_1} & \delta_{t_1} \\ p_2 & v_2 & \delta_{f_2} & \delta_{t_2} \\ \vdots & \vdots & \vdots & \vdots \\ p_N & v_N & \delta_{f_N} & \delta_{t_N} \end{bmatrix} \cdot \begin{bmatrix} \hat{L}_p \\ \hat{L}_v \\ \hat{L}_{\delta_f} \\ \hat{L}_{\delta_t} \end{bmatrix} \tag{19}$$

$$= A(\mathbf{x}) \cdot \hat{\theta}_L$$

$$m \cdot \begin{bmatrix} \dot{v}_1^* \\ \dot{v}_2^* \\ \vdots \\ \dot{v}_N^* \end{bmatrix} = \begin{bmatrix} p_1 & v_1 & \delta_{f_1} & \delta_{t_1} \\ p_2 & v_2 & \delta_{f_2} & \delta_{t_2} \\ \vdots & \vdots & \vdots & \vdots \\ p_N & v_N & \delta_{f_N} & \delta_{t_N} \end{bmatrix} \cdot \begin{bmatrix} \hat{Y}_p \\ \hat{Y}_v \\ \hat{Y}_{\delta_f} \\ \hat{Y}_{\delta_t} \end{bmatrix} \tag{20}$$

$$= A(\mathbf{x}) \cdot \hat{\theta}_Y$$

Where N is the total number of data-points. In Equation (20) $\dot{v}^*$ is shown instead of $\dot{v}$ since there are constant terms in the equation for $\dot{v}$ which need to be put to the left hand side of the equation. The $\dot{v}^*$ is defined in Equation (21).

$$\dot{v}^* = \dot{v} - w_0 \cdot p - g \cdot \cos(\theta_0) \cdot \cos(\phi_0) \cdot \phi \tag{21}$$

When the ordinary least-squares (OLS) approach is used, it is assumed that the residual ε resembles white noise with a mean of zero. The stability and control derivatives can then be estimated using the OLS estimators shown in Equations (22) and (23).

$$\hat{\theta}_L = \left(A(\mathbf{x})^T \cdot A(\mathbf{x})\right)^{-1} \cdot A(\mathbf{x})^T \cdot \frac{I_c}{I_{zz}} \cdot \dot{p} \tag{22}$$

$$\hat{\theta}_Y = \left(A(\mathbf{x})^T \cdot A(\mathbf{x})\right)^{-1} \cdot A(\mathbf{x})^T \cdot m \cdot \dot{v}^* \tag{23}$$

The main advantage is that the OLS estimator is a simple algorithm. However, this method is very sensitive to sensor noise. Outliers in the data can greatly influence the identified parameters, leading to a very different mathematical model. One of the ways this issue can be resolved is to add weights to the measurement points. When this is done the weighted least-squares (WLS) approach is used. The weights are added using a weight matrix, defined in Equation (24).

$$W = \begin{bmatrix} \sigma_1^2 & 0 & \dots & 0 \\ 0 & \sigma_2^2 & \ddots & \vdots \\ \vdots & \ddots & \ddots & 0 \\ 0 & \dots & 0 & \sigma_N^2 \end{bmatrix} \tag{24}$$

Where $\sigma_1^2, \sigma_2^2, ..., \sigma_N^2$ are the sensor noise variances of each data point. The weight matrix is determined using prior knowledge about the system. This prior knowledge can be obtained by first using a OLS estimator, and determine the covariance matrix of the residuals. The terms of the diagonal of the covariance are then the variances of the individual data points, which are used to develop the weight matrix, as shown in Equations (25) and (26).

$$COV_\varepsilon = E\left\{\varepsilon \cdot \varepsilon^T\right\} \tag{25}$$

$$W = diag\left(COV_\varepsilon\right) \tag{26}$$

The diagonal elements of COV_{OLS} are the variances of the data-points. The stability and control derivatives can then be estimated using the WLS estimators shown in Equations (27) and (28).

$$\hat{\theta}_L = \left(A(\mathbf{x})^T \cdot W^{-1} \cdot A(\mathbf{x})\right)^{-1} \cdot A(\mathbf{x})^T \cdot W^{-1} \cdot \frac{I_c}{I_{zz}} \cdot \dot{p} \tag{27}$$

$$\hat{\theta}_Y = \left(A(\mathbf{x})^T \cdot W^{-1} \cdot A(\mathbf{x})\right)^{-1} \cdot A(\mathbf{x})^T \cdot W^{-1} \cdot m \cdot \dot{v}^* \tag{28}$$

Additionally, the maximum likelihood estimator was also tested, but due to the unstable nature of the identified state-space model convergence was not achieved.

V. Flight data experiments

One of the main difficulties in running the experiments was that they had to be done in closed-loop, for the Delfly Nimble is inherently unstable. The natural dynamics could then be dampened by the controller, which leads to less information contained in the flight data. There are three methods which have been proposed for the system identification of closed-loop systems: the direct approach, the indirect approach, and the joint input-output approach [33, 34]. In this research the direct approach is taken, where the controller is ignored in the model identification process. When using this approach it is important that there is sufficient information contained in the measurement data. The identifiability of the data, i.e. the information contained in the data, is maximized by exciting the natural motions as much as possible [32]. The following measures can be been used to achieve maximum excitation [32, 34, 35]: reducing the controller gains, giving larger commands, or giving direct commands to the control surfaces. In this research the first two measures were applied in order to maximize the excitation of the natural motions. For the identification of a mathematical model of the lateral body dynamics the roll control mechanisms were used primarily for the excitation of the lateral natural motions. A PD-controller was used to control the roll attitude and for the experiments the gains of this controller were adjusted. An overview of the gains is shown in Table 2.

Table 2 Overview of the gains of the roll controller which were used during the open-loop and closed-loop experiments. The closed-loop gains are identical to those used in the research of Karásek et al. [8].

Gain	Open-loop gains (fast gains)	Closed-loop gains (slow gains)
Proportional	1.406	0.625
Derivative	0.200	0.156

The proportional gain was increased in order to maximize excitation. When this gain would be increased too much it induced oscillations in the roll direction during hover. In order to minimize the oscillations, the derivative gain was also increased slightly. In the remainder of this research, the gains of the open-loop experiments are indicated as the 'fast' gains, and the gains of the closed-loop experiments are indicated as 'slow' gains. In total, there were four categories of maneuvers used during the flight data experiments: identification maneuvers, validation maneuvers, coupled maneuvers

and nonlinear maneuvers. The following section will further explain the details of the experiments.

A. Identification maneuvers

The data captured during the identification maneuvers is used for the estimation of the parameters. Therefore, it is important that sufficient information is contained in the data, which is ensured by maximizing the excitation during the maneuver. To acquire the most excitation, the fast gains shown in Table 2 were used during these experiments. A train of doublets was chosen as the maneuver for the identification experiments, with hovering as the initial condition. The maneuver was carried out by giving roll angle and throttle commands to the Delfly Nimble. The increase in throttle was necessary to prevent the Delfly Nimble from losing altitude, for the lift is decreased due to the rolling motion. The required increase of throttle was determined by applying a throttle factor THR_F, calculated using Equation (29).

$$THR_F = \frac{1}{\cos(\phi_{sp})} \tag{29}$$

Where ϕ_{sp} is the maximum set-point roll angle during the maneuver. The roll and throttle commands for the doublet train are shown in Figure 5.

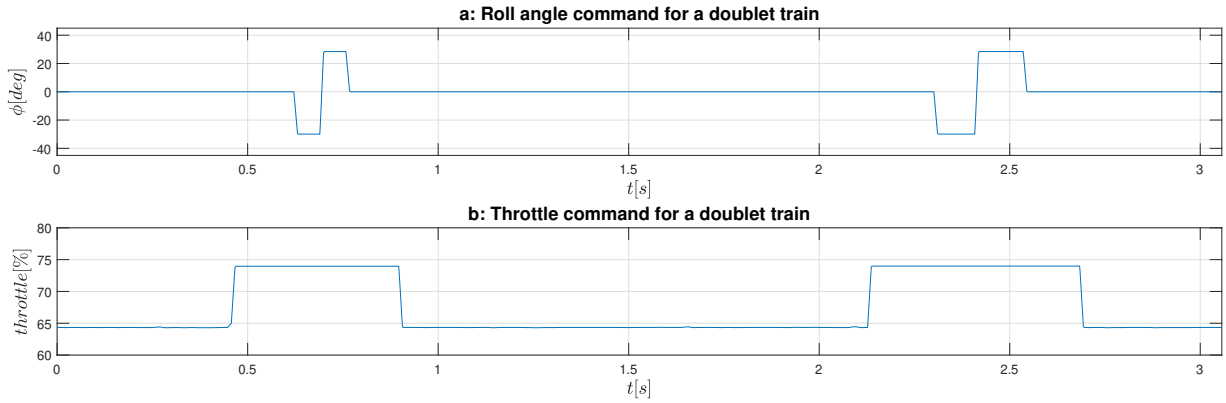

Fig. 5 a) The roll command, and b) the throttle command for the doublet trains. The main frequencies of the doublets are 7 and 4 Hz.

The main frequencies excited during this doublet train are 7 and 4 Hz. These values were chosen iteratively. Initially, the widths of the doublet were determined by estimating the natural frequencies using analytic models of flapping flight, such as the models in the research of Karásek et al. [8, 36], where the flapping flight dynamics of the drone fly was analyzed. However, the main frequencies of the natural motions of the lateral body dynamics were estimated to be around 1 and 2 Hz. When using these frequencies, the Delfly Nimble moves away a lot from the hover condition, which is not desirable when identifying a linear model. Therefore, doublets with a higher main frequencies, i.e. a smaller width, in order to minimize the movement away from the initial condition, while maintaining maximum excitation.

B. Validation maneuvers

Two types of validation experiments were conducted: open-loop data and closed-loop data. For generating the open-loop data the fast gains were used, and for the closed-loop data the slow gains were used. For the validation experiments, two maneuvers were used: doublets and the 112-maneuver. The doublets which were used for the validation of the mathematical had different main frequencies from the doublets used in the identification data. The roll commands given for the 112-maneuver are illustrated in Figure 6. This 112-maneuver used the fast gains. For the closed-loop validation data the main frequencies were set lower, namely 4 and 2 Hz, for there was very little excitation of the 7 Hz pulse when using the slow gains. The initial condition of all the validation maneuvers was also the Delfly Nimble hovering.

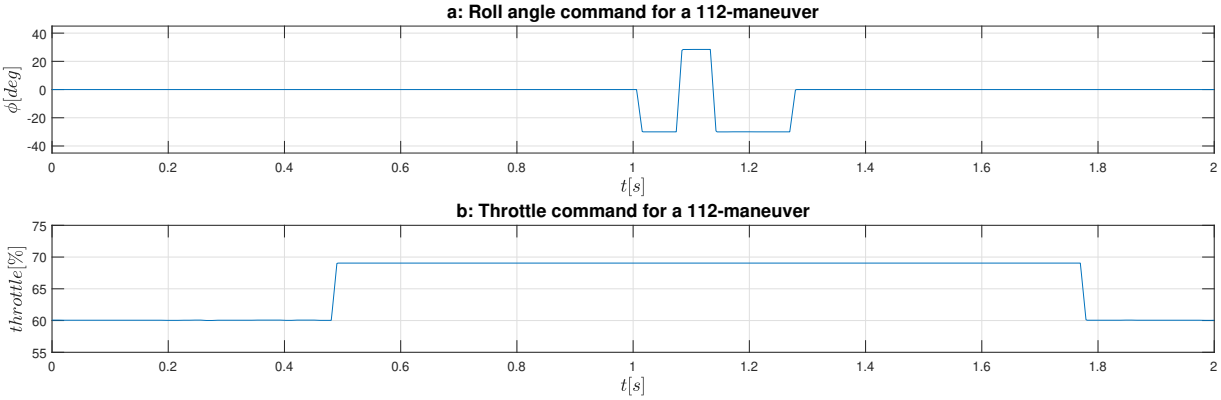

Fig. 6 a) The roll command, and b) the throttle command for the 112-maneuvers. The main frequencies in the maneuver shown are 7 and 3.5 Hz.

C. Coupled maneuvers

One of the assumptions made for the derivation of the state-space system shown in Equation (15) is that the longitudinal and lateral dynamics are decoupled. In order to verify the justifiability of this assumption, the accuracy of the identified model was analyzed for coupled maneuvers. These maneuvers are coupled in the sense that inputs are given to multiple control mechanisms. The coupled maneuver used during the experiments is the coupled doublet, where first an input is given in pitch angle, making the Delfly Nimble fly forward, and then an input is given in roll angle, making the Delfly do a doublet. The fast gains were used during this maneuver. The roll angle commands for the coupled doublet is shown in Figure 7. The main frequency of this coupled doublet is 6 Hz, and the initial condition is the Delfly Nimble hovering. Similar to the previous maneuver, the throttle was increased during the maneuver to prevent the Delfly Nimble from losing altitude.

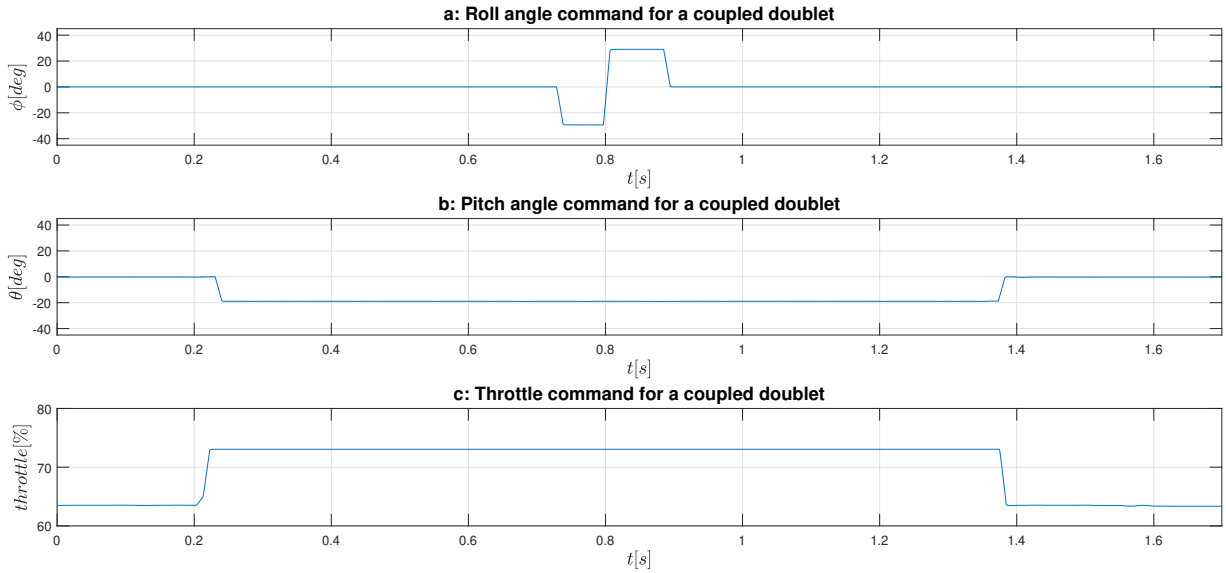

Fig. 7 a) The roll command, b) the pitch command, and c) the throttle command for the coupled doublet maneuver. The main frequency of this maneuver is 6 Hz.

D. Nonlinear maneuvers

For the derivation of the state-space model the nonlinear equations for the aerodynamic forces, the aerodynamic moments, and the kinematic equations were linearized using a Taylor series expansion and the small perturbation theorem. It is then implicitly assumed that the lateral body dynamics of the Delfly Nimble can be modeled using a linear model structure. In order to verify the justifiability of this assumption, experiments using nonlinear maneuvers were also conducted. These maneuvers are nonlinear since they move away a lot from the initial condition, which was hovering flight of the Delfly Nimble. The maneuvers used are the nonlinear doublets, where the Delfly Nimble is doing a doublet in roll direction while flying sideways. The commands for the nonlinear doublet are illustrated in Figure 8.

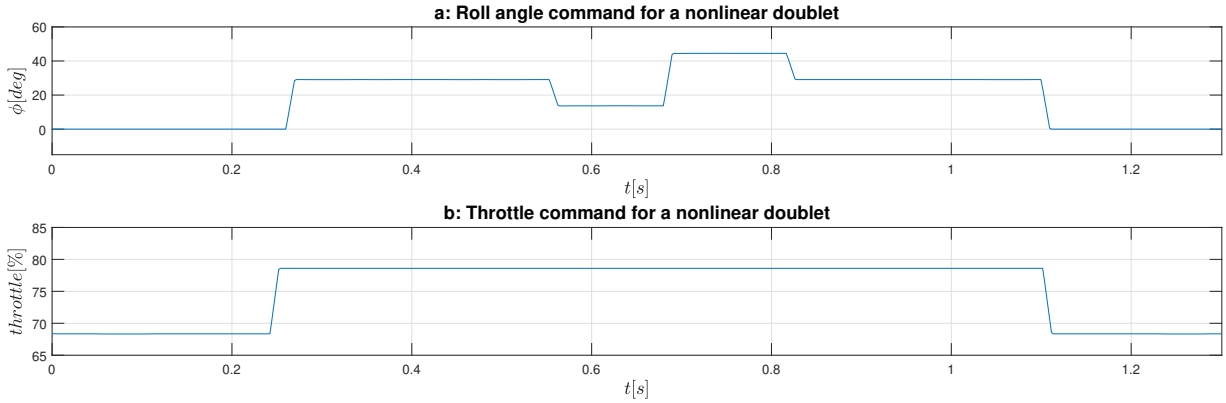

Fig. 8 a) The roll command, and b) the throttle command for the nonlinear doublet maneuver. The initial roll command was 30° to make the Delfly Nimble move sideways, the deflection angle for the doublet was 15°, and the main frequency of the doublet is 4 Hz.

The fast gains were used during these maneuvers. During the nonlinear doublet, a constant roll angle command of 30° is given to make the Delfly Nimble fly sideways, and then an additional roll angle command is given to enforce the doublet. The deflection angle of the doublet is set to 15°. and the main frequency of the is 4 Hz. In addition to this nonlinear doublet, there were also maneuvers which used a constant roll angle of 20°.

E. Influence of the controller

The commands for the roll angle for the maneuvers show in the previous section does not directly go to the flapping mechanisms of the Delfly Nimble, but goes through a reference generator and a PD-controller as shown in Figure 2. The set-point roll angle first goes through the reference generator, which filters the set-point roll angle heavily, and the output is the reference roll angle. The difference between the two angle is shown in Figure 9 for the doublet train used in the identification experiments.

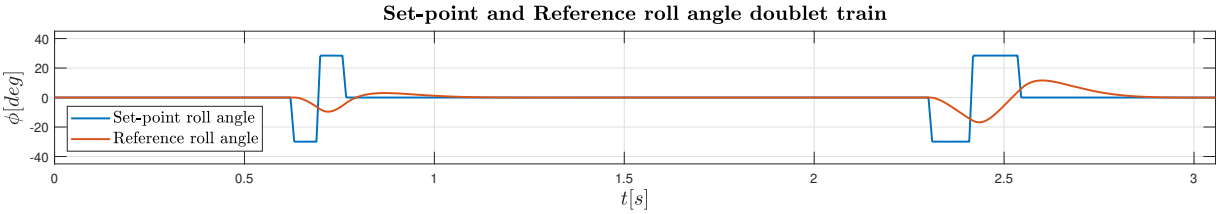

Fig. 9 The set-point roll angle and the reference roll angle for the doublet train maneuver.

From Figure 9 it can be seen that the range of the reference roll angle is much smaller than the range of the set-point roll angle. The reference roll angle goes through the PD-controller, which limits the movement of the Delfly Nimble even more, further decreasing the dynamic excitation. In spite of the reference generator and the PD-controller, there was still movement of the Delfly Nimble visible during the identification experiments. This is illustrated in Figure 10, where the doublet maneuver is clearly visible. The Delfly Nimble follows the reference roll angle well, especially during the first parts of the doublets, when a negative roll angle command is given. In the remainder of the doublet maneuver, when a positive roll angle command is given, there is a substantial overshoot. This is due to the large P-gain which was used during the identification maneuvers, as shown Table 2. There is also a delay visible between the reference roll angle and the actual roll angle. This is caused by the inertia of the Delfly Nimble. When the roll angle command is given, a deflection input is given to the control mechanism for the roll attitude, which in this case are the wings.

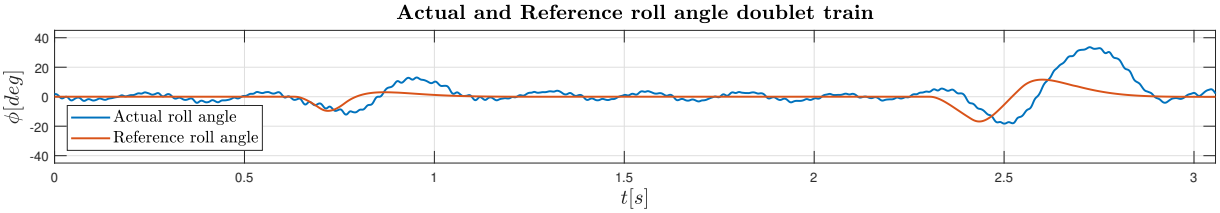

Fig. 10 The reference roll angle and the actual roll angle for the doublet train maneuver.

VI. Results and discussion

A. Identification Results

The identifiability of the data was verified by analyzing the power spectral density (PSD) plots of the states during the maneuver. Two power spectrums of the states are shown in Figure 11: during hover, and during the identification maneuver. The PSD plots of the states during the maneuver have higher values around 1 to 4 Hz compared to the PSD plots of the states during hover. The eigenfrequencies which were estimated using analytic models were found to be in the range of 1-2 Hz. Since there are peaks visible around these frequencies it can be concluded that the natural body dynamics are excited well during the identification maneuver.

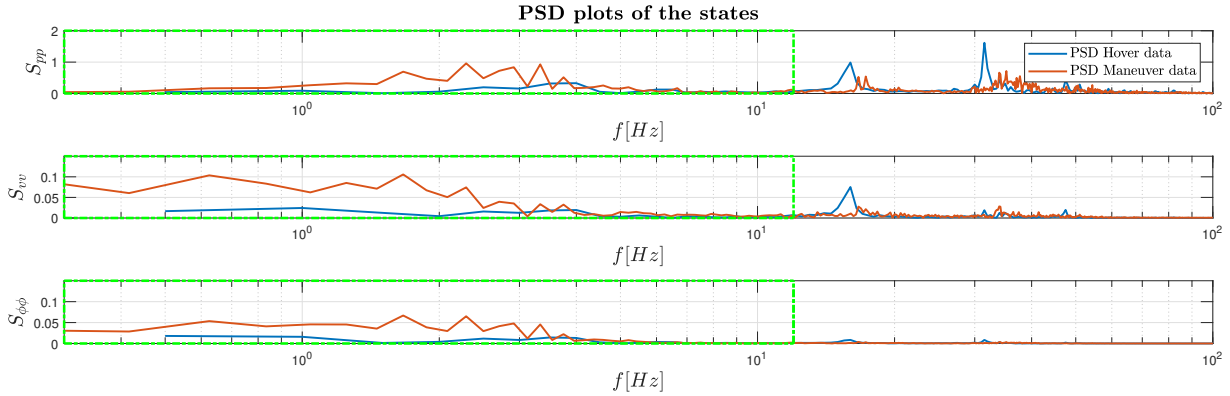

Fig. 11 Power Spectral Density (PSD) plots of the states of the Delfly Nimble during hover and the identification maneuver. The green square in the power spectrums of the states contains the frequency content up to 9 Hz. The components inside this square were filtered out using using a zero-phase Butterworth filter with order of 10.

The green square in the power spectrums of the states contains the frequency content up to 9 Hz. The components **inside** this square were used in the identification data, filtered out using using a zero-phase Butterworth filter with order of 10. The estimation results of the state derivatives using the WLS approach and the state-space system of Equation (15) are presented in Figure 12. The accuracy metrics of the WLS estimation can be found in Table 4, and the estimated stability and control derivatives are presented in Table 3. From Figure 12 and Table 4 it can be seen that the state derivatives are estimated well with the state-space system shown in Equation (15). The residuals also show good whiteness, which can be seen in the autocorrelation plots in Figure C.1. Based on Table 3 it is clear that L_p, L_v and L_{δ_t} have a very high sensitivity to noise, indicated by the high relative value of the standard deviation. This indicates that the parameter estimation process can be improved. Using the estimated stability and control derivatives, the geometric properties of the Delfly, and Equation (15) the state-space model of the lateral body dynamics can be acquired. The resulting numerical state-space system is defined in Equation (B.2). The estimated stability derivatives have been compared to the stability derivatives of the drone fly, discussed in Appendix A.

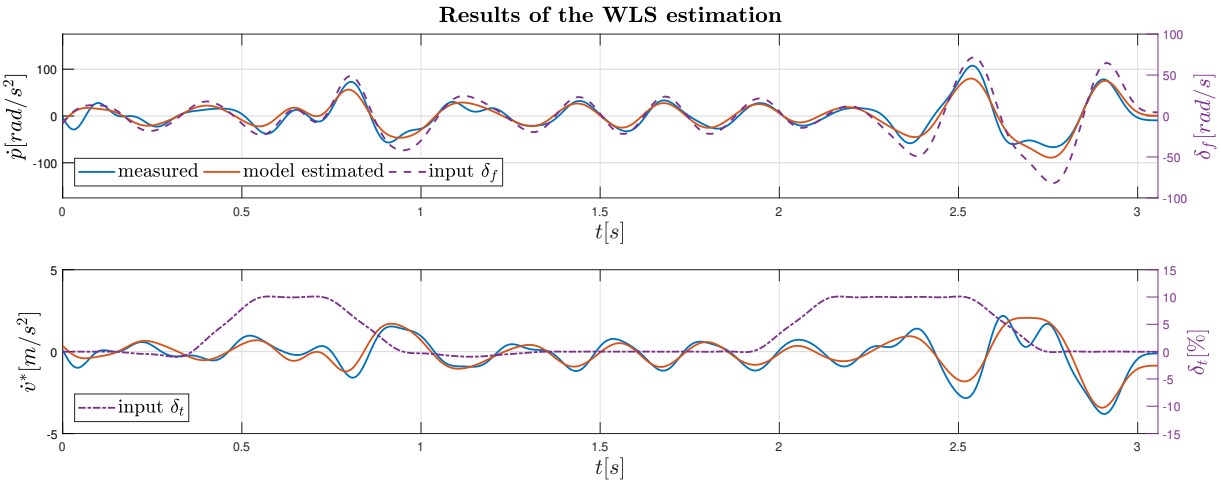

Fig. 12 Results of the WLS estimation for each state derivative. $\dot{v}^*$ is as defined in Equation (21).

Table 3 Estimated parameters for the state-space system shown in Equation (15) as a result of the WLS estimator.

Estimated Parameters Reduced Grey-Box Model			
Stability Derivative	$\hat{\Theta}$	$\lvert\hat{\sigma}\rvert$	$100\lvert\hat{\sigma}/\hat{\Theta}\rvert$
L_p	-2.43×10^{-4}	1.69×10^{-4}	6.96×10^{1}
L_v	-3.74×10^{-4}	1.52×10^{-3}	4.07×10^{2}
Y_p	2.75×10^{-3}	3.31×10^{-6}	1.20×10^{-1}
Y_v	-5.61×10^{-2}	3.32×10^{-5}	5.92×10^{-2}
Control Derivative	$\hat{\Theta}$	$\lvert\hat{\sigma}\rvert$	$100\lvert\hat{\sigma}/\hat{\Theta}\rvert$
L_{δ_f}	1.06×10^{-4}	8.47×10^{-6}	8.02×10^{0}
L_{δ_t}	4.19×10^{-5}	5.48×10^{-5}	1.31×10^{2}
Y_{δ_f}	-8.63×10^{-4}	1.22×10^{-7}	1.41×10^{-2}
Y_{δ_t}	-4.05×10^{-4}	4.55×10^{-7}	1.12×10^{-1}

Table 4 Accuracy metrics for the estimation results shown in Figure 12.

Accuracy Metrics Three-State Grey-Box Model			
Output Variable	$\mathbf{r}_{xy}$	$\mathbf{R}^2$	**RMSE** (% of meas. range)
$\dot{p}$	0.945	0.907	9.99 $\frac{rad}{s^2}$ (5.74)
$\dot{v}$	0.982	0.967	0.38 $\frac{m}{s^2}$ (2.84)

The eigenvalues of the estimated state-space system using four different data-sets are plotted in the complex plane, shown in Figure 13, and the values of the eigenvalues are shown in Table 5. It can be observed that the Delfly Nimble has a stable aperiodic mode and an unstable oscillatory mode in the roll direction. There are variations visible in the eigenvalues between datasets, which is mainly caused by the different amount of excitation during the experiment, with dataset #1 having the most excitation, while dataset #3 having the least. To analyze the physical meaning of the modes the eigenvectors were determined. To account for the differences in numerical ranges of each state, the eigenvectors were non-dimensionalized using Equations (30) to (32)[37].

$$p^+ = \frac{p}{f} \qquad (30) \qquad v^+ = \frac{v}{2 \cdot \phi_f \cdot f \cdot \hat{r}} \qquad (31) \qquad \phi^+ = \frac{\phi}{2 \cdot \pi} \qquad (32)$$

Table 5 Eigenvalues of the state-space system using four different identification data-sets.

Eigenvalues identified models		
ID Data	λ_1	$\lambda_{2,3}$
#1	-5.18	$0.32 \pm 2.73i$
#2	-6.84	$0.39 \pm 3.74i$
#3	-7.19	$0.97 \pm 4.26i$
#4	-7.45	$0.30 \pm 3.65i$

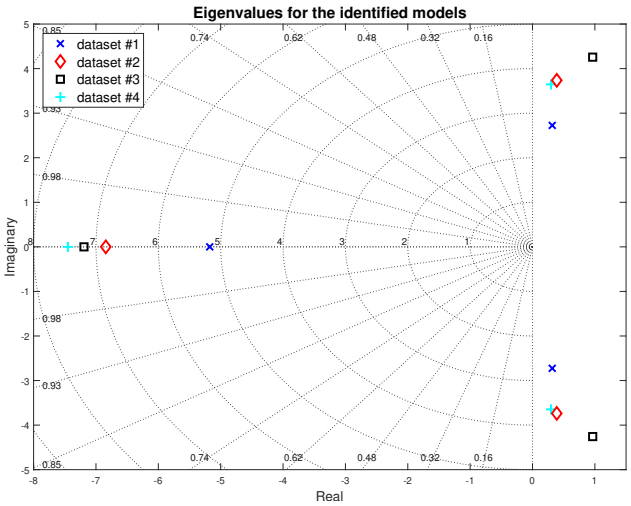

Fig. 13 Eigenvalues of the state-space system using four different identification data-sets plotted on the complex plane.

Where the flapping frequency f was set to 106.8 rad/s (17 Hz), the flapping amplitude ϕ_f to 1.536 rad (88°), and the $\hat{r}$ to 7.45×10^{-2} meter. The terms of the eigenvector are shown in their polar form, and all the states will be normalized with respect tot the roll angle ϕ^+.

Table 6 Eigenvectors of the estimated state-space mode using data-set #1 . The terms in the eigenvectors have been non-dimensionalized and normalized with respect to ϕ^+.

Eigenvector Three-State Grey-Box Model		
State	**Mode 1**	**Mode 2**
p	0.30 (180°)	0.16 (83.4°)
v	0.86 (180°)	0.70 (-53.5°)
ϕ	1.0 (0°)	1.0 (0°)

In the eigenvector of the first mode shown in Table 6 it can be noticed that the variables ϕ^+ and v^+ have a phase shift of 180°, meaning that when the Delfly is for example moving sideways to the left, it is rolled in the opposite direction to the right, which has a stabilizing effect, explaining why the eigenvalue is located in the left half of the complex plane. In the eigenvector of the second mode it can be seen that the main variables are the v^+ and the ϕ^+. However, the phase shift between the v^+ and the ϕ is -53.5°, which means that a large portion of the oscillation cycle of these two variables have the same sign, i.e. when the Delfly is for example moving sideways to the left it is rotated in the same direction, which has a destabilizing effect. This explains why the real part of the eigenvalue of this maneuver is in the right half of the complex plane.

B. Validation Results: Open-Loop

For the open-loop validation the state derivatives were determined with the identified state-space model of Equation (B.2) and the measured states. The following maneuvers are for the open-loop validation: doublets and the 112-maneuver. The estimation results of a doublet with a main frequency of 6 Hz is shown in Figure 14, and the accuracy metrics of this estimation are found in Table 7. The estimation results of a 112-maneuver with main frequencies of 3.5 and 7 Hz are illustrated in Figure 15, and the accuracy metrics of this estimation are indicated in Table 8.

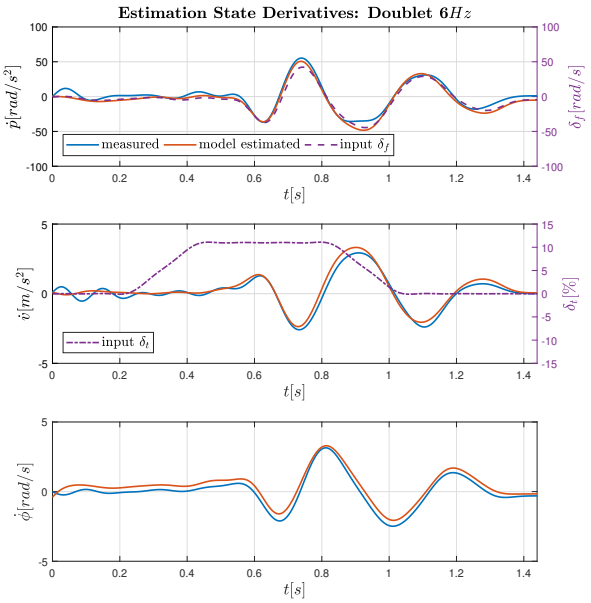

Fig. 14 Estimation results of the state derivatives for a doublet with a main frequency of 6 Hz using the identified state-space model.

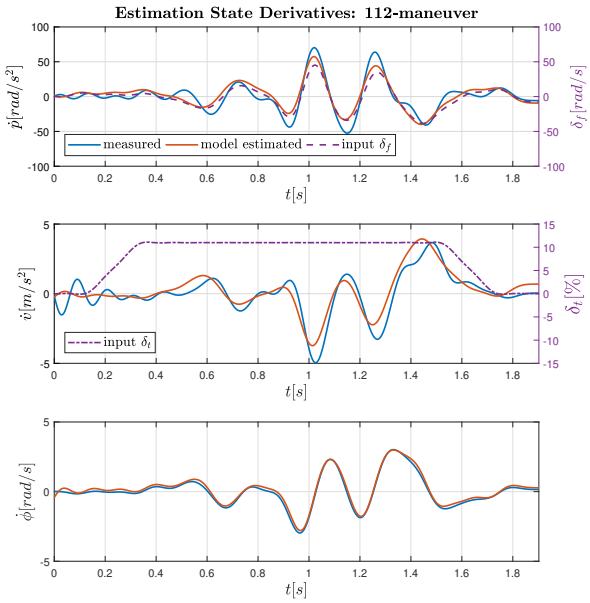

Fig. 15 Estimation results of the state derivatives for a 112-maneuver with main frequencies of 3.5 Hz and 7 Hz using the identified state-space model.

Table 7 Accuracy metrics of the estimation of the state derivatives for a doublet with a main frequency of 6 Hz using the identified state-space model.

Accuracy Metrics OL Validation Data: Doublet 6 Hz			
Output Variable	$\mathbf{r}_{xy}$	$\mathbf{R}^2$	**RMSE** (% of meas. range)
$\dot{p}$	0.985	0.924	5.51 $\frac{rad}{s^2}$ (5.99)
$\dot{v}$	0.981	0.948	0.28 $\frac{m}{s^2}$ (4.99)
$\dot{\phi}$	0.996	0.890	0.38 $\frac{rad}{s^2}$ (6.77)

Table 8 Accuracy metrics of the estimation of the state derivatives for a 112-maneuver with main frequencies of 3.5 and 7 Hz using the identified state-space model.

Accuracy Metrics OL Validation Data: 112-maneuver			
Output Variable	$\mathbf{r}_{xy}$	$\mathbf{R}^2$	**RMSE** (% of meas. range)
$\dot{p}$	0.918	0.848	8.84 $\frac{rad}{s^2}$ (7.20)
$\dot{v}$	0.908	0.823	0.63 $\frac{m}{s^2}$ (7.27)
$\dot{\phi}$	0.998	0.980	0.16 $\frac{rad}{s^2}$ (2.66)

From the presented Figures 14 and 15, and Tables 7 and 8, it can be argued that the state derivatives of both maneuvers are estimated well with the identified state-space model, for the accuracy metrics are in the same range as the

accuracy metrics of the estimation of the identification data. The residuals also resemble whiteness, as can be seen in the autocorrelation plots in Figures C.2 and C.3.

C. Validation Results: Closed-Loop

For the closed-loop validation, the state response during a maneuver is simulated using a Simulink model, which uses a one to one copy of the controller architecture and the identified state-space model. The measured input δ_t was used in the simulation. Furthermore, the actuator dynamics of the flapping mechanism is simulated using a slightly modified version of the model which was developed in the research of Kajak et al. [15, 16]. The only modification to the model of the flapping mechanism was multiplying the output with a gain of $\frac{1}{1.4}$, in order to get the simulated input δ_f as close as possible to the the actual input. The transfer function used to model the flapping dynamics is defined in Equation (33).

$$H_{flap}(s) = \frac{8.97}{s + 12.56} \tag{33}$$

The closed-loop validation was done using both the fast and slow gains of Table 2. For the closed-loop validation using the fast gains, a doublet train was used, where the main frequencies are 7 Hz and 4 Hz. The results of the simulation of the states of the doublet train are shown in Figure 16. Note that this not the same doublet train which was used for the model identification.

The simulated state response seems more oscillatory compared to the measured state response. The main reason for this deviation is that the input δ_f is simulated, which is not coherent with the actual input. The difference is illustrated in Figure 17. It can be seen that the simulated input δ_f is more oscillatory than the actual input, which in turn also leads to a more oscillatory simulated state response. The accuracy metrics of the states and the input are shown in Table 9. The autocorrelation plots of the residuals of this simulation are presented in Figures C.4 and C.5, which show that the residuals are more coloured.

Table 9 Accuracy metrics of the simulated state response of a doublet train. Here the main frequencies of the doublets were 7Hz and 4 Hz, and the simulation was caried out using the fast gains.

Accuracy Metrics CL Validation Data: Doublet Train with fast gains			
Output Variable	$\mathbf{r}_{xy}$	$\mathbf{R}^2$	**RMSE** (% of meas. range)
p	0.868	0.438	1.01 $\frac{rad}{s}$ (12.51)
v	0.687	0.177	0.13 $\frac{m}{s}$ (15.51)
ϕ	0.809	0.429	0.09 rad (12.32)
δ_f	0.866	0.633	12.59 $\frac{rad}{s}$ (10.95)

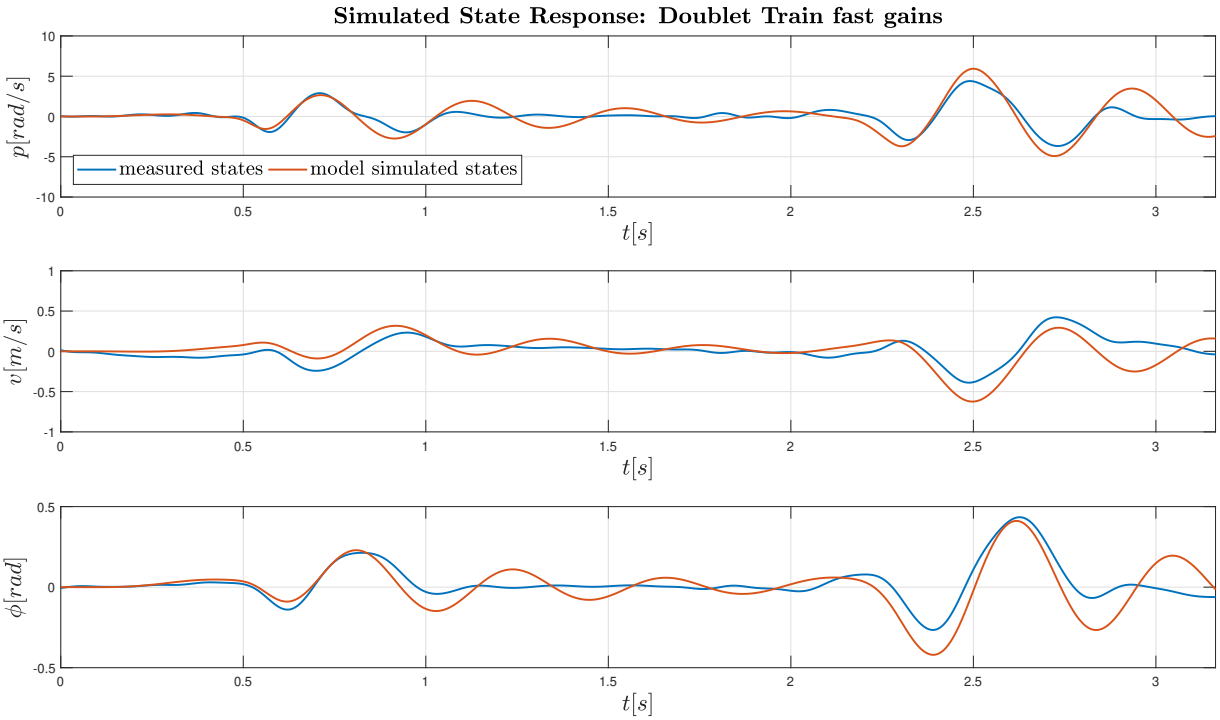

Fig. 16 Measured and simulated state response of a doublet train. Here the main frequencies of the doublets were 7Hz and 4 Hz, and the simulation was caried out using the fast gains.

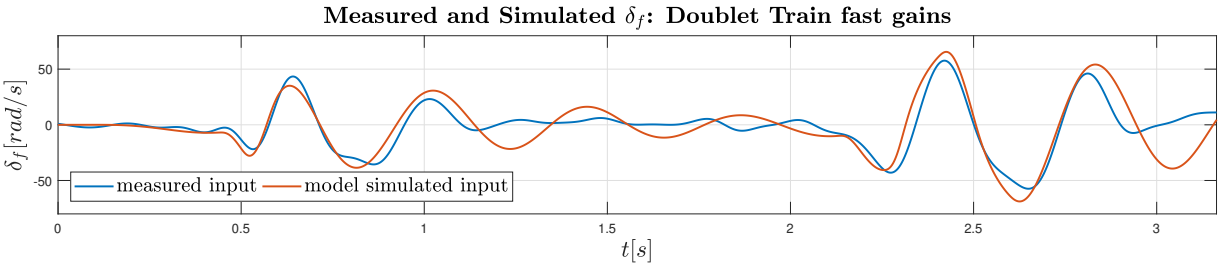

Fig. 17 Measured and simulated input δ_f for a doublet train maneuver. Here the main frequencies of the doublets were 7Hz and 4 Hz, and the simulation was caried out using the fast gains.

For the closed-loop validation using the slow gains of the controller, two maneuvers were used: a doublet train main frequencies of 6, 4 and 2 Hz, and 112-maneuvers with main frequencies of 4 and 2 Hz. The simulated states of the doublet train are shown in Figures 18, the simulated input δ_f for this maneuver can be seen in Figure 20, and the accuracy metrics are found in Table 10. The simulated states of the 112-maneuvers are illustrated in Figures 18, the simulated input δ_f for this maneuver is presented in Figure 20, and the accuracy metrics are indicated in Table 10. The state response of the doublet train is simulated accurately with the Simulink model. The same can be stated for the 112-maneuvers, although there is a noticeable reduction of the accuracy of the state v. The simulated states and the inputs are less oscillatory than those of the simulation which uses the fast gains. The simulations of both the doublet train and the 112-maneuvers are stable, because the Delfly Nimble returns to the hover between maneuvers. However,

when the Delfly Nimble has returned to hover, there are still small oscillations occurring, which are not captured by the identified model. These oscillations can also be seen in the input signal δ_f. This leads to less favorable values of the accuracy metrics, and also to more coloured residuals, as can be see in the autocorrelation plots in Figures C.6, C.8, C.7, and C.9. These oscillations could be caused due to time-varying dynamics, which were not included in this research. Based on these results it can be concluded that the identified model can be used in a closed-loop configuration, making it applicable for the stability analysis of the body dynamics, and for controller design.

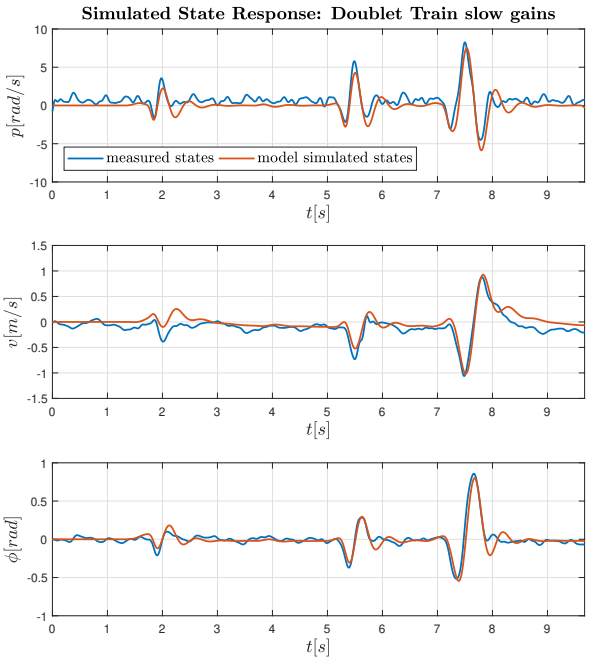

Fig. 18 Simulated state response of a doublet train with three doublets. Here the main frequencies of the doublets were 6, 4 and 2 Hz, and the simulation was carried out using the slow gains.

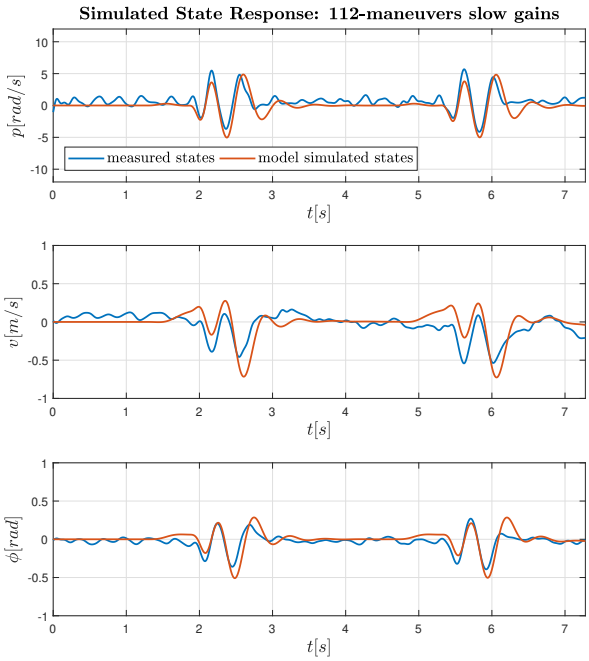

Fig. 19 Simulated state response of multiple 112-maneuvers. Here the main frequencies of the doublets were 4 and 2 Hz, and the simulation was carried out using the slow gains.

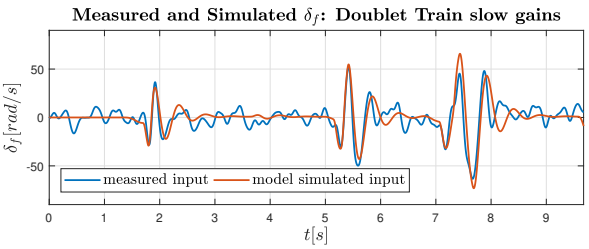

Fig. 20 Measured and simulated input δ_f of a doublet train with three doublets. Here the main frequencies of the doublets were 6, 4 and 2 Hz, and the simulation was carried out using the slow gains.

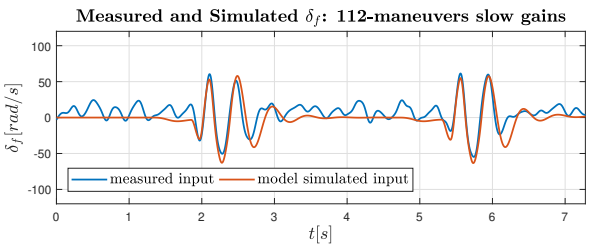

Fig. 21 Measured and simulated input δ_f of multiple 112-maneuvers. Here the main frequencies of the doublets were 4 and 2 Hz, and the simulation was carried out using the slow gains.

Table 10 Accuracy metrics of the simulated state response of a doublet train with three doublets. Here the main frequencies of the doublets were 6, 4 and 2 Hz, and the simulation was carried out using the slow gains.

Accuracy Metrics CL Validation Data: Doublet Train with slow gains			
Output Variable	$\mathbf{r}_{xy}$	$\mathbf{R}^2$	**RMSE** (% of meas. range)
p	0.900	0.542	0.92 $\frac{rad}{s}$ (7.18)
v	0.905	0.657	0.13 $\frac{m}{s}$ (6.49)
ϕ	0.915	0.837	0.06 rad (4.42)
δ_f	0.792	0.575	9.85 $\frac{rad}{s}$ (8.50)

Table 11 Accuracy metrics of the simulated state response of multiple 112-maneuvers. Here the main frequencies of the doublets were 4 and 2 Hz, and the simulation was carried out using the slow gains.

Accuracy Metrics CL Validation Data: 112-maneuvers with slow gains			
Output Variable	$\mathbf{r}_{xy}$	$\mathbf{R}^2$	**RMSE** (% of meas. range)
p	0.865	0.467	0.99 $\frac{rad}{s}$ (10.13)
v	0.650	0.171	0.14 $\frac{m}{s}$ (19.46)
ϕ	0.815	0.387	0.08 rad (11.45)
δ_f	0.856	0.492	12.77 $\frac{rad}{s}$ (11.00)

D. Model accuracy coupled maneuvers

Coupled doublets were used to analyze the justifiability of the assumption of decoupled longitudinal and lateral dynamics. The results of the estimation of the state derivatives of the coupled doublet are shown in Figure 22, and the accuracy metrics of this estimation are indicated in Table 12.

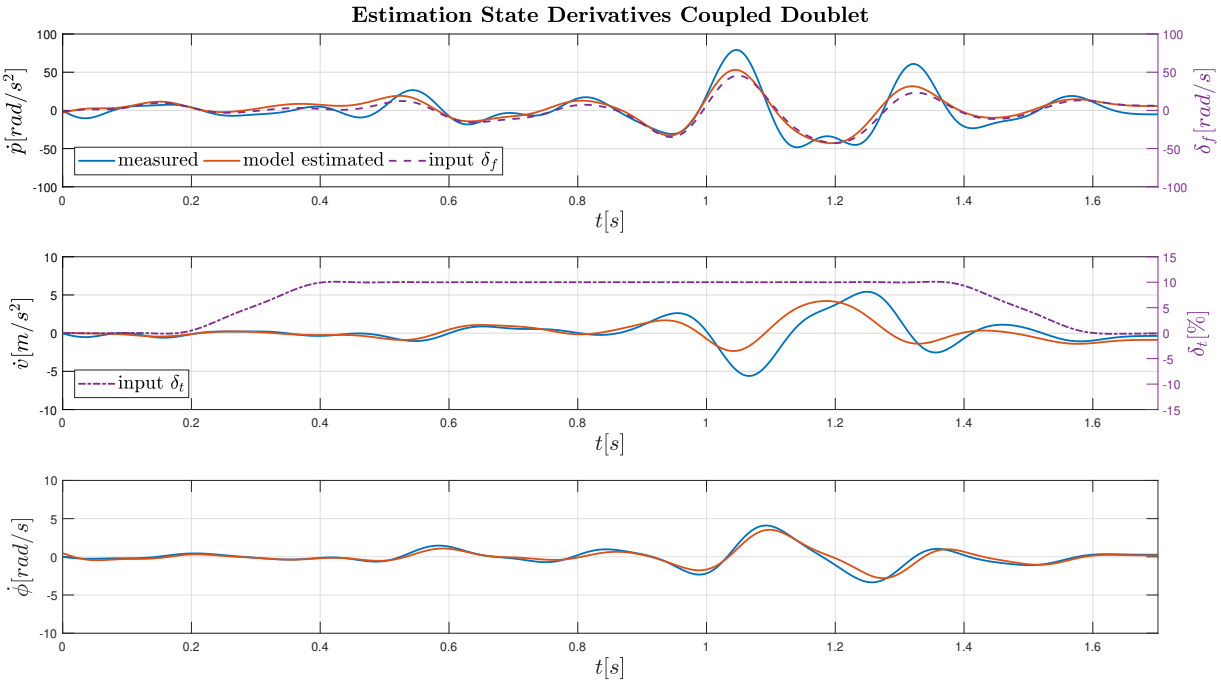

Fig. 22 Estimation results of the state derivatives for a coupled doublet with a main frequency of 6 Hz using the identified state-space model.

Table 12 Accuracy metrics of the estimation shown Figure 22. The validation data was a coupled doublet with a main frequency of 6 Hz, and the estimation was done using the state-space model shown in Equation (15).

Accuracy Metrics Validation Data: Coupled Doublet 6 Hz			
Output Variable	$\mathbf{r}_{xy}$	$\mathbf{R}^2$	**RMSE** (% of meas. range)
$\dot{p}$	0.927	0.845	9.27 $\frac{rad}{s^2}$ (7.27)
$\dot{v}$	0.699	0.523	1.23 $\frac{m}{s^2}$ (11.17)
$\dot{\phi}$	0.964	0.923	0.34 $\frac{rad}{s}$ (4.54)

It can be observed that the estimation accuracy of $\dot{v}$ has decreased significantly. This also leads to more coloured residuals, visible in the autocorrelation plots in Figure C.10. This could indicate that the absence of the dihedral input δ_d does have a significant influence on the model accuracy of coupled maneuvers. In order to verify this, models were also identified which included the input δ_d in the state-space model. However, when the inputs δ_f, δ_d, and δ_t were included in the model, the eigenvalues of the resulting model were very different from those seen in Table 5, which would lead to a less accurate estimation of the state derivatives. This may be due to coupling effects when all three inputs are included in the model structure used for the identification. Though this was not further investigated in this research. Instead, two different combinations of inputs were used in the state-space model to analyze the influence of dynamic coupling. In the first combination, only the input δ_f was included in the state-space model. The numeric state-space model which only includes δ_f is shown in Equation (B.4). The estimation results for this model are shown in Figure 23, and the accuracy metrics for this estimation are found in Table 13. In the second combination of inputs, the inputs δ_f and δ_d were incorperated in the state-space model. The numeric state-space model which includes δ_f and δ_d is shown in Equation (B.6). The estimation results when this model is used are shown in Figure 24, and the accuracy metrics for this estimation are indicated in Table 14.

Table 13 The accuracy metrics for the estimation of a coupled doublet with a main frequency of 6 Hz using an identified state-space model with only the δ_f as input.

Accuracy Metrics Coupled Doublet: δ_f only			
Output Variable	$\mathbf{r}_{xy}$	$\mathbf{R}^2$	**RMSE** (% of meas. range)
$\dot{p}$	0.912	0.832	9.62 $\frac{rad}{s^2}$ (7.55)
$\dot{v}$	0.695	0.509	1.25 $\frac{m}{s^2}$ (11.33)
$\dot{\phi}$	0.964	0.923	0.34 $\frac{rad}{s}$ (4.54)

Table 14 The accuracy metrics for the estimation of a a coupled doublet with a main frequency of 6 Hz using an identified state-space model with δ_f and δ_d as inputs.

Accuracy Metrics Coupled Doublet: δ_f and δ_d			
Output Variable	$\mathbf{r}_{xy}$	$\mathbf{R}^2$	**RMSE** (% of meas. range)
$\dot{p}$	0.915	0.840	9.41 $\frac{rad}{s^2}$ (7.39)
$\dot{v}$	0.689	0.506	1.25 $\frac{m}{s^2}$ (11.36)
$\dot{\phi}$	0.964	0.923	0.34 $\frac{rad}{s}$ (4.54)

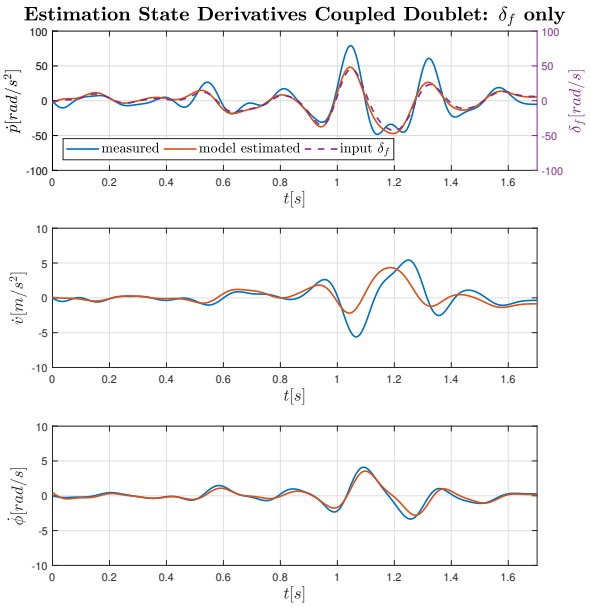

Fig. 23 Estimation results of the state derivatives for a coupled doublet with a main frequency of 6 Hz using an identified state-space model with only the δ_f as input.

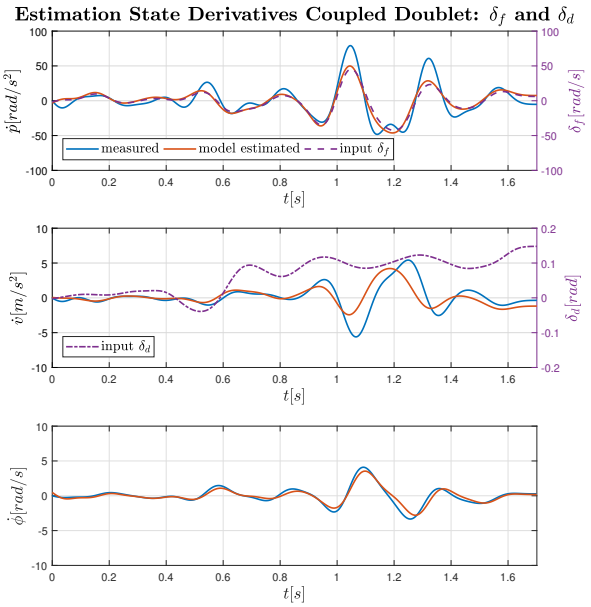

Fig. 24 Estimation results of the state derivatives for a coupled doublet with a main frequency of 6 Hz using an identified state-space model with δ_f and δ_d as inputs.

From Figures 23 and 23, it can be seen that when only the input δ_f is included in the state-space model, the accuracy of the estimated state derivatives is very similar compared to the accuracies of the estimation shown in Figure 22 and Table 12. Furthermore, the autocorrelation plots are similar when comparing Figure C.11 to Figure C.10. When the input δ_d is included in the state-space model, there is no improvement in the accuracy of the estimation of $\dot{v}$, as can be seen in Figure 24 and Table 14. Furthermore, the autocorrelation plots are again very similar when comparing Figure C.12 to Figure C.10. This indicates that the model accuracy is not influenced when coupled inputs are given, suggesting that the assumption that the longitudinal and lateral dynamics are uncoupled can be made. The main cause of the reduction in accuracy of the estimation of $\dot{v}$ could instead be the forward motion during the maneuver. The maximum value of the forward velocity u was $1.22\frac{m}{s}$, while a maximum of $0.40\frac{m}{s}$ was reached in the identification data, suggesting that the reduced accuracy may not mainly be due to the coupled inputs, but also because of the Delfly Nimble moving away a lot from the initial condition of the identification maneuver, which was the Defly Nimble hovering.

The influence of forward flight on the lateral dynamics has been researched by Xu et al. [38]. In this research, the lateral dynamics of a bumblebee were analyzed by determining the stability derivatives with different forward flight velocities. From the results it could be seen that the unstable mode, which for the bumblebee was aperiodic, became more stable as the forward flight velocity increases. The main cause of this is the influence of lateral inflow on the leading edge vortex (LEV). For insects, it has been shown that such a vortex is present on the leading edge of their wings [39]. When there is lateral inflow from the wingroot to the wingtip, the LEV is intensified and the amount of

lift generated increases. In the opposite case, when the lateral inflow goes from the tip to the root, the LEV is less concentrated and the amount of lift generated decreases [40, 41]. This leads to a difference in lift generated between the wings, causing instability. In forward flight, the mean position of the wings is more backwards, due to which there is less lateral inflow moving along the leading edge. Consequently, there is less effect on the LEV, thus little effect on the lift generation. Then, the difference in generated lift between the wings is smaller, leading to a more stable motion in forward flight. A similar influence can be the cause for the reduced accuracy of the coupled doublet maneuver of the Delfly Nimble. Whether the Delfly Nimble is more stable in forward flight has not been investigated in this research.

E. Model accuracy nonlinear maneuvers

Nonlinear doublets were used to analyze the justifiability of the assumption that modeling the the lateral body dynamics of the Delfly Nimble can be modeled using a linear model structure. The estimation results of a nonlinear doublet with a constant roll angle of 30° shown in Figure 25, and the accuracy metrics for this estimation are found in Table 15. The estimation results of a nonlinear doublet with a constant roll angle of 20° are shown in Figure 26, and the accuracy metrics for this estimation are indicated in Table 16.

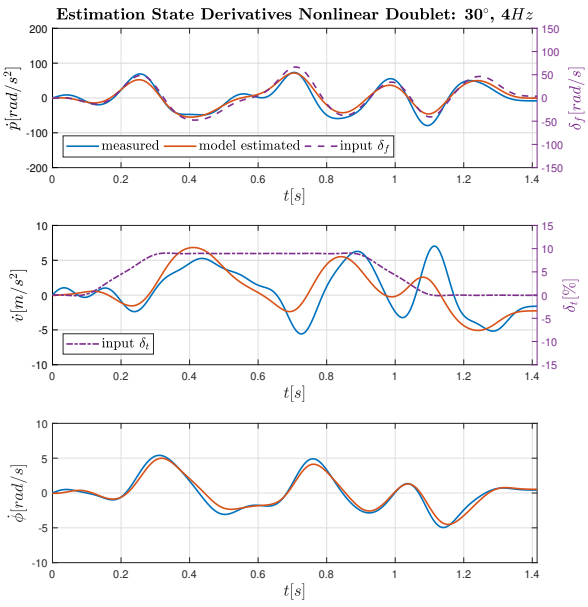

Fig. 25 Estimation results of the state derivatives for a nonlinear doublet with a main frequency of 4 Hz, constant roll angle of 30° and a roll deflection of 15°, using the identified state-space model.

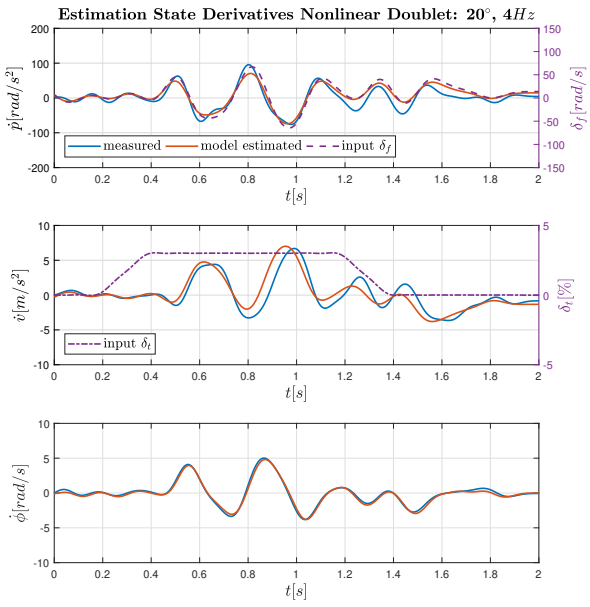

Fig. 26 Estimation results of the state derivatives for a nonlinear doublet with a main frequency of 4 Hz, constant roll angle of 20° and a roll deflection of 15°, using the identified state-space model.

When a constant roll angle of 30° is used the estimation accuracy of $\dot{v}$ has decreased significantly. This reduction in accuracy is primarily due to the sideways motion of the Delfly Nimble during this maneuver. The maximum lateral velocity v reached in this nonlinear doublet maneuver was $1.60\frac{m}{s}$, while in the identification maneuver the maximum

Table 15 The accuracy metrics for the estimation of a nonlinear doublet with a main frequency of 4 Hz, a constant roll angle of 30° and a roll deflection of 15°.

Accuracy Metrics Nonlinear Doublet: 30°, 4 Hz			
Output Variable	$\mathbf{r}_{xy}$	$\mathbf{R}^2$	**RMSE** (% of meas. range)
$\dot{p}$	0.952	0.900	7.91
$\dot{v}$	0.783	0.618	16.16
$\dot{\phi}$	0.985	0.965	4.45

Table 16 The accuracy metrics for the estimation of a nonlinear doublet with a main frequency of 4 Hz, a constant roll angle of 20° and a roll deflection of 15°.

Accuracy Metrics Nonlinear Doublet: 20°, 4 Hz			
Output Variable	$\mathbf{r}_{xy}$	$\mathbf{R}^2$	**RMSE** (% of meas. range)
$\dot{p}$	0.927	0.824	8.02
$\dot{v}$	0.892	0.791	10.18
$\dot{\phi}$	0.994	0.985	2.40

v was $1.00\frac{m}{s}$. When a constant roll angle of 20° is used, the estimation accuracy of $\dot{v}$ is more in the range of those in Section VI.A. The main reason for the improvement is the lower maximum of the later velocity in this maneuver, which was $1.43\frac{m}{s}$. This demonstrates that the further the Delfly Nimble moves away from the initial condition of the identification data, the hover condition, the lower the model accuracy. The reduction of model accuracy might be caused by the influence of lateral inflow on the LEV, which can increase or decrease the lift generation [38, 39, 41], as was described earlier in the validation results of the coupled maneuvers in Section V.C.

VII. Conclusion and recommendations

In this paper a mathematical model of the lateral body dynamics of a tailless four-winged flapping wing micro air vehicle was determined. The flapping wing micro air vehicle analyzed here is the Delfly Nimble, a tailless member of the Delfly Family, a group of flapping robots which have been developed at the Delft University of Technology. The rigid body approximation was used in order to develop the model structure, which led to a linear time-invariant state-space system for known initial conditions. The parameters of the state-space model were stability and control derivatives, which were determined using the least-squares approach. Due to tailless design of the Delfly Nimble it is inherently unstable. As a consequence, all flight experiments needed to be conducted in closed-loop. The direct approach was taken for the system identification of this closed-loop system, where the controller is ignored in the model identification. One of the main difficulties encountered here is that the controller can dampen the natural response, reducing the information contained in the measurement data, leading to less accurate models. In order to cope with this, the gains of the controller were altered such that the influence of the controller was minimized, and large commands were given during the identification experiments. With these two measurements sufficient excitation was obtained for the identification of a mathematical model of the lateral body dynamics. The identifiability was checked by analysis of the power spectral density plots of the measures states, where peaks visible around the expected frequencies. For the identification experiments a train of doublets were used, with hovering as the initial condition. Two natural modes of the Delfly Nimble were identified using the state-space model, a stable aperiodic mode and an unstable oscillatory

mode, confirming the inherent instability of the Delfly Nimble. During the validation experiments doublets and the 112-maneuver was used, conducted using both the altered gains and the original gains of the PD-controller on the Delfly Nimble. The identified state-space model was able to estimate the state derivatives of the Delfly Nimble accurately, reaching accuracies of over 90%. The identified model was also used in a closed-loop configuration using a Simulink model, in which a one to one copy of the PD-controller was implemented. The simulated states were also close to the actual states, with the accuracy exceeding 85%, and stable simulation. However, there was oscillatory motion visible when the Delfly Nimble was hovering which was not captured by he identified model. This could be due to time-varying dynamics, which were not considered in this research. The developed model can be used in a closed-loop configuration for the stability analysis of the body dynamics, which are time-averaged, and for the controller design. The justifiability of two assumptions which were used for the development of the state-space model: the longitudinal and lateral dynamics are decoupled, and the body dynamics can be modeled using a linear model structure. For the assumption on decoupled dynamics coupled maneuvers were performed, where inputs are given to more than one control mechanism. For the coupled maneuver the coupled doublet was used, where the Delfly Nimble is flying forward and performs a doublet. The model accuracy for the coupled maneuver decreased the most for the lateral body acceleration $\dot{v}$, most likely due to the influence of incoming lateral airflow on the intensity of the leading edge vortex, rather than the inputs of multiple control mechanism. This suggests that the assumption of uncoupled dynamics can be made. For the assumption on the linear model structure nonlinear maneuvers were performed, where the Delfly Nimble moves away greatly from the initial condition of the identification maneuvers, the hover condition. The nonlinear doublet was used as the nonlinear maneuver, where the Delfly Nimble is flying sideways and performs a doublet. The model accuracy for the nonlinear maneuver also reduced the most for $\dot{v}$, most likely also due to the influence of the lateral incoming airflow on the intensity of the leading edge vortex. It was shown that for lower sideways velocities the model accuracy improved. This indicates that the linearity assumption is not a valid one.

There are still improvements to apply for the development of a mathematical model of the lateral body dynamics of the Delfly Nimble, and thus recommendations are given for future research. The first recommendation is to give direct inputs to the control surfaces during the identification experiments. This can be done by giving a disturbance input to the roll control mechanism. The advantage of doing this is that the influence of the controller is then further minimized, leading to more excitation of the lateral body dynamics. The more excitation during the identification experiment, the more information is contained in the data, which leads to better identified models. The second recommendation is to use a different parameter estimation approach. This is mainly due to the high noise sensitivity of the stability derivatives L_p, L_v, and the control derivative L_{δ_t}. The parameter estimation approach which could be used to reduce the noise sensitivity is the maximum likelihood estimator. This estimation approach was also tried in this research, but due to the unstable nature of the identified state-space model the maximum likelihood estimator did not converge. When the maximum likelihood estimator is used, the controller must be included. The third recommendation is therefore is to

use a different approach for the system identification of the closed-loop system, such as the indirect approach and the joint input-output approach. Using either one of these may help to ensure convergence of the maximum likelihood estimator. The fourth recommendation, is to use foam between the IMU and the mounting point to the fuselage. In this research the IMU was mounted directly to the fuselage, which led to a lot of noise in the IMU data. This was especially the case for the yaw rate data, which had a very high frequency content around the 11 Hz. This peak was most likely due to internal vibration. Next to the issue of the high frequency components in the yaw rate data, there was also very little excitation seen in the PSD plot of the yaw rate. This was the main reason for the bad estimation of the yaw dynamics. It is therefore recommended to use yaw inputs to increase the excitation of the yaw dynamics, improving the model identification of them. One of the main disadvantages of using the foam between the IMU and the fuselage is the robustness of the setup. The IMU is attached to the foam with double-sided tape, which is prone to detaching during rapid maneuvers. The fifth recommendation it to include the time-varying dynamics in the model, for it was seen that oscillations which occur during hover are not captured when using the identified model in closed-loop configuration. This can be done by modeling each wing of the Delfly Nimble as a separate body, which leads to a multi-body dynamic system with five bodies, or to model the time-varying components using a Fourier series. The last recommendation is to use a nonlinear model structure in order to expand the range of the identified model. The lateral body dynamics are very sensitive to incoming airflow. The range can be expanded using for example the linear parameter-varying model structure, similar to what was done for the model identification of the Delfly II.

Appendices

A. Comparison between stability derivatives Delfly Nimble and Drone Fly

In order to compare the stability derivatives of the Delfly Nimble with those of the dron efly, they have been non-dimensionalized using Equations (A.1) to (A.4).

$$L_p^+ = \frac{L_p \cdot f}{\rho \cdot U^2 \cdot A_w \cdot \bar{c}} \quad \text{(A.1)} \qquad L_v^+ = \frac{L_v}{\rho \cdot U \cdot A_w \cdot \bar{c}} \quad \text{(A.2)} \qquad Y_p^+ = \frac{Y_p \cdot f}{\rho \cdot U^2 \cdot A_w} \quad \text{(A.3)} \qquad Y_v^+ = \frac{Y_v}{\rho \cdot U \cdot A_w} \quad \text{(A.4)}$$

Where the flapping frequency f = 17 Hz, the air density ρ = 1.225 $\frac{kg}{m^3}$, the wing area A_w = 1.043×10^{-2} m^2, and the mean chord length c = 7.611×10^{-2} m, and the center of pressure velocity U is defined in Equation (A.5).

$$U = 2 \cdot \phi_f \cdot f \cdot \hat{r} \tag{A.5}$$

Where the flapping angle ϕ_f is 1.536 rad (88°), and the radius of the second moment of inertia of the wing $\hat{r}$ is 7.45×10^{-2} m. The non-dimensionalized stability derivatives of the Delfly Nimble and of the analytic model are shown in Table A.1. The stability derivatives of the drone fly have been determined using various analytic models.

Table A.1 The non-dimensionalized stability derivatives of the Delfly Nimble and the analytic model of flapping flight. 'ASL' indicates the eigenvalues determined by Karásek et al. [19] where 'tr' indicates the wing translational forces, 'rot' indicates the wing rotational forces and 'add' indicates the forces due to the inertia of the added air mass. 'Zhang' the ones determined by Zhang et al. [23] and 'Cheng' the ones by Cheng et al. [42]. All the analytic stability derivatives shown have been determined with the morphological data of the drone fly. The values shown may differ from the values in the work, for some sources used different body axis systems. The ones shown are for the axis system used for the Delfly Nimble, as shown in Figure 4.

Stability Derivatives: Delfly Nimble vs. Drone Fly						
Stability Derivative	**Delfly Nimble**	**Zhang [23] (CFD)**	**ASL [19] (tr+rot+add)**	**ASL [19] (tr+rot)**	**ASL [19] (tr)**	**Cheng** [42]
L_p^+	−0.28	−1.2	−1.3	−1.27	−2.29	−1.25
L_v^+	−0.10	0.806	0.97	0.601	−0.434	−0.381
Y_p^+	0.24	−0.104	1.47	1.47	−0.055	0
Y_v^+	−1.13	−0.876	−0.705	−0.705	−0.705	−0.618

From Table A.1 it can be seen that all the values of L_p^+ are and Y_v^+ are negative, while this is not the case for the L_v^+ and Y_p^+. The sign of L_v of the Delfly Nimble was negative in all the data sets used for estimation of the stability derivatives, while positive and negative values have been seen for Y_p. The change in sign of L_v^+ can be due to the different wing configurations, for the Delfly Nimble has a four-wing configuration, while the drone fly only has two wings. There is also a difference in magnitude seen when comparing the stability derivatives of the Delfly Nimble to the analytic stability derivatives. The inequality in magnitude can be a result of the difference in morphological data between the Delfly Nimble and the drone fly used to determine the stability derivatives.

B. Numerical state-space model used for validation

There were three different state-space models which were used as the model structure, the only difference between them being the inputs which were included. The symbolic equation for the state-space model which includes the inputs δ_f and δ_t is shown in Equation (B.1).

$$\begin{bmatrix} \dot{p} \\ \dot{v} \\ \dot{\phi} \end{bmatrix} = \begin{bmatrix} \frac{I_{zz}}{I_c} \cdot L_p & \frac{I_{zz}}{I_c} \cdot L_v & 0 \\ \frac{Y_p}{m} + w_0 & \frac{Y_v}{m} & g \cdot \cos(\theta_0) \cdot \cos(\phi_0) \\ 1 & 0 & 0 \end{bmatrix} \cdot \begin{bmatrix} p \\ v \\ \phi \end{bmatrix} + \begin{bmatrix} \frac{I_{zz}}{I_c} \cdot L_{\delta_f} & \frac{I_{zz}}{I_c} \cdot L_{\delta_t} \\ \frac{Y_{\delta_f}}{m} & \frac{Y_{\delta_t}}{m} \\ 0 & 0 \end{bmatrix} \cdot \begin{bmatrix} \delta_f \\ \delta_t \end{bmatrix} \tag{B.1}$$

The numeric state-space using the values of the stability and control derivatives of Table 3 is shown in (B.2).

$$\begin{bmatrix} \dot{p} \\ \dot{v} \\ \dot{\phi} \end{bmatrix} = \begin{bmatrix} -2.59 & -4.00 & 0 \\ 0.10 + w_0 & -1.95 & 9.81 \cdot \cos(\theta_0) \cdot \cos(\phi_0) \\ 1 & 0 & 0 \end{bmatrix} \cdot \begin{bmatrix} p \\ v \\ \phi \end{bmatrix} + \begin{bmatrix} 1.13 & 0.45 \\ -0.03 & -0.01 \\ 0 & 0 \end{bmatrix} \cdot \begin{bmatrix} \delta_f \\ \delta_t \end{bmatrix} \tag{B.2}$$

The symbolic equation for the state-space model which includes only the input δ_f is shown in Equation (B.3), and the estimated stability and control derivatives are shown in Table B.1. This model structure was used only for the validation of the coupled doublet maneuver. For the estimation of the parameters, only data-set 1 was used to estimate the stability and control derivatives.

$$\begin{bmatrix} \dot{p} \\ \dot{v} \\ \dot{\phi} \end{bmatrix} = \begin{bmatrix} \frac{I_{zz}}{I_c} \cdot L_p & \frac{I_{zz}}{I_c} \cdot L_v & 0 \\ \frac{Y_p}{m} + w_0 & \frac{Y_v}{m} & g \cdot \cos(\theta_0) \cdot \cos(\phi_0) \\ 1 & 0 & 0 \end{bmatrix} \cdot \begin{bmatrix} p \\ v \\ \phi \end{bmatrix} + \begin{bmatrix} \frac{I_{zz}}{I_c} \cdot L_{\delta_f} \\ \frac{Y_{\delta_f}}{m} \\ 0 \end{bmatrix} \cdot \begin{bmatrix} \delta_f \end{bmatrix} \tag{B.3}$$

Table B.1 Estimated parameters for the three-state state-space system shown in Equation (B.3) **as a result of the WLS estimator, using the first identification data-set.**

Estimated Parameters Reduced Grey-Box Model: input δ_f			
L-parameters:	L_p -2.68×10^{-4}	L_v -6.69×10^{-4}	L_{δ_f} 1.06×10^{-4}
Y-parameters:	Y_p 2.96×10^{-3}	Y_v -5.33×10^{-2}	Y_{δ_f} -8.66×10^{-4}

The numeric state-space using the values of the stability and control derivatives of Table B.1 is shown in Equation (B.4).

$$\begin{bmatrix} \dot{p} \\ \dot{v} \\ \dot{\phi} \end{bmatrix} = \begin{bmatrix} -2.86 & -7.14 & 0 \\ 0.10 + w_0 & -1.85 & 9.81 \cdot \cos(\theta_0) \cdot \cos(\phi_0) \\ 1 & 0 & 0 \end{bmatrix} \cdot \begin{bmatrix} p \\ v \\ \phi \end{bmatrix} + \begin{bmatrix} 1.13 \\ -0.03 \\ 0 \end{bmatrix} \cdot \begin{bmatrix} \delta_f \\ \delta_t \end{bmatrix} \tag{B.4}$$

The symbolic equation for the state-space model which includes only the input δ_f is shown in Equation (B.5), and the estimated stability and control derivatives are shown in Table B.2. This model structure was used only for the validation of the coupled doublet maneuver. For the estimation of the parameters, only data-set 1 was used to estimate

the stability and control derivatives.

$$\begin{bmatrix} \dot{p} \\ \dot{v} \\ \dot{\phi} \end{bmatrix} = \begin{bmatrix} \frac{I_{zz}}{I_c} \cdot L_p & \frac{I_{zz}}{I_c} \cdot L_v & 0 \\ \frac{Y_p}{m} + w_0 & \frac{Y_v}{m} & g \cdot \cos(\theta_0) \cdot \cos(\phi_0) \\ 1 & 0 & 0 \end{bmatrix} \cdot \begin{bmatrix} p \\ v \\ \phi \end{bmatrix} + \begin{bmatrix} \frac{I_{zz}}{I_c} \cdot L_{\delta_f} & \frac{I_{zz}}{I_c} \cdot L_{\delta_d} \\ \frac{Y_{\delta_f}}{m} & \frac{Y_{\delta_d}}{m} \\ 0 & 0 \end{bmatrix} \cdot \begin{bmatrix} \delta_f \\ \delta_d \end{bmatrix} \tag{B.5}$$

Table B.2 Estimated parameters for the three-state state-space system shown in Equation (B.5) **as a result of the WLS estimator, using the first identification data-set.**

Estimated Parameters Reduced Grey-Box Model: inputs δ_f and δ_d				
L-parameters:	L_p -2.57×10^{-4}	L_v -4.91×10^{-4}	L_{δ_f} 1.06×10^{-4}	L_{δ_d} 1.20×10^{-3}
Y-parameters:	Y_p 2.42×10^{-3}	Y_v -6.00×10^{-2}	Y_{δ_f} -8.86×10^{-4}	Y_{δ_d} -5.41×10^{-2}

The numeric state-space using the values of the stability and control derivatives of Table B.2 is shown in Equation (B.6).

$$\begin{bmatrix} \dot{p} \\ \dot{v} \\ \dot{\phi} \end{bmatrix} = \begin{bmatrix} -2.74 & -5.24 & 0 \\ 0.08 + w_0 & -2.09 & 9.81 \cdot \cos(\theta_0) \cdot \cos(\phi_0) \\ 1 & 0 & 0 \end{bmatrix} \cdot \begin{bmatrix} p \\ v \\ \phi \end{bmatrix} + \begin{bmatrix} 1.14 & 12.77 \\ -0.03 & -1.88 \\ 0 & 0 \end{bmatrix} \cdot \begin{bmatrix} \delta_f \\ \delta_d \end{bmatrix} \tag{B.6}$$

The lateral state-space can be combined with the longitudinal state-space system which was developed in the research of Nijboer et al.[17, 18]. The numeric state-space model using the paramters identified in this research are shown in Equation (B.7).

$$\begin{bmatrix} \dot{q} \\ \dot{u} \\ \dot{w} \\ \dot{\theta} \end{bmatrix} = \begin{bmatrix} -2.64 & 26.94 & -2.64 & 0 \\ 0.14 - w_0 & -3.52 & 0.31 & -9.81 \cdot \cos(\theta_0) \\ -0.19 + u_0 & 0.68 & -0.21 & -9.81 \cdot \sin(\theta_0) \\ 1 & 0 & 0 & 0 \end{bmatrix} \cdot \begin{bmatrix} q \\ u \\ w \\ \theta \end{bmatrix} + \begin{bmatrix} 3862.82 \\ 25.10 \\ 10.37 \\ 0 \end{bmatrix} \cdot \begin{bmatrix} \delta_d \end{bmatrix} \tag{B.7}$$

C. Autocorrelation plots

The autocorrelation plots of the identification data, for which a doublet train with main frequencies 4 and 7 Hz was used, is shown in Figure C.1. The autocorrelation plots of the open-loop validation data, in which a doublet with main frequency of 6 Hz was used and a 112-maneuver with main frequencies of 3.5 and 7 Hz, are shown in Figures C.2 and C.3.

Fig. C.1 Autocorrelation plot of the residuals of the state derivatives for a doublet train with main frequencies of 4 and 7 Hz. The state derivatives were determined using the state-space system shown in Equation (B.2)**.**

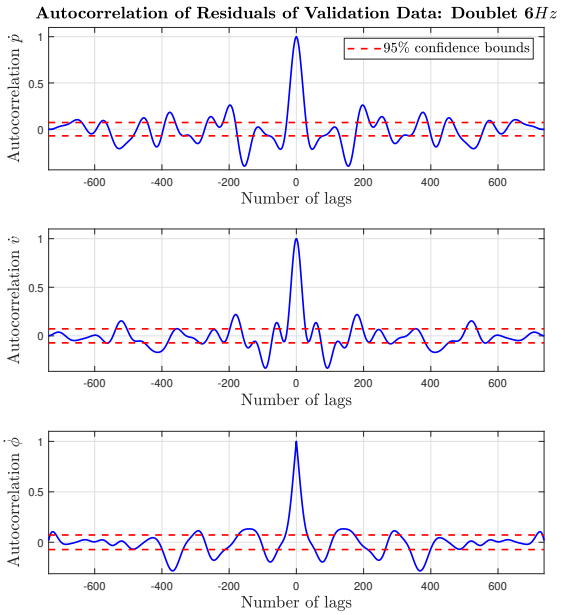

Fig. C.2 Autocorrelation plot of the residuals of the state derivatives for a doublet with a main frequency of 6 Hz. The state derivatives were determined using the state-space system shown in Equation (B.2)**.**

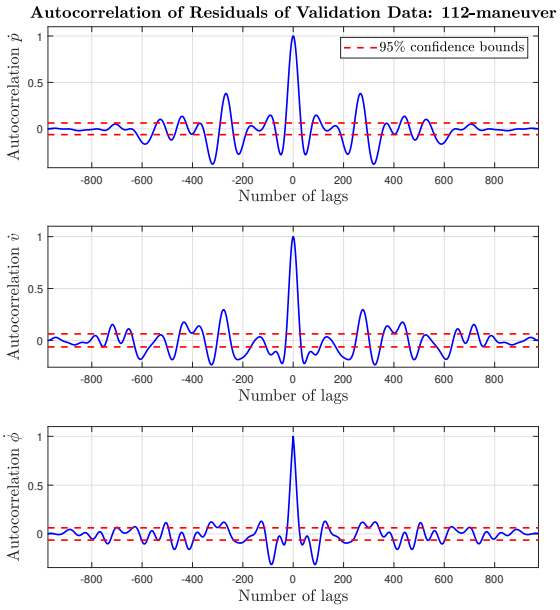

Fig. C.3 Autocorrelation plot of the residuals of the state derivatives for a 112-maneuver with main frequencies of 3.5 and 7 Hz. The state derivatives were determined using the state-space system shown in Equation (B.2)**.**

Closed-loop validation was also done in this research, using a Simulink model which used a one to one copy of the PD-controller used on the Delfly Nimble. Both the fast gains and the slow gains shown in Table 2 were used in the closed-loop validation. The autocorrelation plots of the residuals of the simulation of a doublet train using the fast gains are shown in Figures C.4 and C.5.

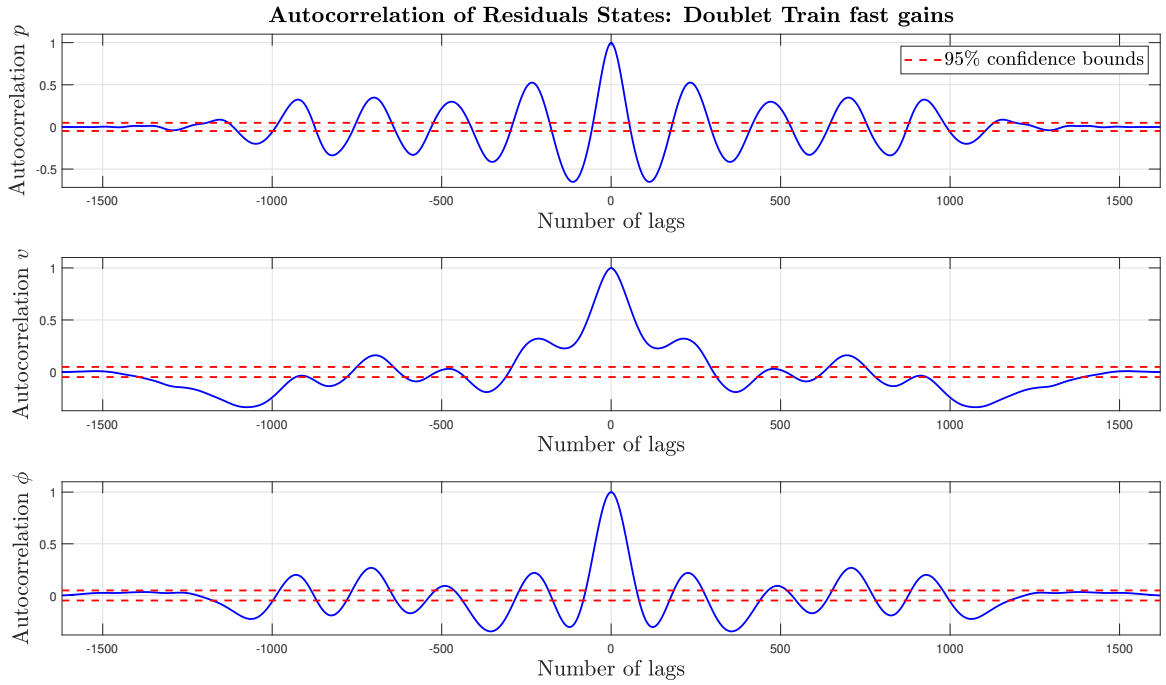

Fig. C.4 Autocorrelation plot of the residuals of the states of a doublet train. The states are determined using the the state-space model shown in Equation (B.2) **in closed-loop configuration. For this simulation the fast gains shown in Table 2 were used.**

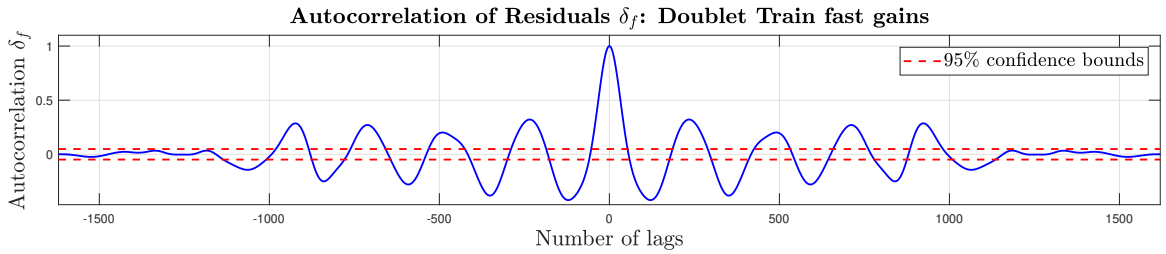

Fig. C.5 Autocorrelation plot of the residuals of the input δ_f of a doublet train. The states are determined using the the state-space model shown in Equation (B.2) **in closed-loop configuration. For this simulation the fast gains shown in Table 2 were used.**

There were also maneuvers which were performed using the slow gains for the closed-loop validation, namely a doublet train and 112-maneuvers. The main frequencies in the doublet train were 6, 4, and 2 Hz. The main frequencies of the 112-maneuvers were 2 and 4 Hz. The autocorrelation plots of the doublet train are shown in Figures C.6 and C.8. The autocorrelation plots of the 112 maneuvers are shown in Figures C.7 and C.9.

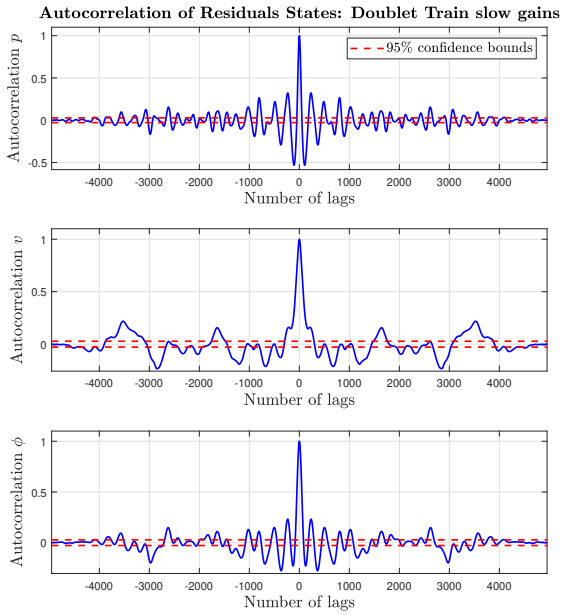

Fig. C.6 Autocorrelation plot of the residuals of the states of a doublet train. The states are determined using the the state-space model shown in Equation (B.2) in closed-loop configuration. For this simulation the slow gains shown in Table 2 were used.

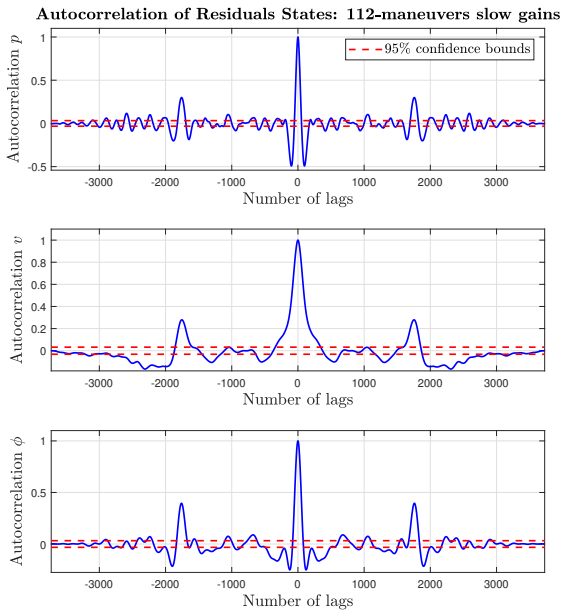

Fig. C.7 Autocorrelation plot of the residuals of the states of multiple 112-maneuvers. The states are determined using the the state-space model shown in Equation (B.2) in closed-loop configuration. For this simulation the slow gains shown in Table 2 were used.

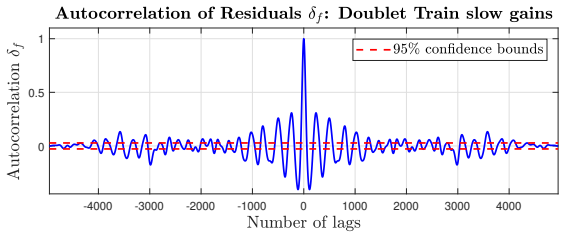

Fig. C.8 Autocorrelation plot of the residuals of the input δ_f of a doublet train. The states are determined using the the state-space model shown in Equation (B.2) in closed-loop configuration. For this simulation the slow gains shown in Table 2 were used.

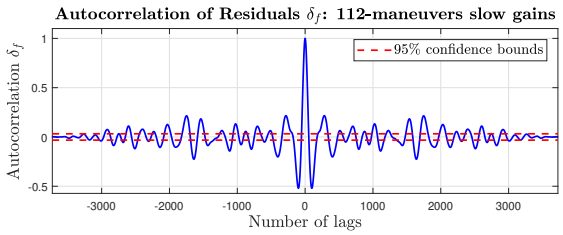

Fig. C.9 Autocorrelation plot of the residuals of the input δ_f of multiple 112-maneuvers. The states are determined using the the state-space model shown in Equation (B.2) in closed-loop configuration. For this simulation the slow gains shown in Table 2 were used.

There were also coupled maneuvers which were performed during the experiments. To estimate the state derivatives of the coupled maneuver, three different state-space models were used, the only difference being which inputs were included. The first model included the inputs δ_f and δ_t, and the autocorrelation plots of the residuals are shown in Figure C.10. The second model included only the input δ_f, and the autocorrelation plots of the residuals are shown in Figure C.11. The third model included the inputs δ_f and δ_d, and the autocorrelation plots of the residuals are shown in Figure C.12.

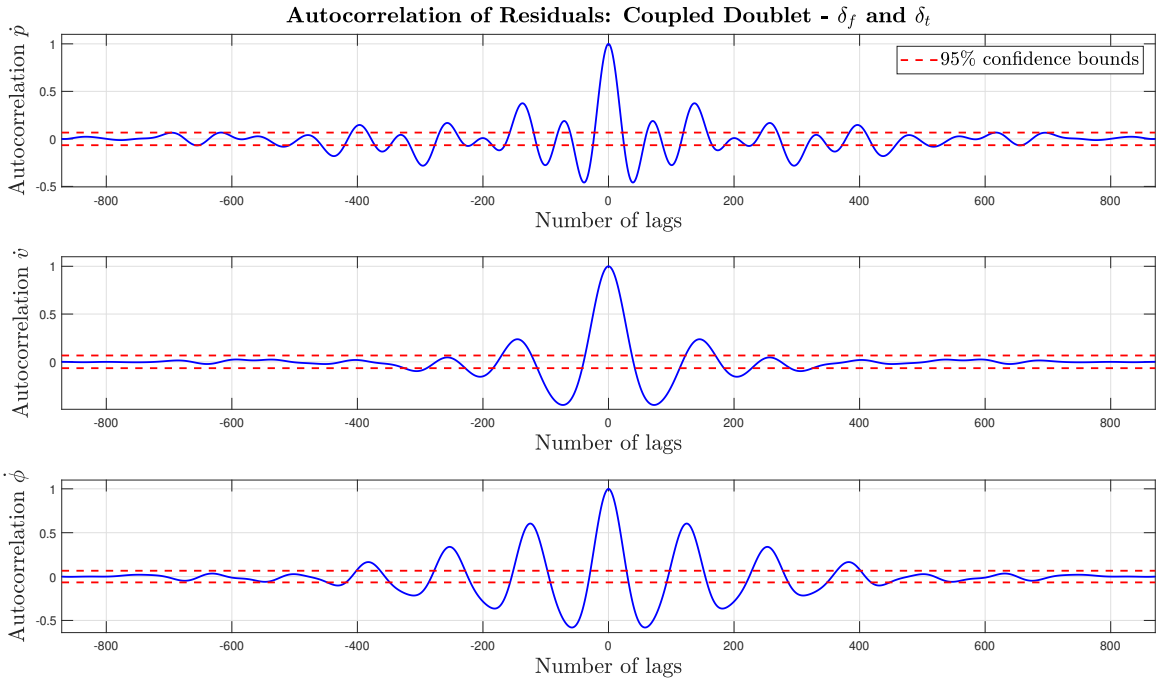

Fig. C.10 Autocorrelation plot of the residuals of the state derivatives of a coupled doublet with a main frequency of 6 Hz. The states derivatives are determined using the the state-space model shown in Equation (B.2)**.**

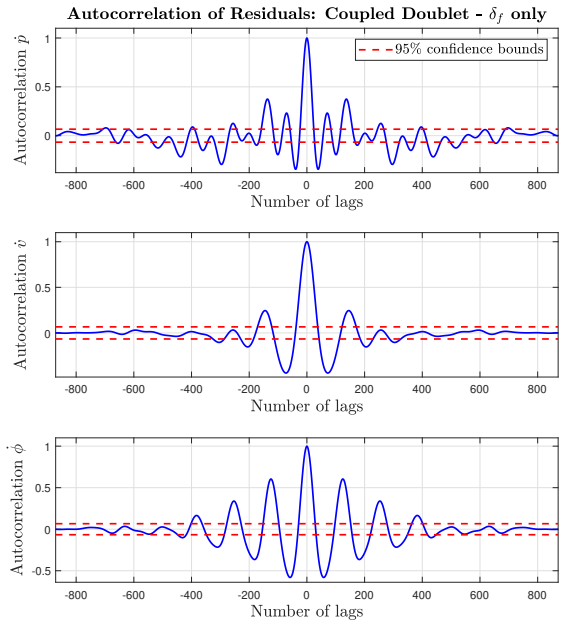

Fig. C.11 Autocorrelation plot of the residuals of the state derivatives of a coupled doublet. The states derivatives are determined using the the state-space model shown in Equation (B.4)**.**

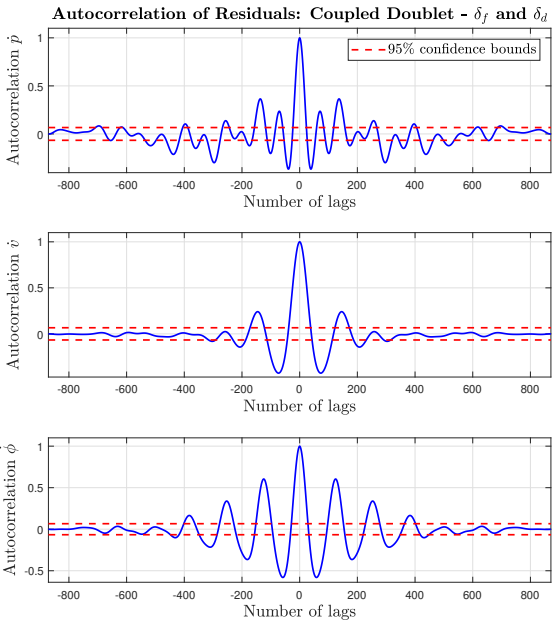

Fig. C.12 Autocorrelation plot of the residuals of the state derivatives of a coupled doublet. The states derivatives are determined using the the state-space model shown in Equation (B.6)**.**

The last type of maneuver used during the experiments were nonlinear doublets. Two types of nonlinear doublets were performed. The autocorrelation of the residuals of the nonlinear doublet with a constant roll angle of 30°, a main frequency of 4 Hz and a roll deflection angle of 15° is shown in Figure C.13. The autocorrelation of the residuals of the nonlinear doublet with a constant roll angle of 20°, a main frequency of 4 Hz and a roll deflection angle of 15° is shown in Figure C.14.

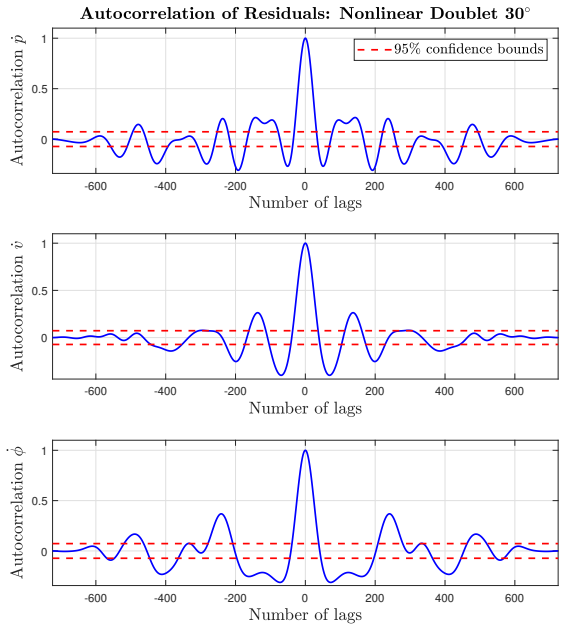

Fig. C.13 Autocorrelation plot of the residuals of the state derivatives of a nonlinear doublet with a constant roll angle of 30°. The states derivatives are determined using the the state-space model shown in Equation (B.2)**.**

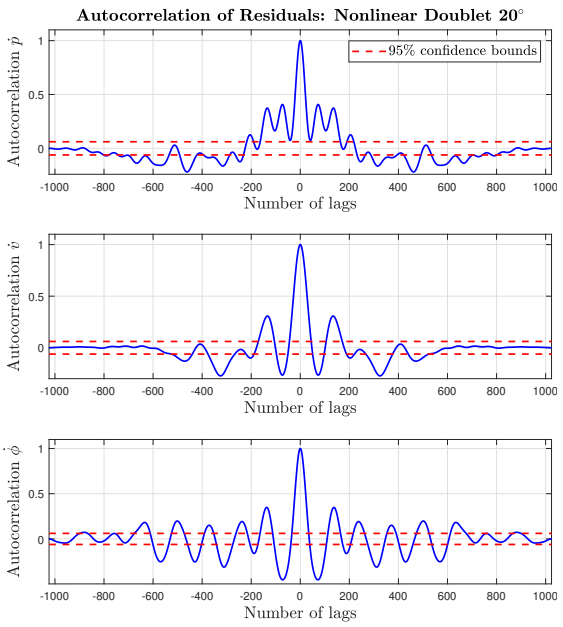

Fig. C.14 Autocorrelation plot of the residuals of the state derivatives of a nonlinear doublet with a constant roll angle of 20°. The states derivatives are determined using the the state-space model shown in Equation (B.2)**.**

D. Power Spectrum Yaw Dynamics

During the identification experiments there was very little excitation seen in the yaw direction. This is confirmed when analyzing the power spectrum of the yaw rate r, illustrated in Figure D.1.

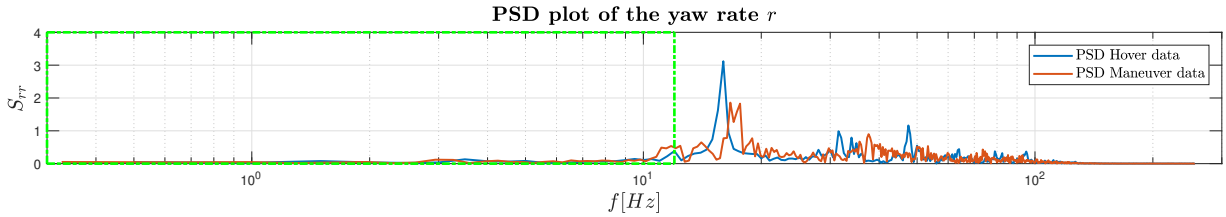

Fig. D.1 PSD plot of the yaw rate r of the Delfly Nimble during hover the identification maneuver. The green square in the power spectrum contains the frequency content up to 12 Hz. The components inside this square were filtered out using using a zero-phase Butterworth filter with order of 10.

The green square in the power spectrum of the states contains the frequency content up to 12 Hz. The components **inside** this square were filtered out using using a zero-phase Butterworth filter with order of 10. Very little excitation is seen around the expected frequencies for the body dynamics, around 1-2 Hz. There is a very small peak visible around the 11 Hz, which can be seen in the power sprectrums after the filter has been applied. This is presented in Figure D.2.

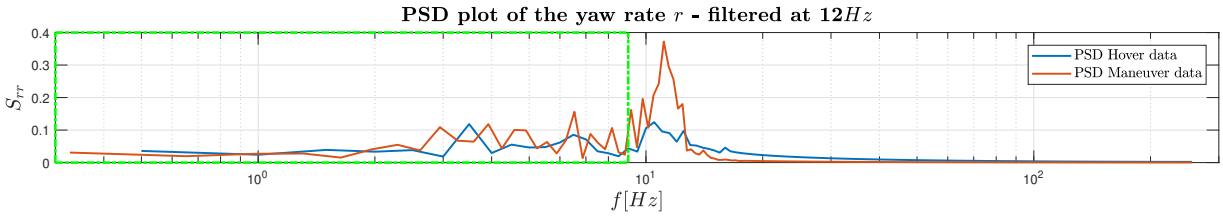

Fig. D.2 PSD plot of the yaw rate r of the Delfly Nimble during hover the identification maneuver. The green square in this power spectrum contains the frequency content up to 9 Hz.

The green square in this power spectrum of contains the frequency content up to 9 Hz. The peak around 11 Hz in the maneuver data is clearly visible. These high frequency components in the data for r resulted in very poor estimation of the yaw rate, and is most likely due to internal vibration, rather than excitation of the dynamics. When the filter was applied using a cut-off frequency of 9 Hz, there is very little difference between the PSD plots of the maneuver and the hover data, indicating that there is little excitation of the body dynamics. This was the main reason that the yaw dynamics were omitted from the equations of motion.

References

[1] Coffey, T., and Montgomery, J. A., "The Emergence of Mini UAVs for Military Applications," *Defense Horizons*, , No. 22, 2002, p. 1.

[2] Costa, F. G., Ueyama, J., Braun, T., Pessin, G., Osorio, F. S., and Vargas, P. A., "The use of unmanned aerial vehicles and wireless sensor network in agricultural applications," *International Geoscience and Remote Sensing Symposium (IGARSS)*, 2012, pp. 5045–5048. https://doi.org/10.1109/IGARSS.2012.6352477.

[3] Erdelj, M., Natalizio, E., Chowdhury, K. R., and Akyildiz, I. F., "Help from the Sky: Leveraging UAVs for Disaster Management," , 1 2017. https://doi.org/10.1109/MPRV.2017.11.

[4] Torresan, C., Berton, A., Carotenuto, F., Di Gennaro, S. F., Gioli, B., Matese, A., Miglietta, F., Vagnoli, C., Zaldei, A., and Wallace, L., "Forestry applications of UAVs in Europe: a review," *International Journal of Remote Sensing*, Vol. 38, No. 8-10, 2017, pp. 2427–2447. https://doi.org/10.1080/01431161.2016.1252477.

[5] Zeldovich, L., "The drone and the honey," *Mechanical Engineering*, Vol. 141, No. 5, 2019, pp. 32–37. https://doi.org/10.1115/1.2019-MAY2.

[6] Decroon, G. C., Perçin, M., Remes, B. D., Ruijsink, R., and De Wagter, C., *The delfly: Design, aerodynamics, and artificial intelligence of a flapping wing robot*, Springer Netherlands, 2015. https://doi.org/10.1007/978-94-017-9208-0.

[7] Armanini, S. F., de Visser, C. C., de Croon, G. C. H. E., and Mulder, M., "Time-Varying Model Identification of Flapping-Wing Vehicle Dynamics Using Flight Data," *Journal of Guidance, Control, and Dynamics*, Vol. 39, No. 3, 2016, pp. 526–541. https://doi.org/10.2514/1.G001470, URL http://arc.aiaa.org/doi/10.2514/1.G001470.

[8] Karásek, M., Muijres, F. T., De Wagter, C., Remes, B. D. W., and de Croon, G. C. H. E., "A tailless aerial robotic flapper reveals that flies use torque coupling in rapid banked turns," *Science*, Vol. 361, No. 6407, 2018, pp. 1089–1094. https://doi.org/10.1126/science.aat0350, URL http://www.sciencemag.org/lookup/doi/10.1126/science.aat0350.

[9] Keennon, M., Klingebiel, K., Won, H., and Andriukov, A., "Development of the Nano Hummingbird: A Tailless Flapping Wing Micro Air Vehicle," 2012. https://doi.org/10.2514/6.2012-588, URL http://arc.aiaa.org.

[10] Phan, H. V., Kang, T., and Park, H. C., "Design and stable flight of a 21 g insect-like tailless flapping wing micro air vehicle with angular rates feedback control," *Bioinspiration and Biomimetics*, Vol. 12, No. 3, 2017, p. 036006. https://doi.org/10.1088/1748-3190/aa65db.

[11] Ramezani, A., Shi, X., Chung, S. J., and Hutchinson, S., "Bat Bot (B2), a biologically inspired flying machine," *Proceedings - IEEE International Conference on Robotics and Automation*, Vol. 2016-June, Institute of Electrical and Electronics Engineers Inc., 2016, pp. 3219–3226. https://doi.org/10.1109/ICRA.2016.7487491.

[12] Ma, K. Y., Chirarattananon, P., Fuller, S. B., and Wood, R. J., "Controlled flight of a biologically inspired, insect-scale robot," *Science*, Vol. 340, No. 6132, 2013, pp. 603–607. https://doi.org/10.1126/science.1231806.

[13] Caetano, J. V., Percin, M., Van Oudheusden, B. W., Remes, B., De Wagter, C., De Croon, G. C., and De Visser, C. C., "Error analysis and assessment of unsteady forces acting on a flapping wing micro air vehicle: Free flight versus wind-tunnel experimental methods," *Bioinspiration and Biomimetics*, Vol. 10, No. 5, 2015. https://doi.org/10.1088/1748-3190/10/5/056004.

[14] Armanini, S., "Identification of time-varying models for flapping-wing micro aerial vehicles," Ph.D. thesis, 2018. https://doi.org/10.4233/UUID:37BE4591-3E02-4AD3-B800-30BF41A85F1C, URL https://repository.tudelft.nl/islandora/object/uuid%3A37be4591-3e02-4ad3-b800-30bf41a85f1c?collection=research.

[15] Kajak, K., "A minimal longitudinal dynamic model of a tailless flapping wing robot," Ph.D. thesis, 2018. URL https://repository.tudelft.nl/islandora/object/uuid%3A717e7e15-94c3-47ac-a348-12f5c2275aa2?collection=education.

[16] Kajak, K. M., Karásek, M., Chu, Q. P., and de Croon, G. C. H. E., "A minimal longitudinal dynamic model of a tailless flapping wing robot for control design," *Bioinspiration & biomimetics*, Vol. 14, No. 4, 2019, p. 46008. https://doi.org/10.1088/1748-3190/ab1e0b.

[17] Nijboer, J., "Longitudinal grey-box model identification of a tailless flapping-wing MAV based on free-flight data," Ph.D. thesis, 2019. URL https://repository.tudelft.nl/islandora/object/uuid%3Aa37b96b7-90de-4f22-99ce-87cc97d414d9?collection=education.

[18] Nijboer, J., Armanini, S. F., Karasek, M., and de Visser, C. C., "Longitudinal Grey-Box Model Identification of a Tailless Flapping-Wing MAV Based on Free-Flight Data," American Institute of Aeronautics and Astronautics (AIAA), 2020. https://doi.org/10.2514/6.2020-1964.

[19] Karásek, M., and Preumont, A., "Flapping Flight Stability in Hover: A Comparison of Various Aerodynamic Models," Vol. 4, 2012. URL https://journals-sagepub-com.tudelft.idm.oclc.org/doi/pdf/10.1260/1756-8293.4.3.203.

[20] Sun, M., Wang, J., Xiong, Y., Sun, M., Wang, J., and Xiong, Y., "Dynamic flight stability of hovering insects," *Acta Mech Sin*, Vol. 23, 2007, pp. 231–246. https://doi.org/10.1007/s10409-007-0068-3, URL https://link-springer-com.tudelft.idm.oclc.org/content/pdf/10.1007%2Fs10409-007-0068-3.pdf.

[21] Sun, M., and Wang, J. K., "Flight stabilization control of a hovering model insect," *Journal of Experimental Biology*, Vol. 210, No. 15, 2007, pp. 2714–2722. https://doi.org/10.1242/jeb.004507.

[22] Xiong, Y., and Sun, M., "Dynamic flight stability of a bumblebee in forward flight," *Acta Mech Sin*, Vol. 24, 2008, pp. 25–36. https://doi.org/10.1007/s10409-007-0121-2, URL https://link-springer-com.tudelft.idm.oclc.org/content/pdf/10.1007%2Fs10409-007-0121-2.pdf.

[23] Zhang, Y., Sun, M., Zhang, Y., and Sun, M., "Dynamic flight stability of a hovering model insect: lateral motion," *Acta Mech Sin*, Vol. 26, 2010, pp. 175–190. https://doi.org/10.1007/s10409-009-0303-1, URL https://link-springer-com.tudelft.idm.oclc.org/content/pdf/10.1007%2Fs10409-009-0303-1.pdf.

[24] Sun, M., "Dynamic flight stability of a hovering bumblebee," *Journal of Experimental Biology*, Vol. 208, No. 3, 2005, pp. 447–459. https://doi.org/10.1242/jeb.01407.

[25] Zhang, Y.-L., Wu, J.-H., Sun, M., Zhang, Y.-L., Wu, J.-H., and Sun, M., "Lateral dynamic flight stability of hovering insects: theory vs. numerical simulation," *Acta Mech. Sin*, Vol. 28, No. 1, 2012, pp. 221–231. https://doi.org/10.1007/s10409-012-0011-0, URL https://link-springer-com.tudelft.idm.oclc.org/content/pdf/10.1007%2Fs10409-012-0011-0.pdf.

[26] Roshanbin, A., Altartouri, H., Karásek, M., and Preumont, A., "COLIBRI: A hovering flapping twin-wing robot," *International Journal of Micro Air Vehicles*, Vol. 9, No. 4, 2017, pp. 270–282. https://doi.org/10.1177/1756829317695563, URL http://journals.sagepub.com/doi/10.1177/1756829317695563.

[27] Armanini, S. F., Karasek, M., De Croon, G. C., and De Visser, C. C., "Onboard/offboard sensor fusion for high-fidelity flapping-wing robot flight data," *Journal of Guidance, Control, and Dynamics*, Vol. 40, No. 8, 2017, pp. 2116–2127. https://doi.org/10.2514/1.G002527.

[28] Stengel, R. F., *Flight dynamics*, Princeton University Press, 2015.

[29] Stevens, B. L., Lewis, F. L., and Johnson, E. N., *Aircraft control and simulation: Dynamics, controls design, and autonomous systems: Third edition*, wiley, 2015. https://doi.org/10.1002/9781119174882.

[30] Mulder, J. A., van Staveren, W., van der Vaart, J. C., de Weerdt, E., Veld, A. C. i. t., and Mooij, E., "Flight Dynamics - Lecture Notes," Tech. rep., 2013. https://doi.org/10.2514/1.34515, URL http://app.knovel.com/web/toc.v/cid:kpFD000016/viewerType:toc/root_slug:flight-dynamics/url_slug:kt00UQFX02?b-q=ailerons&b-within-title=true&b-group-by=false&b-search-type=tech-reference&b-sort-on=default.

[31] Olsder, G. J., Van Der Woude, J. W., Maks, J. G., and Jeltsema, D., *Mathematical Systems Theory 4th edition*, VSSD, 2011.

[32] Klein, V., and Morelli, E. A., *Aircraft System Identification: Theory and Practice*, AIAA education series, American Institute of Aeronautics and Astronautics, 2006. URL https://books.google.nl/books?id=SC90QgAACAAJ.

[33] Keesman, K. J., *System identification: An introduction*, 9780857295217, Springer International Publishing, 2011. https://doi.org/10.1007/978-0-85729-522-4.

[34] Ljung, L., *System identification : theory for the user*, Prentice Hall PTR, 1999.

[35] Jategaonkar, R. V., *Flight Vehicle System Identification: A Time-Domain Methodology, Second Edition*, American Institute of Aeronautics and Astronautics, Inc., 2015. https://doi.org/10.2514/4.102790.

[36] Karásek, M., "Robotic hummingbird: Design of a control mechanism for a hovering flapping wing micro air vehicle," Ph.D. thesis, 2014.

[37] Cheng, C., Wu, J., Zhang, Y., Li, H., and Zhou, C., "Aerodynamics and dynamic stability of micro-air-vehicle with four flapping wings in hovering flight," *Advances in Aerodynamics*, Vol. 2, No. 1, 2020, p. 5. https://doi.org/10.1186/s42774-020-0029-0, URL https://aia.springeropen.com/articles/10.1186/s42774-020-0029-0.

[38] Xu, N., and Sun, M., "Lateral dynamic flight stability of a model bumblebee in hovering and forward flight," *Journal of Theoretical Biology*, Vol. 319, 2013, pp. 102–115. https://doi.org/10.1016/j.jtbi.2012.11.033.

[39] Ellington, C. P., van den Berg, C., Willmott, A. P., and Thomas, A. L. R., "Leading-edge vortices in insect flight," *Nature*, Vol. 384, No. 6610, 1996, pp. 626–630. https://doi.org/10.1038/384626a0, URL https://doi.org/10.1038/384626a0.

[40] Sun, M., "Insect flight dynamics: Stability and control," *Reviews of Modern Physics*, Vol. 86, No. 2, 2014, pp. 615–646. https://doi.org/10.1103/RevModPhys.86.615, URL https://journals.aps.org/rmp/abstract/10.1103/RevModPhys.86.615.

[41] Han, J.-S., Nguyen, A. T., and Han, J.-H., "Aerodynamic characteristics of flapping wings under steady lateral inflow," *J. Fluid Mech*, Vol. 870, 2020, pp. 735–759. https://doi.org/10.1017/jfm.2019.255, URL https://doi.org/10.1017/jfm.2019.255.

[42] Cheng, B., and Deng, X., "Translational and rotational damping of flapping flight and its dynamics and stability at hovering," *IEEE Transactions on Robotics*, Vol. 27, No. 5, 2011, pp. 849–864. https://doi.org/10.1109/TRO.2011.2156170.

II

Literature Study

2

Introduction Literature Study

In this part of the thesis the literature study is shown. The literature study presented here and the follow-up experimental work are for the MSc. thesis research in which a mathematical model will be identified for the lateral body dynamics of a tailless flapping wing micro air vehicle (FWMAV) that has been developed at the Delft University of Technology, known as the Delfly Nimble.

In this Chapter the research perspective is discussed in Section 2.1. The method which will be used for the identification of the model, the System Identification Procedure, is elaborated on in Section 2.2. The research questions are discussed in Section 2.3. The lay-out of the literature study is described in Section 2.4.

2.1. Research Perspective

Unmanned aerial vehicles (UAV's), and their smaller counterpart micro air vehicles (MAV's), have been found to be useful for a large variety of civil and military applications [14, 15, 17, 19, 75, 84]. A subcategory of UAV's are flapping wing micro air vehicles (FWMAV's). These FWMAV's have favorable properties such as: being able to fly at low velocities, having high agility and maneuvrability and some even have the ability to hover[3]. Most of the FWMAV's are bio-inspired, either using the basic principles of the flapping motions for the thrust generation or trying to mimic the flapping mechanism of the animal as closely as possible. Inspirations for the design of the FWMAV's have been birds, as is the case for the Nano Hummingbird [37], insects, as is the case for the Delfly family [17] and the KU Beetle [58], and bats, such as the Bat Bot B2 [59]. Figure 2.1 shows the Nano Hummingbird, the KU Beetle and the Bat Bot B2.

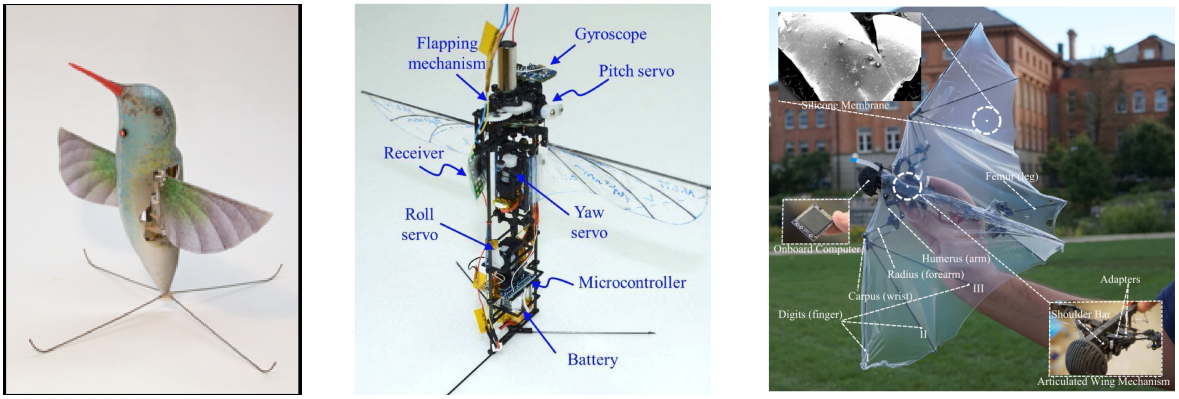

(a) Nano Hummingbird [37] (b) KU Beetle [58] (c) Bat Bot B2 [59]

Figure 2.1: Examples of FWMAV's.

The main difficulty with FWMAV's is the design of the control mechanisms. Tailed FWMAV's have passive stability, as is the case for the original Delfly [17]. Tailless ones require active control solutions in order to

remain airborne, as is the case for the Nano Hummingbird, KU Beetle and the Delfly Nimble [36, 37, 58].

Nano Hummingbird

The Nano Hummingbird was developed by AeroVironment as part of the Nano Air Vehicle program of the Defence Advanced Research Projects Agency (DARPA)[29]. It is a tailless FWMAV which has a wingspan of 16.5 cm and a mass of 19 grams, unveiled in 2011. This FWMAV was able to hover and reach forward velocities up to 6.7 ms^{-1}. It was also able to do a lateral flip maneuver. The main flight time was four minutes, had a flapping frequency of 30 Hz and a wing stroke angle of 200°. The Nano Hummingbird was kept airborne using a flight controller and the pilot would give rate control inputs to the FWMAV. Without the closed-loop control the FWMAV was to unstable to fly.

For the control of the attitude the Tailless Control Approach was taken. In this approach only the wings are used for the generation of the required torques. These torques are generated using wing deformation, also called wing deformations. Two types of wing modulation was use for the Nano Hummingbird: wing rotation modulation and wing twist modulation. In wing rotation modulation the wing is passively rotating about the leading edge of the wing. If the angle of allowed rotation is smaller more lift is generated. The wing rotation modulation was used for control of the yaw attitude. The wing rotation modulation is illustrated in Figure 2.2 [37].

(a) (b)

Figure 2.2: Illustration of the wing rotation modulation as used in the Nano Hummingbird [37]. In situation (a) the wing is allowed less to rotate about the leading edge compared to (b). The wing in (a) will generate more lift. This technique was used to control the yaw attitude.

The second technique used was the wing twist modulation. In wing twist modulation the root spar is moved. This can reduce or increase the amount of lift produced per wing, due to the difference in how tight the wing is. The wing twist modulation was used for controlling the pitch and roll attitude. This modulation is illustrated in Figure 2.3 [37].

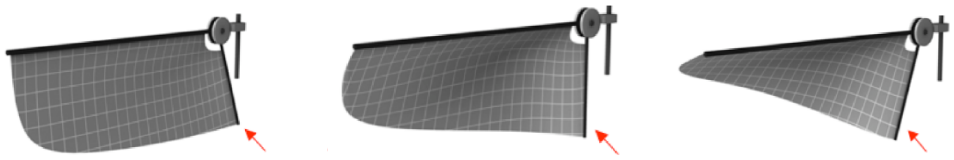

(a) (b) (c)

Figure 2.3: Illustration of the wing twist modulation as used in the Nano Hummingbird [37]. In this technique the wing root is moved in order to change the tightness of the wings. The lift generated is the highest in (a) and the the lowest in (c).

To control the pitch attitude the root of the wing was moved to the front or back on both wings, while for the control of the roll attitude it moved the wing roots either to the left or right.

There is not much information about the design of the controller of the Nano Hummingbird. However, the design of the controller for a similar FWMAV, called the Robotic Hummingbird, is described in the PhD research of Karásek et al. [35]. For the design of the controller, linearized analytic models of flapping flight are used in order to predict the states of the Robotic Hummingbird.

KU Beetle

The KU Beetle was developed at Konkuk University in 2016 and was also a tailless design. It has a weight of 21 grams and was based on the flight of Rhinoceros beetles. It is similar to the Nano Hummingbird in that it could also maintain hover, that it had a 190° flapping amplitude and that it also used the wing modulation technique similar to the one used for the Nano Hummingbird. The control mechanism for the KU Beetle is shown in Figure 2.4 [58].

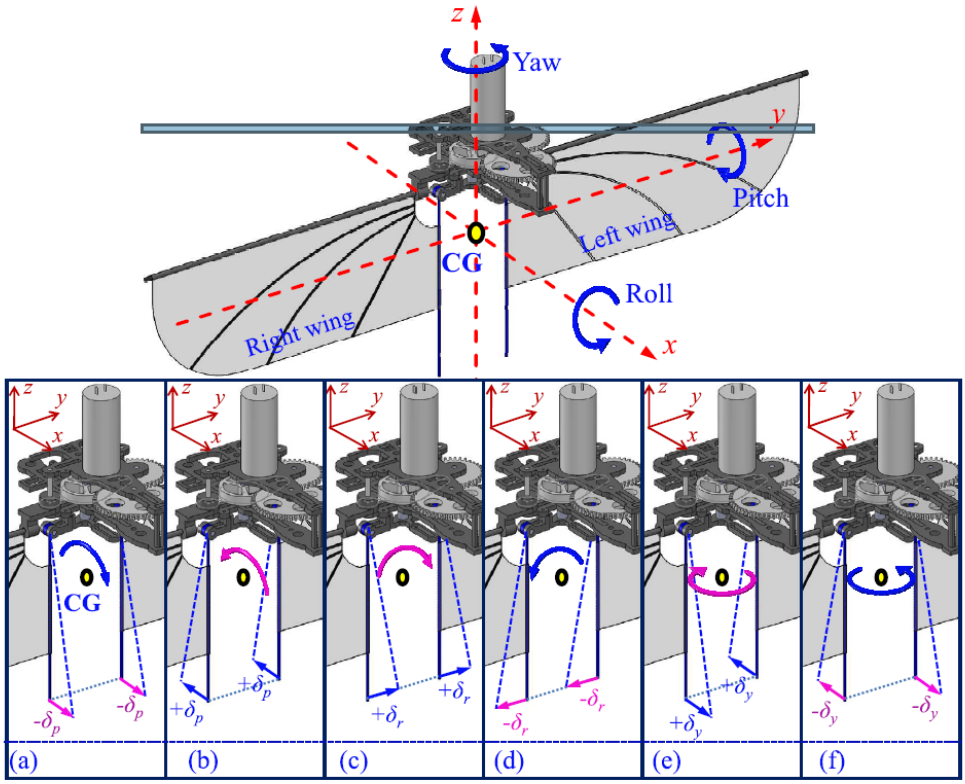

Figure 2.4: Control mechanism of the KU Beetle [58]. This FWMAV used wing twist modulation for the control of the pitch, roll and yaw attitude. In (a) and (b), it is shown that the pitch attitude is controlled by moving the wing roots to the front or back. In (c) and (d) it is shown that the roll attitude is controlled by moving the wing roots to the left or right. In (e) and (f) it can be seen that the yaw attitude is controlled by twisting both wing roots around the z-axis of the KU Beetle.

For control of the pith attitude it moves the wing roots to the front or back. For control of the roll attitude it moves the wing roots to the left or right. The main difference with the Nano Hummingbird is the control of the yaw attitude, which is done by twisting the wing roots around the fuselage of the KU Beetle. A proportional differential (PD) rate feedback controller was used in order to provide stability during flight, the block diagram of which is shown in Figure 2.5 [58].

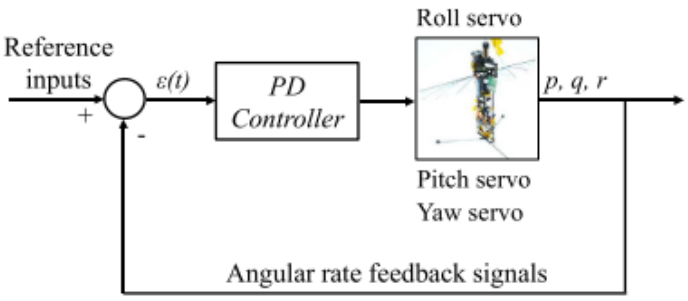

Figure 2.5: Block-diagram of the PD rate controller used on the KU Beetle [58].

A linear model of the KU Beetle has been identified for near hover conditions which could be used for the design and implementation of more complicated controllers [39]. The KU Beetle is the first FWMAV with two wings which could make use of the clap-and-fling effect in order to increase the lift generation [58]. This is possible due to the large flapping amplitude. The clap-and-fling effect is illustrated in Figure 2.6 [5, 64].

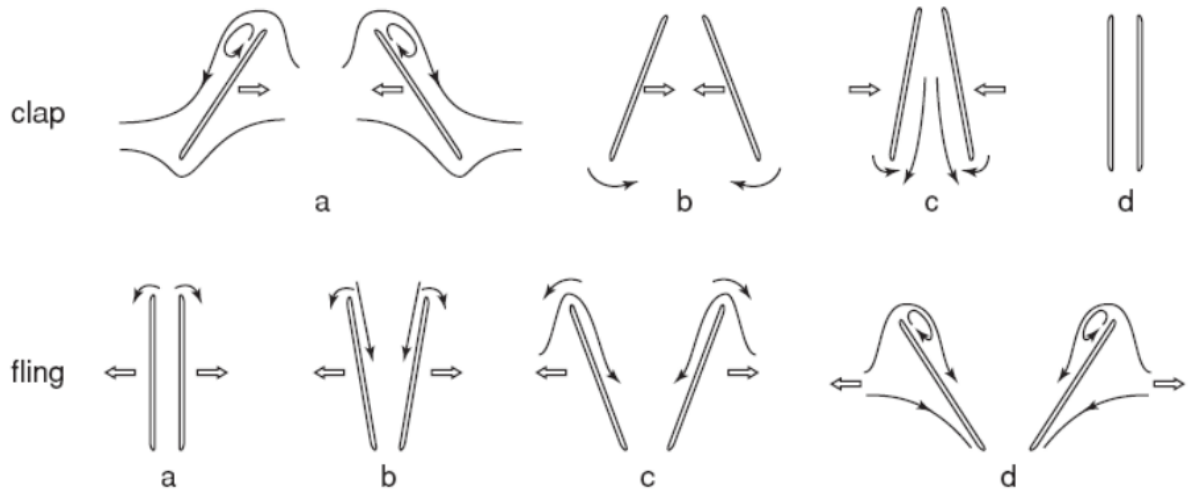

Figure 2.6: Illustration of the clap-and-fling-effect between two interacting wings [5, 64]. The thick arrows indicate the wing motion, while the thin arrows indicate the air flow. In the 'clap' phase, the two wings are moving towards each other, meeting initially at the leading edge. Then, the trailing edges move closer to each other, closing the gap between the wings. As a consequence, the air which was present in the gap is pushed downwards, increasing the thrust generation. In the 'fling' phase, the wings separate, starting with the leading edge. This creates a gap with a low pressure in which air will move, also creating additional lift.

In the 'clap' phase, the two wings are moving towards each other, meeting initially at the leading edge. Then, the trailing edges move closer to each other, closing the gap between the wings. As a consequence, the air which was present in the gap is pushed downwards, increasing the thrust generation. In the 'fling' phase, the wings separate, starting with the leading edge. This creates a gap with a low pressure in which air will move, also creating additional lift. Then, the leading edges also start to separate.

Bat Bot B2

The Bat Bot B2 is a tailed FWMAV which was developed in order to gain more knowledge about the flight of bats. The basis of the morphological design of this FWMAV was based on the *Rousettus Aegyptiacus* bat. It used a 5 ° of actuation system for the flapping mechanism. These degrees are: the forelimb flapping motion, the forelimb mediolateral folding motion, the forelimb mediolateral unfolding motion, the hindlimb dorsoventral upward motion and the hindlimb dorsoventral downward motion. It is able to do a forward flight with 4 ms^{-1}, but it is not able to hover. A custom-made silicon membrane was used for the wing. The attitude control is done using a tail mechanism with a PD-controller. This controller is designed by use of a mathematical dynamic model which is developed using the Lagrange method and the following assumptions: the wings and tails are massless, the wings and tail are separate, no consideration for aeroelasticity, both wings are flapping synchronously and both legs move at the same time with respect to the body.

The Delfly Family

The first development of the Delfly started in 2005 at the Delft University of Technology as an design synthesis exercise for Bachelor students [17]. It had a wingspan of 50 cm and used a single motor for the flapping mechanism and it had four wings instead of two. This design had passive stability due to the presence of the tail. It had control surfaces on the tail similar to those of an aircraft, namely an elevator and a rudder. Because there were two pairs of flapping wings, the Delfly could make use of the clap and fling effect, increasing the lift generation [17]. A smaller version was developed with the financial support of the Netherlands Organisation for applied scientific research TNO, called the Delfly II. This smaller version of the Delfly was presented in 2007 and had a wingspan of 28 cm, the ability to hover, fly forward with 7 ms^{-1} and fly backward with 1 ms^{-1}. Multiple variations of the Delfly have been developed since, including a tailless version called the Delfly Nimble. The Delfly II and the Delfly Nimble[36] are shown in Figure 2.7.

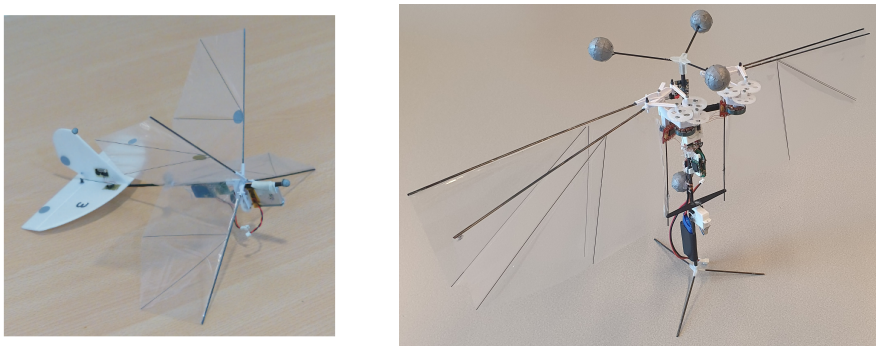

(a) Delfly II [9] (b) Delfly Nimble

Figure 2.7: Two iterations in the Delfly family, the Delfly II and the Delfly Nimble.

The Delfly II used the same control strategies as the original Delfly. The Delfly Nimble uses very different control mechanisms in order to maintain airborne. Since the Delfly Nimble was a tailless design, it was inherently unstable, as is the case for tailless FWMAV's [37, 45, 58]. It therefore requires an active controller for stable flight. The control mechanisms used in the Delfly Nimble are shown in Figure 2.8.

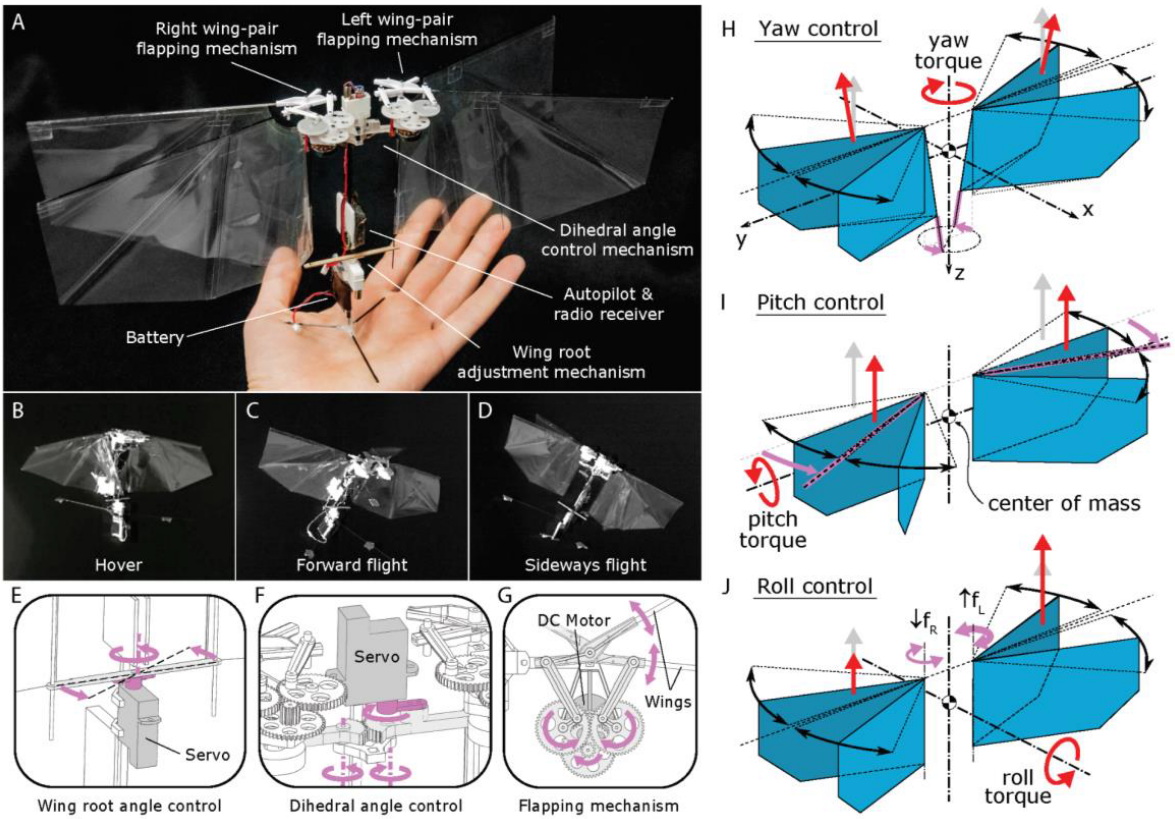

Figure 2.8: Explanation of the working principle of the Nimble [36]. In **A** an overview of the various components. In **B** to **D**, three different flights are shown, hover, forward and sideways. **E** to **G** show the working principle of the servos and flapping mechanism. **H** to **J** explain the control of the yaw, pitch and roll attitude.

From this Figure it can be seen that the Delfly Nimble also uses wing modulation techniques. For the yaw attitude control, it uses the same wing twist modulation technique as is done in the KU Beetle. A servo is used in order to change the wing root angle angle, shown in **H** of Figure 2.8. For the control of the pitch attitude, it changes the dihedral angle using a servo, shown in **I** of Figure 2.8. This wing modulation technique is

different form either the Nano Hummingbird or the KU Beetle. For control of the roll attitude it does not use wing modulation. Instead, the roll attitude is controlled by generating a difference in the flapping frequencies of both wings, shown in **J** of Figure 2.8. This difference in flapping frequency generates a roll torque. The side with the lower frequency is the one where the Delfly Nimble rolls towards.

The amount of torque which is required for stable flight is determined by a controller. The schematics of the controller is shown in Figure 2.9 [36]. The controller for the pitch and roll angle is shown in **A** and **B** of Figure 2.9. A reference generator is used to determine the input to the proportional and derivative controller. The controller for the yaw angle is show in **C** of Figure 2.9. This controller uses a proportional gain and also an additional feed-forward loop. The gains have been determined by trial and error, first by observing the stability of the Delfly Nimble while holding it in hand, and then by observing the stability in flight. For more complex maneuvers, such as rapid bank turns and pitch and roll flips, an open-loop program can be switched to. The autopilot is then in the open-loop configuration, switching back to the closed-loop one in order to recover the Delfly Nimble after the maneuver and preventing crashing [36].

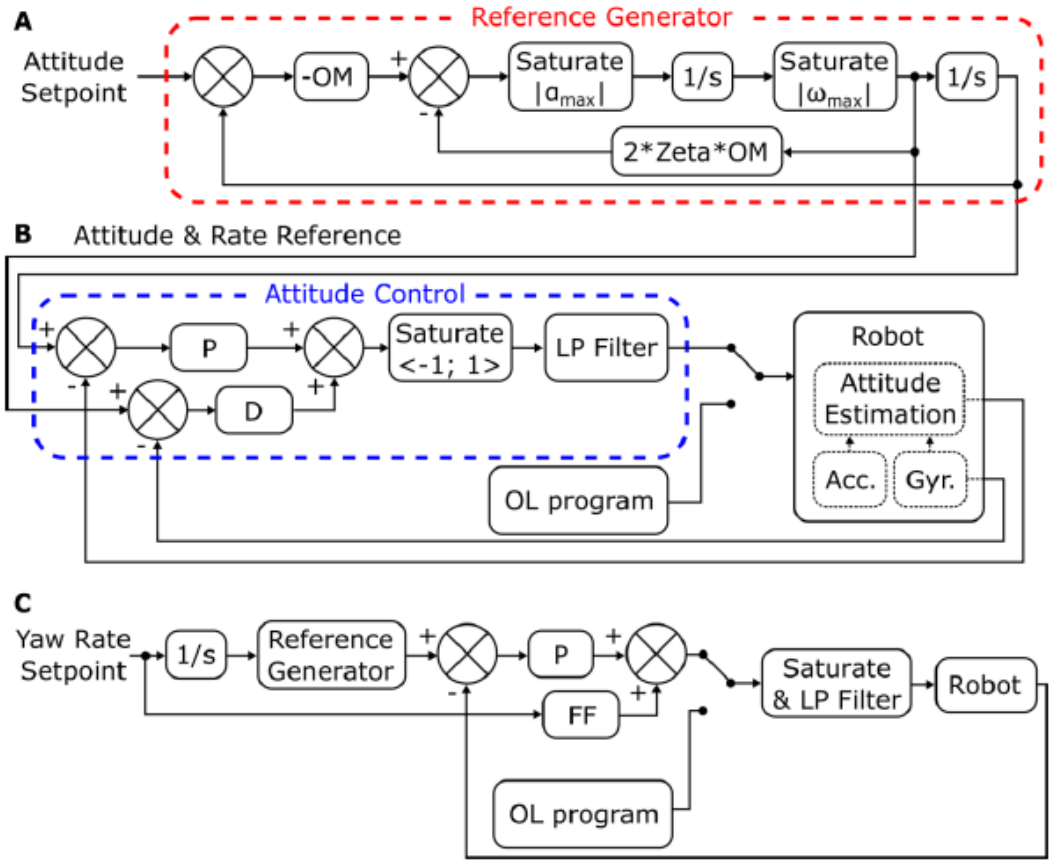

Figure 2.9: Overview of the on-board controller [36]. The Delfly Nimble is indicated as 'Robot' in this figure. In **A** the reference generator is shown. In **B** the attitude controller is shown which has proportional and derivative terms. For pitch and roll, the control structure is identical. In the research of Karásek et al. an open-loop program was used for rapid bank turns. In **C** the yaw loop is shown, which only uses a proportional controller and an additional feedforward term.

For the Delfly II, mathematical models have been identified for the body dynamics using free flight data [1, 3], whereas for the Delfly Nimble only the **longitudinal** dynamics have been modeled [32, 51, 52]. Mathematical models of the body dynamics can be applied for the development of control systems and can be used in order to gain greater understanding of the physical system [30, 40]. The main goals of this project are the identification of a mathematical model for the **lateral** body dynamics of the Delfly Nimble and to obtain a better understanding of these dynamics. The mathematical model will be developed using the System Identification Procedure [16], which is further elaborated on in Section 2.2.

2.2. System Identification Procedure

Klein et al. [40] and Zadeh [83] define System Identification as follows:

"One of the oldest and most fundamental of all human scientific pursuits is developing mathematical models for physical systems based on imperfect observations or measurements. This activity is known as system identification."[40, p. 1]

"System identification is the determination, on the basis of observation of input and output, of a system within a specified class of systems to which the system under test is equivalent."[83, p. 857]

In other words, System Identification is a procedure used to develop mathematical models of physical systems using the input and output data. This is further clarified in Figure 2.10[30].

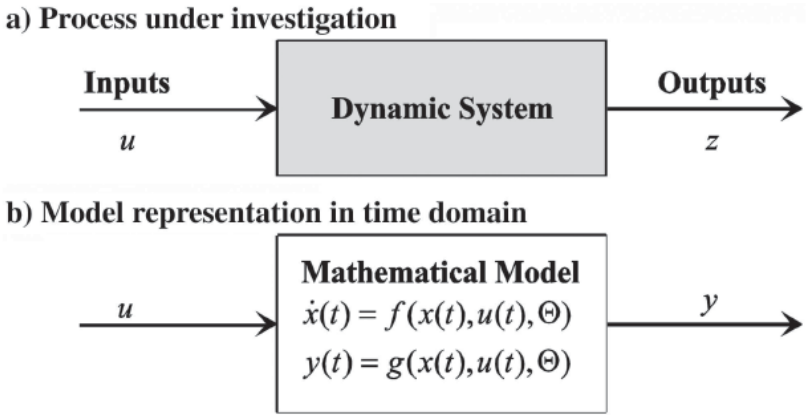

Figure 2.10: Clarification of System identification. The goal is the development of a mathematical which mimics the physical system based on the input u and the output z [30].

For the model identification of aircraft systems, the input and output data is gathered during free flight-tests. The developed models using System Identification can be used for the following applications in aircraft systems [16, 30, 40]: the development of flight simulators with high fidelity requirements, the verification of data obtained during wind-tunnel experiments, the development of control systems for inherently unstable aircraft, the analysis of the flight envelope and the development of pilot-models.

The development of a mathematical model is done by applying the System Identification Cycle. This cycle consists of three phases, each with its own aspects which have to be dealt with:

- Experiment Phase
  - Analysis of the physical system
  - Design and execution of the experiment
  - Logging and pre-processing of the data
- Model Identification Phase
  - Estimation of the states
  - Choice of model structure
  - Estimation of the parameters
- Model Validation Phase
  - Validation of the model

The System Identification Cycle is an iterative process, which is illustrated in Figure 2.11[16].

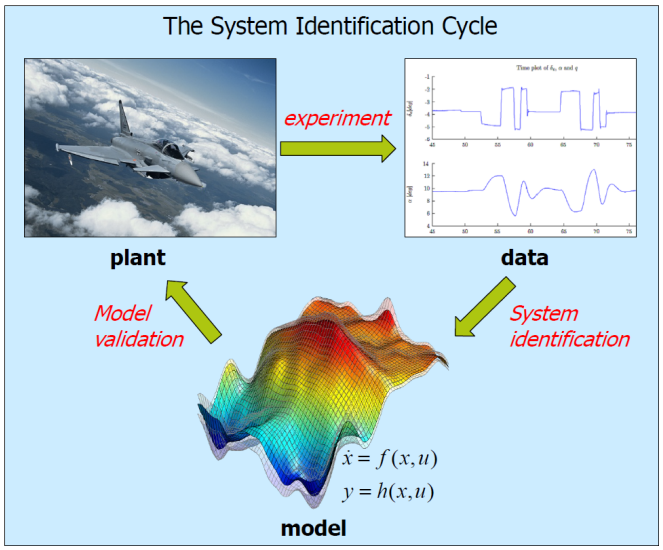

Figure 2.11: The System Identification Cycle. This cycle contains three phases: the experiment phase, the model identification phase and the model validation phase.[16]

From Figure 2.11 it can be seen that System Identification is an iterative process. It is possible that additional experiments have to be conducted or a different model structure needs to be used if the accuracy of the model is not sufficient. The System Identification Cycle is the Research Framework in this thesis. This framework will be used for the formulation of the research questions, which are shown in Section 2.3

2.3. Research Questions

The main goals of this research are to gain more knowledge about the lateral dynamics of the system and to develop a mathematical model of these dynamics. This model could then also be used for the design of control systems for the Nimble. Such a model can be determined using the System Identification Procedure which was described in Section 2.2. Based on the goal the following research objective has been formulated using the theory of Verschuren et al. [78]:

*The research objective is to identify a mathematical model for the lateral body dynamics of the Delfly Nimble **by** using the System Identification Procedure for the development of a linear grey-box state-space model.*

In order to reach this objective, one central question has been formulated:

"Can the full envelope of the lateral body dynamics of the Delfly Nimble be modeled using a linear time-invariant state-space model, and what is the influence of the dynamic coupling and the non-linearities on the predictive power of this model?"

Three sub-questions with their respective subsub-questions have been formulated for answering the central question. The formulation of these questions has been done using the Research Framework in this thesis, which is the System Identification Cycle:

SQ1. What is the experimental procedure to be followed in order to gather the required data?

(a) Which assumptions and simplifications can be used for the analysis of the dynamic system?
(b) What are the difficulties for experiment design when doing open-loop identification on a closed-loop system?
(c) Which maneuvers are available to gather the required Identification and Validation data, which inputs are required to make these maneuvers, and which trim condition is used?
(d) Do these maneuvers excite the dynamics of the system sufficiently?
(e) Which maneuvers are available to gather the required data for the analysis of the influence of the coupling of the dynamics, which inputs are required to make these maneuvers, and which trim

condition is used?

(f) Which maneuvers are available to gather the required data for the analysis of the influence of the non-linearities, which inputs are required to make these maneuvers, and which trim condition is used?

(g) Which sensors will be used and how will the data be pre-processed?

SQ2. Which System Identification approach needs to be taken for:

(a) the estimation of the states?

(b) the choice of model structure?

(c) the estimation of the parameters?

SQ3. What is the quality of the identified model?

(a) Which metrics can be used for validating the model?

(b) Is the decoupling of the dynamics a justifiable assumption?

(c) Is the linearity of the aerodynamic forces a justifiable assumption?

Each sub-question covers a phase in the System Identification Cycle. The Experiment Phase is covered by **SQ1**, while the Model Identification Phase is covered by **SQ2** and the Model Validation Phase is covered by **SQ3**. These questions were used to search for the relevant literature which is required to reach the research objective. The lay-out of this literature study is based on the sub-questions, which is elaborated on in Section 2.4.

2.4. Lay-out of the Literature study

The literature study is structured around the sub-questions defined in Section 2.3. Chapter 3 will treat the experiment phase and thus answer **SQ1**. Chapter 5 will treat the model identification phase and therefore answer **SQ2**. Chapter 5 will treat the model validation phase hence answer **SQ3**. The lay-out of this part is illustrated in Figure 2.12.

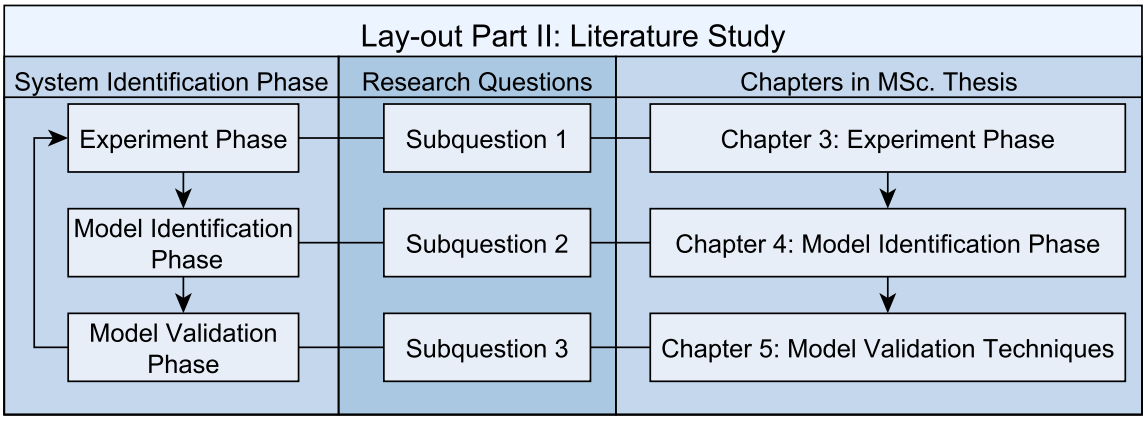

Figure 2.12: Lay-out of Part II of the thesis: the Literature Study.

3

Experiment Phase

This Chapter will cover the experiment phase of the System Identification Cycle and thus answer Subquestion **SQ1**, which was phrased as follows:

SQ1. What is the experimental procedure to be followed in order to gather the required data?

(a) Which assumptions and simplifications can be used for the analysis of the dynamic system?
(b) What are the difficulties for experiment design when doing open-loop identification on a closed-loop system?
(c) Which maneuvers are available to gather the required Identification and Validation data, which inputs are required to make these maneuvers, and which trim condition is used?
(d) Do these maneuvers excite the dynamics of the system sufficiently?
(e) Which maneuvers are available to gather the required data for the analysis of the influence of the coupling of the dynamics, which inputs are required to make these maneuvers, and which trim condition is used?
(f) Which maneuvers are available to gather the required data for the analysis of the influence of the non-linearities, which inputs are required to make these maneuvers, and which trim condition is used?
(g) Which sensors will be used and how will the data be pre-processed?

Section 3.1 will answer **SQ1a**. Question **SQ1b** will be answered in Section 3.2. Section 3.3 will answer questions **SQ1c** to **SQ1d**. This is followed by Section 3.4, which answers questions **SQ1e** and **SQ1f**. The chapter ends with Section 3.5, which answers question **SQ1g**.

3.1. Plant Analysis

This section will answer **SQ1a**. In previous research, the stability analysis of hovering insects and the modeling of flapping flight dynamics was done using the rigid body approximation [5, 34, 51, 60, 69, 70, 72, 81, 85, 86]. In this research the same approach will be taken. With the rigid-body approximation the equations of motion for a fixed-wing rigid-body aircraft can be used, shown in Equation 3.1 [67].

$$
\begin{aligned}
\dot{u} &= -(qw - rv) + \frac{X}{m} - g\cdot\sin(\theta) & I_{xx}\dot{p} &= (I_{yy} - I_{zz})\cdot qr + I_{xz}\cdot(\dot{r} + pq) + L \\
\dot{v} &= -(ru - pw) + \frac{Y}{m} + g\cdot\cos(\theta)\cdot\sin(\phi) & I_{yy}\dot{q} &= (I_{zz} - I_{xx})\cdot rp + I_{xz}\cdot(r^2 - p^2) + M \\
\dot{w} &= -(pv - qu) + \frac{Z}{m} + g\cdot\cos(\theta)\cdot\cos(\phi) & I_{zz}\dot{r} &= (I_{xx} - I_{yy})\cdot pq + I_{xz}\cdot(\dot{p} - rq) + N \\
\dot{\phi} &= p + q\cdot\sin(\phi)\cdot\tan(\theta) + r\cdot\cos(\phi)\cdot\tan(\theta) & & \\
\dot{\theta} &= q\cdot\cos(\phi) - r\cdot\sin(\phi) & & \\
\dot{\psi} &= q\cdot\frac{\sin(\phi)}{\cos\theta} + r\cdot\frac{\cos(\phi)}{\cos(\theta)} & &
\end{aligned}
\tag{3.1}
$$

Where u, v and w are the body velocities, $\dot{u}$, $\dot{v}$ and $\dot{w}$ are the body accelerations, p, q and r are the angular rates, $\dot{p}$, $\dot{q}$ and $\dot{r}$ are the angular accelerations, X, Y, Z are the aerodynamic forces, L, M and N are the aerodynamic moments, I_{xx} are the inertia terms, ϕ, θ and ψ are the attitude angles and $\dot{\phi}$, $\dot{\theta}$ and $\dot{\psi}$ are the attitude angular rates. These equations have been obtained by use of the following assumptions [48, 66, 67]:

- The body of the vehicle is rigid.
- The mass of the vehicle is constant.
- The Earth is flat and non-rotating.
- X_bZ_b is a symmetry plane, so I_{xy} and I_{yz} are assumed to be zero.

Are these assumptions also valid for the Delfly Nimble? The wings of the Nimble are not rigid, which would violate the first assumption. However, for FWMAV's one additional assumption that is frequently made is that the wing dynamics and the body dynamics can be decoupled [1, 5]. This is the case when the frequency of the flapping motion is higher than the system's bandwidth [34]. For the lateral dynamics of the Delfly Nimble, this is the case based on analytic calculations of the natural frequencies, which is shown in Section 3.3.1. The remaining parts of the Nimble are rigid, so for the modeling of the body dynamics this assumption is valid. The other assumptions are also valid for this research. The axis system of the Delfly Nimble used for the equations of motion is shown in Figure 3.1.

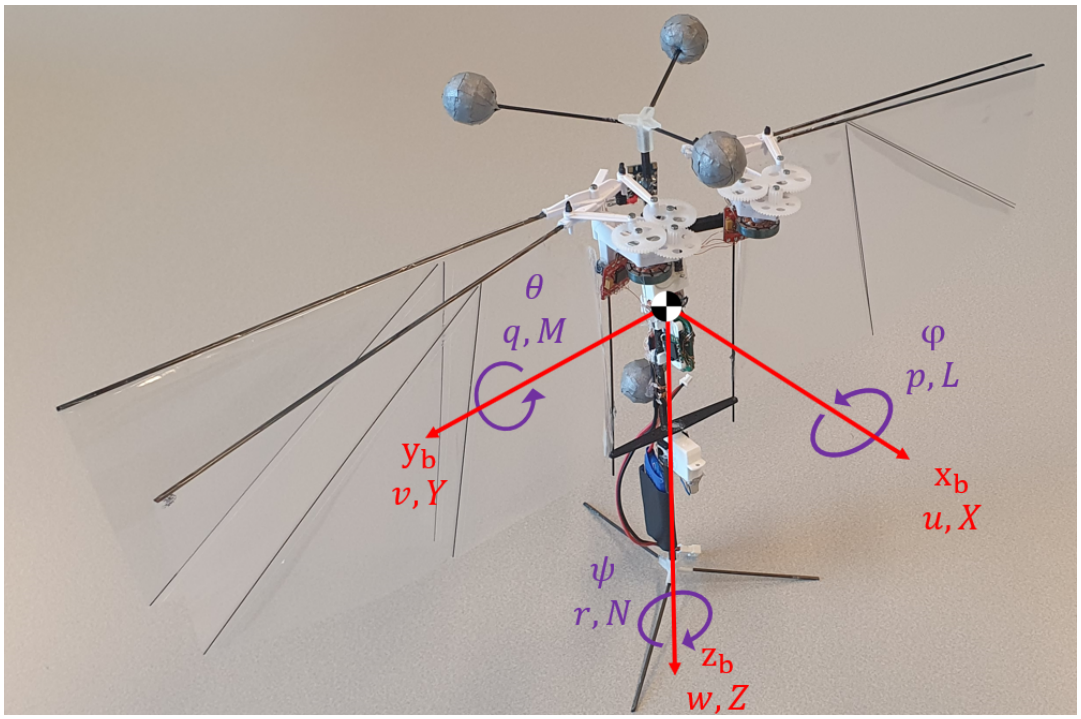

Figure 3.1: Axis system used on the Delfly Nimble.

The equations of motion shown in Equation 3.1 can be simplified by use of two additional assumptions. The first additional assumption is that there is no coupling between the longitudinal and lateral dynamics. This is an often made assumption for FWMAV's [1, 33, 34]. With this assumption, two dynamic systems are developed, one for the longitudinal dynamics and one for the lateral dynamics. The second additional assumption is that the aerodynamic forces and moments are quasi-steady, because of which these forces and moments can be modeled using a linear model structure. The linear modeling of the aerodynamic forces and moments can be done because the influence of the flapping motion on the body dynamics is considered to be negligible. Consequently, the cycle-averaged values of the forces and moments can be used. Then, small perturbation theory and a Taylor series expansion can be used for the linearization of the aerodynamic forces and moments. Using these two additional assumptions and by linearizing the equations of motion shown in Equation 3.1, two state space systems can be developed. The full derivation of the state space systems is shown in Appendix B. The **longitudinal** state space system is shown in Equation 3.2.

$$\begin{bmatrix} \dot{q} \\ \dot{u} \\ \dot{w} \\ \dot{\theta} \end{bmatrix} = \begin{bmatrix} \frac{M_q}{I_{yy}} & \frac{M_u}{I_{yy}} & \frac{M_w}{I_{yy}} & 0 \\ \frac{X_q}{m} - w_0 & \frac{X_u}{m} & \frac{X_w}{m} & -g \cdot \cos(\theta_0) \\ \frac{Z_q}{m} + u_0 & \frac{Z_u}{m} & \frac{Z_w}{m} & -g \cdot \sin(\theta_0) \cdot \cos(\phi_0) \\ \cos(\phi_0) & 0 & 0 & 0 \end{bmatrix} \cdot \begin{bmatrix} q \\ u \\ w \\ \theta \end{bmatrix} + \begin{bmatrix} \frac{M_{\delta_d}}{I_{yy}} & \frac{M_{\delta_f}}{I_{yy}} & \frac{M_{\delta_w}}{I_{yy}} & \frac{M_{\delta_t}}{I_{yy}} \\ \frac{X_{\delta_d}}{m} & \frac{X_{\delta_f}}{m} & \frac{X_{\delta_w}}{m} & \frac{X_{\delta_t}}{m} \\ \frac{Z_{\delta_d}}{m} & \frac{Z_{\delta_f}}{m} & \frac{Z_{\delta_w}}{m} & \frac{Z_{\delta_w}}{m} \\ 0 & 0 & 0 & 0 \end{bmatrix} \cdot \begin{bmatrix} \delta_d \\ \delta_f \\ \delta_w \\ \delta_t \end{bmatrix} \tag{3.2}$$

In previous research [5, 51, 52] the dimensional stability derivatives M_q, M_u, M_w, X_q, X_u, X_w, Z_q, Z_u and Z_w were determined using free-flight data, i.e. the dimensional stability derivatives were the estimated model parameters. Furthermore, M_{δ_d}, M_{δ_f}, M_{δ_w}, M_{δ_t}, X_{δ_d}, X_{δ_f}, X_{δ_w}, X_{δ_t}, Z_{δ_d}, Z_{δ_f}, Z_{δ_w} and Z_{δ_t} are the dimensional control derivatives, where δ_d, δ_f, δ_w and δ_t are the dihedral, the difference in flapping frequency between the left and right wing, the wingroot angle and the throttle input. These are the control inputs which are used in the Delfly Nimble. In the research of Nijboer et al. [51, 52] where the mathematical model for the longitudinal dynamics was developed only the dihedral angle input was used, thus only the M_{δ_d}, X_{δ_d} and Z_{δ_d} were parameters which were determined using free-flight data. The trim velocities are u_0 and w_0 and the trim angles are the initial pitch angle θ_0 and the initial roll angle ϕ_0. The **lateral** state space system, which will be used in this thesis for the determination of the mathematical mode of the lateral dynamics, is shown in Equation 3.3.

$$\begin{bmatrix} \dot{p} \\ \dot{r} \\ \dot{v} \\ \dot{\phi} \end{bmatrix} = \begin{bmatrix} \frac{I_{zz}}{I_c} \cdot L_p + \frac{I_{xz}}{I_c} \cdot N_p & \frac{I_{zz}}{I_c} \cdot L_r + \frac{I_{xz}}{I_c} \cdot N_r & \frac{I_{zz}}{I_c} \cdot L_v + \frac{I_{xz}}{I_c} \cdot N_v & 0 \\ \frac{I_{xz}}{I_c} \cdot L_p + \frac{I_{xx}}{I_c} \cdot N_p & \frac{I_{xz}}{I_c} \cdot L_r + \frac{I_{xx}}{I_c} \cdot N_r & \frac{I_{xz}}{I_c} \cdot L_v + \frac{I_{xx}}{I_c} \cdot N_v & 0 \\ \frac{Y_p}{m} + w_0 & \frac{Y_r}{m} - u_0 & \frac{Y_v}{m} & g \cdot \cos(\theta_0) \cdot \cos(\phi_0) \\ 1 & \tan(\theta_0) \cdot \cos(\phi_0) & 0 & 0 \end{bmatrix} \cdot \begin{bmatrix} p \\ r \\ v \\ \phi \end{bmatrix} +$$
$$\begin{bmatrix} \frac{I_{zz}}{I_c} \cdot L_{\delta_d} + \frac{I_{xz}}{I_c} \cdot N_{\delta_d} & \frac{I_{zz}}{I_c} \cdot L_{\delta_f} + \frac{I_{xz}}{I_c} \cdot N_{\delta_f} & \frac{I_{zz}}{I_c} \cdot L_{\delta_w} + \frac{I_{xz}}{I_c} \cdot N_{\delta_w} & \frac{I_{zz}}{I_c} \cdot L_{\delta_t} + \frac{I_{xz}}{I_c} \cdot N_{\delta_t} \\ \frac{I_{xz}}{I_c} \cdot L_{\delta_d} + \frac{I_{xx}}{I_c} \cdot N_{\delta_d} & \frac{I_{xz}}{I_c} \cdot L_{\delta_f} + \frac{I_{xx}}{I_c} \cdot N_{\delta_f} & \frac{I_{xz}}{I_c} \cdot L_{\delta_w} + \frac{I_{xx}}{I_c} \cdot N_{\delta_w} & \frac{I_{xz}}{I_c} \cdot L_{\delta_t} + \frac{I_{xx}}{I_c} \\ \frac{Y_{\delta_d}}{m} & \frac{Y_{\delta_f}}{m} & \frac{Y_{\delta_w}}{m} & \frac{Y_{\delta_t}}{m} \\ 0 & 0 & 0 & 0 \end{bmatrix} \cdot \begin{bmatrix} \delta_d \\ \delta_f \\ \delta_w \\ \delta_t \end{bmatrix} \tag{3.3}$$

Where $I_c = I_{xx} \cdot I_{zz} - I_{xz}^2$. What's more L_p, L_r, L_v, N_p, N_r, N_v, Y_p, Y_r and Y_v are the dimensional stability derivatives, which are parameters that will be estimated in this research. The dimensional control derivatives are the L_{δ_d}, L_{δ_f}, L_{δ_w}, L_{δ_t}, N_{δ_d}, N_{δ_f}, N_{δ_w}, N_{δ_t}, Y_{δ_d}, Y_{δ_f}, Y_{δ_w} and Y_{δ_t}. Which dimensional control derivatives will be determined using the free-flight data gathered during the experiments will depend on which control inputs are used in the model structure. For example, if only the dihedral angle and the wingroot angle are considered only the L_{δ_d}, N_{δ_d}, Y_{δ_d}, L_{δ_w}, N_{δ_w} and Y_{δ_w} are estimated.

If it is assumed that the dimensional stability and control derivatives shown in the longitudinal and lateral state space systems shown in Equations 3.2 and 3.3 are constant, these systems are linear time-invariant (LTI) state-space system for given initial conditions.

3.2. Experiment Design for Closed-loop Systems

This section will answer question **SQ1b**. As has been explained in Section 2.2 and visualized in Figure 2.10, the procedure of System Identification is used to determined a mathematical model which is able to predict the output y using the input u. For an open-loop system it is less difficult to excite the system dynamics compared to a closed-loop system due to the absence of an active controller. This makes it generally easier to design experiments in which the measurements z due to an input u will contain sufficient information of the dynamics of the system in order to develop a valid mathematical model. For a closed-loop system, an active controller is present which dampens the natural response of the system, which in turn reduces the information contained in the measurements z [40], making experiment design more difficult. The reduced information content in the measurements will then lead to a mathematical model which is only valid for a certain set of gains of the controller. However, such a model will not be useful for the design of controllers and to increase the knowledge of the system. Figure 3.2 [30] shows an example of a closed-loop system, which in this case is an aircraft.

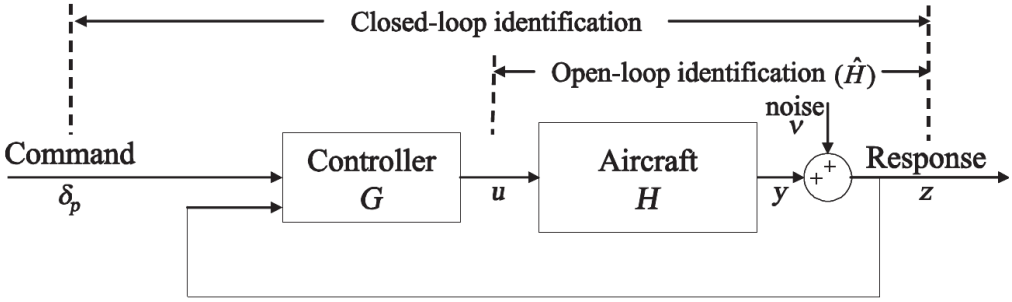

Figure 3.2: Example of a dynamic system, in this case an aircraft, in closed-loop configuration [30].

The controller G does not change the dynamics of the system H, it only changes the input u, which in turn gives a difference in the output y[40]. The goal is to get a good estimation of the system H, indicated by $\hat{H}$ in Figure 3.2. The Delfly Nimble is a tailless FWMAV, which have been shown to be inherently unstable [34]. Such vehicles require active stabilization to remain airborne, which for the Delfly Nimble is done by the controller described in Section 2.1. This controller makes the FWMAV in flight a closed-loop system. All the experiments will have to be conducted in closed-loop, for the Nimble will not stay airborne for very long without it.

For the identification of closed-loop systems, three methods have been proposed[38, 43]:

- **Direct Approach**
  The input u and out y are used in order to determine the model $\hat{H}$, ignoring the command δ_p and the controller. This is the Open-loop identification shown in Figure 3.2.
- **Indirect Approach**
  δ_p is seen as the input and y is seen as the output. This is the closed-loop identification shown in Figure 3.2. The open-loop model is then retrieved with the knowledge of the controller G.
- **Joint Input-Output Approach**
  u and y are both considered outputs of δ_p and the noise v. The knowledge of the system and the controller is then retrieved from the joint model.

The first approach has been used for the identification of the longitudinal dynamics model of the Nimble [32, 33, 51, 51]. The same approach will also be used in this research. During these researches, a command δ_p was given and the input u and the output y were measured. The disadvantage of this approach is that the input is not given directly to the system, but through a controller, which decreases the excitation and the information contained in the data. In spite of this, the identified longitudinal models the Nimble were able to predict the response well.

In order to identify such models, it is important that the data contains sufficient information. Klein et al. [40] states the following about the experiments for closed-loop aircraft systems:

"When conducting flight tests for aircraft dynamic modeling, ***the objective is to excite the natural aircraft motion as much as possible****, within the practical constraints of the flight test."* [40, p. 327]

The controller dampens the natural response of the system. The following measures have been used to excite the natural motions as much as possible [30, 40, 43]:

- **Reducing the gains of the controller**
  This decreases the damping of the natural motions.

- **Giving larger command**
  Most of the time in closed-loop systems, a command δ_p is given, and the input to the system is given by the controller. Larger commands generally lead to larger inputs to the dynamic system, which leads to more excitation of the natural motions.

- **Giving direct inputs to the control surfaces**
  In this way the u is given directly by the pilot. The input is then not disturbed by the feedback loop.

However, the last part of the statement of Klein et al. should be considered when using any of these approaches. Too much excitation of the natural motions can lead to an uncontrollable system which as a consequence will crash.

For the longitudinal dynamics model identification of the Nimble the first two approaches were used. The third one has the most risk, since acceleration control is then used for the Delfly Nimble. Controlling acceleration dynamics is very difficult for aircraft pilots [2]. An additional option is the use of open-loop maneuvers, which has been done in the research of Karásek et al. [36]. However, the maneuvers are very short, which leads to short datasets, containing less information. The use of longer open-loop maneuvers has a high probability of leading to damage to the Delfly Nimble, which is also unfavorable. Therefore, closed-loop maneuvers will be used with reduced controller gains and using larger commands. Several closed-loop maneuvers which have been used for the model identification of FWMAV's will be discussed in Section 3.3.

3.3. Maneuver Selection and input design

This section answers questions **SQ1c** to **SQ1d**. The available maneuvers which will be used for the generation of the identification and validation data are discussed. Susection 3.3.1 will explain how the natural frequencies of the lateral dynamics of the Delfly Nimble are determined. Subsection 3.3.2 elaborates the available maneuvers for gathering of the identification data, while Subsection 3.3.3 discusses the available maneuvers for the generation of the validation data. Subsection 3.3.4 answers question **SQ1d**, whether the selected maneuvers excite dynamics sufficiently.

3.3.1. Determining the natural frequencies of the Delfly Nimble

In Section 3.2 it was described that exciting the natural motions of a dynamic system is the main objective of the experiment. For the lateral dynamics of insects, three main frequency modes have been identified [12, 34, 86]. The pole maps of the eigenvalues is show in Figure 3.3.

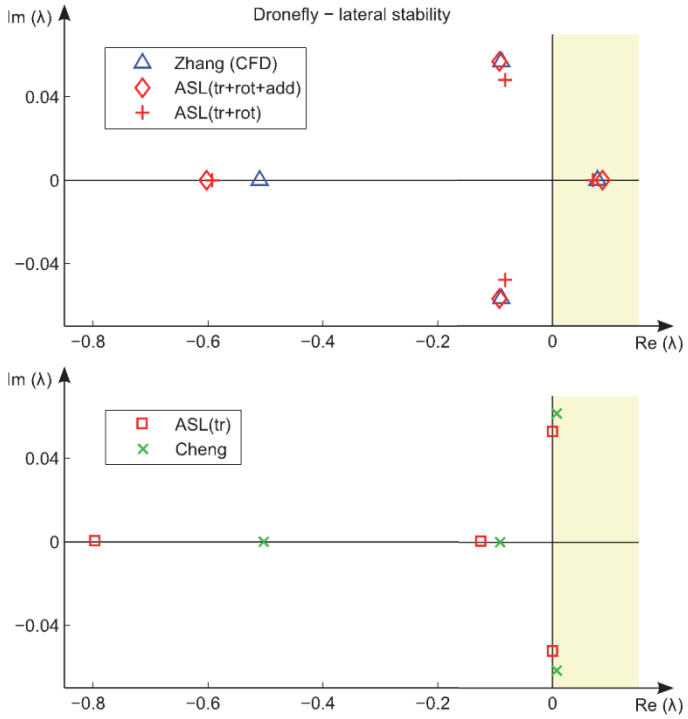

Figure 3.3: The analytic non-dimensionalized eigenvalues for the lateral dynamics of FWMAV's [34]. 'ASL' indicates the eigenvalues determined by Karásek et al. [34] where 'tr' indicates the wing translational forces, 'rot' indicates the wing rotational forces and 'add' indicates the forces due to the inertia of the added air mass. 'Zhang' the ones determined by Zhang et al. [86] and 'Cheng' the ones by Cheng et al. [12]. All the eigenvalues shown have been determined with the morphological data of the drone fly. The eigenvalues determined by Cheng et al. were recalculated, since the eigenvalues in this work were determined for four different insects: the fruit fly, hawkmoth, stalk-eyed fly and the bumblebee.

The eigenvalues shown in Figure 3.3 are non-dimensionalized in order to better compare the various models for insect dynamics. As can be seen from this figure, there are three main frequency modes for the lateral dynamics of FWMAV's. One aperiodic and two periodic. One of these three is unstable. Due to different assumptions, either the periodic mode is unstable [34, 86] or an aperiodic one [12]. As is the case for the natural modes of aircraft, each eigenvalue shown in Figure 3.3 represents a physical movement, which have been described in the research of Zhang et al. [86], the eigenvalues of which are shown in the top plot of Figure 3.3.

The first mode is known as the unstable slow divergence mode, indicated by the eigenvalue in the right-half plane. In this mode the insect is moving sideways, while it is rolled towards the same direction as the movement. For example, the insect is moving sideways to the right while being rolled towards the right. The second mode is known as the stable slow oscillatory mode, indicated by the two eigenvalues with an imaginary component. In this mode the the insect is moving sideways, while it is rolled in the opposite direction of the movement. For example, the insect is moving sideways to the right while being rolled towards the left. The third and final mode is known as the stable fast subsidence mode, indicated by the eigenvalue in left-half plane. In this mode the insect is rotating about the long axis of its body, i.e. a small yaw movement occurs. On the bottom plot of Figure 3.3, the modes are different. The unstable divergence mode is now stable and convergent, while the oscillatory mode is unstable. The fast subsidience mode remains the same.

The eigenvalues shown in Figure 3.3 are determined using the non-dimensionalized stability derivatives. When the **non-dimensional** stability derivatives are used, the eigenvalues are also **non-dimensional**. In order to determine the natural frequencies of the Delfly Nimble, the **dimensional** eigenvalues are required, which are determined using the **dimensional** stability derivatives. The natural frequencies can then be used for the design of the experiments. The non-dimensionalizing of the stability derivatives in the research of Karásek et al. [34] was done using several reference values. These are the reference velocity U, which is the average center of pressure velocity of the wing, the reference length $\bar{c}$, which is the mean chord length, and the reference time T, which is the wing beat period. Equations for these variables are shown in Equation 3.4.

$$U = 2\phi_m f \hat{r}, \quad \bar{c} = \frac{A_w}{b}, \quad T = \frac{1}{f} \tag{3.4}$$

Where ϕ_m is the flapping angle amplitude, f is the flapping frequency, $\hat{r}$ is the radius of the second moment of inertia of the wing, A_w is the wing area and b is the width of one wing. The latter three values are properties of the wing, which for the Delfly Nimble are determined using Figure 3.4 [1].

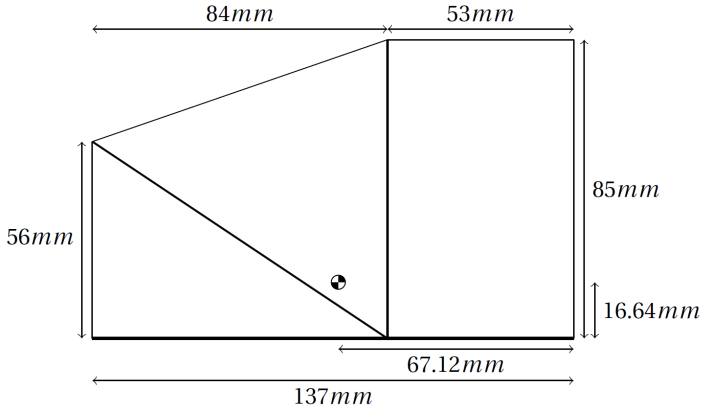

Figure 3.4: Schematics of the wings of the Delfly Nimble [1].

From this Figure the required characteristics for non-dimensionalizing the stability derivatives can be determined. The full calculation of the characteristics are shown in Appendix A.2. The b is set to 137 mm, the A_w was calculated to be 0.0104 m^2, the $\hat{r}$ was computed to be 74.5 mm, the f was set at 17 Hz and ϕ_m was set at 0.768 rad, or 44°. The non-dimensional stability derivatives can be found in the research of Karásek et al. [34]. With these values, the analytical values for the dimensional stability derivatives can be determined using Equation 3.5.

$$
\begin{aligned}
L_v &= L_v^+ \rho U A_w \bar{c} \qquad N_v = N_v^+ \rho U A_w \bar{c} \qquad Y_v = Y_v^+ \rho U A_w \\
L_p &= \frac{L_p^+ \rho U^2 A_w \bar{c}}{f} \qquad N_p = \frac{N_p^+ \rho U^2 A_w \bar{c}}{f} \qquad Y_p = \frac{Y_p^+ \rho U^2 A_w}{f} \\
L_r &= \frac{L_r^+ \rho U^2 A_w \bar{c}}{f} \qquad N_r = \frac{N_r^+ \rho U^2 A_w \bar{c}}{f} \qquad Y_r = \frac{Y_r^+ \rho U^2 A_w}{f}
\end{aligned} \tag{3.5}
$$

Where L_p^+, L_r^+, L_v^+, N_p^+, N_r^+, N_v^+, Y_p^+, Y_r^+ and Y_v^+ are the non-dimensional stability derivatives, and A_w is the area of one wing. Using the state space representation used in the research of Karásek et al. [34], the estimated natural frequencies of the Delfly Nimble can be determined, which are shown in Table 3.1.

Model	$\omega_1 \left(\frac{rad}{s}\right)$	$\omega_2 \left(\frac{rad}{s}\right)$ (periodic)	$\omega_3 \left(\frac{rad}{s}\right)$
Zhang (CFD)	4.38	6.09	14.01
ASL (tr+rot+add)	4.86	6.32	16.17
ASL (tr+rot)	4.00	5.49	16.03
ASL (tr)	7.10	3.48	16.23
Cheng	5.54	3.70	11.87

Table 3.1: Analytic eigenfrequencies of the lateral dynamics of the Delfly Nimble, based on the models developed by Karásek et al., Zhang et al. and Cheng et al. [12, 34, 86]. The models of Karásek et al. are indicated by 'ASL'. Here, 'tr' indicates the wing translational forces, 'rot' indicates the wing rotational forces and 'add' indicates the forces due to the inertia of the added air mass.

From this table it can be seen that all eigenvalues are in same order of magnitude, however, there are differences, especially for the ω_1 and the ω_2. To verify that the estimated analytic eigenfrequencies can be used, the eigenvalues for the longitudinal dynamics in hover have also been computed, and compared to the experimental results of Nijboer et al. [51, 52]. The results are shown in Table 3.2.

Model	$\omega_1 \left(\frac{rad}{s}\right)$	$\omega_2 \left(\frac{rad}{s}\right)$ (periodic)	$\omega_3 \left(\frac{rad}{s}\right)$
Wu (CFD)	8.42	7.63	0.11
ASL (tr+rot+add)	10.46	7.13	0.26
ASL (tr+rot)	9.97	6.84	0.26
ASL (tr)	7.53	6.14	0.26
Cheng	7.16	5.94	0.20
Nijboer (experimental)	8.89	5.36	0.13

Table 3.2: Analytic eigenfrequencies of the longitudinal dynamics of the Delfly Nimble, based on the models developed by Karásek et al., Wu et al. and Cheng et al. [12, 34, 80], and the experimental eigenfrequencies of Nijboer et al. [51]. The models of Karásek et al. are indicated by 'ASL'. Here, 'tr' indicates the wing translational forces, 'rot' indicates the wing rotational forces and 'add' indicates the forces due to the inertia of the added air mass.

From this table it can be seen that the analytic eigenfrequencies are close to the experimental ones. Therefore, the analytic eigenfrequencies can thus be used as an initial estimate for the natural frequencies of the Delfly Nimble. What is more, all the estimated natural frequencies are lower then the average flapping frequency of the Delfly Nimble, which was 17 Hz. Because of this the assumption that the flapping and body dynamics can be decoupled, which was described in Section 3.1, can be made. The analytic estimates of the natural frequencies can be used for the developments of the maneuvers which will be used for the generation of the data, discussed in Sections 3.3.2 and 3.3.3.

3.3.2. Maneuvers for the identification data

This section answers the first part of question **SQ1c**, which maneuvers are available for the generation of the identification data. Since this research focused on the lateral dynamics, the maneuvers will be done using inputs to the roll actuators in order to excite these dynamics. On the Nimble the roll torque is generated by creating a difference in flapping frequency between the left and right wing δ_f [36], as shown in Figure 2.8. The

roll actuator input might not be the only input during the maneuver however, since the controller might add inputs to the dihedral angle δ_d and the wing root angle δ_w for stabilization. For example, in the third natural mode for insects, known as the stable fast subsidence mode, the insect is making a small yaw movement, as was described in Subsection 3.3.1. The controller might give a command to the wing root angle actuator. Also the throttle δ_t could be increased in order to maintain altitude during a maneuver. If an input does not have a significant influence on the model accuracy, the input can be omitted in the state space system shown in Equation 3.3, reducing the number of parameters which have to be estimated.

Various maneuvers have been used for the excitation of dynamics, such as: the pulse, the doublet [5, 40, 51], the triplet[1], the 3211 maneuver[30, 40, 68] and the frequency sine sweep[53]. Such maneuvers have been used for the identification of aircraft models [30, 40, 43], where the maneuver was performed by a pilot. The disadvantage is that this decreases the repeatibility of the research, since it is difficult to perform the exact same maneuver by the pilot. This issue can be resolved using automated maneuvers, performed using an autopilot, which improves the repeatibility of the research and the quality of the identification data [21, 41].

The input required for a pulse is shown in Figure 3.5, while the input for a doublet is shown in Figure 3.6. When the command for a pulse is given, the Delfly Nimble will move to on side, in the case of the command shown to the right. When the command for the doublet is given to the Nimble, it moves first to the right, and then to the left. The amplitude in this figure is either the roll angle ϕ or the δ_f if direct inputs are given to the roll actuators. If the roll angle ϕ is given as the input, the actual command will be different due to the filtering of the controller shown in Figure 2.9.

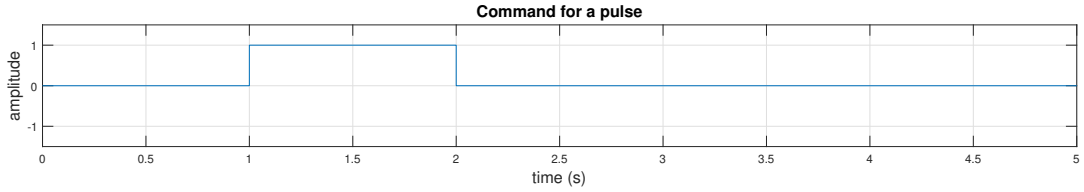

Figure 3.5: Command for a single pulse.

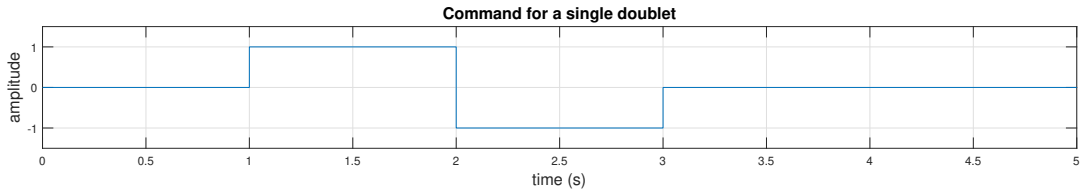

Figure 3.6: Command for a single doublet.

The main frequency which is excited is equal to $1/T$, where T is the time of the whole maneuver. For a linear system system, the output frequency is equal to the input frequency [54]. In order to achieve the best excitation, the T must be chosen such that the main frequency of the doublet is close to the natural frequencies of the Delfly Nimble. There are three natural frequencies which have been estimated for the Delfly Nimble, as was shown in Subsection 3.3.1. A doublet only excites one main frequency. In order to excite all frequencies, a train of roll doublets can be used with different main frequencies [40], the input for which is shown in Figure 3.7. Instead of doublets, pulses can also be used. In this case, the Delfly Nimble will only move to one side.

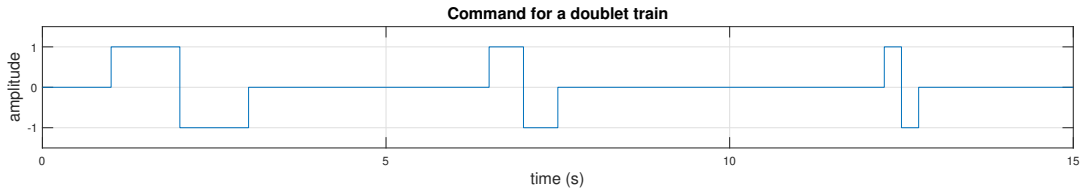

Figure 3.7: Command for a doublet train.

Multiple frequencies can also be excited using more complicated maneuvers, such as the triplet and the 3211. The input for these maneuvers are shown in Figure 3.8. With the triplet, two frequencies are excited, while three are excited with the 3211.

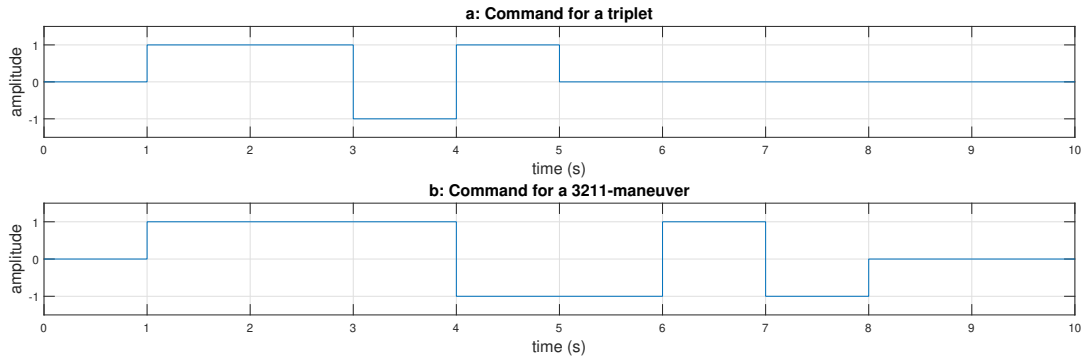

Figure 3.8: Command for the triplet, shown in **a**, and the 3211-maneuver, shown in **b**.

While these can excite multiple frequencies in a single maneuver, the main disadvantages are that these maneuvers are longer and have a larger drift from the initial condition, especially at the longer pulse. These can both lead to the Nimble ending up in the nets of the Cyberzoo, ending the experiment abruptly. There are ways to reduce the drift by using variations of these maneuvers. Examples of variations of the 3211 are shown in Figure 3.9.

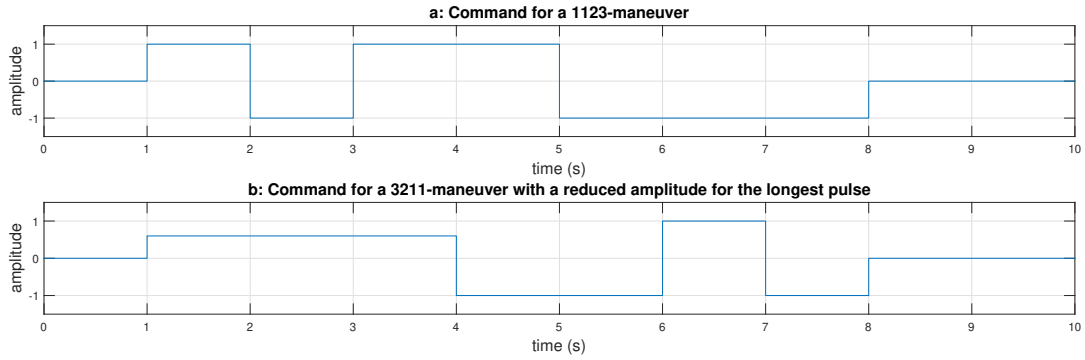

Figure 3.9: Commands for variations of the 3211-maneuver: **a** the reverse of the 3211. the 1123. **b** using a lower amplitude for the longest pulse.

Two variations are shown. A 1123-maneuver can be used instead, the advantage with this maneuver is that the largest drift from the initial condition is at the end of the maneuver. The influence of drifting from the initial condition is then minimized. What is also done is to reduce the amplitude of the command during the longest pulse. This also reduces the drift from the initial condition. If excitation of more frequencies is required or when little is known about the dynamics of the system, another option is to use a frequency sweep maneuver. An example of the command is shown in Figure 3.10. This approach has the same disadvantages as the triplet and the 3211-maneuver. This maneuver is even longer than these two, making it even more difficult to execute in practice.

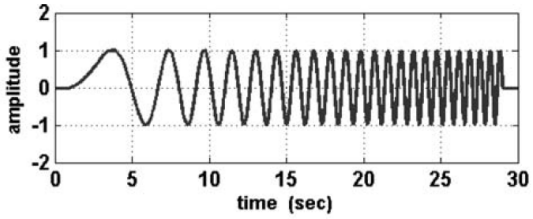

Figure 3.10: Command for the sine sweep maneuver[40].

3.3.3. Maneuvers for the validation data

This section answers the second part of question **SQ1c**, which maneuvers are selected for the generation of the validation data. As has been described in Section 3.2, the experiments have to be conducted in closed-loop. The effects of the controller can be minimized using the methods described in Section 3.2, which ensures that the identified model will be as similar as possible to the open-loop model. The initial condition chosen for the identification experiments is the hover condition. If the identified open-loop model is valid, then it should be able to be used for a different set of gains for the controller. The validation of this model can then be done using different gains for the controller and doing a maneuver, such as doublets, while using the hover as the initial condition. This approach has been used for the identification of the longitudinal dynamics of the Delfly Nimble [32, 51]. What is also an option is to use the doublet-train as the identification maneuver, and using a 1123-maneuver as the validation maneuver.

3.3.4. Analysis of the excitation of the dynamics

This section answers question **SQ1d**. The main goal during experiments is to excite the natural frequencies of the Delfly Nimble, as has been described in Section 3.2. This can be achieved using the maneuvers described in Subsection 3.3.2. Even if all this has been applied during the experiments, the excitation must still be verified. This can be done by analysing the data in the frequency domain. The frequency-domain data can be displayed in bode plots. In the magnitude plot there will then be peaks at the natural frequencies, for resonance can occur here for the plot of a closed-loop system [54]. If such peaks are visible, then the dynamics have been excited sufficiently. An example of such a plot is shown in Figure 3.11 [76].

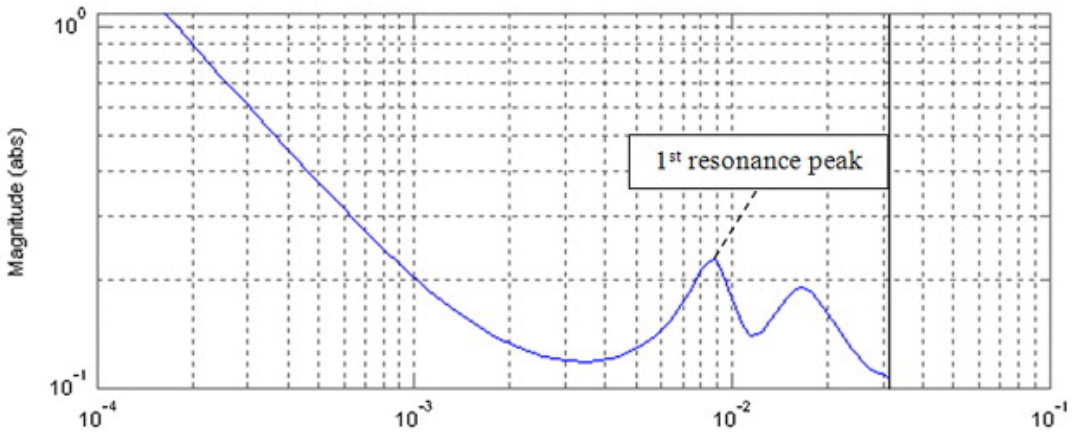

Figure 3.11: Example of a magnitude plot of a bode diagram with multiple resonance peaks [76].

In Figure 3.11 it can be seen that there are two frequency peaks in the magnitude plot. For the experiments for generation of the identification data done with the Delfly Nimble, at least three of those peaks are expected, one for each of the three natural modes which have been estimated in Subsection 3.3.1. More peaks can be visible, such as at the flapping frequency or harmonic frequencies. The transformation of the data from the time-domain to the frequency-domain can be achieved by estimating the power spectral densities of the data, which can be done using the Fast-Fourier transform [49].

3.4. Justifiability of decoupled dynamics and linearity assumptions

This section will answer questions **SQ1e** and **SQ1f**. In Section 3.1, it was described that two additional assumptions were made for the simplifications of the equations of motion, the decoupling of the longitudinal and lateral dynamics, and that the aerodynamic forces can be modeled using a linear model structure. In order to analyse the validity of these assumptions, coupled maneuvers will be used for the former and non-linear maneuvers will be used for the latter. The coupled maneuvers are described in Subsection 3.4.1, while the non-linear maneuvers are described in Subsection 3.4.2.

3.4.1. Maneuvers for the analysis of the influence of the coupling of the dynamics

This subsection answers question **SQ1e**. An often made assumption for FWMAV's is that the longitudinal and lateral dynamics are decoupled [1, 10, 31, 33]. This assumptions can be investigated by using coupled maneuvers, for example the evasive roll maneuver which was used in the research of Karásek et al. [36]. In this maneuver, there are three input signals, in pitch, roll and yaw. Another maneuver which can be used is performing a roll doublet while the Nimble is flying forward. Here, there are two inputs, in pitch and in roll. If the model is able to match the actual output well, the decoupling of the dynamics is a justifiable assumption.

3.4.2. Maneuvers for the analysis of the influence of the non-linearities

This section answers question **SQ1f**. The state space shown in Equation 3.3 is a linear time invariant system, which means that the parameters are constant. It is then implicitly assumed that the lateral dynamics of the Delfly Nimble can be modeled using such a linear system. This assumption can be verified by using maneuvers with a different initial condition. The trim condition can be accounted for by the initial velocities u_0, w_0 and the initial attitude angles θ_0 and ϕ_0 shown in the state space system in Equation 3.3. In a linear system, the dynamics can be modeled accurately using such a model structure regardless of the initial condition. The linearity assumption can be validated by using maneuvers with different initial conditions. One of the available maneuvers is that the Delfly Nimble is doing a doublet, while it has a non-zero value for the lateral velocity v_0. The sideways movement should then be accounted for by changing the value of the initial roll angle ϕ_0 in the state space system. If the model is able to match the actual output well, the assumption that a linear model of the lateral dynamics can be used is a justifiable one.

3.5. Sensors and processing of the data

This section answers question **SQ1g**. For the model identification of the Delfly II and the Delfly Nimble [1, 5, 32, 51] there were two main sources of gathering the data: from the Inertial Measurement Unit (IMU) and from the OptiTrack Motion tracking system. For the former source ring laser gyros and accelerometers are used to determine the rates and the accelerations. What is also logged are the flapping frequencies of both wings and the positions of the pitch and yaw servos, which can be used to determine the pitch and yaw angles. The data is logged onto an SD-card which is connected to an autopilot. For the latter source markers are required to register the position of the Delfly Nimble. The marker setup used in the research of Karásek et al.[36], Kajak et al [33] and Nijboer et al. [51] is shown in Figure 3.12.

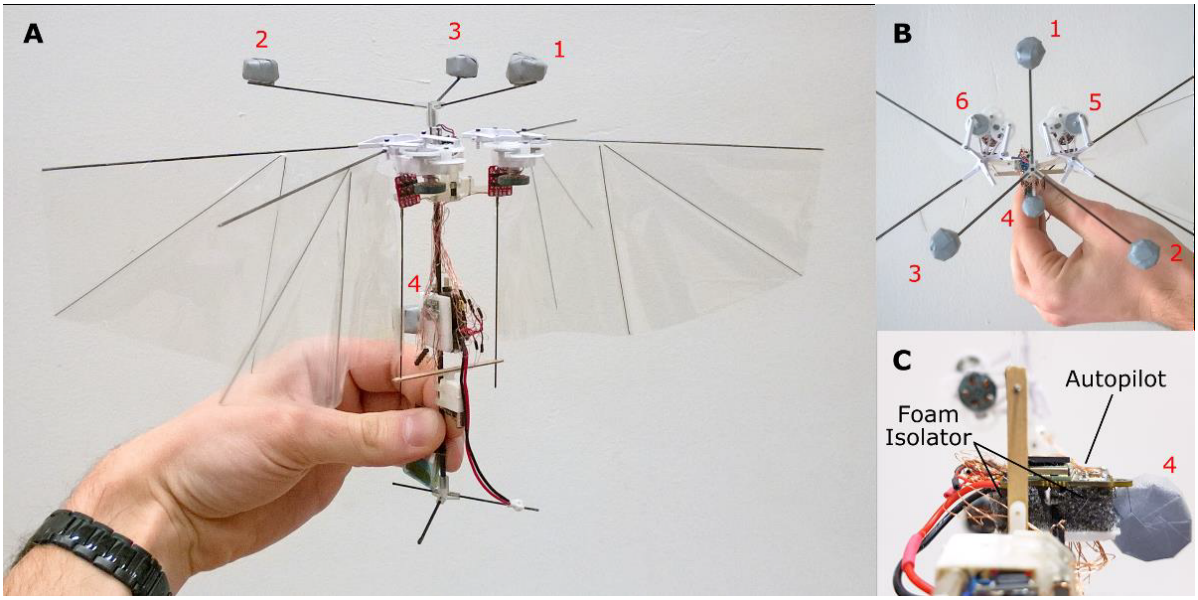

Figure 3.12: Locations of the markers on the Delfly Nimble, as used by Karasek and Nijboer [36, 51]. In **A**, the four markers define the body of the Nimble. In **B**, a top view is shown which displays two additional markers, 5 and 6, which were used in order to determine the dihedral angle of the system. However, in this research these markers won't be used. **C** shows a close up of the attachment of the fourth marker.

With this set-up the maneuvers will be performed in the flight arena "Cyberzoo". All the maneuvers were programmed using Paparazzi Autopilot [8] and are automatic in order to improve the repeatability of the research. The Delfly Nimble will be piloted using a DEVO 10 RC Transmitter. An overview of all the variables logged by both sources is shown in Table 3.3.

Source	Obtained measurements
OptiTrack	Position (x,y,z)
	Attitude Quaternions (q_0, q_1, q_2, q_3)
On-board	Angular Velocities (p, q, r)
	Linear Accelerations (a_x, a_y, a_z)
	Flapping frequency right (f_R)
	Flapping frequency left (f_L)
	Dihedral servo deflection (δ_d)
	Wing root servo deflection (δ_w)
	Throttle value (δ_t)

Table 3.3: Overview of the measurement obtained from the various data sources.

The data from both sources will have to be pre-processed before it can be used for the model identification. Firstly, sensor fusion will have to be applied to the data of both sources, which is done by a procedure developed by Armanini et al. [4]. Secondly the data will have to be filtered, especially the on-board data. This is due to the vibrations caused by the flapping motion of the wings. This generates noise in the logged data. Another solution is to use numerical differentiation on the OptiTrack data in order to attain the angular velocities (p, q, r) and the linear accelerations (a_x, a_y, a_z). This leaves only the flapping frequencies to be acquired from the On-board sensors. A flow diagram of this procedure is shown in figure 3.13 [5].

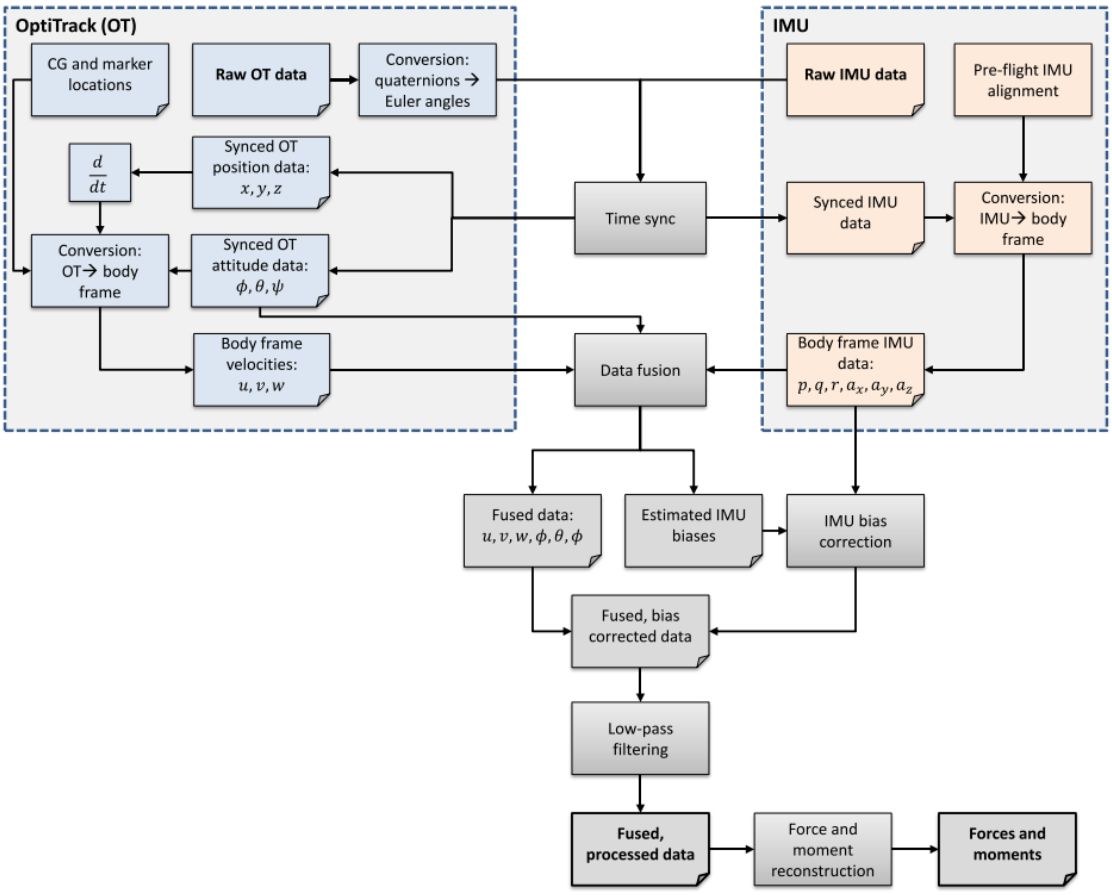

Figure 3.13: Flow diagram illustrating the fusion of the data of the sources: OptiTrack Motion system and the On-board sensors [5].

4

Model Identification Phase

This Chapter covers the model identification of the System Identification Cycle, thus answering Subquestion **SQ2**, which was phrased as follows:

SQ2. Which System Identification approach needs to be taken for:
- (a) the estimation of the states?
- (b) the choice of model structure?
- (c) the estimation of the parameters?

Firstly, Section 4.1 answers **SQ2a**. Secondly, Question **SQ2b** is answered in Section 4.2. Finally, Section 4.3 answers Question **SQ2c**.

4.1. State Estimation

This section answers Question **SQ2a**. Getting accurate estimates of the states is vital for the identification of a mathematical model which represents a dynamic system. Measurements are often subjected to sensor noise, sensor bias and process noise. Low-quality state estimates lead to low-quality identified mathematical models.

For the identification of aircraft models, the states have been estimated using Kalman Filters [30, 40]. These filters calculate a weighted average of the measured state and the predicted state. It uses the weighted error to correct the predicted state. This principle is shown in Equation 4.1.

$$\underline{x}_{est} = \underline{x}_{pred} + K \cdot (\underline{z}_{meas} - \underline{z}_{pred}) \tag{4.1}$$

Where $\underline{x}_{est}$ and $\underline{x}_{pred}$ are the estimated and the predicted state vector, $\underline{z}_{meas}$ and $\underline{z}_{pred}$ are the measured and the predicted measurement vector, and K is the Kalman gain. This gain determines the uncertainty in the measurement. The higher the gain, the lower the uncertainty. The calculation of the Kalman gain has been explained in various sources [16, 22, 30].

How the Kalman gain is determined depends on the type of Kalman Filter which is used. Which type of Kalman Filter is used depends on the dynamic system. The Conventional Kalman Filter can be used for the state estimation of linear systems. When a non-linear dynamic system is considered, the Extended Kalman Filter (EKF) is used instead. However, this filter does not guarantee convergence. This problem can be solved using a more advanced algorithm for the Kalman Filter, such as the Iterated Extended Kalman Filter (IEKF). Various other types of Kalman Filters exist. Kalman Filters can be used to filter out the noise and determine the sensor bias [5, 11]. It is also used for data fusion [5, 61], where the measurements of multiple sources are combined. For the development of dynamics models of the Delfly II, the EKF was also used in order to estimate sensor biases [4, 5]. Since the EKF has been used for the model identification of the Delfly II, it will also be used in the research of this thesis. If, however, this does not converge, the IEKF will be considered.

4.2. Model Structure Definition

This section answers Question **SQ2b**. There are several things one must take into consideration when choosing a model structure. Firstly, which model structure type is suitable? One will have to decide whether to use a white-box, black-box or grey box model structure. The definitions of these are explained in Subsection 4.2.1. Secondly, which model structures have been used in the past which lead to good identified mathematical models? Several examples of model structures for the identification of FWMAV's are shown in Subsection 4.2.2. Finally, how many parameters are required to get an accurate model. While it is the case that more parameters often lead to more accurate input-output mapping, this also comes at a higher computational cost [5]. What's more, for the grey-box model structure it is also important to consider which parameters are physically meaningful in order to better understand the dynamics [5]. The minimization of the number of parameters is elaborated in Subsection 4.2.3.

4.2.1. Model structure types

Three types of model structures have been classified in the field of System Identification [30, 38, 42]: white-box, black-box and grey-box models. The classification of the identified model depends on how much prior knowledge used for the development of the model. An illustration of the various model structure types is shown in figure 4.1 [46].

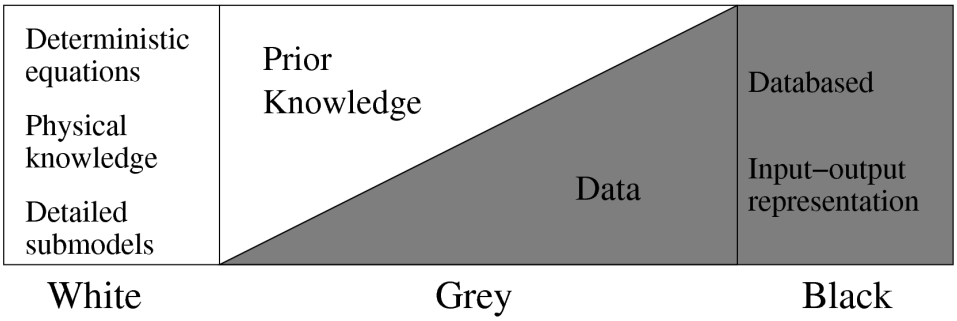

Figure 4.1: Explanation of the various model types [46]. Where a model structure fits on the spectrum depends on the amount of prior knowledge used for the identification. The more prior knowledge used, the 'whiter' the model structure. For the opposite case, the model structure is 'blacker'.

White-box model structures are developed using underlying physical knowledge, deterministic equations and detailed submodels. They require full understanding of the dynamic system. The advantage is that such models give good input-output mapping, while also giving good insight to the physics of a dynamic system. The disadvantage is that they are computationally expensive. Examples of white-box models are Kepler models [50], used in orbital mechanics and Maxwell's Equations [74], used in electrodynamics.

On the other end of the spectrum are black-box model structures. These models models only focus on getting the correct input-output relationships based on experimental data. The advantage of such systems is that they can accurately map complex and non-linear systems without prior knowledge of the dynamic system. However, these models give little to no insight into the physics of the system and they are more difficult to validate. A very common type of black-box model structure are neural networks [25, 26, 42].

In the middle of the spectrum are grey-box model structures, which are a combination of the two former types. These models use prior knowledge of the system, while also using experimental data on order to estimate certain parameters. Such models give good input-output mapping, while also giving more insight into the physics of the dynamic system then black-box models. They are also computationally less expensive than white-box models[16]. An example of a grey-box model is the state-space representation of aircraft dynamics shown in Equations 3.2 and 3.3. They are developed using the equations of motion shown in Equation 3.1, but the aerodynamic forces are estimated using experimental flight-data.

4.2.2. Examples of model structures used for FWMAV's

In this Subsection various model structures are elaborated on which have been used for the modeling of flapping flight dynamics. The following model structures are discussed: analytic models as used by Karásek et al. [34, 35], the grey-box model used for the modeling of the KU Beetle [39], black-box, local grey-box and

global grey-box modeling of the Delfly II as done in the research of Armanini et al. [3–6], multi-body dynamic modeling of the Delfly II as was done by Caetano et al. [9], and the modeling of the longitudinal dynamics as done by Kajak et al. and Nijboer et al. [32, 33, 51, 52].

Analytic Models of flapping flight

In Section 3.3 the natural frequencies were determined using analytic models of insect body dynamics. The various analytic models have been described and compared in the research of Karásek et al. [34]. These model structures are the most white of those described in this subsection. The free body diagram shown in Figure 4.2 was used to identify the mathematical models.

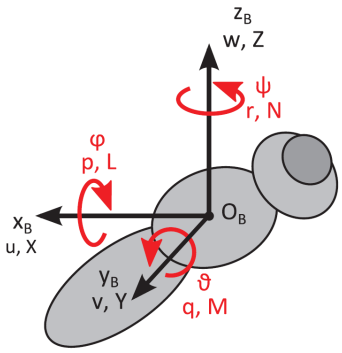

Figure 4.2: Axis system as used by Karásek et al. [34]. The insect depicted is the drone fly.

Using this axis system the state-space systems for the longitudinal and lateral dynamics have been determined, shown in Equations 4.2 and 4.3.

$$\begin{bmatrix} \dot{u} \\ \dot{w} \\ \dot{q} \\ \dot{\theta} \end{bmatrix} = \begin{bmatrix} \frac{X_u}{m} & \frac{X_w}{m} & \frac{X_q}{m} & g \\ \frac{Z_u}{m} & \frac{Z_w}{m} & \frac{Z_q}{m} & 0 \\ \frac{M_u}{I_{yy}} & \frac{M_w}{I_{yy}} & \frac{M_q}{I_{yy}} & 0 \\ 0 & 0 & 1 & 0 \end{bmatrix} \cdot \begin{bmatrix} u \\ w \\ q \\ \theta \end{bmatrix} + B_{lon} \cdot \underline{u}_{lon} \tag{4.2}$$

$$\begin{bmatrix} \dot{v} \\ \dot{p} \\ \dot{r} \\ \dot{\phi} \end{bmatrix} = \begin{bmatrix} \frac{Y_v}{m} & \frac{Y_p}{m} & \frac{Y_r}{m} & -g \\ \frac{L_v}{I_1} + \frac{N_v}{I_2} & \frac{L_p}{I_1} + \frac{N_p}{I_2} & \frac{L_r}{I_1} + \frac{N_r}{I_2} & 0 \\ \frac{L_v}{I_2} + \frac{N_v}{I_3} & \frac{L_p}{I_2} + \frac{N_p}{I_3} & \frac{L_r}{I_2} + \frac{N_r}{I_3} & 0 \\ 0 & 1 & 0 & 0 \end{bmatrix} \cdot \begin{bmatrix} v \\ p \\ r \\ \phi \end{bmatrix} + B_{lat} \cdot \underline{u}_{lat} \tag{4.3}$$

Where the definition of the inertia terms I_1m I_2 and I_3 are shown in Equation 4.4.

$$I_1 = \frac{I_{xx} \cdot I_{zz} - I_{xz}^2}{I_{zz}}, \quad I_2 = \frac{I_{xx} \cdot I_{zz} - I_{xz}^2}{I_{xz}}, \quad I_3 = \frac{I_{xx} \cdot I_{zz} - I_{xz}^2}{I_{xx}} \tag{4.4}$$

The wing kinematics were added to the model using two degree of freedoms, the inclination angle α^* and the wing sweep angle ϕ shown in Figure 4.3.

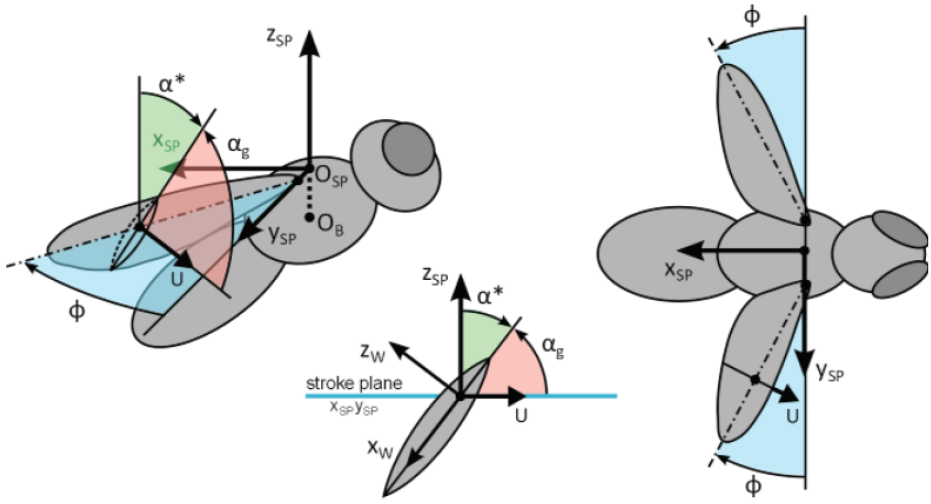

Figure 4.3: Wing kinematics as defined by Karásek et al. [34]. The insect depicted is the drone fly.

The aerodynamic forces X, Y and Z are determined using thin airfoil theory in combination with experimentally obtained force coefficients which include some unsteady effects [34, 62]. The full mathematical equations can be found in the research of Karásek et al. [34]. The same techniques were used for the development of a mathematical model for the Robotic Hummingbird [35]. For the analysis of the stability in hover condition four reduced models were used. One for the pitch dynamics, shown in Equation 4.5, one for the vertical dynamics. shown in Equation 4.6, one for the roll dynamics. shown in Equation 4.7 and one for the yaw dynamics, shown in Equation 4.8.

$$\begin{bmatrix} \dot{u} \\ \dot{q} \\ \dot{\theta} \end{bmatrix} = \begin{bmatrix} \frac{X_u}{m} & \frac{X_q}{m} & g \\ \frac{M_u}{I_{yy}} & \frac{M_q}{I_{yy}} & 0 \\ 0 & 1 & 0 \end{bmatrix} \cdot \begin{bmatrix} u \\ q \\ \theta \end{bmatrix} + \begin{bmatrix} 1 & 0 \\ 0 & 1 \\ 0 & 0 \end{bmatrix} \cdot \begin{bmatrix} \frac{X_{ext}}{m} \\ \frac{M_{ext}}{m} \end{bmatrix} \tag{4.5}$$

$$\dot{w} = \frac{Z_w}{m} \cdot w + \frac{Z_{ext}}{m} \tag{4.6}$$

$$\begin{bmatrix} \dot{v} \\ \dot{p} \\ \dot{\phi} \end{bmatrix} = \begin{bmatrix} \frac{Y_v}{m} & \frac{Y_p}{m} & -g \\ \frac{L_v}{I_{xx}} & \frac{L_p}{I_{xx}} & 0 \\ 0 & 1 & 0 \end{bmatrix} \cdot \begin{bmatrix} v \\ p \\ \phi \end{bmatrix} + \begin{bmatrix} 1 & 0 \\ 0 & 1 \\ 0 & 0 \end{bmatrix} \cdot \begin{bmatrix} \frac{Y_{ext}}{m} \\ \frac{L_{ext}}{m} \end{bmatrix} \tag{4.7}$$

$$\dot{r} = \frac{N_r}{I_{zz}} \cdot r + \frac{N_{ext}}{I_{zz}} \tag{4.8}$$

Where X_{ext}, Y_{ext}, Z_{ext} are the external forces, L_{ext}, M_{ext} and N_{ext} are the external moments. The axis system shown in Figure 4.2 was used with these reduced models.

Modeling of the KU Beetle

For the KU Beetle a linear model has been designed which could be used for the design of the controller [39]. The axis sytem used for the model identication is shown in Figure 4.4.

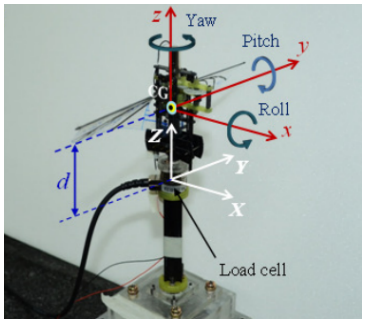

Figure 4.4: Axis system as used by Khan et al.[39]. The red axis system indicated the body frame and the white one indicates the inertial frame.

The reconstruction of the states was done using the equations shown in Equation 4.9 [39].

$$\begin{aligned} \dot{x}(t_{i+1}) &= \dot{x}(t_i) + \frac{F(t_i)}{m}\Delta t \\ x(t_{i+1}) &= x(t_i) + \left(\dot{x}(t_i) + \frac{F(t_i)}{m}\Delta t\right)\Delta t \end{aligned} \tag{4.9}$$

Where $\dot{x}(t_{i+1})$ is velocity state vector and $x(t_{i+1})$ is the position state vector at time t_{i+1}, $F(t_i)$ is the aerodynamic force vector at time t_i and Δt is the time step. The angular positions and rates can be determined using the moments at time t_i, indicated by $M(t_i)$ and the inertia I instead of the forces and mass. For the calculation of the inertia terms the following assumptions were made: the wings are rectangles and have negligible thickness, the wings have no mass and the body is assumed to be a cylinder with the mass of the cylinder concentrated in the center of gravity, and the body is rigid and the products of inertia are neglected.

For the modeling of the aerodynamic forces and moments a linear model structure was used, similar to the one shown in Section 3.1. The linear model fort the forces and moments is shown in Equation 4.10.

$$\begin{aligned} X &= X_0 + X_u\Delta u + X_{\dot{u}}\Delta\dot{u} + X_\theta\Delta\theta + X_{\dot{\theta}}\Delta\dot{\theta} + X_\phi\Delta\phi + X_{\dot{\phi}}\Delta\dot{\phi} + X_{\psi_{flap}}\Delta\psi_{flap} \\ Y &= Y_0 + Y_v\Delta v + Y_{\dot{v}}\Delta\dot{v} + Y_{\dot{\theta}}\Delta\dot{\theta} + Y_\phi\Delta\phi + Y_{\dot{\phi}}\Delta\dot{\phi} + Y_\psi\Delta\psi + Y_{\dot{\psi}}\Delta\dot{\psi} + Y_{\psi_{flap}}\Delta\psi_{flap} \\ Z &= Z_0 + Z_w\Delta w + Z_{\dot{w}}\Delta\dot{w} + Z_\theta\Delta\theta + Z_{\dot{\theta}}\Delta\dot{\theta} + Z_\phi\Delta\phi + Z_{\dot{\phi}}\Delta\dot{\phi} + Z_{\psi_{flap}}\Delta\psi_{flap} \\ L &= L_0 + L_u\Delta u + L_{\dot{u}}\Delta\dot{u} + L_\theta\Delta\theta + L_{\dot{\theta}}\Delta\dot{\theta} + L_\phi\Delta\phi + L_{\dot{\phi}}\Delta\dot{\phi} + L_{\psi_{flap}}\Delta\psi_{flap} \\ M &= M_0 + M_u\Delta u + M_{\dot{u}}\Delta\dot{u} + M_\theta\Delta\theta + M_{\dot{\theta}}\Delta\dot{\theta} \\ N &= N_0 + N_v\Delta v + N_{\dot{v}}\Delta\dot{v} + N_{\dot{\theta}}\Delta\dot{\theta} + N_\phi\Delta\phi + N_{\dot{\phi}}\Delta\dot{\phi} + N_\psi\Delta\psi + N_{\dot{\psi}}\Delta\dot{\psi} + N_{\psi_{flap}}\Delta\psi_{flap} \end{aligned} \tag{4.10}$$

The aerodynamic forces (X, Y, Z), moments (L, M, N), and the states were measured during the experiments for 0.04 seconds. The stability derivatives were determined using the ordinary least-squares approach, which is explained in Subsection 4.3.1.

Delfly II: Black-box model

In the work of Armanini et al. [6], a LTI-state space model structure was used. No assumptions were made on the terms inside the A and B matrices.

$$\dot{x}_{lon} = \begin{bmatrix} \dot{q} \\ \dot{u} \\ \dot{w} \\ \dot{\theta} \end{bmatrix} = \begin{bmatrix} a_{11} & a_{12} & a_{13} & a_{14} \\ a_{21} & a_{22} & a_{23} & a_{24} \\ a_{31} & a_{32} & a_{33} & a_{34} \\ a_{41} & a_{42} & a_{43} & a_{44} \end{bmatrix} \cdot \begin{bmatrix} q \\ u \\ w \\ \theta \end{bmatrix} + \begin{bmatrix} b_1 \\ b_2 \\ b_3 \\ b_4 \end{bmatrix} \cdot \delta_e \tag{4.11}$$

$$\dot{x}_{lat} = \begin{bmatrix} \dot{p} \\ \dot{r} \\ \dot{v} \\ \dot{\phi} \end{bmatrix} = \begin{bmatrix} a_{11} & a_{12} & a_{13} & a_{14} \\ a_{21} & a_{22} & a_{23} & a_{24} \\ a_{31} & a_{32} & a_{33} & a_{34} \\ a_{41} & a_{42} & a_{43} & a_{44} \end{bmatrix} \cdot \begin{bmatrix} p \\ r \\ v \\ \phi \end{bmatrix} + \begin{bmatrix} b_1 \\ b_2 \\ b_3 \\ b_4 \end{bmatrix} \cdot \delta_r \tag{4.12}$$

Where δ_e is the elevator deflection and δ_r is the rudder deflection. The body-fixed coordinate system shown in Figure 4.5. The parameters of this model, which are all the entries of the A and B matrix in Equations 4.11 and 3.3, were determined using the input and output data, and the output-error approach was used to determine these. The output-error approach is explained later in Subsection 4.3.2.

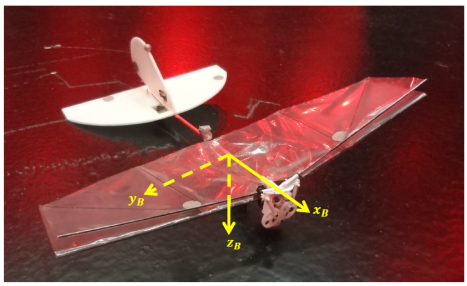

Figure 4.5: Axis system as used by Armanini et al. for the model identification of the Delfly II [5].

Delfly II: Local Grey-box model

A grey-box model structure has also been used for the model identification of he Delfly II [3, 5]. An LTI state-space system was used, shown in Equations 3.2 and 3.3, the only difference being the input matrices. The Delfly II had all its control surfaces in the tail. The inputs which were used for the excitation of the dynamics. The input vectors used for the longitudinal and lateral dynamics are shown in Equation 4.13.

$$B_{lon} \cdot \underline{u}_{lon} = \begin{bmatrix} \frac{M_{\delta_D}}{I_{yy}} & b_{\dot{q}} \\ \frac{X_{\delta_D}}{m} & b_{\dot{u}} \\ \frac{Z_{\delta_D}}{m} & b_{\dot{w}} \\ 0 & b_{\dot{\theta}} \end{bmatrix} \cdot \begin{bmatrix} \delta_e \\ 1 \end{bmatrix}, \quad B_{lat} \cdot \underline{u}_{lat} = \begin{bmatrix} \frac{I_{zz}}{I_c} \cdot L_{\delta_r} + \frac{I_{xz}}{I_c} \cdot N_{\delta_r} & b_{\dot{p}} \\ \frac{I_{xz}}{I_c} \cdot L_{\delta_r} + \frac{I_{xx}}{I_c} \cdot N_{\delta_r} & b_{\dot{r}} \\ \frac{Y_{\delta_r}}{m} & b_{\dot{v}} \\ 0 & b_{\dot{\phi}} \end{bmatrix} \cdot \begin{bmatrix} \delta_r \\ 1 \end{bmatrix} \tag{4.13}$$

Where $b_{\dot{q}}$, $b_{\dot{u}}$, $b_{\dot{w}}$ $b_{\dot{\theta}}$, $b_{\dot{p}}$, $b_{\dot{r}}$, $b_{\dot{v}}$ and $b_{\dot{\phi}}$ are bias terms, which include all the dynamics which were not captured by the model structure. Lower values of the biases are favourable. This LTI state-space system was used for the determination of time-invariant body dynamics of the Delfly II. The time-varying component have been determined using a Fourier Series [3]. The parameters were determined using the output-error approach, explained in Subsection 4.3.2.

Delfly II: Global Grey-box model

For a non-linear dynamic system, the LTI state-space model will only be accurate if the operating conditions are around the trim condition. The equations of motions have been linearized in this condition, making the identified model only accurate locally. In order to identify a more global model, a linear parameter-varying (LPV) model was identified. This approach is closely related to the gain scheduling approach [7, 23, 57]. In the LPV modeling approach, multiple trim conditions are chosen, which leads to multiple local models. Then, a global model is identified by finding a function which can interpolate between the local models. An arbitrary scheduling variable is used for this function. In the research of Armanini et al. the trim velocity and the angle of attack were used as the scheduling variable [5]. Figure 4.6 shows the various trim conditions, a total of 46, used for the identification of the global LPV model [5].

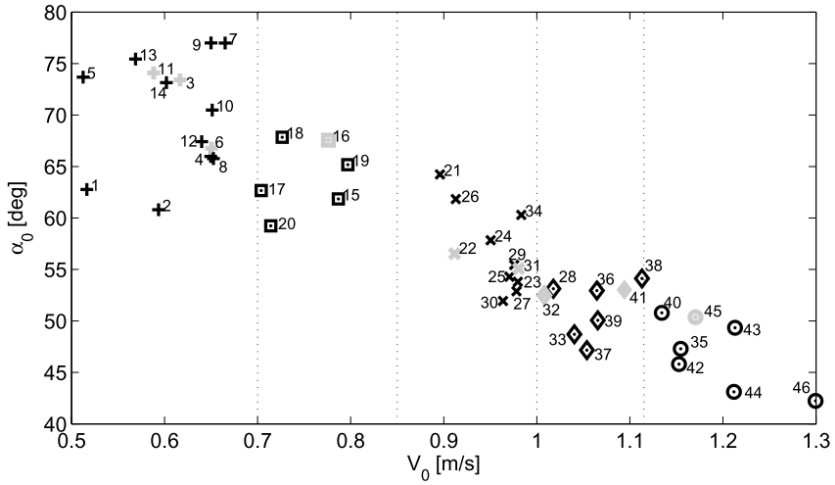

Figure 4.6: The various trim conditions, 46 in total, used in the research of Armanini et al. for the identification of a global LPV state-space model [5].

The parameters, in this case the stability derivatives in the state-space model, are assumed to be a function of the trim velocity V_0 and the trim angle of attack α_0. A bivariate polynomial structure was used as the function for the stability derivative, shown in equation 4.14.

$$p\left(V_0, \alpha_0, \theta^{LPV}\right) = \sum_{0}^{d} \sum_{n+m=d} \theta_{n,m}^{LPV} \frac{d!}{n!\,m!} V_0^n \alpha_0^m \tag{4.14}$$

The number of parameters was minimized using a stepwise regression approach, which is explained in Subsection 4.2.3. The model structure for all the stability derivatives of the pitching moment M are shown in Equation 4.15 as an example [5].

$$\begin{aligned}
\tilde{M}_q &= \theta_{0,0}^{M_q} + \theta_{1,0}^{M_q} \cdot V + \theta_{3,0}^{M_q} \cdot V^3 \\
\tilde{M}_u &= \theta_{0,0}^{M_u} + \theta_{1,0}^{M_u} \cdot V + \theta_{2,0}^{M_u} \cdot V^2 + \theta_{3,0}^{M_u} \cdot V^3 \\
\tilde{M}_w &= \theta_{0,0}^{M_w} \\
\tilde{M}_{\delta_e} &= \theta_{0,0}^{M_{\delta_e}} + \theta_{2,0}^{M_{\delta_e}} \cdot V^2 + \theta_{2,1}^{M_{\delta_e}} \cdot V^2 \alpha + \theta_{3,0}^{M_{\delta_e}} \cdot V^3
\end{aligned} \tag{4.15}$$

The parameters in this equation, indicated by $\theta_{n,m}^{M_i}$, are then determined using an Ordinary Least-squares approach, which is explained in Section 4.3.1. For the research in this thesis, the trim sideways velocity v_0 and the trim roll angle ϕ_0 will be used the scheduling variables if the LPV state-space system is used as the model structure.

Multi-body dynamic model

Previous research has shown that the influence of the wing dynamics on the body dynamics is greater when the flapping frequency is closer to the natural frequency of the system [73, 85]. In order to account for this, each wing of the FWMAV can be considered a separate body [1, 31, 56].

For the model identification of the Delfly II, this approach has been used by Caetano et al., for which the free-body diagram is shown on Figure 4.7 [1].

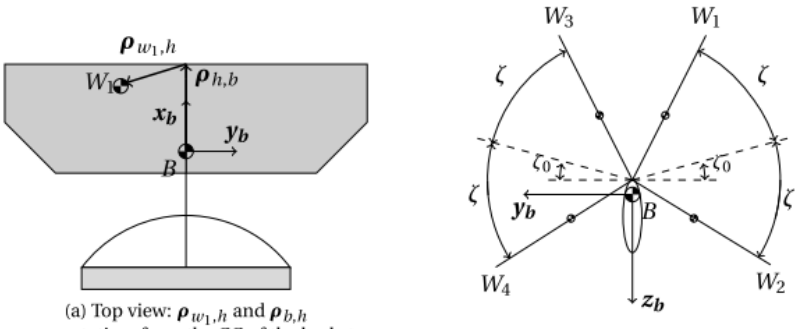

(a) Top view: $\rho_{w_1,h}$ and $\rho_{b,h}$ representation, from the CG of the body to the CG of the wing, with closed wings.

(b) Front view: wings open at angle ζ; dashed line represents the position of the closed wings at ζ_0.

Figure 4.7: The free-body diagram used in the research of Caetano et al. [1]. The bodies which represent the wings are W_1, W_2, W_3 and W_4.

The bodies which represent the wings are indicated by W_1, W_2, W_3 and W_4 in Figure 4.7. There are two degrees of freedom, active rotation around x_b with a wing sweep angle ζ and passive rotation about y_b.

Delfly Nimble: Karl Kajak

Kajak et al. used a model with the center of pressure (COP) and the center of mass (COM). The free-body diagram of the model is shown in Figure 4.8[32, 33]. The equations of motions used for the identification are shown in Equation 4.16.

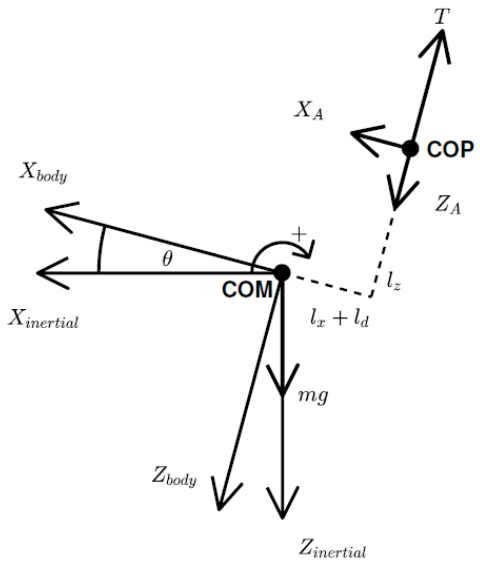

Figure 4.8: Free body diagram of the Delfly Nimble as used by Kajak et al. [32, 33].

$$
\begin{aligned}
m\begin{bmatrix}\dot{u}+qw\\ \dot{w}-qu\end{bmatrix} &= mg_0\begin{bmatrix}-\sin(\theta)\\ \cos(\theta)\end{bmatrix}+\begin{bmatrix}X\\ Z\end{bmatrix}\\
\ddot{\theta} &= \frac{M}{I_{yy}}
\end{aligned}
\tag{4.16}
$$

The cycle-averaged aerodynamic forces X and Z and the aerodynamic moment M were calculated using the equations shown in Equation 4.17.

$$\begin{aligned} u_{COP} &= u - l_z\dot{\theta} - \dot{l}_d \qquad & X &= -2b_x u_{COP} \\ w_{COP} &= w + (l_d + l_x)\dot{\theta} & Z &= -2T - 2b_z w_{COP} \\ & & M &= -Xl_z + Z(l_d + l_x) \end{aligned} \tag{4.17}$$

Where u_{COP} and w_{COP} are the longitudinal and vertical velocities of the center of pressure, l_x and l_z are fixed linear offsets between the COM and COP along the X_{body} and the Z_{body} axes, l_d is the adjustable linear displacement of the COP with respect to the COM used for the control of the pitch attitude, and T is the thrust force vector of one wing. The parameters which need to be estimated are the constants b_x and the b_z, which were determined using a least-squares estimation. This parameter estimation technique is explained in Section 4.3.1. The thrust force was modeled as a linear function of the flapping frequency, shown in Equation 4.18.

$$T = 2 \cdot \left(0.0114f - 0.0449\right) \tag{4.18}$$

Kajak et al. also modeled the actuator dynamics in order to account for the actuator delay. This was done for the flapping and the dihedral mechanisms, using the transfer functions shown in Equation 4.19.

$$H_{flap}(s) = \frac{12.56}{s + 12.56}, \quad H_{dihedral}(s) = \frac{554.2}{s^2 + 30.25s + 554.2} \tag{4.19}$$

The flapping mechanism was modeled as a first order system which had a non-dimensional time constant equal to 0.08. The dihedral mechanism was modeled as a second order system which had a natural frequency of $0.04s$ and a damping ratio of 0.634.

Delfly Nimble: Jorgen Nijboer

Nijboer et al. used the same coordinate system shown in Figure 3.1. A LTI state-space system was used for the identification of the model, shown in Equation 3.2. The input vector used for the identification is shown in Equation 4.20 [51].

$$B_{lon} \cdot \underline{u}_{lon} = \begin{bmatrix} \frac{M_{\delta_D}}{I_{yy}} \\ \frac{X_{\delta_D}}{m} \\ \frac{Z_{\delta_D}}{m} \\ 0 \end{bmatrix} \cdot \delta_D \tag{4.20}$$

Where δ_D is the deflection of the dihedral mechanism of the Delfly Nimble. The parameters which needed to be estimated are the same as the ones shown in Equations 3.3 and 4.20. These were determined using the least-squares approach, which is explained in subsection 4.3.1.

For this thesis the LTI state-space model shown in Equation 3.3 will be used. Initially, all the inputs will be considered in the input vector. However, if an input does not have a significant influence on the model accuracy, that input can be omitted, reducing the size of the input matrix. If the bias terms are included and all the inputs are considered, the input matrix is as shown in Equation 4.21.

$$B_{lat} \cdot \underline{u}_{lat} = \begin{bmatrix} \frac{I_{zz}}{I_c} \cdot L_{\delta_d} + \frac{I_{xz}}{I_c} \cdot N_{\delta_d} & \frac{I_{zz}}{I_c} \cdot L_{\delta_f} + \frac{I_{xz}}{I_c} \cdot N_{\delta_f} & \frac{I_{zz}}{I_c} \cdot L_{\delta_w} + \frac{I_{xz}}{I_c} \cdot N_{\delta_w} & \frac{I_{zz}}{I_c} \cdot L_{\delta_t} + \frac{I_{xz}}{I_c} \cdot N_{\delta_t} & b_{\dot{p}} \\ \frac{I_{xz}}{I_c} \cdot L_{\delta_d} + \frac{I_{xx}}{I_c} \cdot N_{\delta_d} & \frac{I_{xz}}{I_c} \cdot L_{\delta_f} + \frac{I_{xx}}{I_c} \cdot N_{\delta_f} & \frac{I_{xz}}{I_c} \cdot L_{\delta_w} + \frac{I_{xx}}{I_c} \cdot N_{\delta_w} & \frac{I_{xz}}{I_c} \cdot L_{\delta_t} + \frac{I_{xx}}{I_c} & b_{\dot{r}} \\ \frac{Y_{\delta_d}}{m} & \frac{Y_{\delta_f}}{m} & \frac{Y_{\delta_w}}{m} & \frac{Y_{\delta_t}}{m} & b_{\dot{v}} \\ 0 & 0 & 0 & 0 & b_{\dot{\phi}} \end{bmatrix} \cdot \begin{bmatrix} \delta_d \\ \delta_f \\ \delta_w \\ \delta_t \\ 1 \end{bmatrix} \tag{4.21}$$

4.2.3. Minimization of model structure

When choosing a model structure, it is important to consider the accuracy of the identified model. In general, more parameters will lead to a more accurate model. However, the model may start fitting noise, which is not part of the system dynamics. Another issue with using too many parameters is that the model becomes more computationally expensive, while not leading to a more accurate mapping of the system output. Therefore it is advantageous that as few parameters are used, while the accuracy is as high as required. The optimum model which has the desired accuracy with the lowest number of parameters is known as the parsimonious model [77].

The black-box model structure used by Armanini et al. [6] had the most parameters out of all the model structures discussed in Subsection 4.2.2. The number of parameters can be reduced by applying the stepwise regression method [5, 63]. With this method the parameter that has the least effect on the model accuracy is removed.

4.3. Parameter Estimation

This section answers Question **SQ2c**. The main goal of system identification is the development of a mathematical model which is able to accurately simulate the system dynamics. It is then desirable that the output of the model matches the output of the real dynamic system. Quantifying how well the model achieves this can be done using a loss-function, also known as cost function, shown in Equation 4.22 [43, 44, 65].

$$V_N = \frac{1}{N}\sum_{t=1}^{N} l(t,\theta,\varepsilon(t,\theta)) \tag{4.22}$$

Where l is a quantifying norm which is a function of the parameters, t and the residual ε. This method is generally known as the the prediction error approach, which is a collection of wide family of system identification methods [44]. The variations are in the choice of cost function. If the cost function is the square of the residuals, the equation-error approach is used, discussed in subsection 4.3.1. Another possibility is that the cost function is the maximum likelihood equation, then the output-error or the filter-error approach is often used, explained in Subsections 4.3.2 and 4.3.3. In aircraft system identification, the most used methods are the equation-error and the output-error approach [30, 40].

4.3.1. Equation-error approach

The equation-error approach is one of the most used parameter estimation procedures in aircraft system identification [30, 40]. The flow-diagram of the equation-error approach is shown in Figure 4.9 [40].

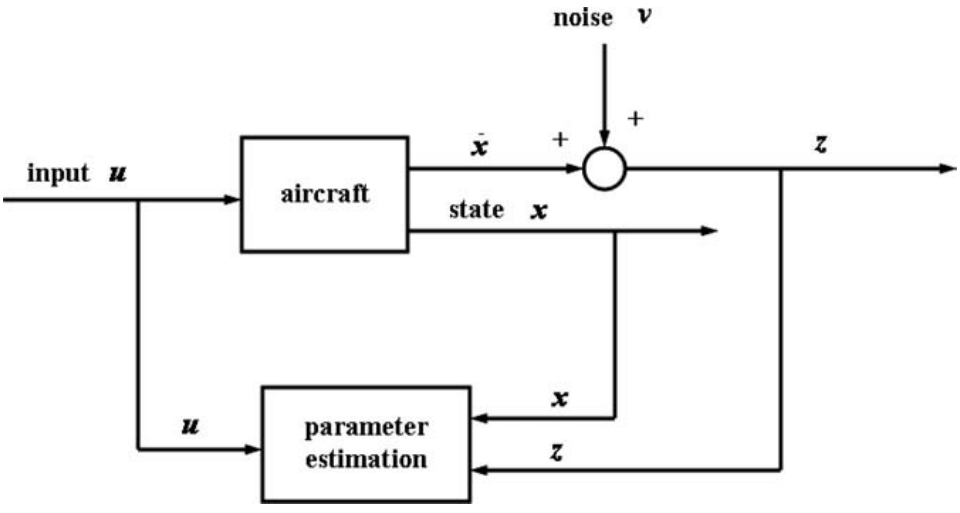

Figure 4.9: Flow diagram of the equation-error approach for the parameter estimation [40].

In this approach the input u, the aircraft states x and the measurements z are used for the parameter estimation. Linear regression techniques are a very well known equation-error approach. This technique will be

explained using the model structure shown in Equation 4.23, which is a model with a univariate polynomial structure.

$$p(\mathbf{x},\bar{\theta}) = \theta_0 + \theta_1\mathbf{x} + \theta_2\mathbf{x}^2 + \theta_3\mathbf{x}^3 = A(\mathbf{x})\cdot\bar{\theta} \tag{4.23}$$

The model $p(x,\theta)$ can be written in a state space form shown in Equation 4.24.

$$A(\mathbf{x})\cdot\bar{\theta} = \begin{bmatrix} 1 & x_1 & x_1^2 & x_1^3 \\ 1 & x_2 & x_2^2 & x_2^3 \\ : & : & : & : \\ 1 & x_N & x_N^2 & x_N^3 \end{bmatrix} \cdot \begin{bmatrix} \theta_0 \\ \theta_1 \\ \theta_2 \\ \theta_3 \end{bmatrix} \tag{4.24}$$

Where N is the total number of data-points. The main goal is to find to find a set of parameters $\bar{\theta}$ which minimize the error between the actual output and the output of the mathematical model. The error can be determined using Equation 4.25.

$$\bar{\varepsilon} = \mathbf{y} - A(\mathbf{x})\cdot\bar{\theta} \tag{4.25}$$

Where $\mathbf{y}$ is the actual system output. The linear regression estimator uses a cost function J to determine the best set of parameters, which are those which minimize the model error ε. This is shown in Equation 4.26.

$$\hat{\theta} = \arg\min J(\mathbf{y} - A(\mathbf{x})\cdot\bar{\theta}) \tag{4.26}$$

An often used cost function is the one shown in Equation 4.27. In this function, the squares of the errors are minimized. When this cost function is used, the approach is also called the least squares parameter estimation [16].

$$J(\mathbf{x},\bar{\theta}) = \sum_{i=1}^{N} \varepsilon_i^2 = \sum_{i=1}^{N} (y_i - A(x_i)\cdot\hat{\theta})^2 \tag{4.27}$$

There are different types of least-squares estimators, such as the Ordinary Least-Squares (OLS) parameter estimator, the Weighted Least-Squares (WLS) parameter estimator and the General Least-Squares (GLS) parameter estimator. A variation of the linear regression method is also used for system identificatio, known as the Instrument Variable method.

Ordinary Least-Squares
When using this estimator it is assumed that the model error ε is Gaussion White noise and that the sensor noise has a mean of zero and the variance is constant [5, 16]. The best set of parameters are then determined using the OLS estimator shown in Equation 4.28.

$$\hat{\theta}_{OLS} = \left(A^T(\mathbf{x})\cdot A(\mathbf{x})\right)^{-1}\cdot A^T(\mathbf{x})\cdot\mathbf{y} \tag{4.28}$$

The main advantage is that the OLS estimator is a simple algorithm. However, this method is very sensitive to sensor noise. Outliers in the data can greatly influence the identified parameters, leading to a very different mathematical model. There are various ways how this can be improved, such as using the WLS estimator or the GLS estimator.

Weighted Least-Squares
The main disadvantage of the OLS estimator was that it is every sensitive to sensor noise. In real measurements, it is often the case that not every data-point has the same variance. This can be accounted for by assigning weights to the individual data-points. A data-point with a higher variance is assigned a lower weight. The weights are applied using a weight matrix W, shown in Equation 4.29 [16].

$$W = \begin{bmatrix} \sigma_1^2 & 0 & \dots & 0 \\ 0 & \sigma_2^2 & \ddots & \vdots \\ \vdots & \ddots & \ddots & 0 \\ 0 & \dots & 0 & \sigma_N^2 \end{bmatrix} \tag{4.29}$$

Where $\sigma_1^2, \sigma_2^2, ..., \sigma_N^2$ are the sensor noise variances of each data point. The weight matrix is determined using prior knowledge about the system. What is a possibility, is to first use a OLS estimator, and determine the covariance matrix of the residuals. The terms of the diagonal of the covariance are then the variances of the individual data points, which are used to develop the weight matrix. This is shown in Equation 4.30.

$$\begin{aligned} COV_\varepsilon &= E\left\{\varepsilon \cdot \varepsilon^T\right\} \\ W &= diag\left(COV_\varepsilon\right) \end{aligned} \tag{4.30}$$

The diagonal elements of COV_{OLS} are the variances of the data-points. The parameters can then be determined using the WLS estimator, shown in Equation 4.31.

$$\hat{\theta}_{WLS} = \left(A^T(\mathbf{x}) \cdot W^{-1} \cdot A(\mathbf{x})\right)^{-1} \cdot A^T(\mathbf{x}) \cdot W^{-1} \cdot \mathbf{y} \tag{4.31}$$

This estimator has a better performance then the OLS estimator, since it is more robust to sensor noise. It is assumed that the residuals are uncorrelated [16]. However, if this is not the case more complicated estimators can be used, such as the GLS estimator.

General Least-Squares
The GLS estimator is a more general form of the WLS estimator. Instead of a W matrix, it uses the residual covariance matrix Σ, which can be calculated using Equation 4.30. While the weight matrix W uses only the diagonal terms of COV_ε, Σ is set equal to COV_ε. When the Σ has been determined, the GLS estimator can be used shown in Equation 4.32.

$$\hat{\theta}_{GLS} = \left(A^T(\mathbf{x}) \cdot \Sigma^{-1} \cdot A(\mathbf{x})\right)^{-1} \cdot A^T(\mathbf{x}) \cdot \Sigma^{-1} \cdot \mathbf{y} \tag{4.32}$$

Instrument-variable approach
A modification of the equation-error approach is the instrument-variable approach. The difference is in the estimator for the parameters, shown in Equation 4.33 [30, 43, 65].

$$\hat{\theta}_{IV} = \left(\zeta^T \cdot A(\mathbf{x})\right)^{-1} \cdot A^T(\mathbf{x}) \cdot \mathbf{y} \tag{4.33}$$

Where ζ is a correlation vector, which is comprised of signals which are uncorrelated with the equation-error $\bar{\varepsilon}$, but are strongly correlated with the independent variables. The elements of this vector are called 'instrument variables, hence the name of the method. There are several ways to determine such a vector ζ [47, 79].

Equation-error approach for a state-space-system
For a state-space system, the equation-error approach can also be applied by rewriting it. Consider the state-space system shown in Equation 4.34 [43].

$$\begin{aligned}\dot{\mathbf{x}}(t) &= A\cdot\mathbf{x}(t) + B\cdot\mathbf{u}(t) + w(t)\\ \mathbf{y}(t) &= C\cdot\mathbf{x}(t) + D\cdot\mathbf{u}(t) + v(t)\end{aligned} \tag{4.34}$$

The elements in the state-space systems can be arranged in larger matrices shown in Equation 4.35 [43].

$$\begin{aligned}Y(t) &= \begin{bmatrix}\dot{x}(t)\\ y(t)\end{bmatrix}, \qquad \Theta = \begin{bmatrix}A & B\\ C & D\end{bmatrix}\\ \Phi(t) &= \begin{bmatrix}x(t)\\ u(t)\end{bmatrix}, \quad E(t) = \begin{bmatrix}w(t)\\ v(t)\end{bmatrix}\end{aligned} \tag{4.35}$$

Using the matrices defined in Equation 4.35, the state-space system can be rewritten into Equation 4.36.

$$Y(t) = \Theta\cdot\Phi(t) + E(t) \tag{4.36}$$

This is very similar to the polynomial model shown in Equation 4.23. The full derivation of the regression matrices for the grey-box and black-box model structures used for the parameter estimation are shown in Chapter C.

4.3.2. Output-error approach

Next to the equation-error approach, the output-error approach is one of the two most used approached for the system identification of aircraft systems [30, 40]. In the equation-error approach is assumed that the residuals are uncorrelated white noise [16, 40]. If this is not the case, the output-error approach is a more suitable method, since this approach is able to cope with non-white noise in the residuals. A flow-diagram of the output-error approach is shown in Figure 4.10.

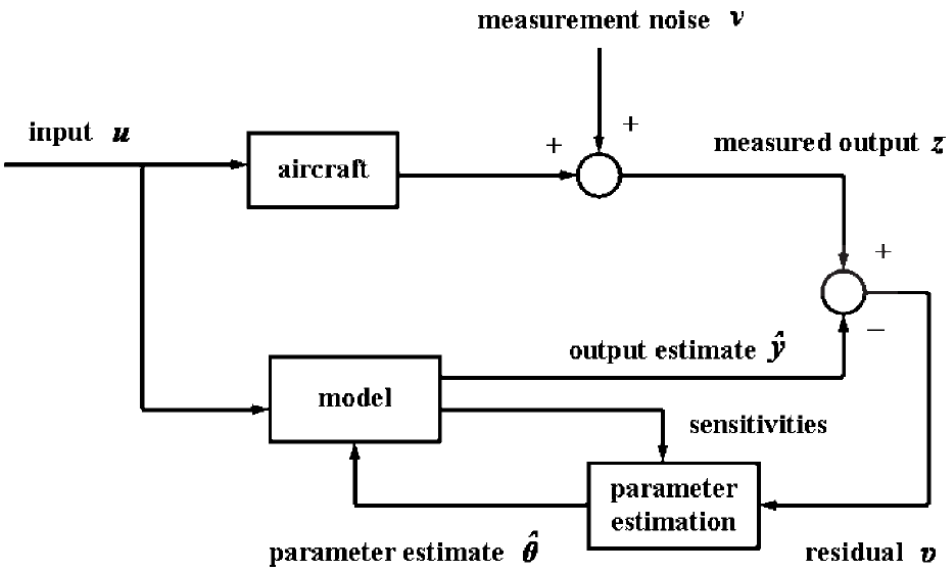

Figure 4.10: Flow diagram of the output-error approach for the parameter estimation [40].

The working principle of the output-error approach is explained using a LTI state-space system, shown in Equation 4.37 [40].

$$\begin{aligned}
\dot{\mathbf{x}}(t) &= A\cdot\mathbf{x}(t) + B\cdot\mathbf{u}(t) && \mathbf{x}(0) = x_0 \\
\mathbf{y}(t) &= C\cdot\mathbf{x}(t) + D\cdot\mathbf{u}(t) \\
\mathbf{z}(i) &= \mathbf{y}(i) + \boldsymbol{v}(i) && i = 1,2,...,N \\
Cov[\mathbf{v}(i)] &= E[\boldsymbol{v}(i)\cdot\boldsymbol{v}^T(i)] = \mathbf{R}\delta_{ij}
\end{aligned} \tag{4.37}$$

Where $\mathbf{x}(t)$ is the state vector, $\mathbf{y}(t)$ is the model output vector, $\mathbf{z}(i)$ are the measurement points, $\boldsymbol{v}(i)$ are the residuals and $\mathbf{R}$ is the covariance matrix. In this approach it is assumed that every measurement point in $\mathbf{z}(i)$ is an independent sample of a normal distribution probability density function [16, 40]. The goal is to have a maximum probability of observing a measurement for a given parameter vector θ_0. This is done by minimizing the negative log-likelihood function, shown in Equation 4.38 [5, 40].

$$J(\boldsymbol{\Theta},\mathbf{R}) = -\ln p(\mathbf{z}|\boldsymbol{\Theta}) = \frac{1}{2}\sum_{i=1}^{N}\left[\boldsymbol{v}^T(i)\mathbf{R}^{-1}\boldsymbol{v}(i) + \frac{N}{2}\ln|\mathbf{R}|\right] + \frac{Nn_0}{2}\ln(2\pi) \tag{4.38}$$

Where n_0 is the number of output variables measured during the experiments. The covariance matrix $\mathbf{R}$ can be approximated by $\hat{\mathbf{R}}$, which can be computed using Equation 4.39.

$$\hat{\mathbf{R}} = \frac{1}{N}\sum_{i=1}^{N}\boldsymbol{v}^T(i)\boldsymbol{v}(i) \tag{4.39}$$

Often only the diagonal terms of $\hat{\mathbf{R}}$ are used only in order to reduce the computational complexity. Using the full matrix will lead to better parameter estimates, but it also increases the computational cost drastically, due to which it is not practical to do so [40].

With the use of $\hat{\mathbf{R}}$ Equation 4.38 can be simplified using relaxation techniques [5, 40]. With this technique the $\hat{\mathbf{R}}$ is determined at each iteration, making it a constant term at the given iteration. Because the $\hat{\mathbf{R}}$ is now constant and not a function of $\boldsymbol{\Theta}$, the two latter terms of Equation 4.38 can be omitted. This leads to a simpler cost equation, shown in Equation 4.40.

$$\begin{aligned}
J(\boldsymbol{\Theta}) &= \frac{1}{2}\sum_{i=1}^{N}\boldsymbol{v}^T(i)\hat{\mathbf{R}}^{-1}\boldsymbol{v}(i) \\
&= \frac{1}{2}\sum_{i=1}^{N}[\mathbf{z}(i)-\mathbf{y}(i)]^T\hat{\mathbf{R}}^{-1}[\mathbf{z}(i)-\mathbf{y}(i)]
\end{aligned} \tag{4.40}$$

In the research of Armanini et al. updated cost value was determined using a second order Taylor series expansion, shown in Equation 4.41 [5].

$$\left(\frac{\partial J}{\partial\boldsymbol{\Theta}}\right)_{i+1} \approx \left(\frac{\partial J}{\partial\boldsymbol{\Theta}}\right)_i + \left(\frac{\partial^2 J}{\partial\boldsymbol{\Theta}^2}\right)_i \Delta\boldsymbol{\Theta} \tag{4.41}$$

The left hand side is then equated to zero, which leads to an equation for the parameter estimation update, shown in Equation 4.42.

$$\Delta\boldsymbol{\Theta} = -\left(\frac{\partial^2 J}{\partial\boldsymbol{\Theta}^2}\right)^{-1}\left(\frac{\partial J}{\partial\boldsymbol{\Theta}}\right) \tag{4.42}$$

In order to use Equation 4.42, the first and second derivatives of the cost function $J(\boldsymbol{\Theta})$ need to be determined. This can be done using the Newton-Raphson technique, shown in Equations 4.43 and 4.44[40].

$$\frac{\partial J}{\partial\boldsymbol{\Theta}} = -\sum_{i=1}^{N}\frac{\partial\mathbf{y}^T(i)}{\partial\boldsymbol{\Theta}}\hat{\mathbf{R}}^{-1}\boldsymbol{v}(i) \tag{4.43}$$

$$\frac{\partial^2 J}{\partial \theta_j \theta_k} = \sum_{i=1}^{N} \frac{\partial \mathbf{y}^T(i)}{\partial \theta_j} \hat{\mathbf{R}}^{-1} \frac{\partial \mathbf{y}(i)}{\partial \theta_k} - \frac{\partial \mathbf{y}^2(i)}{\partial \theta_j \theta_k} \hat{\mathbf{R}}^{-1} \boldsymbol{v}(i) \tag{4.44}$$

This algorithm can be simplified by omitting the last term in Equation 4.44. If this is done, the algorithm is called the Gauss-Newton one.

With the parameter update determined using Equations 4.42 to 4.44, the parameters can be updated. When this is done, the residuals can be determined with the updated parameters, which will be used to determine the $\hat{\mathbf{R}}$ for the next iteration. Then, the next parameter update is determined using the updated $\hat{\mathbf{R}}$, making it an iterative process. The iterative process will stop when certain convergence criteria are met. In the research of Armanini et al., the convergence criteria were the value of the cost function $J(\boldsymbol{\Theta})$ and the change in the cost function after an iteration, which both needed to be lower than specified values [5].

In order to start the iterative process, an initial estimate of the parameters is required. In the research of Armanini et al. the initial estimate can be determined using the OLS estimator which was explained in Subsection 4.3.1. A flow diagram of the parameter estimation algorithm used in the research of Armanini et al. is shown in 4.11.

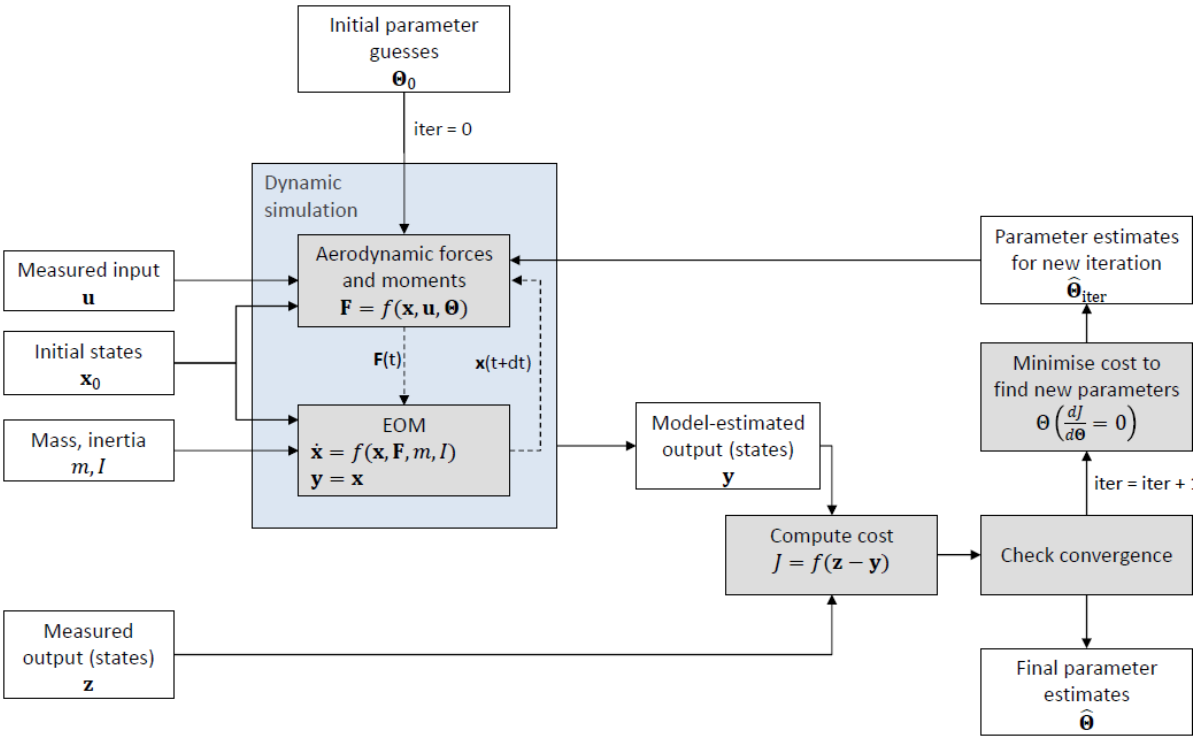

Figure 4.11: Parameter estimation algorithm as used in the research of Armanini et al. [5]. The output error approach was used in combination with a maximum likelihood estimator.

The dynamic simulation was done using a fourth-order Runge-Kutta Integrator. For the research of this Thesis, the output-error approach will be used for the estimation of the parameters, since it has been done successfully in the research of Armanini et al. [4, 5] and because it leads to more robust estimates than the equation-error approach. However, one important difference between the Delfly II and the Delfly Nimble is that the Delfly II was open-loop stable. According to Klein et al. there is no proof that the estimation using the output-error approach will converge, however it has been shown that in practive this method can converge [40].

A disadvantage of the output-error approach assumes that there is no process noise, when this is not the case, more general approach is needed, such as the filter-error approach.

4.3.3. Filter-error approach

When there is sensor and process noise present in the system, neither the equation-error nor the output-error approach can guarantee the identification of a good mathematical model. When this is the case, a different approach is required, namely the filter-error approach. Since this approach allows for sensor noise as well as process noise, the filter-error approach has been called the most general method for parameter estimation in aircraft system identification[40]. A flow-diagram of this approach is shown in Figure 4.12[40].

When compared to the output-error flow-diagram shown in Figure 4.10, the only difference is that the states are now estimated using a Kalman filter instead of a model. The cost function which needs to be optimized is also different, shown in Equation 4.45.

$$J(\boldsymbol{\Theta}) = \frac{1}{2}\sum_{i=1}^{N}\left[\boldsymbol{v}^T(i)\mathscr{B}^{-1}(i)\boldsymbol{v}(i) + \frac{N}{2}\ln|\mathscr{B}(i)|\right] \tag{4.45}$$

Where $\mathscr{B}(i)$ is covariance matrix of the innovations $\boldsymbol{v}(i)$. In the output-error approach, the last two terms were omitted since they were constant. In the filter-error approach, only the last term is considered to be constant. The optimization can be done using similar techniques as the ones shown in Subsection 4.3.2.

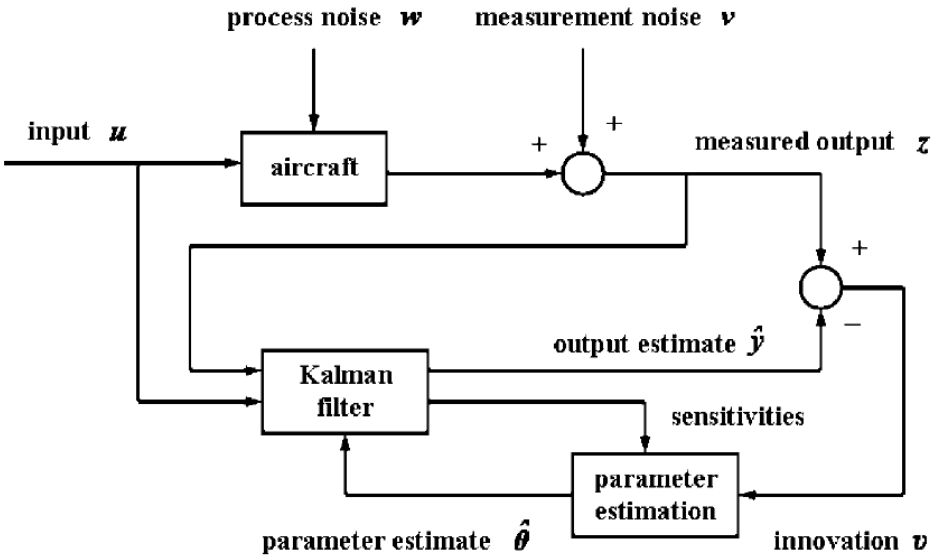

Figure 4.12: Flow diagram of the output-error approach for the parameter estimation [40].

5

Model Validation Techniques

This Chapter covers the model validation phase of the System Identification Cycle, thus answering Subquestion **SQ3**, which was phrased as follows:

SQ3. What is the quality of the identified model?
- (a) Which metrics can be used for validating the model?
- (b) Is the decoupling of the dynamics a justifiable assumption?
- (c) Is the linearity of the aerodynamic forces a justifiable assumption?

This phase is a crucial one, since it is determined here whether the performance of the model is adequate enough for it to be used for getting more insight into the dynamic system or the development of controllers[30]. If from the validation phase it turns out that the model does not generate the same output for the same input accurately, one should go back to the previous phases and implement improvements, making the identification of model an iterative process. The validation phase can also be used in order to check for the possibility of model reduction [38], where fewer parameters are used. Section 5.1 answers Question **SQ3a** and Section 5.3 answers Questions **SQ3b** and **SQ3c**.

5.1. Validation metrics

This section answers Question **SQ3a**. Various metrics are available for the validation of the identified model. These can be put into two categories [30], the analysis of the statistical properties of the parameter estimates, described in Subsection 5.1.1 and the residuals, described in Subsection 5.1.2. The validation of the model identified for the Delfly II was done using these metrics [5].

5.1.1. Statistical properties of parameters

The statistical properties of the parameters can be determined by analysis of the covariance matrix [5, 30]. The diagonal elements indicate the variance of the parameters. All the other entities indicate the covariances. It is desirable that all these values are as low as possible. Large values for the variance would suggest that the estimation of the parameters is sensitive to the noise in the data sets. High covariance values could mean that certain parameters are correlated with each other.

5.1.2. Residual analysis

Before the residuals can be analyzed they have to be determined. These are determined using Equation 5.1.

$$\epsilon = y_i - \hat{y}_i \tag{5.1}$$

Where y_i is a measurement point $\hat{y}_i$ is the predicted value from the model. The predicted value can be determined using a Simulink model in MATLAB, while using the same input as in the experiment. There are several metrics which can be used for the analysis of the residuals. The accuracy of the fit can be quantified by the goodness of fit $\mathbf{R}^2$ or the root mean-squared error **RMSE**. A high value for R^2 is desired, while a low value for the **RMSE** is preferred. These values are calculated using Equations 5.2 and 5.3.

$$\mathbf{R}^2 = 1 - \frac{\sum_{i=1}^{N}(y_i - \hat{y}_i)^2}{\sum_{i=1}^{N}(y_i - \overline{y})^2} \cdot \frac{N-1}{N-P} \tag{5.2}$$

$$\mathbf{RMSE} = \sqrt{\frac{1}{N} \cdot \sum_{i=1}^{N}(y_i - \hat{y}_i)^2} \tag{5.3}$$

Where $\overline{y}$ is the mean of all measurements, N is the total number of measurements, and P is the total number of parameters. While it is true that using more parameters will decrease the **RMSE**, this does not mean that the model is more accurate. The model may start fitting noise, which is not part of the system dynamics. The second fraction in Equation 5.2 punishes the use of too many parameters. Using more parameters will decrease the $\mathbf{R}^2$.

Another metric for the analysis of the residuals is the whiteness of the residuals. For certain estimation methods, such as the equation error approach, it is assumed that all the noise in the data set is white. The residuals would then resemble white noise. This can be checked by determining the auto-correlation spectrum of the residuals, and then then be compared to the spectrum of white noise. It is desirable that these two spectra are as similar as possible[38]. The autocorrelation matrix is determined using Equation 5.4 [30].

$$C(\tau) = \frac{1}{N}\sum_{k=\tau}^{N}[v(k) - \overline{v}][v(k-\tau) - \overline{v}]^T \tag{5.4}$$

Where v is the residual, $\overline{v}$ is the mean of the residuals and τ is the lag. If the residuals resemble white noise, the correlation coefficients are zero for every value of τ [30]. However, this is can only be accomplished when there is an infinite data set. while there are only a finite amount of datapoints N. In order to cope with this practical limitation, a confidence interval is used. A confidence level of 95% is often used, but this is an arbitrary value. In the case of this interval, 95% of the values of τ should lie in the band $\pm 1.96/\sqrt{N}$[30].

5.1.3. Output Correlation

The output correlation coefficient can show how similar the estimated output and the measures output are. This can be quantified using the Pearson's Correlation coefficient, the Equation for which is shown in Equation 5.5 [20].

$$\mathbf{r}_{xy} = \frac{\sum_{i=1}^{N}\sum_{i=1}^{N}(x_i - \overline{x}) \cdot \sum_{i=1}^{N}(y_i - \overline{y})}{\sqrt{\sum_{i=1}^{N}(x_i - \overline{x})^2 \cdot \sum_{i=1}^{N}(y_i - \overline{y})^2}} \tag{5.5}$$

Where x and y are both vectors of length N. A value close to 1 indicates a positive correlation, while a value close to -1 indicates a negative correlation. A value of 0 indicates no correlation between the two variables. It is desired that the values of $\mathbf{r}_{xy}$ is as close to 1 as possible.

5.2. Physical plausibility of parameter

Another metric that can be used for the validation of the identified model is to check whether the estimated parameter is logical. The parameters in this research are the stability and control derivatives when using the grey-box model structure. The plausibility of the estimated stability or control derivative can be checked by analyzing the sign and the magnitude of it. This technique has been used in previous research, such as in the work of Karásek et al. [34, 35].

For example, the expectation is that the sign of the control derivative L_{δ_f} is positive, for a positive δ_f will create a positive moment L. Using multiple identification data-sets can be used to verify the consistency of the sign and magnitude of the stability and control derivatives.

The signs and magnitudes can also be analyzed by comparing them to those of other FWMAV's, such as the Delfly II, for which the stability and control derivatives were determined by Armanini et al. [4, 5]. When comparing to the Delfly II, only the stability derivatives can be compared, and not the control derivatives can't

be compared, since the Delfly II uses very different control mechanisms compared to the Delfly Nimble. The magnitude of the estimated stability derivatives can also be compared to those of the Delfly II. Apart from the Delfly II, the sign and magnitude of the stability derivatives can also be compared to the analytic parameter values that were estimated using the model structure used by Karásek et al. [34, 35]. For the determination of these parameters the morphological data of the drone-fly was used. Therefore, only the stability derivatives can be compared, since the drone-fly has two wings and uses very different control strategies compared to the Delfly Nimble.

5.3. Analysis of decoupled dynamics and linearity

This section describes the procedure which will be used for answering Questions **SQ3b** and **SQ3c**. The assumption of decoupled dynamics and the linearity of the system can be verified using the experiments described in Section 3.4. By analysis of the residual and the statistical parameters, these assumptions can be validated.

III

Modeling Results

6

Introduction Modeling Results

In this part of the thesis the modeling results are shown. There are three main chapters in this part, each covering the results of one of the phases in the System Identification Cycle. Each chapter will also provide answers to the research questions which were not answered completely in the literature study. The results of the experiments are shown in Chapter 7. This is followed by Chapter 8, where the results of the model identification are discussed. The final chapter, Chapter 9, elaborates on the validation results. The lay-out of this part is illustrated in Figure 6.1.

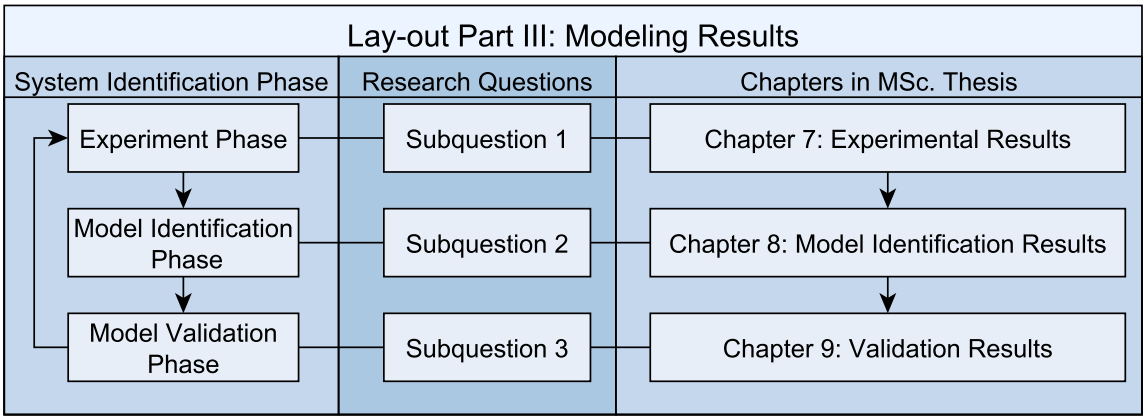

Figure 6.1: Lay-out of Part II of the thesis: Modeling Results.

7

Experimental Results

In this Chapter the results of the experiment phase are shown. First, the gain-tuning of the controller is discussed in Section 7.1. Second, an overview of all the maneuvers used during the experiments is shown in Section 7.2, thus answering Questions **SQ1c**, **SQ1e** and **SQ1f**. Third, the influence of the controller on the experiments is explained in Section 7.3. At last, the identifiability of the data is elaborated in Section 7.4, answering Question **SQ1d**.

7.1. Gain-tuning the controller

The first obstacle during the experiments was the gain-tuning of the controller. The Delfly Nimble requires an active controller in order to ensure safe flight, as was explained in Section 2.1. The original gains on the Delfly are those which were used in the research of Karásek et al. [36]. However, when using these gains there was little to no excitation of the dynamics. The excitation was initially analysed by looking at the reaction of the Delfly Nimble when a command for a doublet was given. It could be seen that for a doublet with a main frequency higher than approximately 8 Hz, there was no visible movement of the Delfly Nimble. Based on these observations, the proportional (P) gain and the derivative (D) gain of the PD-controller were changed to ensure that there was visible movement of the Delfly Nimble during a doublet with a main frequency of 14 Hz. An overview of the gains is shown in Table 7.1. One should note that only the gains for the roll control were adjusted, since this research focuses on the lateral body dynamics of the Delfly Nimble. The gains of the pitch and yaw controller were left unchanged.

Gain	**Open-loop gains (fast gains)**	**Closed-loop gains (slow gains)**
Proportional	1.406	0.625
Derivative	0.200	0.156

Table 7.1: Overview of the gains of the roll controller which were used during the open-loop and closed-loop experiments. The closed-loop gains are the same as those used in the research of Karásek et al. [36]. The open-loop gains are indicated as the 'fast' gains, while the closed-loop gains are indicated as the 'slow' gains.

The open-loop gains will be indicated as the 'fast' gains, while the closed-loop gains will be indicated as the 'slow' gains. The fast P-gain was set higher than the slow P-gain. This was done to have a more aggressive response of the Delfly Nimble to the doublet input, which was one of the possible ways to acquire more excitation explained in Section 3.2. The fast D-gain was initially set lower than the slow D-gains in order to reduce the damping of the natural response of the Delfly Nimble. However, in combination with the higher P-gain this led to oscillations while the Delfly Nimble was hovering. In order to reduce these oscillations, the fast D-gain was set higher, being even a bit larger than the slow D-gain. This made sure that there were minimal oscillations during hover, while also ensuring excitation of the dynamics of the lateral body dynamics.

7.2. Maneuvers used in experiments

This section explains which maneuvers were used to generate the data for the development of the mathematical model of the lateral body dynamics of the Delfly Nimble. There were four categories of maneuvers which were used during the experiments: identification maneuvers, validation maneuvers, coupled maneuvers and nonlinear maneuvers. The identification maneuvers are discussed in Subsection 7.2.1, while the validation maneuvers are explained in Subsection 7.2.2. This is followed by elaborating on the coupled maneuvers in Subsection 7.2.3 and clarifying the nonlinear maneuvers in Subsection 7.2.4.

7.2.1. Identification maneuvers

In this subsection the first category of maneuvers, the identification maneuvers, are discussed and thus part of Question **SQ1c** is answered. The main goal of these maneuvers was to excite the natural motion of the Delfly Nimble as much as possible, as has been discussed in Section 3.2. In order to achieve this goal the natural frequencies of the lateral body dynamics of the Delfly Nimble were estimated using analytic models of flapping flight, as shown in Section 3.3.1. With this information the maneuvers for the identification data were chosen. A train of doublets was chosen as the maneuver for the identification data, with hovering as the initial condition. The maneuver was done by giving roll angle commands to the Delfly Nimble. If the thrust was kept constant during the doublet maneuver, the Delfly would lose altitude because it loses lift due to the rolling motion. Therefore, in addition to roll angle commands, throttle commands were also given. This prevented the Delfly Nimble losing altitude when doing the doing the doublet maneuver. The increase in throttle was done by applying a throttle factor THR_F, which was calculated using Equation 7.1.

$$THR_F = \frac{1}{\cos(\phi_{sp})} \tag{7.1}$$

Where ϕ_{sp} is the maximum set-point roll angle. The roll angle and throttle commands for the doublet train are shown in Figure 7.1.

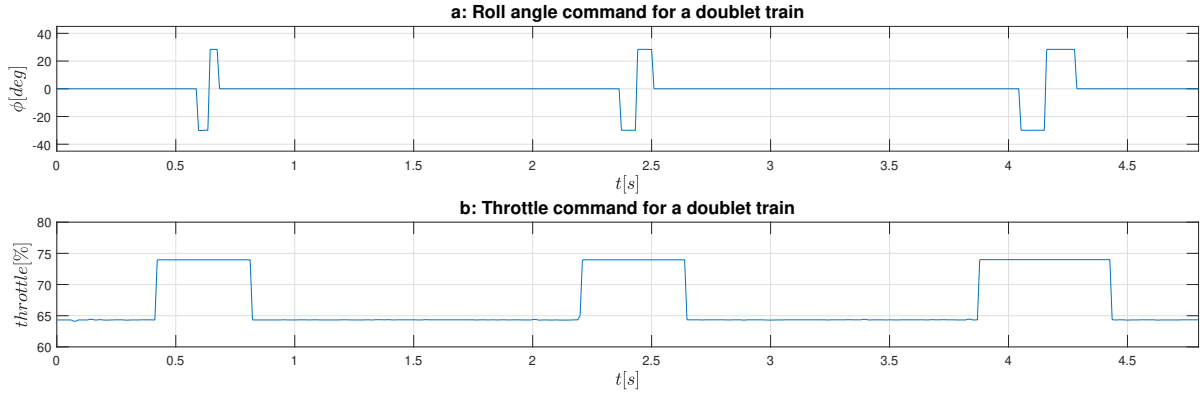

Figure 7.1: The roll angle command, shown in **a**, and throttle command, shown in **b** as used for the doublet trains. The throttle was increased during the doublet maneuvers in order to prevent the Delfly Nimble from losing altitude. The main frequencies of the doublets are 11, 7 and 4 Hz.

The main frequencies which were excited using the doublet train shown in Figure 7.1 are 11, 7 and 4 Hz. These values were chosen iteratively. Initially, the estimated values of Section 3.3.1 were used for the doublet train, which were around the 1 and 2 Hz. However, using these frequencies in the maneuver made the Delfly Nimble move a lot form the initial condition, which is the Delfly Nimble hovering. Therefore, higher main frequencies were chosen iteratively in order to reduce this. Then, the main frequencies were updated by inspecting the Power Spectral Density plots of the states. Based on this the frequencies were updated to those shown in Figure 7.1. During the identification maneuvers, the fast gains shown in Table 7.1 were used.

7.2.2. Validation maneuvers

In this subsection the second category of maneuvers, the validation ones, are explained and thus the remainder of Question **SQ1c** is answered. With this data the models which were developed using the identification

were validated. Two types of validation data were generated: OL data and CL data. The difference between the datasets are the gains which were implemented to the controller. The gains are shown in Table 7.1. Two maneuvers were used for the validation experiments: doublets and the 112-maneuver. The main frequencies for the CL doublets were 6, 4 and 2 Hz. The roll commands given for the 112-maneuver are shown in Figure 7.2.

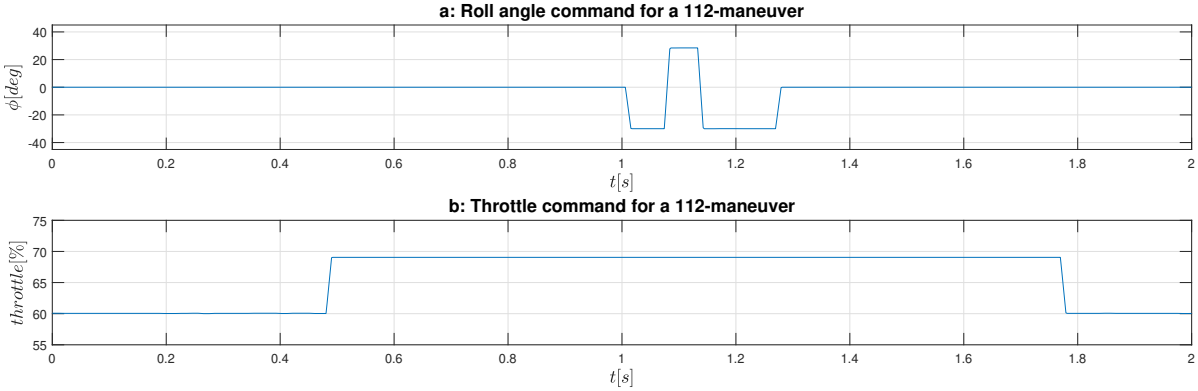

Figure 7.2: The roll angle command, shown in **a**, and throttle command, shown in **b** for the 112-maneuvers. The main frequencies in the maneuver shown are 7 and 3.5 Hz.

The 112-maneuver shown in Figure 7.2 is the one used for the OL validation data. For the CL validation data the main frequencies were 4 and 2 Hz, for there was very little excitation of the 7 Hz pulse when using the slow gains. The initial condition of all the validation maneuvers was the Delfly Nimble hovering.

7.2.3. Coupled maneuvers

In this subsection the third category of maneuvers, the coupled maneuvers, are elaborated on and thus Question **SQ1e** is answered. These maneuvers are coupled since inputs are given to more than one control mechanism, whereas for the doublets and 112-maneuvers inputs are given only to the roll control mechanism. The coupled maneuver which was used during the experiments is the coupled doublet, where first an input is given in pitch angle, making the Delfly Nimble fly forward, and then an input is given in roll angle, making the Delfly do a doublet. The fast gains were used during this maneuver. The roll angle, pitch angle and throttle commands for the coupled doublet is shown in Figure 7.3.

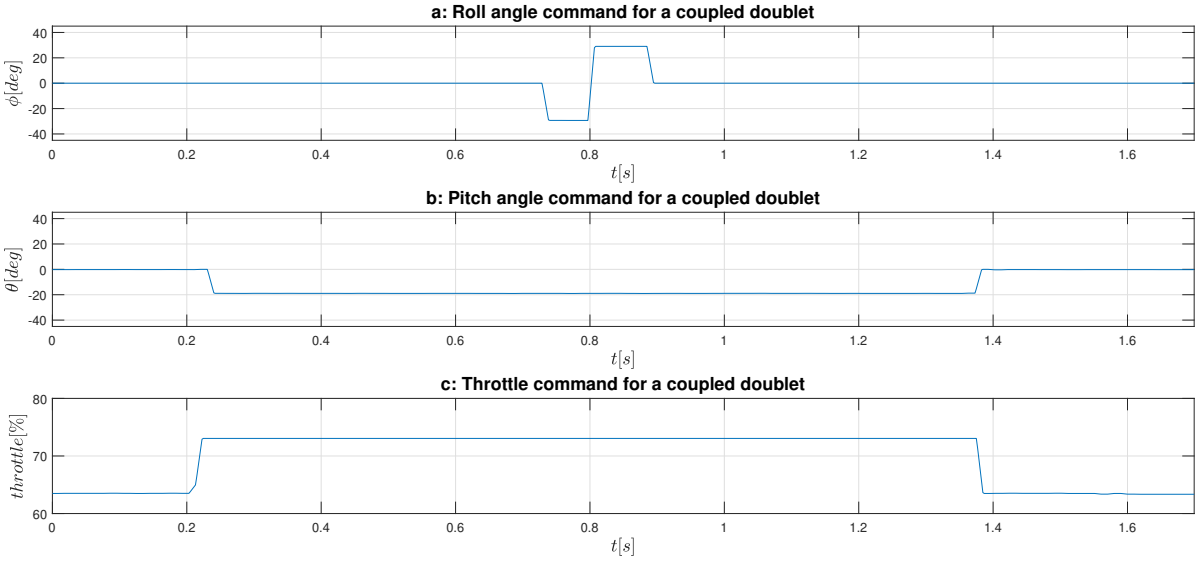

Figure 7.3: The roll angle command, shown in **a**, pitch angle command, shown in **b**, , and throttle command, shown in **c**, as used for the coupled doublet maneuver. The main frequency of the doublet maneuver shown is 6 Hz.

The main frequency of the coupled doublet shown in Figure 7.3 is 6 Hz, and the initial condition of the coupled maneuvers was the Delfly Nimble hovering.

7.2.4. Nonlinear maneuvers

In this subsection the fourth and last category of maneuvers, the nonlinear ones, are clarified and thus Question **SQ1f** is answered. These maneuvers are nonlinear since they move away a lot from the initial condition. The initial condition of the nonlinear maneuvers was the Delfly Nimble hovering. The maneuvers used are the nonlinear doublets. First, a constant roll angle input is given, making the Delfly move sideways, and then a roll angle input is which makes the Delfly do a doublet. The fast gains were used for these maneuvers. The roll angle and throttle commands given for the nonlinear doublet is shown in Figure 7.4.

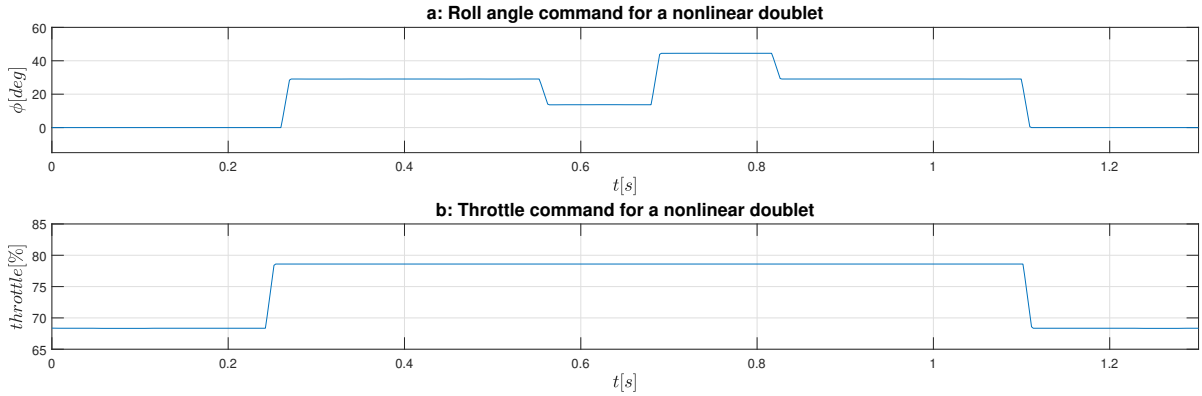

Figure 7.4: Roll angle commands, shown in **a**, and throttle commands, shown in **b**, as used for the nonlinear doublet maneuver. In the maneuver shown, the constant angle was 30°, the deflection was 15°, and the main frequency shown was 4 Hz.

The main frequency of the maneuver shown in Figure 7.4 is 4 Hz. There were also variations in the constant roll angle. In Figure 7.4, the constant roll angle is 30°, but there was also data captured where the constant angle was 20°. The deflection remained 15°.

7.3. Influence of the controller

The figures in Section 7.2 show the set-point roll and pitch commands used to perform the maneuvers. However, these commands do not go directly to the actuators of the Delfly Nimble. This is because of the active controller of the Delfly Nimble, which is required to remain airborne. The controller for the roll attitude is shown in Figure 7.5, which is a snip of the controller shown in Figure 2.9 [36].

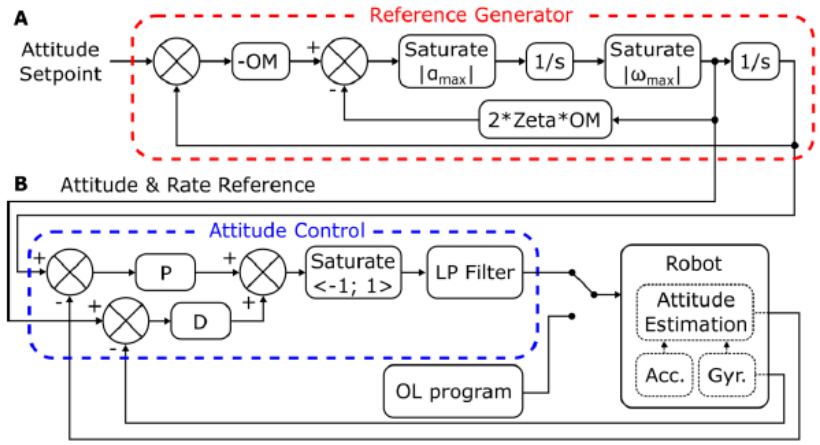

Figure 7.5: Overview of the on-board controller for the roll and pitch attitude [36]. The Delfly Nimble is indicated as 'Robot' in this figure. This figure only shows the controller for the pitch and roll attitude. In **A** the reference generator is shown. In **B** the attitude controller is shown which has proportional and derivative terms. There is also an open-loop program which was used for the rapid bank turns used in the research of Karásek et al.[36].

From Figure 7.5 it can be seen that the set-point roll command first goes through a reference generator, which filters the set-point heavily. The reference roll command then goes into a PD-controller, which uses the gains specified in Table 7.1. The output of the PD-controller then goes to the Delfly Nimble, which is indicated as 'Robot' in Figure 7.5. The influence of the reference generator is shown in Figure 7.6. The influence is shown by using the doublet train maneuver shown in Figure 7.1.

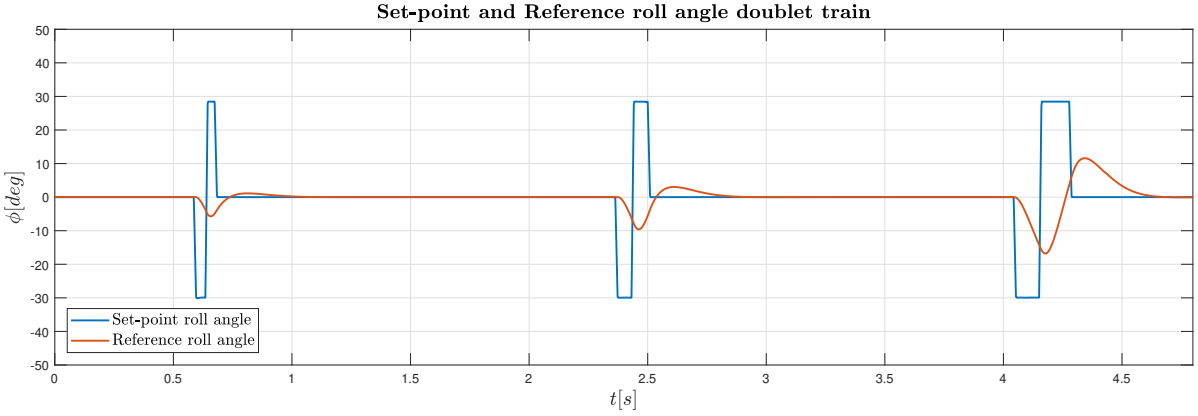

Figure 7.6: Set-point and Reference roll angle for the doublet train maneuver which is used for gathering identification data, as was explained in Section 7.2.1.

From Figure 7.6 it can be seen that there is a large influence of the reference generator on the commanded roll angle, which in this figure is these set-point roll angle. The Reference roll angle has a range which is significantly smaller than the range of the set-point roll angle. The reference roll angle still has to go through the PD-controller shown in Figure 7.5, which will limit the movement of the Delfly Nimble more, which can decrease the dynamic excitation even more. In spite of the reference generator and the PD-controller, there was still movement of the Delfly Nimble visible during the identification experiments. This is illustrated in Figure 7.7.

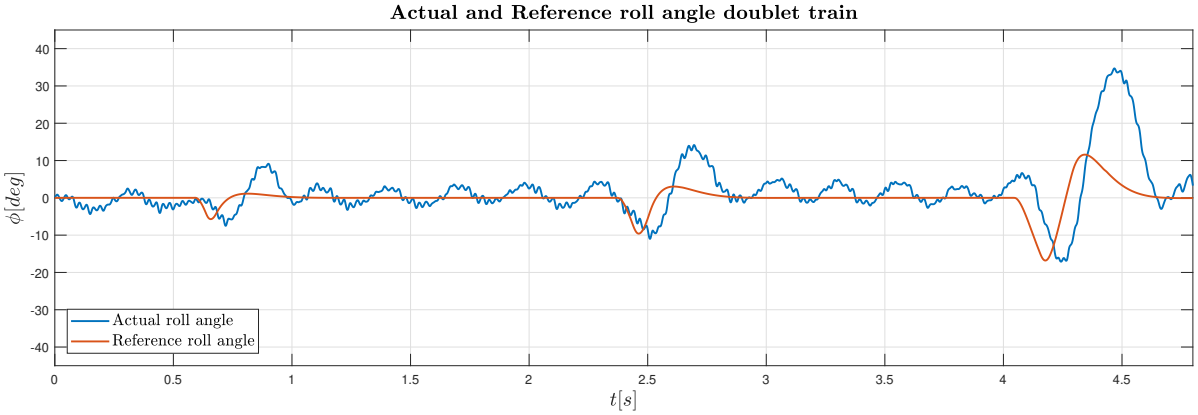

Figure 7.7: Actual roll angle of the Delfly Nimble and the Reference roll angle during the doublet train which was used as the identification maneuver. The actual roll angle is determined by using the Extended Kalman Filter which was developed by Armanini et al. [5].

From Figure 7.7 it can be seen that the doublet maneuver is visible, i.e. that the Delfly Nimble follows the reference roll angle well, especially during the first parts of the doublets, where a negative roll angle command is given. During the second part of the doublet, where a positive roll angle command is given, there is a large overshoot. This is due to the large P-gain which was used during the identification maneuvers, as shown Table 7.1. There is also a delay visible between the Reference roll angle and the Actual roll angle. This is due to the inertia of the Delfly Nimble. When the roll angle command is given, a deflection input is given to the control mechanism for the roll attitude, which in this case are the wings. The roll attitude is controller by

having a difference in flapping frequency between the left and right wings, δ_f. A positive δ_f will make the Delfly Nimble roll in the positive direction. Figure 7.8 shows the δ_f during the doublet train maneuver.

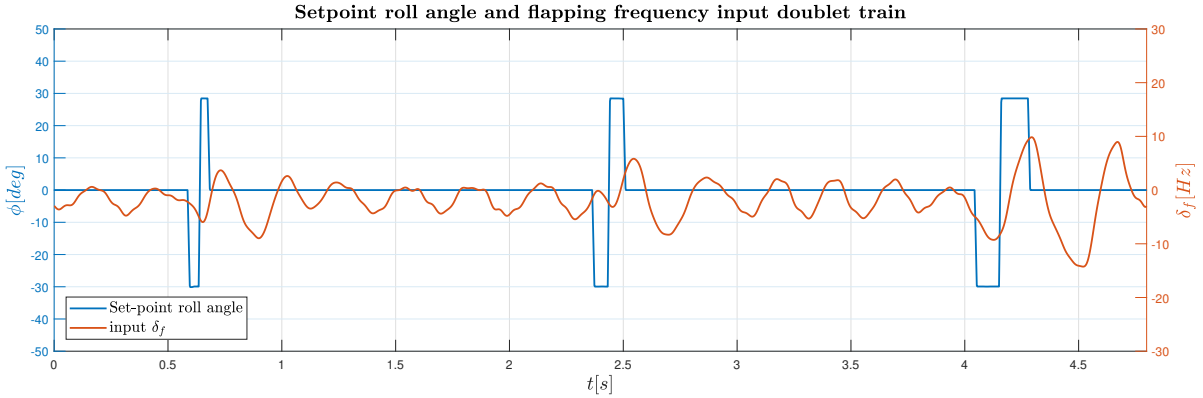

Figure 7.8: Set-point roll angle and the flapping frequency input δ_f for the doublet train which was used as the identification maneuver. A positive δ_f will make the Delfly Nimble roll in the positive direction. From this figure it van be seen that the appropriate δ_f is given for the doublet maneuver directly the start of the maneuver.

From Figure 7.8 it can be seen that the appropriate δ_f is given for the doublet maneuver directly the start of the maneuver. Thus the delay which was visible in figure 7.7 is due the inertia of the Delfly Nimble.

7.4. Identifiability of identification data

This section will answer Question **SQ1d**, the identifiability of the data. Even though there was movement visible on the Delfly Nimble when the identification maneuver, which was the doublet train, the identifiability still needs more verification. This can be done using the magnitude plot of a bode diagram, which was discussed in Section 3.3.4. Instead of the bode diagram, the Power Spectral Density (PSD) plots of the states are used for verifying the identifiability. The power spectrums of the raw data is shown in Figure 7.9.

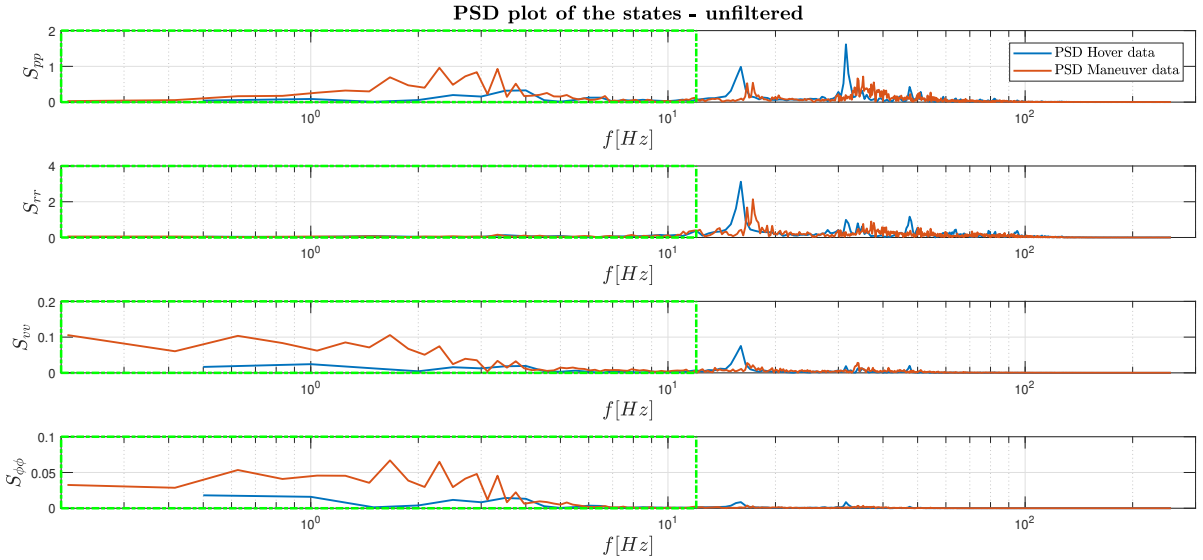

Figure 7.9: The Power Spectral Density (PSD) plots of the states of the Delfly Nimble while hovering and while doing the identification maneuver, which was discussed in Section 7.2.1. The PSD plots are of the raw data. Both the maneuver and hover data are from the same dataset. The green square in the power spectrums of the states contains the frequency content up to 12 Hz. The components inside this square were filtered out using using a zero-phase Butterworth filter with order 10.

In Figure 7.9 it can be seen that there are peaks around the 16 Hz in the PSD Hover data, which is the flapping frequency in hover. There also peak visible at the upper harmonics of the flapping frequency, which are

32 and 48 Hz. When looking at the PSD Maneuver data it can be seen that the peaks around the flapping frequencies are lower. This is because of the change in flapping frequencies which are applied during the doublet maneuver, which leads to multiple flapping frequencies during the maneuver. This also explains why there are more than one peak around the flapping frequency. What is more, the flapping frequencies peaks are shifted to the right. This is due to the increase in throttle, which as a consequence increases the flapping frequency of the Delfly Nimble. Furthermore, at the lower frequencies there is more power in the maneuver data. This can be better illustrated by filtering out the flapping frequencies from the signal. For the identification data, only the frequency components inside the red square in Figure 7.9 was used. Everything outside the square was filtered out. This was done using a Butterworth filter with an order of 10 and a cut-off frequency of 12 Hz. The filtered PSD plots are shown in Figure 7.10.

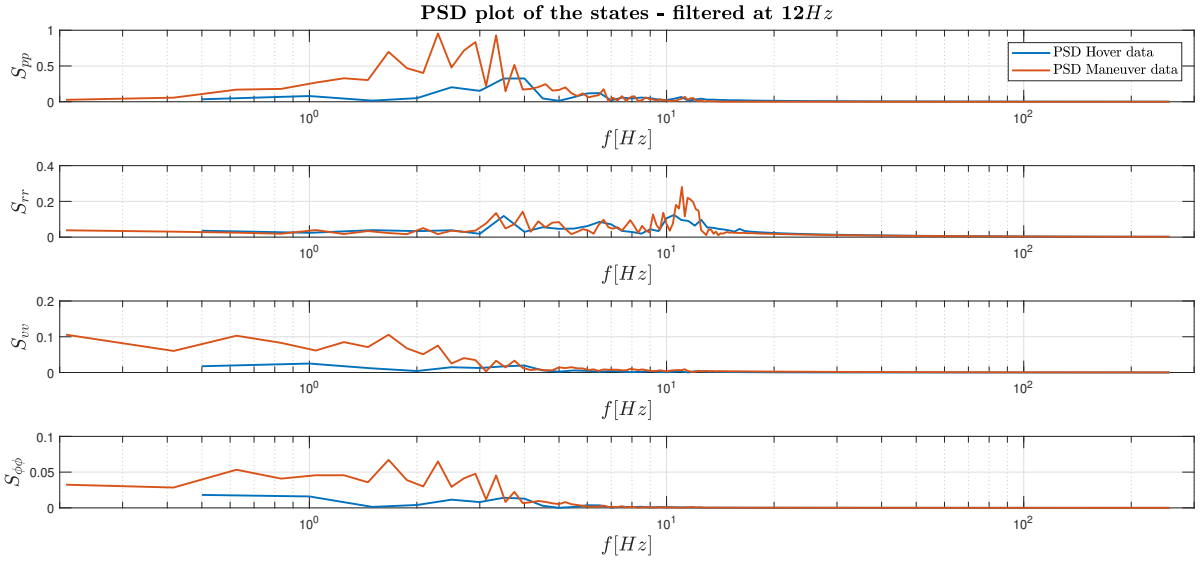

Figure 7.10: The Power Spectral Density (PSD) plots of the states of the Delfly Nimble while hovering and while doing the identification maneuver, which was discussed in Section 7.2.1. The PSD plots are of the filtered data, with a cutoff frequency of 12 Hz. A Butterworth filter was used with an order of 10. Both the maneuver and hover data are from the same dataset.

In Figure 7.10 it can be seen that there is more power in the signal at the lower frequencies. There are visible peaks around the 2 to 4 Hz for the p, v and ϕ, and there is a peak visible at 11 Hz in the PSD plot of r. These peaks are in line with the expectations of Section 3.3.1. Based on Figures 7.9 and 7.10 the identifiability of the data is verified, since there is a visible difference between the PSD plots of the hover and maneuver data, and there are peaks visible at the frequencies of the doublets used for the identification maneuver.

8

Model Identification Results

In this Chapter the results of model identification are discussed. Firstly, the results of the State Estimation using an Extended Kalman Filter are discussed in Section 8.1, further answering Question **SQ2a**. Secondly, the four model structures which have been used for the estimation are elaborated on in Section 8.2, thus answering Question **SQ2b**. Thirdly, the parameter estimation results are clarified in Section 8.3, answering **SQ2c**. Lastly, Section 8.4 explains what the natural motions of the Delfly Nimble are based on the identified model.

8.1. State Estimation Results

This section discusses the results state estimation, further answering Question **SQ2a**. For logging the data during the experiments described in Section 7.2, two sources of data were used: the OptiTrack Motion (OT) tracking system and On-board measurements. An overview of what was measured is shown in Table 8.1.

Source	**Obtained measurements**
OptiTrack	Position (x,y,z)
	Attitude Quaternions (q_0, q_1, q_2, q_3)
On-board	Angular Velocities (p, q, r)
	Linear Accelerations (a_x, a_y, a_z)
	Flapping frequency right (f_R)
	Flapping frequency left (f_L)
	Dihedral servo deflection (δ_d)
	Wing root servo deflection (δ_w)
	Throttle value (δ_t)

Table 8.1: Overview of the measurement obtained from the Optitrack Motion (OT) tracking system and the On-board data. The on-board data consisted of IMU data, which logged the angular velocities and linear accelerations, and it also consisted of logging of the deflections of the control mechanisms, such as the flapping frequencies of both wings, servo deflections, and throttle values.

The Attitude Quaternions obtained from the OT system were converted to the attitude angles ϕ, θ and ψ. The on-board data consisted of IMU data, which logged the angular velocities and linear accelerations, and it also consisted of logging of the deflections of the control mechanisms, such as the flapping frequencies of both wings, servo deflections, and throttle values. In order to improve the accuracy of the data, sensor fusion applied, using both sources of data. This was done using the same process as in the research of Armanini et al. [5]. The process for the sensor fusion is shown in Figure 3.13. An Extended Kalman Filter (EKF) was used for the sensor fusion. The complete working principle of the EKF can be found in the literature of Klein et al. [40] and Grewal et al. [22]. In the EKF which was developed by Armanini et al. [4, 5], the vectors shown in Equation 8.1 were used for the states x , input u , output z, the measurement noise v and the process noise w.

$$
\begin{aligned}
x &= \begin{bmatrix} \Phi & \Theta & \Psi & u_b & v_b & w_b & b_p & b_q & b_r & b_{a_x} & b_{a_y} & b_{a_z} \end{bmatrix}^T \\
u &= \begin{bmatrix} p & q & r & a_x & a_y & a_z \end{bmatrix}^T \\
z &= \begin{bmatrix} \Phi_m & \Theta_m & \Psi_m & u_b^* & v_b^* & w_b^* \end{bmatrix}^T \\
v &= \begin{bmatrix} v_\Phi & v_\Theta & v_\Psi & v_{u_b} & v_{v_b} & v_{w_b} \end{bmatrix}^T \\
w &= \begin{bmatrix} w_p & w_q & w_r & w_{a_x} & w_{a_y} & w_{a_z} \end{bmatrix}^T
\end{aligned} \tag{8.1}
$$

Here Φ, Θ and Ψ are the attitude angles, u_b, v_b and w_b are the body velocities, b_p, b_q and b_r are the bias terms for the gyroscopes , and b_{a_x}, b_{a_y} and b_{a_z} are the bias terms for the accelerometers in the state vector x. In the input vector u, the p, q and r are the angular rates measured from the gyroscopes, and the a_x, a_y and a_z are the accelerations measured by the accelerometers. In the output vector z, the Φ_m, Θ_m and Ψ_m are the measured attitude angles from the OT system, and the u_b^*, v_b^* and w_b^* are the measured body velocities from the OT system. The attitude angles were determined by transforming the attitude quaternions to angles, and the body velocities were determined by derivation of the position data. The terms in the vector v denote the measurement noise of the measured attitude angles and body velocities. The terms in the vector w denote the process noise in the angular rates and linear accelerations. The process and measurement Equations can be found in the work of Armanini et al. [4, 5]. The covariance matrix for the states Q and the covariance matrix for the measurements R are shown in Equation 8.2.

$$
\begin{aligned}
Q &= diag\begin{pmatrix} 7.60, & 2.60, & 12.07, & 26.99, & 36.66, & 56.12 \end{pmatrix} \\
R &= diag\begin{pmatrix} 0.125\times10^{-3}, & 0.057\times10^{-3}, & 0.037\times10^{-3}, & 0.113\times10^{-3}, & 0.216\times10^{-3}, & 0.135\times10^{-3} \end{pmatrix}
\end{aligned} \tag{8.2}
$$

The matrices were determined in such a way in order to make sure that the bounds were as small as possible, while containing the data-point within these bounds. The results of the EKF for the attitude angles is shown in Figure 8.1, while the results of the EKF for the body velocities are shown in Figure 8.2. These are the results for the doublet train maneuver shown in Figure 7.7.

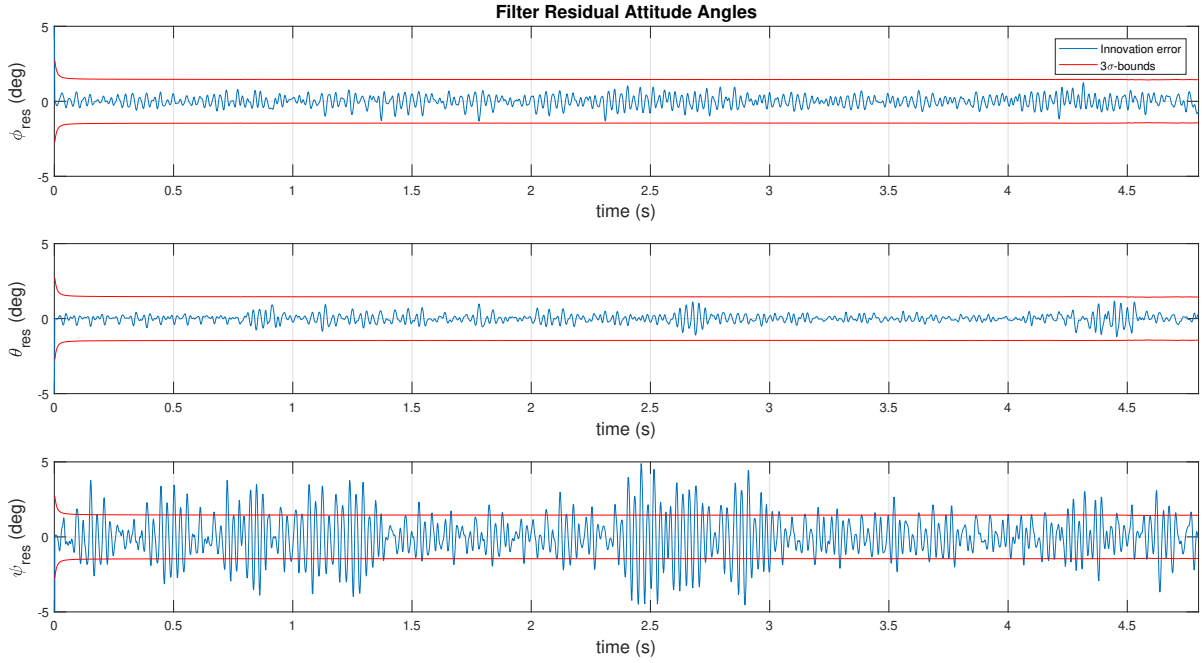

Figure 8.1: Residuals of the attitude angles ϕ, θ and ψ after the EKF was applied to the measurement data of the doublet train maneuver shown in Figure 7.7. The standard deviation σ of the residual of ϕ_{res} is 0.5°, the σ of θ_{res} is 0.3°, and the σ of ψ_{res} is 0.6°.

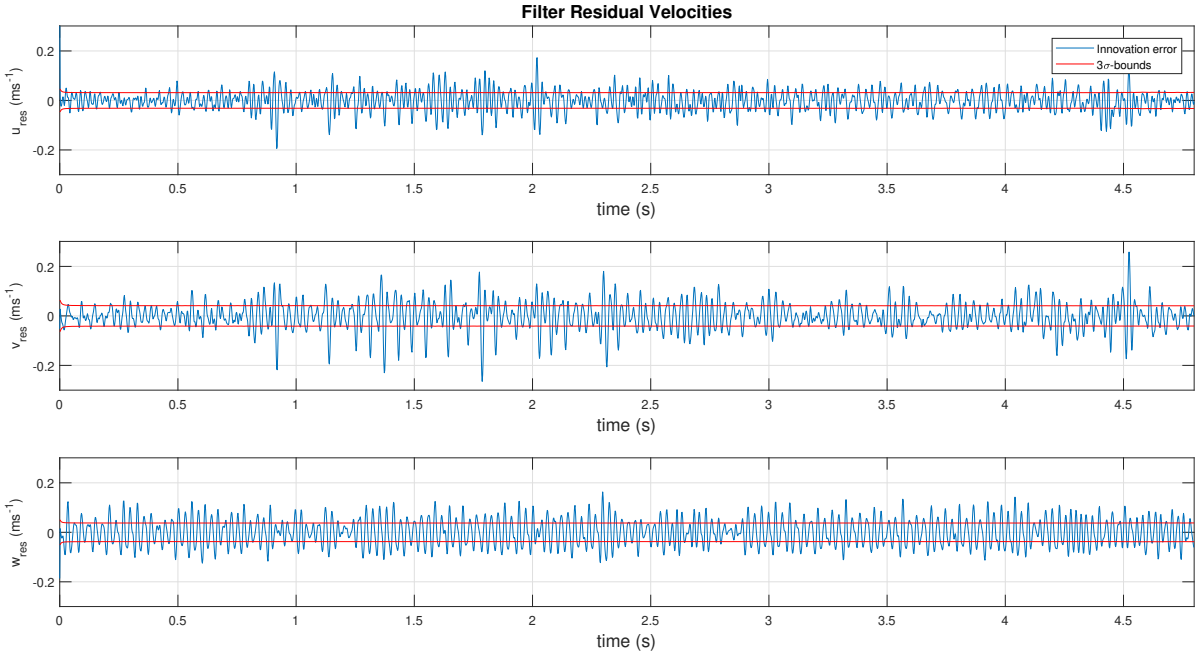

Figure 8.2: Residuals of the body velocities u, v and w after the EKF was applied to the measurement data of the doublet train maneuver shown in Figure 7.7. The standard deviation σ of the residual of u_{res}, v_{res} and w_{res} is $0.01 ms^{-1}$.

8.2. Model Structures

This section elaborates on the model structures used for the estimation, thus answering Question **SQ2b**. Two types of model structures were used for the identification of a mathematical mode of the lateral body dynamics of the Delfly Nimble: a grey-box state-space model and a black-box state-space model, both of which are linear time-invariant. The grey-box state-space model was developed by deriving the equations of motion (EOM's), the full derivation of which is shown in Appendix A. The grey-box model is shown in Equation 8.3.

$$\begin{bmatrix} \dot{p} \\ \dot{r} \\ \dot{v} \\ \dot{\phi} \end{bmatrix} = \begin{bmatrix} \frac{I_{zz}}{I_c} \cdot L_p + \frac{I_{xz}}{I_c} \cdot N_p & \frac{I_{zz}}{I_c} \cdot L_r + \frac{I_{xz}}{I_c} \cdot N_r & \frac{I_{zz}}{I_c} \cdot L_v + \frac{I_{xz}}{I_c} \cdot N_v & 0 \\ \frac{I_{xz}}{I_c} \cdot L_p + \frac{I_{xx}}{I_c} \cdot N_p & \frac{I_{xz}}{I_c} \cdot L_r + \frac{I_{xx}}{I_c} \cdot N_r & \frac{I_{xz}}{I_c} \cdot L_v + \frac{I_{xx}}{I_c} \cdot N_v & 0 \\ \frac{Y_p}{m} + w_0 & \frac{Y_r}{m} - u_0 & \frac{Y_v}{m} & g \cdot \cos(\theta_0) \cdot \cos(\phi_0) \\ 1 & \tan(\theta_0) \cdot \cos(\phi_0) & 0 & 0 \end{bmatrix} \cdot \begin{bmatrix} p \\ r \\ v \\ \phi \end{bmatrix} + \begin{bmatrix} \frac{I_{zz}}{I_c} \cdot L_{\delta_d} + \frac{I_{xz}}{I_c} \cdot N_{\delta_d} & \frac{I_{zz}}{I_c} \cdot L_{\delta_f} + \frac{I_{xz}}{I_c} \cdot N_{\delta_f} & \frac{I_{zz}}{I_c} \cdot L_{\delta_w} + \frac{I_{xz}}{I_c} \cdot N_{\delta_w} & \frac{I_{zz}}{I_c} \cdot L_{\delta_t} + \frac{I_{xz}}{I_c} \cdot N_{\delta_t} \\ \frac{I_{xz}}{I_c} \cdot L_{\delta_d} + \frac{I_{xx}}{I_c} \cdot N_{\delta_d} & \frac{I_{xz}}{I_c} \cdot L_{\delta_f} + \frac{I_{xx}}{I_c} \cdot N_{\delta_f} & \frac{I_{xz}}{I_c} \cdot L_{\delta_w} + \frac{I_{xx}}{I_c} \cdot N_{\delta_w} & \frac{I_{xz}}{I_c} \cdot L_{\delta_t} + \frac{I_{xx}}{I_c} \\ \frac{Y_{\delta_d}}{m} & \frac{Y_{\delta_f}}{m} & \frac{Y_{\delta_w}}{m} & \frac{Y_{\delta_t}}{m} \\ 0 & 0 & 0 & 0 \end{bmatrix} \cdot \begin{bmatrix} \delta_d \\ \delta_f \\ \delta_w \\ \delta_t \end{bmatrix} \tag{8.3}$$

The grey-box model shown in Equation 8.3 uses four states, the roll rate p, the yaw rate r, the lateral body velocity v and the roll angle ϕ. A reduced version of the grey-box model was also used, which used three states. Here the yaw dynamics are not considered, which omits all the the terms with the yaw rate r and also omits the N-parameters. This leads to the reduced state-space model shown in Equation 8.4.

$$\begin{bmatrix} \dot{p} \\ \dot{v} \\ \dot{\phi} \end{bmatrix} = \begin{bmatrix} \frac{I_{zz}}{I_c} \cdot L_p & \frac{I_{zz}}{I_c} \cdot L_v & 0 \\ \frac{Y_p}{m} + w_0 & \frac{Y_v}{m} & g \cdot \cos(\theta_0) \cdot \cos(\phi_0) \\ 1 & 0 & 0 \end{bmatrix} \cdot \begin{bmatrix} p \\ v \\ \phi \end{bmatrix} + \begin{bmatrix} \frac{I_{zz}}{I_c} \cdot L_{\delta_d} & \frac{I_{zz}}{I_c} \cdot L_{\delta_f} & \frac{I_{zz}}{I_c} \cdot L_{\delta_w} & \frac{I_{zz}}{I_c} \cdot L_{\delta_t} \\ \frac{Y_{\delta_d}}{m} & \frac{Y_{\delta_f}}{m} & \frac{Y_{\delta_w}}{m} & \frac{Y_{\delta_t}}{m} \\ 0 & 0 & 0 & 0 \end{bmatrix} \cdot \begin{bmatrix} \delta_d \\ \delta_f \\ \delta_w \\ \delta_t \end{bmatrix} \tag{8.4}$$

Next to the grey-box models, black-box models were also used. Similar to the grey-box models, two variations of the black-box model were used. One of which uses the four states p, r, v and ϕ, shown in Equation8.5, while the other uses three states, omitting the state r from the state-space, shown in Equation 8.6.

$$\begin{bmatrix} \dot{p} \\ \dot{r} \\ \dot{v} \\ \dot{\phi} \end{bmatrix} = \begin{bmatrix} a_{11} & a_{12} & a_{13} & a_{14} \\ a_{21} & a_{22} & a_{23} & a_{24} \\ a_{31} & a_{32} & a_{33} & a_{34} \\ a_{41} & a_{42} & a_{43} & a_{44} \end{bmatrix} \cdot \begin{bmatrix} p \\ r \\ v \\ \phi \end{bmatrix} + \begin{bmatrix} b_{11} & b_{12} & b_{13} & b_{14} \\ b_{21} & b_{22} & b_{23} & b_{24} \\ b_{31} & b_{32} & b_{33} & b_{34} \\ b_{41} & b_{42} & b_{43} & b_{44} \end{bmatrix} \cdot \begin{bmatrix} \delta_d \\ \delta_f \\ \delta_w \\ \delta_t \end{bmatrix} \tag{8.5}$$

$$\begin{bmatrix} \dot{p} \\ \dot{v} \\ \dot{\phi} \end{bmatrix} = \begin{bmatrix} a_{11} & a_{12} & a_{13} \\ a_{21} & a_{22} & a_{23} \\ a_{31} & a_{32} & a_{33} \end{bmatrix} \cdot \begin{bmatrix} p \\ v \\ \phi \end{bmatrix} + \begin{bmatrix} b_{11} & b_{12} & b_{13} & b_{14} \\ b_{21} & b_{22} & b_{23} & b_{24} \\ b_{31} & b_{32} & b_{33} & b_{34} \end{bmatrix} \cdot \begin{bmatrix} \delta_d \\ \delta_f \\ \delta_w \\ \delta_t \end{bmatrix} \tag{8.6}$$

The model structures shown in Equations 8.3 and 8.5 will be indicated as 'four-state' models, while the model structures shown in Equations 8.4 and 8.6 will be indicated as 'three-state' models in the following sections.

8.3. Parameter Estimation Results

This section clarifies the parameter estimation results, answering Question **SQ2c**. The parameters, which are the stability and control derivatives of the models shown in Section 8.2, were determined using the Equation-error approach, which was described in Section 4.3.1. Two types of the Equation-error approach were used, the Ordinary Least-Squares (OLS) and the Weighted Least-Squares (WLS) . First an OLS estimation was done and the weight matrix was determined by using the covariance matrix of the residuals, calculated using Equation 4.30. Then the WLS estimation was done by applying the calculated weight matrix. Subsection 8.3.1 will discuss the parameter estimation results when the four-state models are used, while Subsection 8.3.2 will elaborate on the estimation results when the three-state models are used.

8.3.1. Estimation Results Four-State State-Space Models

When Equation-error approach was used in combination with the full grey-box state-space model shown in Equation 8.3, an additional assumption needed to be made, namely that the L- and N-parameters are decoupled. This assumption needed to be made in order to cope with the coupled terms in the first two rows of the A-matrix. This leads to the full grey-box state-space model shown in Equation 8.7.

$$\begin{bmatrix} \dot{p} \\ \dot{r} \\ \dot{v} \\ \dot{\phi} \end{bmatrix} = \begin{bmatrix} \frac{I_{zz}}{I_c} \cdot L_p & \frac{I_{zz}}{I_c} \cdot L_r & \frac{I_{zz}}{I_c} \cdot L_v & 0 \\ \frac{I_{xx}}{I_c} \cdot N_p & \frac{I_{xx}}{I_c} \cdot N_r & \frac{I_{xx}}{I_c} \cdot N_v & 0 \\ \frac{Y_p}{m} + w_0 & \frac{Y_r}{m} - u_0 & \frac{Y_v}{m} & g \cdot \cos(\theta_0) \cdot \cos(\phi_0) \\ 1 & \tan(\theta_0) \cdot \cos(\phi_0) & 0 & 0 \end{bmatrix} \cdot \begin{bmatrix} p \\ r \\ v \\ \phi \end{bmatrix} + \begin{bmatrix} \frac{I_{zz}}{I_c} \cdot L_{\delta_d} & \frac{I_{zz}}{I_c} \cdot L_{\delta_f} & \frac{I_{zz}}{I_c} \cdot L_{\delta_w} & \frac{I_{zz}}{I_c} \cdot L_{\delta_t} \\ \frac{I_{xx}}{I_c} \cdot N_{\delta_d} & \frac{I_{xx}}{I_c} \cdot N_{\delta_f} & \frac{I_{xx}}{I_c} \cdot N_{\delta_w} & \frac{I_{xx}}{I_c} \cdot N_{\delta_t} \\ \frac{Y_{\delta_d}}{m} & \frac{Y_{\delta_f}}{m} & \frac{Y_{\delta_w}}{m} & \frac{Y_{\delta_t}}{m} \\ 0 & 0 & 0 & 0 \end{bmatrix} \cdot \begin{bmatrix} \delta_d \\ \delta_f \\ \delta_w \\ \delta_t \end{bmatrix} \tag{8.7}$$

The set-up of the regression matrices for the modified full grey-box model structure shown in Equation 8.7 and for the other three model structures shown in Section 8.2 are shown in Appendix C. Figure 8.3 shows the results of the WLS estimation when the modified grey-box state-space of Equation 8.7 is used as the model structure. The measurement of the doublet train shown in Figure 7.7 was used as the identification data.

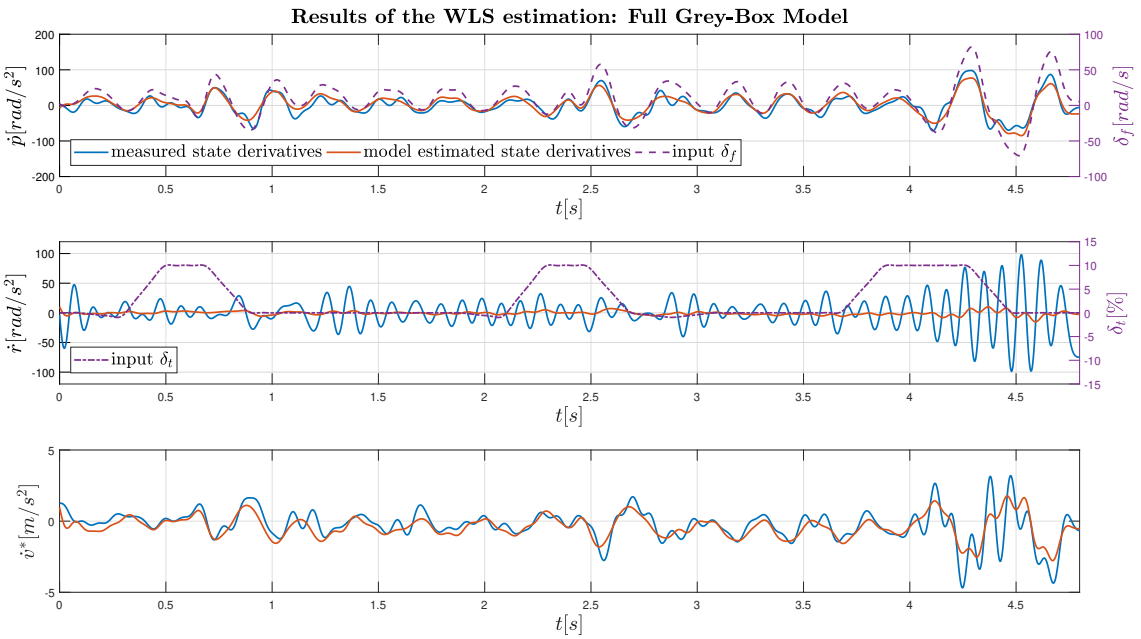

Figure 8.3: Results of the WLS estimation for each state derivative using the maneuver shown in Figure 7.7 as the identification data and the full grey-box state-space system shown in Equation 8.7 as the model structure. A low-pass Butterworth filter with order 10 and cutoff frequency of 12 Hz was used to filter the measured data. The third plot shows $\dot{v}^*$ instead of $\dot{v}$, since there are some constant terms in the Equation for $\dot{v}$ which needed to be put to the left-hand side. This is further elaborated in Appendix C.

From Figure 8.3 it can be seen that the state derivative $\dot{r}$ is very badly estimated with the chosen model structure. The bad estimation of $\dot{r}$ is also visible in the autocorrelation plot shown in Figure 8.4.

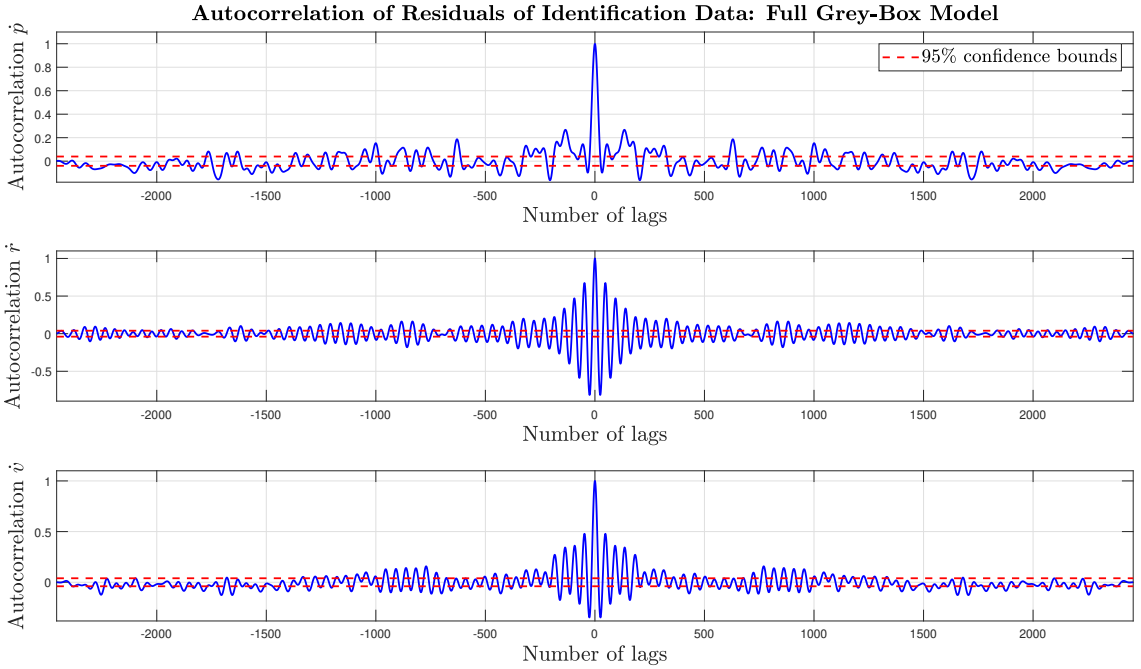

Figure 8.4: Autocorrelation plot of the residuals of the estimation shown in Figure 8.3. For the estimation the maneuver shown in Figure 7.7 as the identification data and the full grey-box state-space system shown in Equation 8.7 as the model structure.

From Figure 8.4, it can be seen that the residuals of $\dot{r}$ do not resemble white noise very well. This indicates that the $\dot{r}$ is badly estimated. The bad estimation is further confirmed by determining the following accuracy metrics for which the calculation is described in Chapter 5: the output correlation, the goodness of fit $\mathbf{R}^2$, and

the absolute and relative root-mean-square error **RMSE**. These are shown in Table 8.2.

Accuracy Metrics Four-State Grey-Box Model				
Output Variable	$\mathbf{r}_{xy}$	$\mathbf{R}^2$	**RMSE**	**RMSE** (% of meas. range)
$\dot{p}$	0.923	0.860	11.11 $\frac{rad}{s^2}$	6.55
$\dot{r}$	0.118	0.192	23.01 $\frac{rad}{s^2}$	11.69
$\dot{v}$	0.941	0.900	0.59 $\frac{m}{s^2}$	3.69

Table 8.2: Accuracy metrics for the estimation results shown in Figure 8.3. For the estimation the maneuver shown in Figure 7.7 as the identification data and the full grey-box state-space system shown in Equation 8.7 as the model structure.

From Table 8.2 it can be seen that the accuracy metrics also indicate a bad estimation of $\dot{r}$. The estimation has a low output correlation value, a low value for $\mathbf{R}^2$ and also a very high absolute and relative value for the **RMSE**. The estimated stability and control derivatives are shown in Table 8.3, which also shows the absolute and relative parameter standard deviation.

Estimated Parameters Full Grey-Box Model			
Stability Derivative	$\hat{\boldsymbol{\Theta}}$	$\lvert\hat{\sigma}\rvert$	$100\lvert\hat{\sigma}/\hat{\boldsymbol{\Theta}}\rvert$
L_p	-3.80×10^{-4}	1.00×10^{-4}	2.64×10^{1}
L_r	-2.81×10^{-4}	3.25×10^{-4}	1.16×10^{2}
L_v	-2.72×10^{-3}	1.01×10^{-3}	3.70×10^{1}
N_p	5.55×10^{-5}	7.58×10^{-4}	1.36×10^{3}
N_r	1.01×10^{-4}	1.16×10^{-3}	1.15×10^{3}
N_v	1.34×10^{-4}	5.51×10^{-3}	4.10×10^{3}
Y_p	-1.24×10^{-3}	9.55×10^{-6}	7.72×10^{-1}
Y_r	8.37×10^{-3}	1.66×10^{-5}	1.98×10^{-1}
Y_v	-2.38×10^{-2}	8.41×10^{-5}	3.53×10^{-1}
Control Derivative	$\hat{\boldsymbol{\Theta}}$	$\lvert\hat{\sigma}\rvert$	$100\lvert\hat{\sigma}/\hat{\boldsymbol{\Theta}}\rvert$
L_{δ_d}	1.41×10^{-3}	6.96×10^{-3}	4.93×10^{2}
L_{δ_f}	1.11×10^{-4}	7.46×10^{-6}	6.72×10^{0}
L_{δ_w}	7.28×10^{-3}	2.29×10^{-3}	3.14×10^{1}
L_{δ_t}	-3.09×10^{-5}	2.64×10^{-5}	8.56×10^{1}
N_{δ_d}	1.89×10^{-3}	4.23×10^{-2}	2.24×10^{3}
N_{δ_f}	-1.44×10^{-7}	3.83×10^{-5}	2.67×10^{4}
N_{δ_w}	-7.09×10^{-4}	1.21×10^{-2}	1.70×10^{3}
N_{δ_t}	8.19×10^{-6}	9.08×10^{-5}	1.11×10^{3}
Y_{δ_d}	-6.06×10^{-2}	8.43×10^{-4}	1.39×10^{0}
Y_{δ_f}	-9.25×10^{-4}	5.44×10^{-7}	5.88×10^{-2}
Y_{δ_w}	-9.16×10^{-2}	1.74×10^{-4}	1.90×10^{-1}
Y_{δ_t}	6.44×10^{-4}	1.01×10^{-6}	1.57×10^{-1}

Table 8.3: Estimated parameters for the four-state state-space system shown in Equation 8.7 as a result of the WLS estimator, using the maneuver data shown in Figure 7.7. $\hat{\boldsymbol{\Theta}}$ indicates the estimated parameter, while $|\hat{\sigma}|$ indicates the parameter standard deviation. The fourth column shows the relative parameter standard deviation in percent.

From Table 8.3 it can be seen that the estimated stability and control derivatives which contain N and r also have a higher parameter standard deviation $|\hat{\sigma}|$, which would indicate the parameters are very sensitive to noise in the data. There was high correlation visible between the parameters, especially for the ones with the state v and the input δ_d, further discussed in Appendix H.1. The estimation results of $\dot{r}$ also did not improve when the black-box state-space system shown in Equation 8.5, as can be seen in the estimation results shown in Figure 8.5, in the autocorrelation plots in Figure 8.6, and in the accuracy metrics shown in Table 8.4.

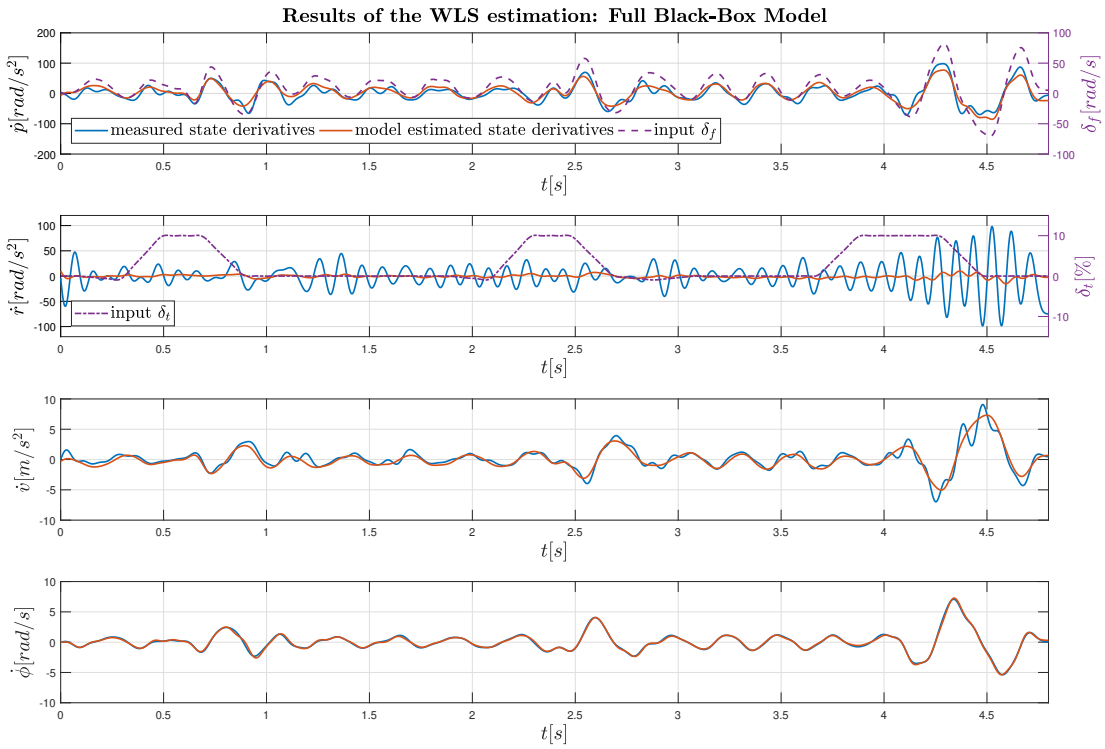

Figure 8.5: Results of the WLS estimation for each state derivative using the maneuver shown in Figure 7.7 as the identification data and using the full black-box state-space system shown in Equation 8.5 as the model structure. A low-pass Butterworth filter with order 10 and cutoff frequency of 12 Hz was used to filter the measured data.

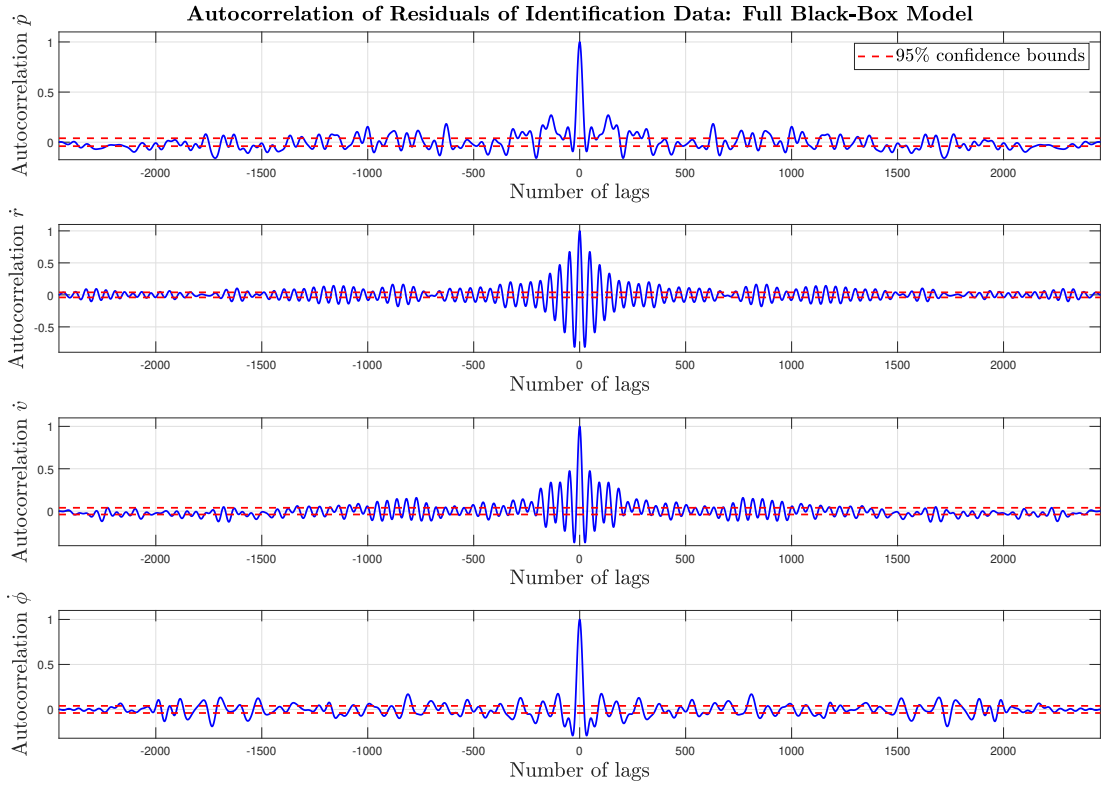

Figure 8.6: Autocorrelation plot of the residuals of the estimation shown in Figure 8.5. For the estimation the maneuver shown in Figure 7.7 as the identification data and the full black-box state-space system shown in Equation 8.5 as the model structure.

Accuracy Metrics Four-State Black-Box Model				
Output Variable	$\mathbf{r}_{xy}$	$\mathbf{R}^2$	**RMSE**	**RMSE** (% of meas. range)
$\dot{p}$	0.923	0.860	11.11 $\frac{rad}{s^2}$	6.55
$\dot{r}$	0.118	0.192	23.01 $\frac{rad}{s^2}$	11.69
$\dot{v}$	0.941	0.900	0.59 $\frac{m}{s^2}$	3.67
$\dot{\phi}$	0.997	0.995	0.12 $\frac{rad}{s}$	0.95

Table 8.4: Accuracy metrics for the estimation results shown in Figure 8.5. The estimation was done using the maneuver shown in Figure 7.7 as the identification data and using the full black-box state-space system shown in Equation 8.5 as the model structure.

The bad estimation of the $\dot{r}$ was visible for all the identification datasets which were used for the WLS parameter estimation. Using fewer inputs decreased the model accuracy of the estimation even more. The main reason for the bad estimation were the high frequency components in the yaw rate. These high frequency components of the yaw dynamics as shown in Figure 7.10 could be vibrations of the fuselage. The IMU is mounted directly to the body of the fuselage, which would mean that these vibrations would be sensed by the gyroscope. When looking at the PSD plot when using only the data of one doublet, the peak was still visible and consistently at around 11 Hz. This could indicate that it is indeed a vibration of the fuselage which can be seen in the PSD plot of the yaw rate. This might be resolved by using foam between the IMU and the fuselage of the Delfly Nimble, which would prevent the vibrations of the fuselage being sensed by the IMU. The foam has been used earlier on the Delfly Nimble, however it was replaced by an autopilot mount for practical reasons. The mount when using the foam was very fragile, which led to having to do a lot of repairs. Whether the peak seen around 11 Hz has to be confirmed by doing the same maneuvers using a Delfly Nimble which has foam between the IMU and the fuselage.

In order to improve the estimation of $\dot{r}$ a lower cut-off frequency was used for the Butterworth filter, however this would leave very little identifiable dynamics in the yaw rate, for there was then little difference between the PSD of the hover and the maneuver data, which is illustrated in Figure 8.7. The data used to generate this PSD plot was filtered using a Butterworth filter a cut-off frequency of 8 Hz and order 10.

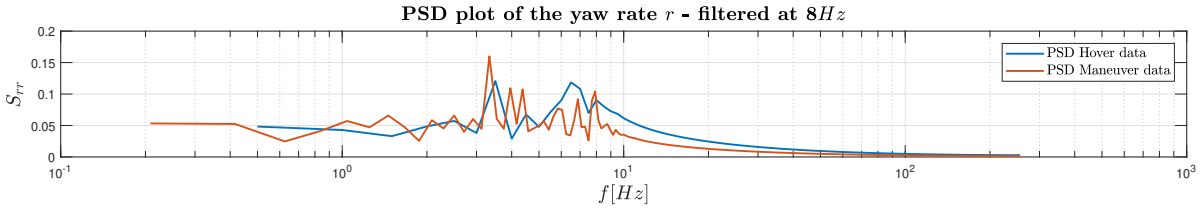

Figure 8.7: The Power Spectral Density (PSD) plots of the state r of the Delfly Nimble while hovering and while doing the identification maneuver, which was discussed in Section 7.2.1. The PSD plots are of the filtered data, with a cutoff frequency of 8 Hz. A Butterworth filter was used with an order of 10. Both the maneuver and hover data are from the same dataset.

The WLS estimation results using a lower cut-off frequency of 8 Hz did lead to a more accurate estimation of $\dot{r}$, however the highest value for the output correlation for the estimated yaw rate did not exceed 0.35, the value of $\mathbf{R}^2$ did not exceed 0.30, and the relative **RMSE** remained around 10 percent when using either the grey-box or the black-box model. Using an even lower cut-off would remove the information contained in the data of the other states too.

Due to the bad estimation of $\dot{r}$ in spite of all the measures taken, it was concluded that the yaw rate can't be modeled properly when using a LTI state-space system. As a consequence it was decided to use the three-state state-space system shown in Equations 8.4 and 8.6, omitting the yaw dynamics completely. The assumption is then made that the yaw and roll dynamics are also decoupled. Since there is little overlap between the dominant frequency components of the r dynamics and the dynamics of the other states when analyzing Figure 7.10, the removal of the r measurement does not influence the estimation of the other state derivatives by much. The results of the identification of mathematical model for the lateral body dynamics of the Delfly Nimble using the three-state models is elaborated on in Subsection 8.3.2.

8.3.2. Estimation Results Three-State State-Space Models

When only a three-state state-space system as shown in Equations 8.4 and 8.6 is used as the model structure, the cut-off frequency was decreased from 12 Hz to 9 Hz in order to filter out more noise, while keeping as much information as possible in the identification data. A cut-off frequency of 9 Hz was chosen since there are no dominant frequency components of the body dynamics at frequencies higher than 9 Hz in the measurements of the states p, v and ϕ. This is verified by the PSD plot shown in Figure 8.8.

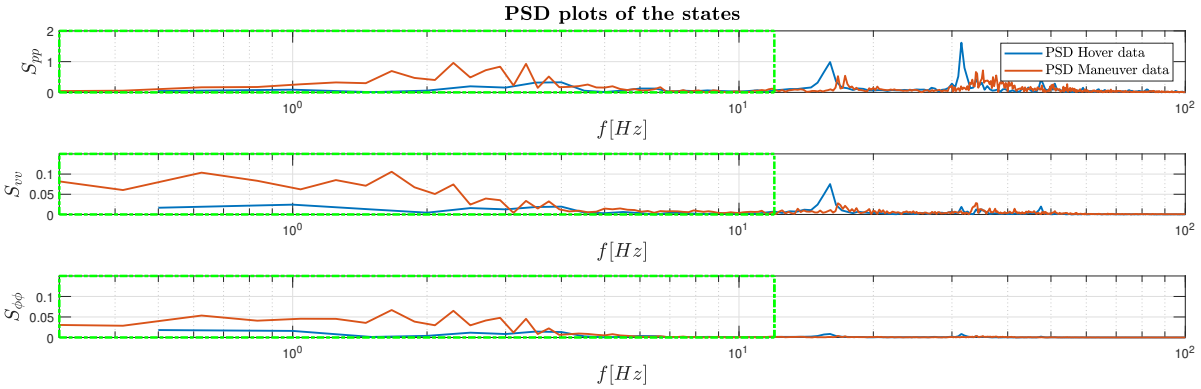

Figure 8.8: Power Spectral Density (PSD) plots of the states of the Delfly Nimble during hover and the identification maneuver. The green square in the power spectrums of the states contains the frequency content up to 9 Hz. The components inside this square were filtered out using using a zero-phase Butterworth filter with order 10.

Also, only the latter two doublets of 4 Hz and 7 Hz were used for the estimation, since the lack of dominant frequency components above 9 Hz in the dynamics of the measured states and because of the very little excitation seen for this doublet in most datasets used for the model identification. What is more, the number of inputs was reduced in order to simplify the model as much as possible. For the identification results shown in this section, only the inputs δ_f and δ_t were used, since the only actual commands given during the doublet train maneuver are commands to the roll angle and the throttle. Omitting the inputs δ_d and δ_w did not influence the model accuracy significantly. The estimation results of the state derivatives using the WLS approach and the model structure shown in Equation 8.4 is shown in Figure 8.9.

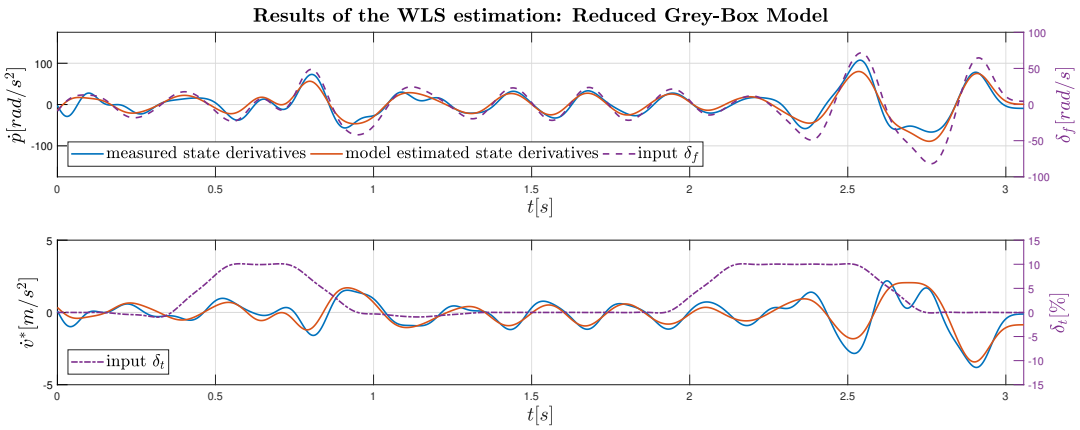

Figure 8.9: Results of the WLS estimation for each state derivative. Two of the three doublets shown in Figure 7.7 were used as the identification data and the reduced grey-box state-space system shown in Equation 8.4 as the model structure. Only the inputs δ_f and δ_t were used in the model structure, setting the inputs δ_d and δ_w to zero. A low-pass Butterworth filter with order 10 and cutoff frequency of 9 Hz was used to filter the measurement data. The second plot shows $\dot{v}^*$ instead of $\dot{v}$, since there are some constant terms in the Equation for $\dot{v}$ which needed to be put to the left-hand side. This is further elaborated in Appendix C.

From Figure 8.9 it can be seen that the state derivatives $\dot{p}$ and $\dot{v}$ are estimated with the chosen model structure. This can also be seen in the autocorrelation plot of the residuals shown in Figure 8.10.

Figure 8.10: Autocorrelation plot of the residuals of the estimation shown in Figure 8.9. For the estimation two doublets of the maneuver shown in Figure 7.7 as the identification data and the reduced grey-box state-space system shown in Equation 8.4 as the model structure.

From Figure 8.10 it can be seen that the residuals of $\dot{v}$ when using the reduced grey-box model resemble white noise more than the residuals of $\dot{v}$ when using the full grey-box model, as was shown in Figure 8.4. This is due to the removal of the yaw dynamics, which are present in the equation for $\dot{v}^*$ and because of the lower cut-off frequency used for the Butterworth filter. The accuracy metrics of this estimation are shown in Table 8.5.

Accuracy Metrics Three-State Grey-Box Model				
Output Variable	$\mathbf{r}_{xy}$	$\mathbf{R}^2$	**RMSE**	**RMSE** (% of meas. range)
$\dot{p}$	0.945	0.907	9.99 $\frac{rad}{s^2}$	5.74
$\dot{v}$	0.982	0.967	0.38 $\frac{m}{s^2}$	2.84

Table 8.5: Accuracy metrics for the estimation results shown in Figure 8.9. The estimation was done using two doublets of the maneuver shown in Figure 7.7 as the identification data and using the reduced grey-box state-space system shown in Equation 8.4 as the model structure, with the inputs δ_d and δ_w set to zero.

From Table 8.5 it can be seen that the state derivatives $\dot{p}$ and $\dot{v}$ are estimated well with the chosen model structure. The values of the accuracy metrics are also more favorable. The output correlation and the $\mathbf{R}^2$ are higher compared to the full grey-box model, while the absolute and relative values for the **RMSE** are both lower. The estimated parameters are shown in Table 8.6.

Estimated Parameters Reduced Grey-Box Model			
Stability Derivative	$\hat{\boldsymbol{\Theta}}$	$\lvert\hat{\sigma}\rvert$	$100\lvert\hat{\sigma}/\hat{\boldsymbol{\Theta}}\rvert$
L_p	-2.43×10^{-4}	1.69×10^{-4}	6.96×10^{1}
L_v	-3.74×10^{-4}	1.52×10^{-3}	4.07×10^{2}
Y_p	2.75×10^{-3}	3.31×10^{-6}	1.20×10^{-1}
Y_v	-5.61×10^{-2}	3.32×10^{-5}	5.92×10^{-2}
Control Derivative	$\hat{\boldsymbol{\Theta}}$	$\lvert\hat{\sigma}\rvert$	$100\lvert\hat{\sigma}/\hat{\boldsymbol{\Theta}}\rvert$
L_{δ_f}	1.06×10^{-4}	8.47×10^{-6}	8.02×10^{0}
L_{δ_t}	4.19×10^{-5}	5.48×10^{-5}	1.31×10^{2}
Y_{δ_f}	-8.63×10^{-4}	1.22×10^{-7}	1.41×10^{-2}
Y_{δ_t}	-4.05×10^{-4}	4.55×10^{-7}	1.12×10^{-1}

Table 8.6: Estimated parameters for the three-state state-space system shown in Equation 8.4 as a result of the WLS estimator, using two doublets of the maneuver data shown in Figure 7.7, and setting the inputs δ_d and δ_w to zero. $\hat{\boldsymbol{\Theta}}$ indicates the estimated parameter, while $\lvert\hat{\sigma}\rvert$ indicates the parameter standard deviation. The fourth column shows the relative parameter standard deviation in percent.

From Table 8.6 it can be seen that the L-parameters are more sensitive to noise in the data compared to the Y-parameters. What is also noteworthy is that the signs of the stability derivative Y_p and of the control derivatives L_{δ_t} and Y_{δ_t} are flipped when compared to the full grey-box model. There was no high correlation between the parameters, as can be seen in Appendix H.2. The aerodynamic moment L and force Y were determined using the estimated stability and control derivatives, and the results are shown in Appendix F. The estimation was also done using the reduced black-box state-space system shown in Equation 8.6, the results of which are shown in Figure 8.11, the accuracy metrics of this estimation are shown in Table 8.7, and the autocorrelation plots of the residuals are shown in Figure 8.12.

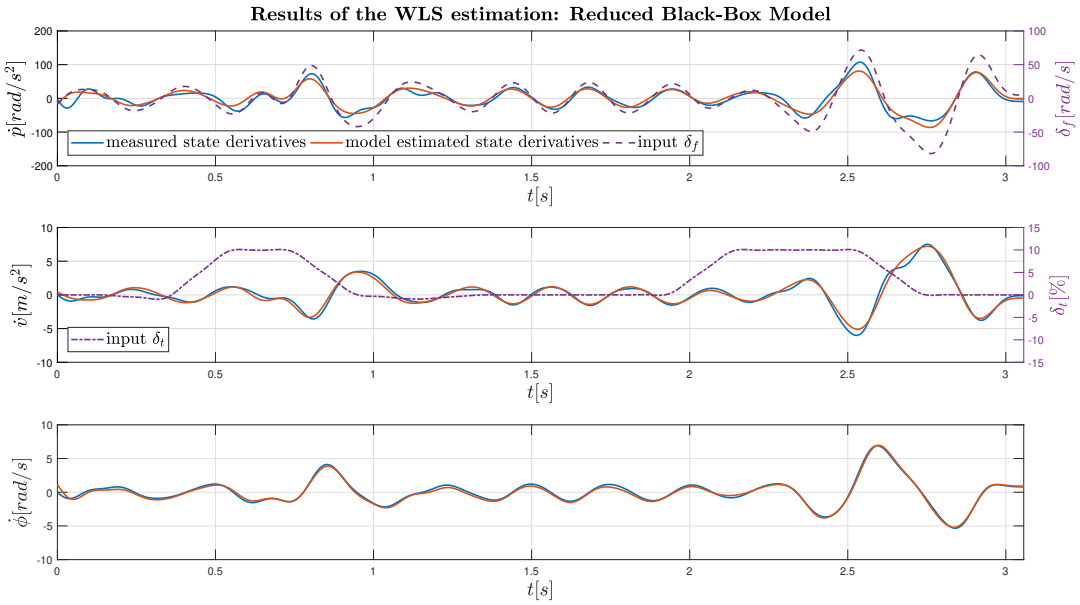

Figure 8.11: Results of the WLS estimation for each state derivative. Two of the three doublets shown in Figure 7.7 were used, and the model structure shown in Equation 8.6 was chosen. Only the inputs δ_f and δ_t were used in the model structure, setting the inputs δ_d and δ_w to zero. A low-pass Butterworth filter with order 10 and cutoff frequency of 9 Hz was used to filter the measured data.

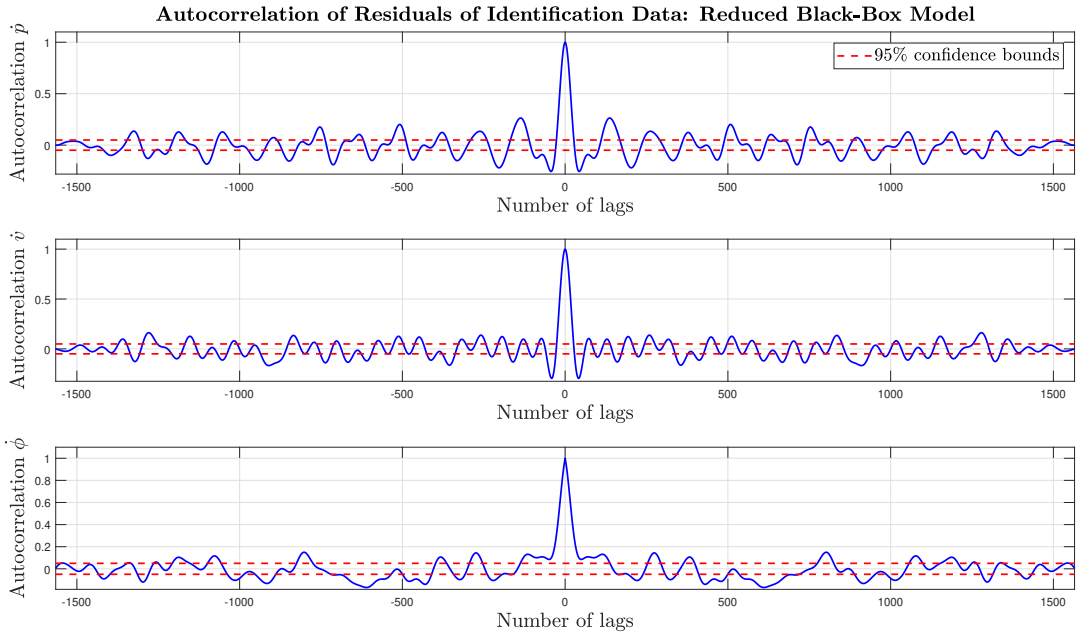

Figure 8.12: Autocorrelation plot of the residuals of the estimation shown in Figure 8.11. For the estimation two doublets of the maneuver shown in Figure 7.7 as the identification data and the reduced black-box state-space system shown in Equation 8.6 as the model structure.

Accuracy Metrics Three-State Black-Box Model				
Output Variable	$\mathbf{r}_{xy}$	$\mathbf{R}^2$	**RMSE**	**RMSE** (% of meas. range)
$\dot{p}$	0.947	0.909	9.88 $\frac{rad}{s^2}$	5.67
$\dot{v}$	0.986	0.976	0.33 $\frac{m}{s^2}$	2.46
$\dot{\phi}$	0.995	0.988	0.21 $\frac{rad}{s}$	1.72

Table 8.7: Accuracy metrics for the estimation results shown in Figure 8.11. The estimation was done using two doublets of the maneuver shown in Figure 7.7 as the identification data and using the reduced black-box state-space system shown in Equation 8.6 as the model structure, with the inputs δ_d and δ_w set to zero.

From Figures 8.11 and 8.12 and Table 8.7 it can be seen that there is little improvement of the estimation of the states $\dot{p}$ and $\dot{v}$ compared to when using the reduced grey-box state-space system as the model structure.

8.4. Natural Lateral Dynamic Motions of the Delfly Nimble

In this section the natural motions of the Delfly Nimble are explained. These motions are determined by analysis of the eigenvectors of the identified models. When the four-state state-space system is used as the model structure, the eigenvector has four components which indicate the states p, r, v and ϕ, while the eigenvector will have three components when the three-state state-space system is used as the model structure, namely the states p, v and ϕ. The states in the eigenvector will be non-dimensionalized using Equation 8.8 [13]. This is done in order to account for the difference in the range of the states.

$$\begin{aligned} p^+ &= \frac{p}{f}, \quad v^+ = \frac{v}{2 \cdot \phi_f \cdot f \cdot \hat{r}} \\ r^+ &= \frac{r}{f}, \quad \phi^+ = \phi \end{aligned} \tag{8.8}$$

Where the flapping frequency f was set to 106.8 rad/s (17 Hz), the flapping amplitude ϕ_f was set to 1.536 rad (88°), and the $\hat{r}$ was set to 7.45×10^{-2} meter. The terms of the eigenvector are shown in their polar form, and all the states will be normalized with respect tot the roll angle ϕ^+. In Subsection 8.4.1 the natural modes of the four-state state-space systems are explained, while the natural modes of the three-state state-space systems are clarified.

8.4.1. Natural Modes Four-State State-Space Models

In this Section the natural modes of the estimated models which use the four-state state-space systems shown in Equations 8.7 and 8.5 as the model structure. The eigenvalues of the identified full grey-box model are shown in Table 8.8.

Eigenvalues Four-State Grey-Box Model			
	λ_1 **(Mode 1)**	$\lambda_{2,3}$ **(Mode 2)**	λ_4 **(Mode 3)**
Eigenvalue	-8.44	$1.99 \pm 5.54i$	2.70

Table 8.8: Eigenvalues for the estimated four-state grey-box state-space model shown in Equation 8.7.

From the eigenvalues shown in Table 8.8 it can be seen that there is one stable aperiodic mode, one unstable oscillatory mode, and one unstable aperiodic mode. Using the eigenvectors it can be determined which movements the Delfly Nimble is making for each eigenvalue. The eigenvectors for the full grey-box system are shown in Table 8.9.

Eigenvectors Four-State Grey-Box Model			
State	**Mode 1**	**Mode 2**	**Mode 3**
p^+	0.49 (180°)	0.34 (69.7°)	0.05 (180°)
r^+	0.10 (0°)	0.07 (-70.4°)	2.08 (180°)
v^+	0.37 (180°)	0.39 (-67.6°)	0.94 (0°)
ϕ^+	1.0 (0°)	1.0 (0°)	1.0 (0°)

Table 8.9: Eigenvectors for the estimated four-state grey-box model shown in Equation 8.7. The terms in the eigenvectors have been non-dimensionalized and normalized with respect to ϕ^+.

In the eigenvector of the first mode shown in Table 8.9 it can be seen that the main variables for this motion are the p^+, v^+ and the ϕ^+. It can be seen that the variables ϕ^+ and v^+ have a phase shift of 180 degrees, meaning that when the Delfly is for example moving sideways to the left, it is rolled in the opposite direction to the right, which has a stabilizing effect, explaining why the eigenvalue is located in the left half of the complex plane. In the eigenvector of the second mode it can be seen that the main variables are again the p^+, v^+ and the ϕ^+. However, the phase shift between the v^+ and the ϕ is only -66.4 degrees, which means that a large portion of the maneuver these two variables have the same sign, i.e. when the Delfly is for example moving sideways to the left it is rotated in the same direction, which has a destabilizing effect. This explains why the real part of the eigenvalue of this maneuver is in the right half of the complex plane. For the thrid mode the most important variables are the r^+. In combination with the positive real part of the eigenvalue, this indicates a yaw motion which is unstable. However, this was not visible during the experiments. This could be due to the controller stabilizing the Delfly Nimble, or the calculated eigenvalue is not reliable, for the yaw dynamics were poorly estimated with the chosen model structure. Similar results were found when the full black-box state-space system was used as the model structure. The eigenvalues for the estimated black-box model is shown in Table 8.10 and the eigenvectors are shown in Table 8.11.

Eigenvalues Four-State Black-Box Model			
	λ_1 **(Mode 1)**	$\lambda_{2,3}$ **(Mode 2)**	λ_4 **(Mode 3)**
Eigenvalue	-7.19	$1.92 \pm 5.32i$	2.66

Table 8.10: Eigenvalues for the estimated four-state black-box state-space model shown in Equation 8.5.

Eigenvectors Four-State Grey-Box Model			
State	**Mode 1**	**Mode 2**	**Mode 3**
p	0.43 (180°)	0.33 (72.9°)	0.01 (0°)
r	0.11 (0°)	0.06 (-66.2°)	2.41 (180°)
v	0.34 (180°)	0.38 (-70.6°)	1.01 (0°)
ϕ	1.0 (0°)	1.0 (0°)	1.0 (0°)

Table 8.11: Eigenvectors for the estimated four-state black-box model shown in Equation 8.5. The terms in the eigenvectors have been non-dimensionalized and normalized with respect to ϕ^+.

8.4.2. Natural Modes Three-State State-Space Models

In this Section the natural modes of the estimated models which use the three-state state-space systems shown in Equations 8.4 and 8.6 as the model structure. The eigenvalues of the identified full grey-box model are shown in Table 8.12.

Eigenvalues Three-State Grey-Box Model		
	λ_1 **(Mode 1)**	$\lambda_{2,3}$ **(Mode 2)**
Eigenvalue	-5.18	$0.32 \pm 2.73i$

Table 8.12: Eigenvalues for the estimated three-state grey-box state-space model shown in Equation 8.4, where the inputs δ_d and δ_w have been put to zero.

From the eigenvalues shown in Table 8.12 it can be seen that there is one stable aperiodic mode and one unstable oscillatory mode. Using the eigenvectors it can be determined which movements the Delfly Nimble is making for each eigenvalue. The eigenvectors for the reduced grey-box system are shown in Table 8.13.

Eigenvector Three-State Grey-Box Model		
State	**Mode 1**	**Mode 2**
p	0.30 (180°)	0.16 (83.4°)
v	0.86 (180°)	0.70 (-53.5°)
ϕ	1.0 (0°)	1.0 (0°)

Table 8.13: Eigenvectors for the estimated three-state grey-box model shown in Equation 8.4, where the inputs δ_d and δ_w have been put to zero. The terms in the eigenvectors have been non-dimensionalized and normalized with respect to ϕ^+.

In the eigenvector of the first mode shown in Table 8.13 it can be seen that all variables for this mode are important. It can be seen that the variables ϕ^+ and v^+ have a phase shift of 180 degrees, meaning that when the Delfly is for example moving sideways to the left, it is rolled in the opposite direction to the right, which has a stabilizing effect, explaining why the eigenvalue is located in the left half of the complex plane. In the eigenvector of the second mode it can be seen that the main variables are the v^+ and the ϕ^+. However, the phase shift between the v^+ and the ϕ is only -52.4 degrees, which means that a large portion of the oscillation cycle these two variables have the same sign, i.e. when the Delfly is for example moving sideways to the left it is rotated in the same direction, which has a destabilizing effect. This explains why the real part of the eigenvalue of this maneuver is in the right half of the complex plane. These motions are similar to those of Mode 1 and Mode 2 of the four-state state-space models. Similar results were also found when the reduced black-box state-space system was used as the model structure. The eigenvalues for the estimated black-box model is shown in Table 8.14 and the eigenvectors are shown in Table 8.15.

Eigenvalues Three-State Black-Box Model		
	λ_1 **(Mode 1)**	$\lambda_{2,3}$ **(Mode 2)**
Eigenvalue	-6.97	$2.04 \pm 2.12i$

Table 8.14: Eigenvalues for the estimated three-state black-box state-space model shown in Equation 8.6, where the inputs δ_d and δ_w have been put to zero.

Eigenvector Three-State Black-Box Model		
State	**Mode 1**	**Mode 2**
p	0.56 (180°)	0.13 (59.6°)
v	0.34 (180°)	0.49 (-36.7°)
ϕ	1.0 (0°)	1.0 (0°)

Table 8.15: Eigenvectors for the estimated three-state black-box model shown in Equation 8.6, where the inputs δ_d and δ_w have been put to zero. The terms in the eigenvectors have been non-dimensionalized and normalized with respect to ϕ^+.

9

Validation Results

In this chapter the reduced models which have been identified in Chapter 8 are validated. The grey-box state-space systems which have been used as the model structure is shown in Equation 9.1.

$$\begin{bmatrix} \dot{p} \\ \dot{v} \\ \dot{\phi} \end{bmatrix} = \begin{bmatrix} \frac{I_{zz}}{I_c} \cdot L_p & \frac{I_{zz}}{I_c} \cdot L_v & 0 \\ \frac{Y_p}{m} + w_0 & \frac{Y_v}{m} & g \cdot \cos(\theta_0) \cdot \cos(\phi_0) \\ 1 & 0 & 0 \end{bmatrix} \cdot \begin{bmatrix} p \\ v \\ \phi \end{bmatrix} + \begin{bmatrix} \frac{I_{zz}}{I_c} \cdot L_{\delta_f} & \frac{I_{zz}}{I_c} \cdot L_{\delta_t} \\ \frac{Y_{\delta_f}}{m} & \frac{Y_{\delta_t}}{m} \\ 0 & 0 \end{bmatrix} \cdot \begin{bmatrix} \delta_f \\ \delta_t \end{bmatrix} \tag{9.1}$$

Using the estimated parameters which are shown in Table 9.1 and the geometric properties of the Delfly Nimble, which are shown in Appendix A.1, the state-space model can be set up. The numeric state-space model which have been used in this chapter are shown in Appendix E.

Estimated Parameters Reduced Grey-Box Model			
Stability Derivative	$\hat{\boldsymbol{\Theta}}$	**Control Derivative**	$\hat{\boldsymbol{\Theta}}$
L_p	-2.43×10^{-4}	L_{δ_f}	1.06×10^{-4}
L_v	-3.74×10^{-4}	L_{δ_t}	4.19×10^{-5}
Y_p	2.75×10^{-3}	Y_{δ_f}	-8.63×10^{-4}
Y_v	-5.61×10^{-2}	Y_{δ_t}	-4.05×10^{-4}

Table 9.1: Stability and control derivatives which are used to set up the reduced grey-box state-space model shown in Equation 9.1. These are the same parameters as the ones shown in Table 8.6. $\hat{\boldsymbol{\Theta}}$ indicates the value of the estimated parameter.

In Section 9.1 the estimated stability and control derivatives are analyzed. Next, in Section 9.2 the open-loop validation is discussed using a doublet and a 112-maneuver. This is followed by Section 9.3, which elaborates on the closed-loop validation, also using doublet trains and 112-maneuvers. The chapter continues with Section 9.4, where it is clarified how justifiable the assumption on uncoupled longitudinal and lateral dynamics is. This is done by analyzing how accurate the state-space system shown in Equation 9.1 can model a coupled doublet, a maneuver which is done using the commands shown in Figure 7.3. This section will thus answer Question **SQ3b**. The final Section is 9.5, where it is explained how justifiable the linearity assumption is. This is done by analyzing how accurate the state-space system shown in Equation 9.1 can model a nonlinear doublet, a maneuver which is done using the commands shown in Figure 7.4. This section will therefore answer Question **SQ3c**.

9.1. Analysis stability and control derivatives

In this section the stability and control derivatives are analyzed. First, the consistency of the estimated parameters is discussed in Subsection 9.1.1. Second, the estimated stability derivatives are compared to the

stability derivatives of analytic models of insect flight in Subsection 9.1.2. At last, the identified stability derivatives are compared to the stability derivatives of the Delfly II in Subsection 9.1.3.

9.1.1. Estimated parameters using different identification data sets

In this section the estimated stability and control derivatives using different data sets are compared. In total there were five data sets, each having two doublets with main frequencies of 4 Hz and 7 Hz. The estimated stability and control derivatives are shown in Table 9.2

Estimated Parameters Reduced Grey-Box Model					
Stability Derivative	$\hat{\Theta}_1$	$\hat{\Theta}_2$	$\hat{\Theta}_3$	$\hat{\Theta}_4$	$\hat{\Theta}_5$
L_p	-2.43×10^{-4}	-3.16×10^{-4}	-4.23×10^{-4}	-5.23×10^{-4}	-2.89×10^{-4}
L_v	-3.74×10^{-4}	-9.34×10^{-4}	-1.38×10^{-3}	-3.42×10^{-3}	-1.01×10^{-3}
Y_p	2.75×10^{-3}	-2.64×10^{-3}	7.01×10^{-3}	-1.82×10^{-3}	-2.31×10^{-3}
Y_v	-5.61×10^{-2}	-7.74×10^{-2}	-2.15×10^{-2}	-4.43×10^{-2}	-1.08×10^{-1}
Control Derivative	$\hat{\Theta}_1$	$\hat{\Theta}_2$	$\hat{\Theta}_3$	$\hat{\Theta}_4$	$\hat{\Theta}_5$
L_{δ_f}	1.06×10^{-4}	9.79×10^{-5}	1.01×10^{-4}	8.85×10^{-5}	9.58×10^{-5}
L_{δ_t}	4.19×10^{-5}	5.40×10^{-5}	7.68×10^{-6}	4.66×10^{-5}	4.54×10^{-5}
Y_{δ_f}	-8.63×10^{-4}	-8.46×10^{-4}	-8.33×10^{-4}	-7.98×10^{-4}	-9.87×10^{-4}
Y_{δ_t}	-4.05×10^{-4}	-7.60×10^{-4}	1.85×10^{-4}	-3.88×10^{-4}	-1.22×10^{-3}

Table 9.2: Estimated parameters for the three-state state-space system shown in Equation 8.4 as a result of the WLS estimator, using various datasets, and setting the inputs δ_d and δ_w to zero. $\hat{\Theta}$ indicates the value of the estimated parameter. The subscript indicates the number of the dataset. $\hat{\Theta}_1$ are the same parameter values as shown in Table 9.1.

From Table 9.2 it can be seen that all the identified L-parameters have the same sign for each data set. For the Y-parameters this is the case for the majority of them, with the exception being the stability derivative Y_p and the control derivative Y_{δ_t}. The change in sign for Y_p can be explained by differences for the initial vertical velocity w_0, which is different for each data set. The values for the initial velocities for each data set is shown in Table 9.3.

Initial vertical velocities identification data					
	id data #1	id data #2	id data #3	id data #4	id data #5
$w_0\left(\frac{m}{s}\right)$	-0.30	0.06	-0.12	0.05	-0.17

Table 9.3: Initial vertical velocities w_0 for each of the identification data sets.

From Tables 9.2 and 9.3 the main trend is that if Y_p is the opposite sign of w_0, though this is not the case for data set #5. The difference can also be because every data set has a different amount of excitation during the maneuver. This difference in excitation can also explain the different values for all the parameters. The highest excitation was seen in data set #1, while the lowest excitation was seen in data set #3. Which data set has the most excitation is determined by calculating at the ranges of the states. These ranges are shown in Table 9.4. The higher the ranges of the states, the more excitation during the identification maneuver.

Ranges of states in identification data					
State	id data #1	id data #2	id data #3	id data #4	id data #5
$p\,(rad/s)$	12.06	7.93	7.21	8.97	8.06
$v\,(m/s)$	1.17	0.82	0.58	0.87	0.81
$\phi\,(rad)$	0.89	0.67	0.60	0.73	0.70

Table 9.4: Ranges of the states p, v and ϕ in each of the identification data sets.

The differences in the amount of excitation also had influence on the eigenvalues of the identified models. The eigenvalues are shown in Table 9.5, and they are plotted in a complex plane which is shown in Figure 9.1.

Eigenvalues identified models					
Eigenvalue	id data #1	id data #2	id data #3	id data #4	id data #5
λ_1	-5.18	-6.84	-7.19	-9.85	-7.45
$\lambda_{2,3}$	$0.32 \pm 2.73i$	$0.39 \pm 3.74i$	$0.97 \pm 4.26i$	$1.36 \pm 5.75i$	$0.30 \pm 3.65i$

Table 9.5: Eigenvalues for each identified model.

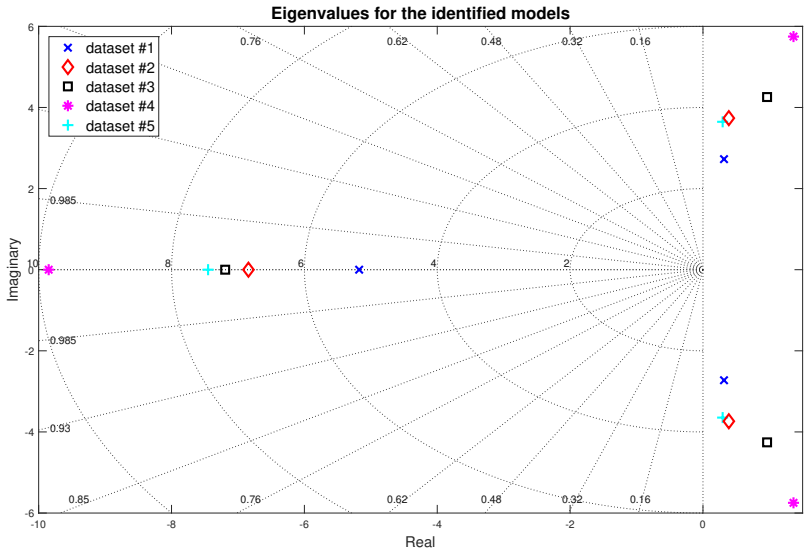

Figure 9.1: Eigenvalues for the estimated grey-box three-state state-space systems for five different data sets.

From Table 9.5 and Figure 9.1 it can be seen that for all the identified models there was a real eigenvalue in the left-half plan and a complex eigenvalue in the right-half plane, meaning that the natural modes of the Delfly Nimble, which have been described in Section 8.4, for each identified model are the same. The overall trend in Figure 9.1 seems to be that the complex eigenvalue has a lower positive real value for a data set which has more excitation. This could indicate that the oscillatory is more stable when the Delfly Nimble is flying sideways, however this needs to be confirmed with additional identification experiments.

9.1.2. Stability Derivatives: Identified vs. Analytic

In this subsection the identified stability derivatives of the Delfly Nimble are compared to the analytic stability derivatives of flapping flight models. In order to compare the stability derivatives to each other, they have been non-dimensionalized, which has been done using Equation 9.2.

$$\begin{aligned} L_p^+ &= \frac{L_p \cdot f}{\rho \cdot U^2 \cdot A_w \cdot \bar{c}}, \quad & Y_p^+ &= \frac{Y_p \cdot f}{\rho \cdot U^2 \cdot A_w} \\ L_v^+ &= \frac{L_v}{\rho \cdot U \cdot A_w \cdot \bar{c}}, \quad & Y_v^+ &= \frac{Y_v}{\rho \cdot U \cdot A_w} \end{aligned} \tag{9.2}$$

Where the flapping frequency f is 17 Hz, the air density ρ is 1.225 $\frac{kg}{m^3}$, the wing area A_w is 1.043×10^{-2} m^2, and the mean chord length c is 7.611×10^{-2} m, and the center of pressure velocity U is defined in Equation 9.3.

$$U = 2 \cdot \phi_f \cdot f \cdot \hat{r} \tag{9.3}$$

Where the flapping angle ϕ_f is 1.536 radians (88°), and the radius of the second moment of inertia of the wing $\hat{r}$ is 7.45×10^{-2} m. The non-dimensionalized stability derivatives of the Delfly Nimble and of the analytic model are shown in Table 9.6.

Stability Derivatives: Delfly Nimble vs. Analytic Models						
Stability Derivative	**Delfly Nimble**	**Zhang [86] (CFD)**	**ASL [34] (tr+rot+add)**	**ASL [34] (tr+rot)**	**ASL [34] (tr)**	**Cheng** [12]
L_p^+	−0.28	−1.2	−1.3	−1.27	−2.29	−1.25
L_v^+	−0.10	0.806	0.97	0.601	−0.434	−0.381
Y_p^+	0.24	−0.104	1.47	1.47	−0.055	0
Y_v^+	−1.13	−0.876	−0.705	−0.705	−0.705	−0.618

Table 9.6: The non-dimensionalized stability derivatives of the Delfly Nimble and the analytic model of flapping flight. 'ASL' indicates the eigenvalues determined by Karásek et al. [34] where 'tr' indicates the wing translational forces, 'rot' indicates the wing rotational forces and 'add' indicates the forces due to the inertia of the added air mass. 'Zhang' the ones determined by Zhang et al. [86] and 'Cheng' the ones by Cheng et al. [12]. All the analytic stability derivatives shown have been determined with the morphological data of the drone fly. The values shown may differ from the values in the work, for some sources used different body axis systems. The ones shown are for the axis system used for the Delfly Nimble, as shown in Figure 3.1.

From Table 9.6 it can be seen that all the values of L_p^+ are and Y_v^+ are negative, while this is not the case for the L_v^+ and Y_p^+. The sign of L_v of the Delfly Nimble was negative in all the data sets used for estimation of the stability derivatives, while positive and negative values have been seen for Y_p. The change in sign of L_v^+ can be due to the different wing configurations, for the Delfly Nimble has a four-wing configuration, while the drone fly only has two wings. There is also a difference in magnitude seen when comparing the stability derivatives of the Delfly Nimble to the analytic stability derivatives. The inequality in magnitude can be a result of the difference in morphological data used to determine the stability, which were those of the drone fly. The analytic stability derivatives which are the most comparable to the stability derivatives of the Delfly Nimble are those of the model of Cheng et al. [12].

9.1.3. Stability Derivatives: Delfly Nimble vs. Delfly II

In this subsection the identified stability derivatives of the Delfly Nimble are compared to the stability derivatives of the Delfly II which were determined in the work of Armanini et al. [5]. In contrast to the previous subsection, the dimensional stability derivatives were used, for both FWMAV's use the same wings and had similar mean flapping frequencies. The stability derivatives of the Delfly Nimble and the Delfly II are shown in Table 9.7.

Stability Derivatives: Delfly Nimble vs. Delfly II				
FWMAV	L_p	L_v	Y_p	Y_v
Delfly Nimble	-2.43×10^{-4}	-3.74×10^{-4}	2.75×10^{-3}	-5.61×10^{-2}
Delfly II	-4.79×10^{-4}	-1.45×10^{-3}	-2.59×10^{-3}	-9.92×10^{-2}

Table 9.7: Identified Stability Derivatives of the Defly Nimble and the Delfly II [5]. The stability derivatives of the Delfly II have different values than indicated in the work of Armanini et al. [5], which is because the Delfly II used a different body axis system. The values shown are for the axis system used for the Delfly Nimble, as shown in Figure 3.1.

From Table 9.7 it can be seen that with the exception of Y_p, all the stability derivatives have the same sign. There is a difference seen in the magnitude of the stability derivatives. Both the L_p and the Y_v are larger for the Delfly II, both of which have a stabilizing effect. This is because of the presence of a tail in the Delfly II, which adds passive stability to the FWMAV. What's more, the initial condition of the identification experiments of the Delfly II was slow forward flight, which also influences the value of the stability derivatives. The influence of the tail was also seen in the eigenvalues of the Delfly II. All of them were in the left-half of the complex plane, while this was not the case for the Delfly Nimble. This indicates that the Delfly II can be characterized as a stable system, which is not the case for the Delfly Nimble.

9.2. Open-loop validation

In this Section the open-loop validation of the state-space model shown in Equation 9.1 is elaborated on. The open-loop validation of the model is done using two maneuvers: the doublet and the 112-maneuver.The open-loop validation using the doublet is discussed in Subsection 9.2.1, while the open-loop validation is discussed in Subsection 9.2.2. During the maneuvers used for the open-loop validation the fast gains of the PD-controller shown in Table 7.1 were used.

9.2.1. Validation Doublet maneuver

The first maneuver used for the validation data was a doublet from a different experiment. The doublet chosen also had a different main frequency compared to the doublets in the doublet train of the identification data. The main frequency of the doublet of the validation data was 6 Hz, while the main frequencies of the doublets in the identification data were 4 Hz and 7 Hz. The state derivatives were determined using the state-space model shown in Equation 9.1. The results of the estimation of the state derivatives of the validation doublet are shown in Figure 9.2.

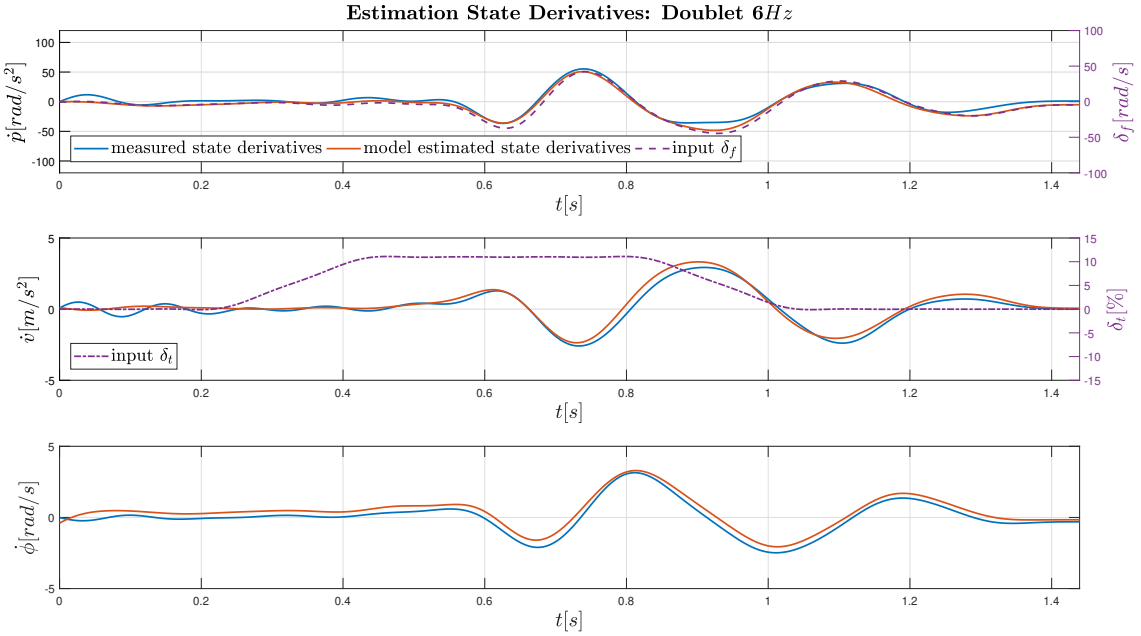

Figure 9.2: Estimation results of the state derivatives for a doublet with a main frequency of 6 Hz. For the estimation the state-space model shown in Equation 9.1 was used.

From Figure 9.2 it can be seen that the state derivatives are estimated well with the state-space model shown in Equation 9.1. The accuracy metrics of the estimation are shown in Table 9.8.

Accuracy Metrics Validation Data: doublet 6Hz				
Output Variable	$\mathbf{r}_{xy}$	$\mathbf{R}^2$	**RMSE**	**RMSE** (% of meas. range)
$\dot{p}$	0.985	0.924	5.51 $\frac{rad}{s^2}$	5.99
$\dot{v}$	0.981	0.948	0.28 $\frac{m}{s^2}$	4.99
$\dot{\phi}$	0.996	0.890	0.38 $\frac{rad}{s^2}$	6.77

Table 9.8: Accuracy metrics of the estimation shown Figure 9.2. The validation data was a doublet with a main frequency of 6 Hz, and the estimation was done using the state-space model shown in Equation 9.1.

The values of the accuracy metrics shown in Table 9.8 are in the same range as the accuracy metrics of the identification data shown in Table 8.5. Next to the doublet with main frequency of 6 Hz, a second maneuver used for the open-loop validation, which is the 112-maneuver. The result are shown in Subsection 9.2.2. The autocorrelation plots of the residuals are shown in Figure 9.3. The autocorrelation plot shown in Figure 9.3 is similar to the autocorrelation plot shown in Figure 8.10, which means that the residuals of the validation data have the same degree of whiteness compared to the residuals of the identification data.

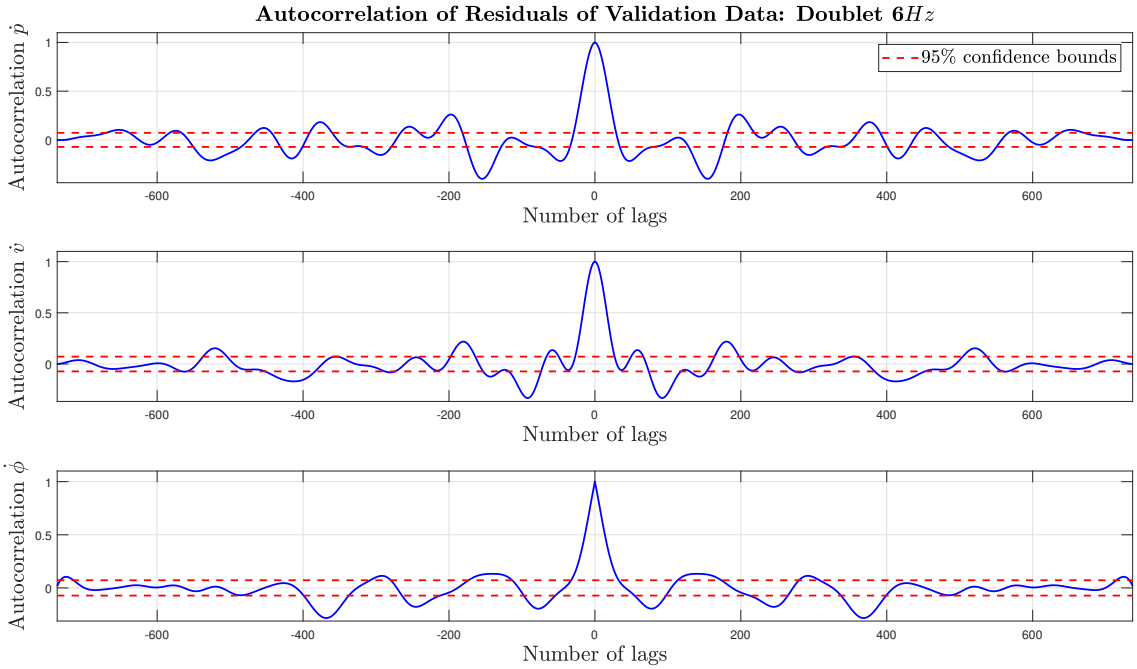

Figure 9.3: Autocorrelation plots for the residuals of the estimation shown Figure 9.2. The validation maneuver was a doublet with a main frequency of 6 Hz, and the estimation was done using the state-space model shown in Equation 9.1.

9.2.2. Validation 112-maneuver

The second maneuver used for the validation of the identified state-space model shown in Equation 9.1 was the 112-maneuver. The main frequencies of the 112-maneuver used for the open-loop validation are 3.5 Hz and 7 Hz. The results of the estimation of the state derivatives of the 112-maneuver are shown in Figure 9.4.

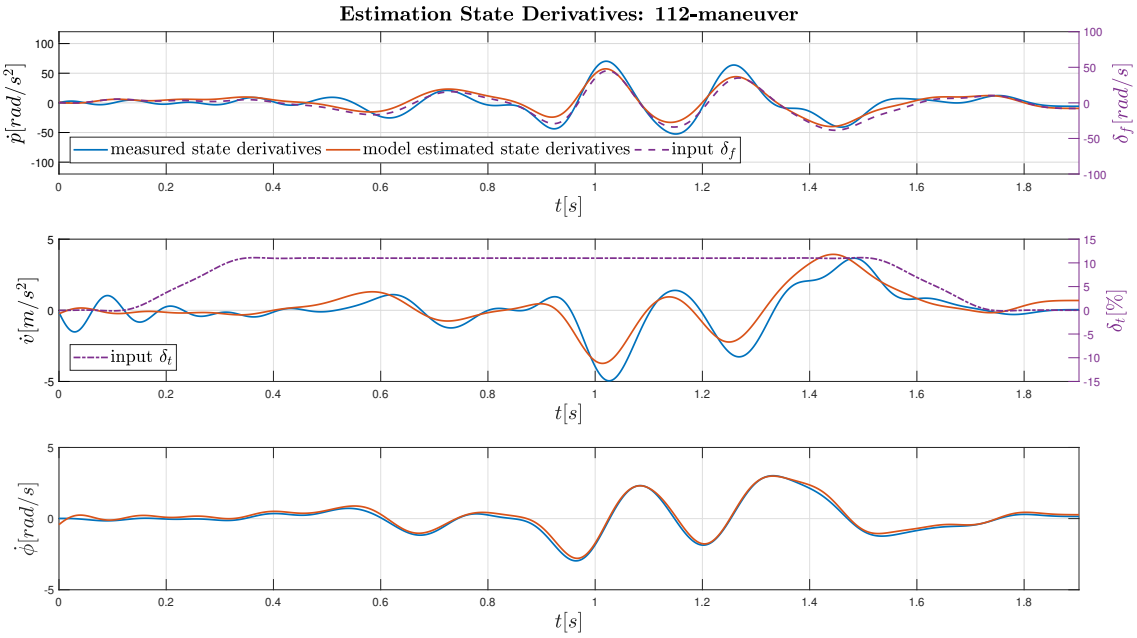

Figure 9.4: Estimation results of the state derivatives for a 112-maneuver with main frequencies of 3.5 Hz and 7 Hz. For the estimation the state-space model shown in Equation 9.1 was used.

From Figure 9.4 it can be seen that the estimation of the state derivatives $\dot{p}$ and $\dot{v}$ are less accurate compared to the estimation of the state derivatives of the doublet. This is also visible in the accuracy metrics, which are shown in Table 9.9.

Accuracy Metrics Validation Data 112-maneuver				
Output Variable	$\mathbf{r}_{xy}$	$\mathbf{R}^2$	**RMSE**	**RMSE** (% of meas. range)
$\dot{p}$	0.918	0.848	8.84 $\frac{rad}{s^2}$	7.20
$\dot{v}$	0.908	0.823	0.63 $\frac{m}{s^2}$	7.27
$\dot{\phi}$	0.998	0.980	0.16 $\frac{rad}{s^2}$	2.66

Table 9.9: Accuracy metrics of the estimation shown Figure 9.4. The validation data was a 112-maneuver with main frequencies of 3.5 Hz and 7 Hz, and the estimation was done using the state-space model shown in Equation 9.1.

Compared to the estimation of the validation doublet, the $\mathbf{R}^2$ is slightly lower, while the $\mathbf{r}_{xy}$ for all state derivatives are in the same range. The residuals of the state derivatives are slightly more coloured for the state derivatives $\dot{p}$ and $\dot{v}$, which can be seen in the autocorrelation plots shown in Figure 9.5.

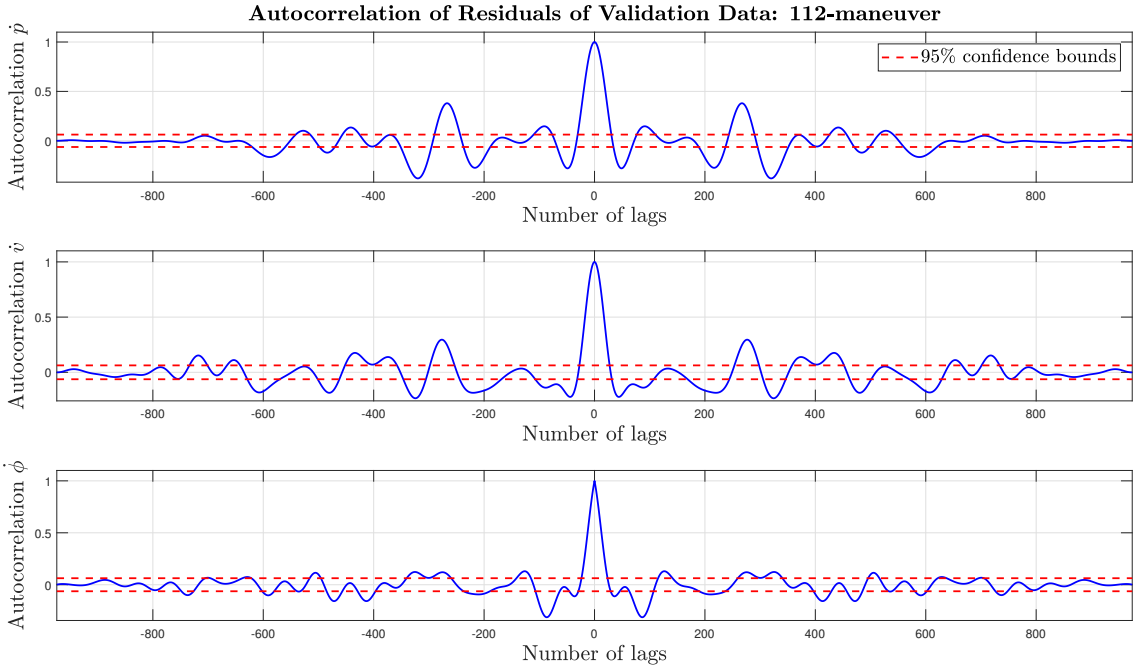

Figure 9.5: Autocorrelation plots for the residuals of the estimation shown Figure 9.4. The validation data was a 112-maneuver with a main frequency of 3.5 Hz and 7 Hz, and the estimation was done using the state-space model shown in Equation 9.1.

9.3. Closed-loop validation

In this section the closed-loop validation of the identified state-space model is shown. For the validation in closed-loop, the state response during a maneuver is simulated using a Simulink model, which uses a one to one copy of the controller architecture. The measured δ_t was used for the simulation. The actuator dynamics of the flapping mechanism is simulated using a slightly modified version of model which was developed in the research of Kajak et al. [32, 33], which is shown in Equation 4.19. The only modification is that the the model is multiplied with a proportional gain of $\frac{1}{1.4}$, which was done to get the simulated input δ_f as close as possible to the actual input, resulting in Equation 9.4.

$$H_{flap}(s) = \frac{8.97}{s + 12.56} \tag{9.4}$$

The state derivatives were simulated using the state-space model shown in Equation 9.1. The closed-loop validation was done using both the fast and slow gains which were shown in Table 7.1. The validation using the fast gains is discussed in subsection 9.3.1, followed by the validation using the slow gains shown in Subsection 9.3.2.

9.3.1. Simulated state response with fast gains

For the closed-loop validation using the fast gains the state response to the doublet train maneuver is determined using the Simulink model. The doublet train consists of two doublets, with main frequencies of 4 Hz and 7 Hz. It should be noted that this is not the same maneuver which was used for the identification of the three state state-space model in Section 8.3.2. The simulation results of the doublet train are shown in 9.6.

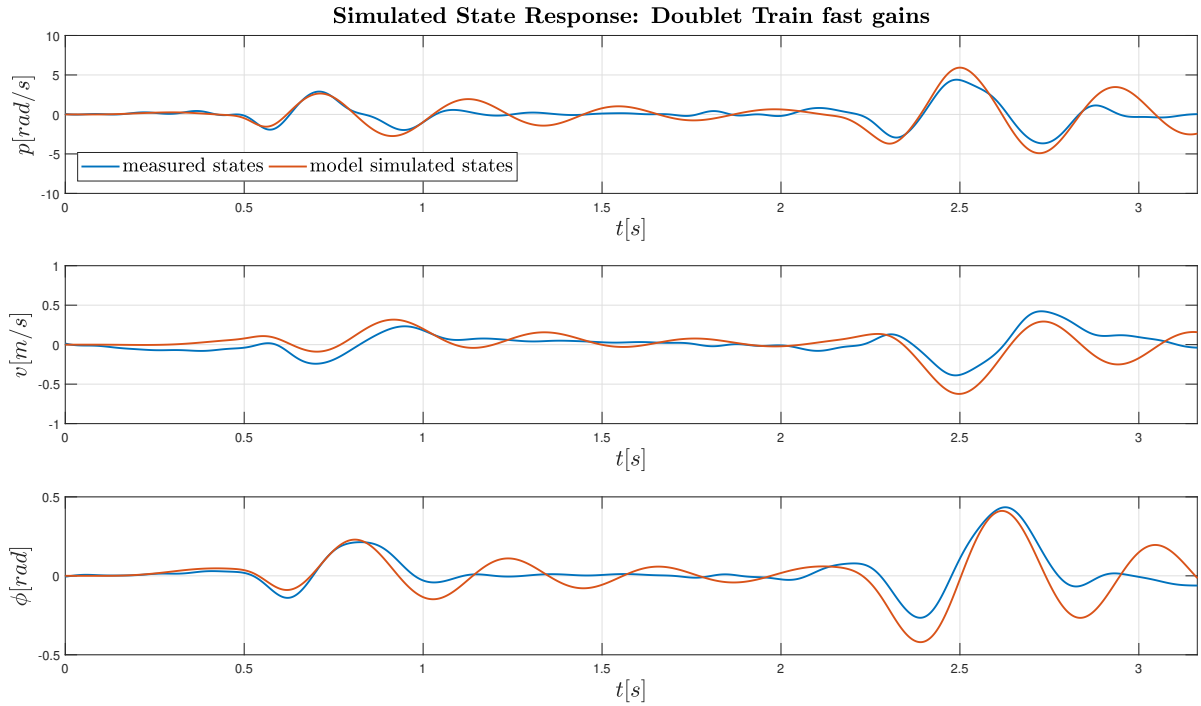

Figure 9.6: Measured and simulated state response of a doublet train. The main frequencies of the doublets were 7Hz and 4 Hz. This simulation was done using the fast gains.

From Figure 9.6 it can be seen that the simulated state response seems more oscillatory compared to the measured state response. The main reason for this difference is that the input δ_f is simulated, which is not one to one to the actual input. The difference is illustrated in Figure 9.7.

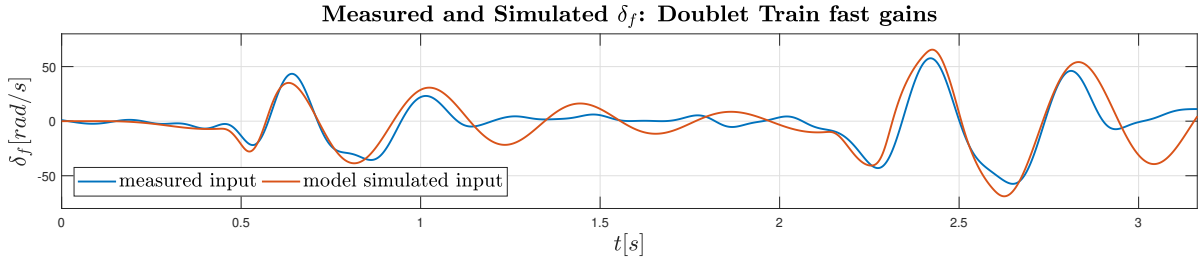

Figure 9.7: Measured and simulated input δ_f for a doublet train maneuver. The main frequencies of the doublets were 7Hz and 4 Hz. This simulation was done using the fast gains.

From Figure 9.7 it can be seen that the simulated input δ_f is more oscillatory than the actual input. Consequently, the simulated state response also becomes more oscillatory than the measured state response. The accuracy metrics of the simulated state response and the the input δ_f are shown in Table 9.10, and the autocorrelation plots of the residuals are shown in Figures G.1 and G.2. It can be seen that the residuals are more coloured compared to the residuals of the identification data, which were shown in Figure 8.10.

Accuracy Metrics CL Validation Data: Doublet Train fast gains				
Output Variable	$\mathbf{r}_{xy}$	$\mathbf{R}^2$	**RMSE**	**RMSE** (% of meas. range)
p	0.868	0.438	1.01 $\frac{rad}{s}$	12.51
v	0.687	0.177	0.13 $\frac{m}{s}$	15.51
ϕ	0.809	0.429	0.09 rad	12.32
δ_f	0.866	0.633	12.59 $\frac{rad}{s}$	10.95

Table 9.10: Accuracy metrics of the simulated state response of a doublet train. The main frequencies of the doublets were 7Hz and 4 Hz. This simulation was done using the fast gains.

9.3.2. Simulated state response with slow gains

For the closed-loop validation using the slow gains of the controller, two maneuvers were used: a doublet train and 112-maneuvers. This doublet train consisted of three doublets, with main frequencies of 6 Hz, 4 Hz and 2 Hz. The main frequencies of the 112-maneuver were 2 Hz and 4 Hz. The main frequencies were chosen to be lower when using the slow gains, in order to acquire more movement of the Delfly Nimble during the experiments. First, the simulation results of the doublet train are elaborated on. The simulation results of the doublet train are shown in Figure 9.8, and the simulated and measured input δ_f is shown in Figure 9.9.

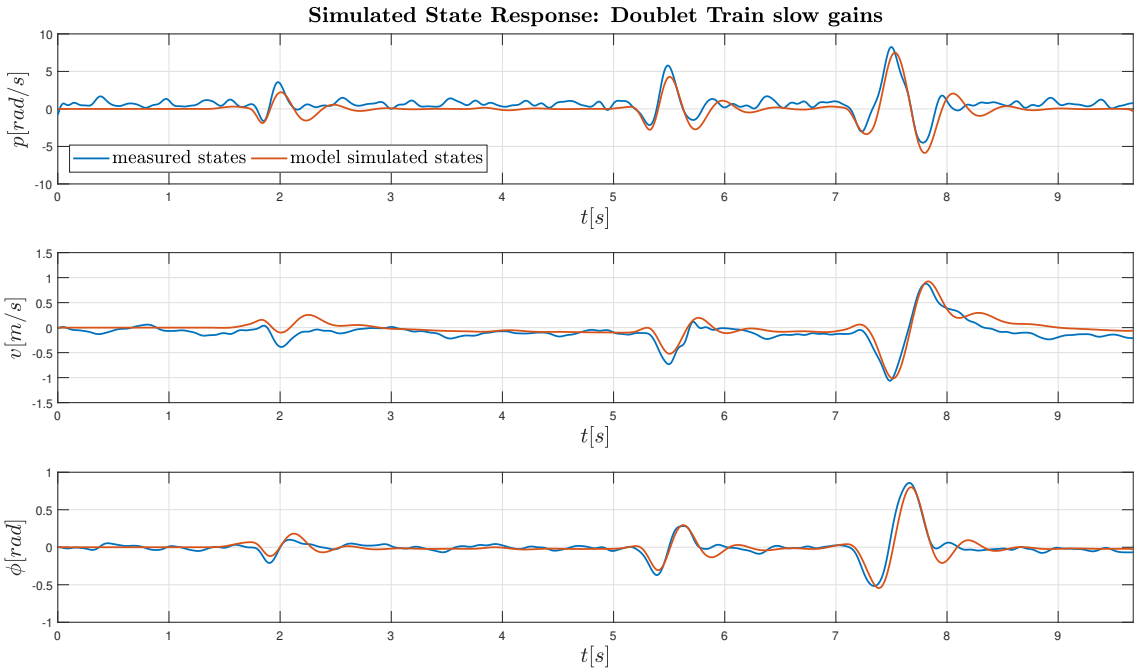

Figure 9.8: Simulated state response of a doublet train with three doublets. The doublets had main frequencies of 6 Hz, 4 Hz and 2 Hz. This simulation was done using the slow gains.

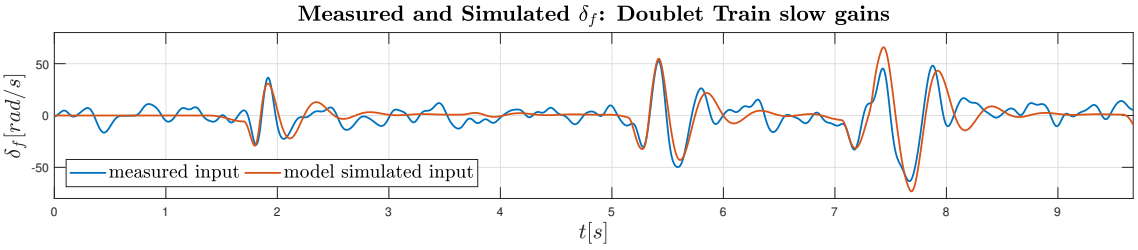

Figure 9.9: Measured and simulated input δ_f of a doublet train with three doublets. The doublets had main frequencies of 6 Hz, 4 Hz and 2 Hz. This simulation was done using the slow gains.

From Figure 9.8 it can be seen that the state response of the doublet train is simulated well with the Simulink model. It can also be seen that the identified model is stable in closed-loop configuration, for the simulated states of the Delfly Nimble return to the hover condition after a doublet maneuver is done. However, when the Delfly Nimble has returned to hover, there are still small oscillations occurring, which are not captured by the identified model. These oscillations can also be seen in the input δ_f during the time in between doublets the doublet train, as shown in Figure 9.9. It can be seen in Figure 9.9 that the simulated input δ_f is less oscillatory when using the slow gains in the simulation. This is also visible in the accuracy metrics of this simulation, which are shown in Table 9.11. The autocorrelation plots of the residuals are shown in Figure G.3 and G.4 in Appendix G. It can be seen that the residuals are more coloured compared to the residuals of the identification data, which were shown in Figure 8.10.

Accuracy Metrics CL Validation Data: Doublet Train slow gains				
Output Variable	$\mathbf{r}_{xy}$	$\mathbf{R}^2$	**RMSE**	**RMSE** (% of meas. range)
p	0.900	0.542	0.92 $\frac{rad}{s}$	7.18
v	0.905	0.657	0.13 $\frac{m}{s}$	6.49
ϕ	0.915	0.837	0.06 rad	4.42
δ_f	0.792	0.575	9.85 $\frac{rad}{s}$	8.50

Table 9.11: Accuracy metrics of the simulated state response of a doublet train with three doublets. The doublets had main frequencies of 6 Hz, 4 Hz and 2 Hz. This simulation was done using the slow gains.

Next to the doublet train maneuver, the closed-loop validation using the slow gains was also done with 112-maneuvers, which had main frequencies of 2 Hz and 4 Hz. The simulation results of the states are shown in Figure 9.10, and the simulation results of δ_f are shown in Figure 9.11. In the simulated stated response of the 112-maneuvers shown in Figure 9.10 it can be seen that there is a reduction of the model accuracy of v, while the accuracy of the states p and ϕ remains similar compared to the accuracy of the simulated state response of the doublet trains shown in Figure 9.8. This is also visible in the accuracy metrics shown in Table 9.12. In Figure 9.11 it can be seen that the simulated input δ_f is also less oscillatory when using the slow gains. The autocorrelation plots of the residuals are shown in Figure G.5 and G.6. It can be seen that the residuals are slightly more coloured compared to the residuals of the doublet train which used slow gains.

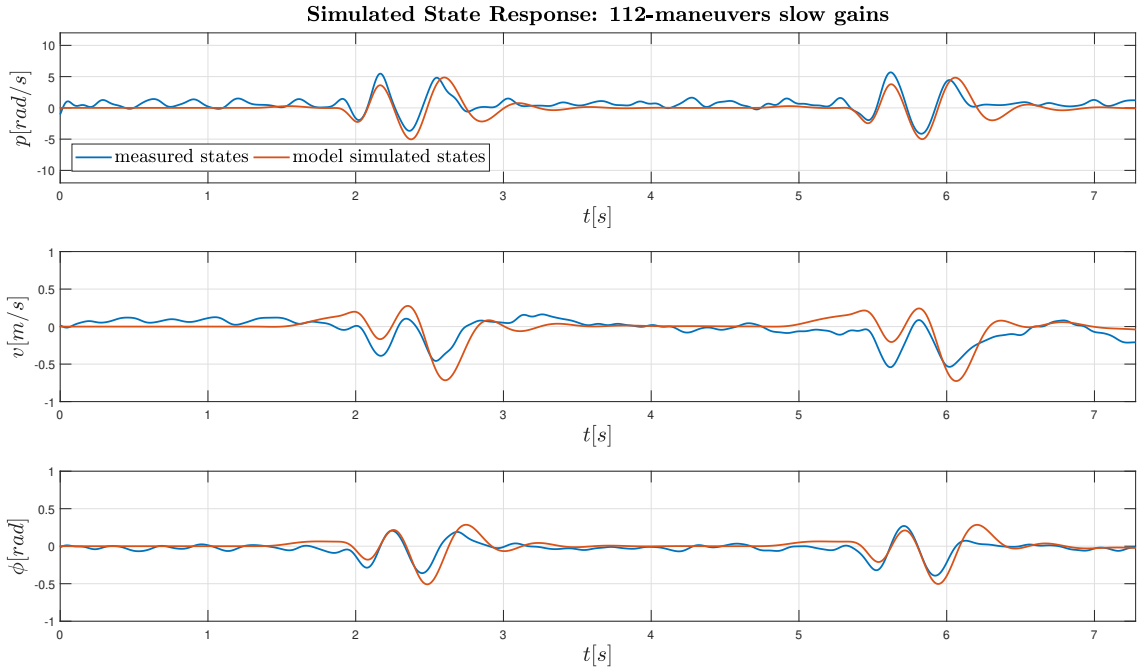

Figure 9.10: Simulated state response of multiple 112-maneuvers. The main frequencies of these maneuvers were 2 Hz and 4 Hz. This simulation was done using the slow gains.

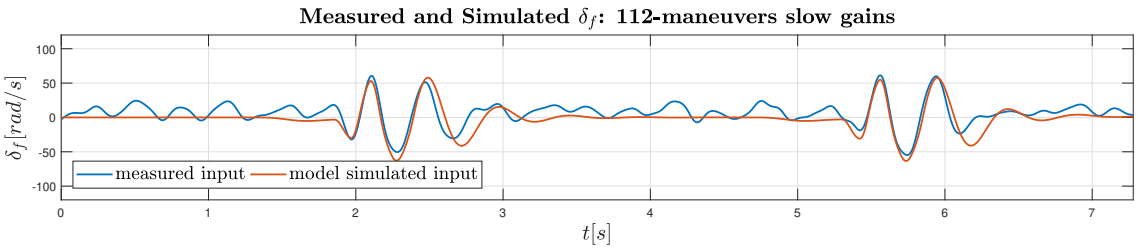

Figure 9.11: Measured and simulated input δ_f of multiple 112-maneuvers. The main frequencies of these maneuvers were 2 Hz and 4 Hz. This simulation was done using the CL-gains.

Similar to what was seen in the simulated state response of the doublet train in Figure 9.8, there are oscillations visible in during the time in between the 112-maneuvers, when the Delfly Nimble is hovering, in both the states and the input δ_f. This could be also due to time varying dynamics which are not captured with the current identified model. The simulations for both the doublet and the 112-maneuvers are stable, for during the time between doublets or 112-maneuvers the Defly Nimble returns to the hover position. Based on these results it can be concluded that the identified model can be used in a closed-loop configuration, making it applicable for the stability analysis of the body dynamics, and for controller design.

Accuracy Metrics CL Validation Data: 112-maneuvers slow gains				
Output Variable	$\mathbf{r}_{xy}$	$\mathbf{R}^2$	**RMSE**	**RMSE** (% of meas. range)
p	0.865	0.467	0.99 $\frac{rad}{s}$	10.13
v	0.650	0.171	0.14 $\frac{m}{s}$	19.46
ϕ	0.815	0.387	0.08 rad	11.45
δ_f	0.856	0.492	12.77 $\frac{rad}{s}$	11.00

Table 9.12: Accuracy metrics of the simulated state response of multiple 112-maneuvers. The main frequencies of these maneuvers were 2 Hz and 4 Hz. This simulation was done using the slow gains.

9.4. Model accuracy coupled maneuvers

In this section Question **SQ3b** is answered. This question is answered by analyzing how well the state-space model shown in Equation 9.1 can predict the state derivatives for a coupled doublet. The main frequency for this maneuver was set to 6 Hz, the roll deflection to 30°, and the pitch angle deflection was set to 20°. During these maneuvers the fast gains were used. The estimation results for the state derivatives are shown in Figure 9.12, and the accuracy metrics of this estimation are shown in Table 9.13. From Figure 9.12 and Table 9.13 it can be seen that the estimation accuracy of $\dot{v}$ has decreased significantly. From the autocorrelation plots of the residuals shown in Figure G.7, it can be seen that the residuals are more coloured compared to the residuals of the identification data shown in Figure 8.10. Initially, it was thought that the absence of the input δ_d was the main cause of the reduced model accuracy of $\dot{v}$. To verify this, the state derivatives were determined using an identified state-space model which would include the inputs δ_f, δ_d, and δ_t. However, the resulting identified model had very different eigenvalues. This may be due to coupling effects when all three inputs are included in the model identification process, but this was not further investigated in this research. Instead, two different combinations of inputs were used in the state-space model.

Accuracy Metrics Validation Data Coupled Doublet				
Output Variable	$\mathbf{r}_{xy}$	$\mathbf{R}^2$	**RMSE**	**RMSE** (% of meas. range)
$\dot{p}$	0.927	0.845	9.27 $\frac{rad}{s^2}$	7.27
$\dot{v}$	0.699	0.523	1.23 $\frac{m}{s^2}$	11.17
$\dot{\phi}$	0.964	0.923	0.34 $\frac{rad}{s}$	4.54

Table 9.13: Accuracy metrics of the estimation shown Figure 9.12. The validation data was a coupled doublet with a main frequency of 6 Hz, and the estimation was done using the state-space model shown in Equation 9.1.

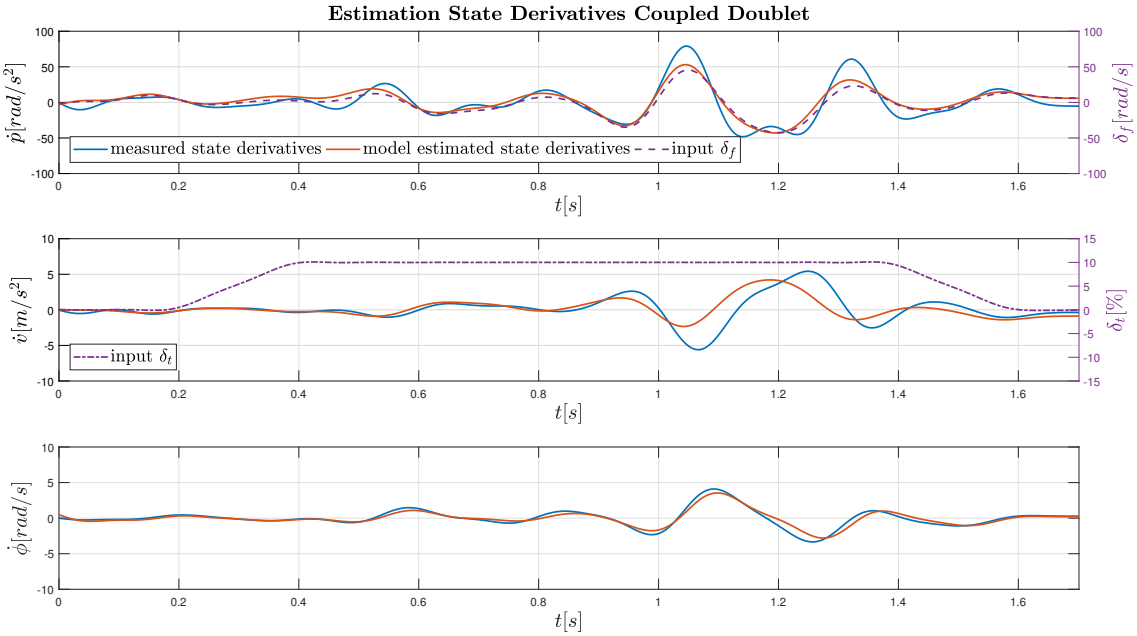

Figure 9.12: Estimation results of the state derivatives for a coupled doublet with a main frequency of 6 Hz. For the estimation the state-space model shown in Equation 9.1 was used.

In the first combination, only the input δ_f was included. The parameters and the numeric state-space system of this model are shown in Appendix E.2. The estimation results for the state derivatives when using these models are shown in 9.13, and the accuracy metrics are shown in Table 9.14. The estimation results in Figure 9.13 and the accuracy metrics in Table 9.14 are very similar to those shown in Figure 9.12 and Table 9.13. This indicates that the model accuracy does not change much when the input δ_t is omitted. The autocorrelation plots of the residuals, shown in Figure G.8, also do not change significantly when only using the input δ_f, as can be confirmed by comparing Figures G.7 and G.8.

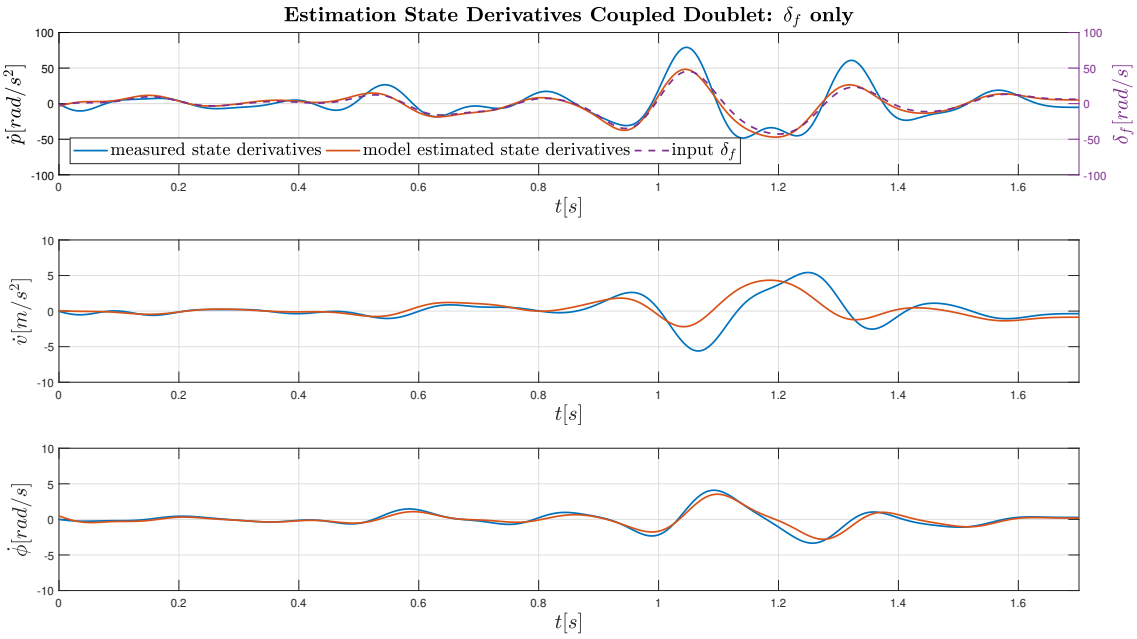

Figure 9.13: Estimation results of the state derivatives for a coupled doublet with a main frequency of 6 Hz. For the estimation the state-space model shown in Equation 9.1 was used.

Accuracy Metrics Validation Data Coupled Doublet: δ_f only				
Output Variable	$\mathbf{r}_{xy}$	$\mathbf{R}^2$	**RMSE**	**RMSE** (% of meas. range)
$\dot{p}$	0.912	0.832	9.62 $\frac{rad}{s^2}$	7.55
$\dot{v}$	0.695	0.509	1.25 $\frac{m}{s^2}$	11.33
$\dot{\phi}$	0.964	0.923	0.34 $\frac{rad}{s}$	4.54

Table 9.14: Accuracy metrics of the estimation shown Figure 9.13. The validation data was a coupled doublet with a main frequency of 6 Hz, and the estimation was done using a modified version the state-space model shown in Equation 9.1, where only the input δ_f was included in the estimation.

In the second combination of inputs the δ_f and δ_d are included in the state-space model. The parameters and the numeric state-space system of this model are shown in Section E.3. The estimation results for state derivatives using a model with this input combination is shown in Figure 9.14, and the accuracy metrics of this estimation are shown in Table 9.15. As can be seen form Figure 9.14 and Table 9.15 the estimation of $\dot{v}$ does not improve when the input δ_d is added to the model. The autocorrelation plots of the residuals, shown in Figure G.9 also does not change significantly. This would suggest that the estimation accuracy is not greatly affected by the coupled input.

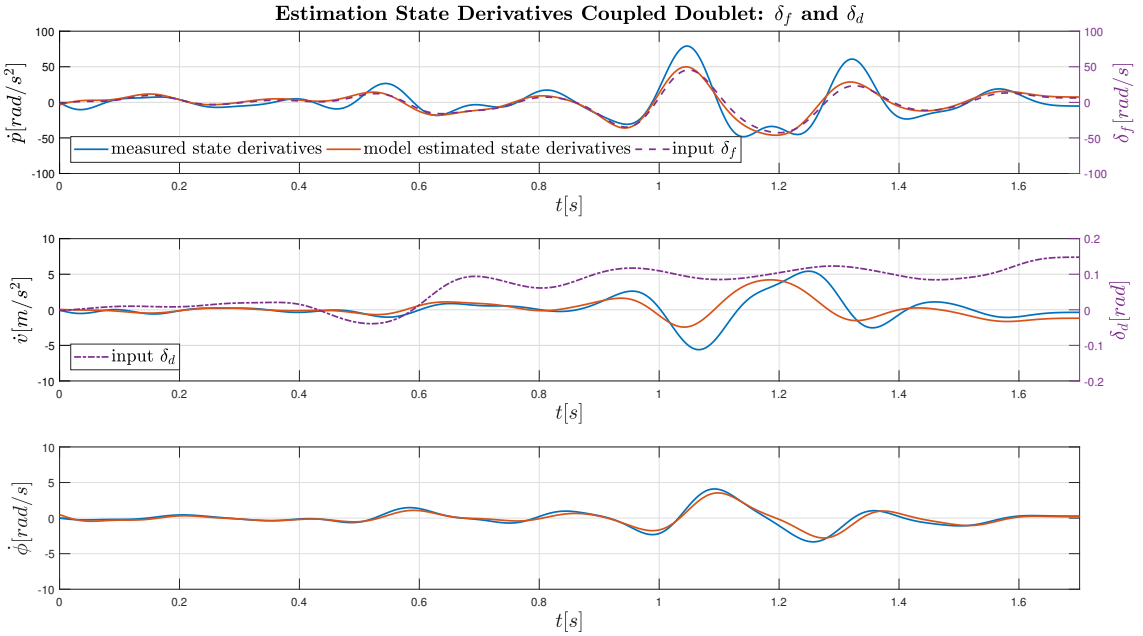

Figure 9.14: Estimation results of the state derivatives for a coupled doublet with a main frequency of 6 Hz. For the estimation the state-space model shown in Equation 9.1 was used.

Accuracy Metrics Validation Data Coupled Doublet: δ_f and δ_d				
Output Variable	$\mathbf{r}_{xy}$	$\mathbf{R}^2$	**RMSE**	**RMSE** (% of meas. range)
$\dot{p}$	0.915	0.840	9.41 $\frac{rad}{s^2}$	7.39
$\dot{v}$	0.689	0.506	1.25 $\frac{m}{s^2}$	11.36
$\dot{\phi}$	0.964	0.923	0.34 $\frac{rad}{s}$	4.54

Table 9.15: Accuracy metrics of the estimation shown Figure 9.14. The validation data was a coupled doublet with a main frequency of 6 Hz, and the estimation was done using a modified version the state-space model shown in Equation 9.1, where only the inputs δ_f and δ_d were included in the estimation.

What could be the cause of the reduced accuracy of $\dot{v}$ is the forward motion during the coupled doublet maneuver. The maximum value of the longitudinal velocity u was 1.22 $\frac{m}{s}$, while the maximum u in the identi-

fication maneuver was 0.40 $\frac{m}{s}$. The reduced accuracy may therefore not only be due to the coupled inputs, but also because the Delfly Nimble is moving away a lot from the initial condition of the identification maneuver. The influence of forward flight on the lateral dynamics has been researched by Xu et al. [82]. In this research, the lateral dynamics of a bumblebee were analyzed by determining the stability derivatives with different forward flight velocities. From the results it could be seen that the unstable mode, which for the bumblebee was aperiodic, became more stable as the forward flight velocity increases. The main cause of this is the influence of lateral inflow on the leading edge vortex (LEV). For insects, it has been shown that such a vortex is present on the leading edge of their wings [18]. When there is lateral inflow from the wingroot to the wingtip, the LEV is intensified and the amount of lift generated increases. In the opposite case, when the lateral inflow goes from the tip to the root, the LEV is less concentrated and the amount of lift generated decreases [24, 71]. This leads to a difference in lift generated between the wings, causing instability. In forward flight, the mean position of the wings is more backwards, due to which there is less lateral inflow moving along the leading edge. Consequently, there is less effect on the LEV, thus little effect on the lift generation. Then, the difference in generated lift between the wings is smaller, leading to a more stable motion in forward flight. A similar influence can be the cause for the reduced accuracy of the coupled doublet maneuver of the Delfly Nimble. Whether the Delfly Nimble is more stable in forward flight has not been investigated in this research.

9.5. Model accuracy nonlinear maneuvers

In this section Question **SQ3c** is answered, i.e. whether the linearity of the aerodynamic forces is a justifiable assumption. This question is answered by analyzing the model accuracy when a nonlinear doublet is used. This maneuver is nonlinear in the sense that it moves away very far away from the initial condition. During these maneuvers the fast gains were used. The estimation results of the state derivatives for a nonlinear doublet with a main frequency of 4 Hz, a constant roll angle of 30° and a roll deflection of 15° for the doublet maneuver is shown in Figure 9.15, and the accuracy metrics of the nonlinear doublet are shown in Table 9.16.

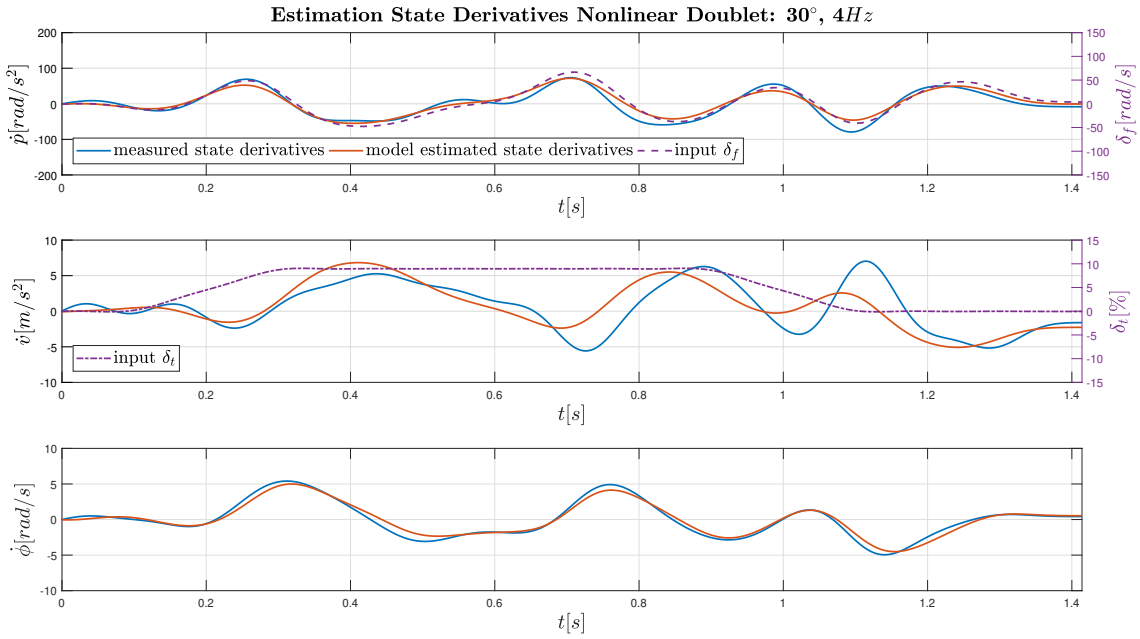

Figure 9.15: Estimation results of the state derivatives for a nonlinear doublet with a main frequency of 4 Hz, constant roll angle of 30° and a roll deflection of 15°. For the estimation the state-space model shown in Equation 9.1 was used.

From Figure 9.15 it can be seen that the estimation for $\dot{v}$ is less accurate compared to the accuracy of $\dot{v}$ in the validation doublet and the 112-maneuver. This is also visible in the accuracy metrics of the estimation shown in Table 9.16. The metrics for $\dot{p}$ and $\dot{\phi}$ are in the same range as accuracy metrics for the validation doublet and 112-maneuver shown in Section 9.2, and the residuals are also more coloured, as can be seen from the autocorrelation plots shown in Figure G.10. The main reason for the reduced estimation accuracy is that the Delfly Nimble is moving away a lot from the initial condition for the identification, which was hover. The maximum lateral velocity v reached in this nonlinear doublet maneuver was 1.60 $\frac{m}{s}$, while in the

identification data used to identify the state-space model shown in Equation 9.1 the maximum v was $1.00\frac{m}{s}$.

Accuracy Metrics Validation Data Nonlinear Doublet: 30°, 4 Hz				
Output Variable	$\mathbf{r}_{xy}$	$\mathbf{R}^2$	**RMSE**	**RMSE** (% of meas. range)
$\dot{p}$	0.952	0.900	12.08 $\frac{rad}{s^2}$	7.91
$\dot{v}$	0.783	0.618	2.04 $\frac{m}{s^2}$	16.16
$\dot{\phi}$	0.985	0.965	0.46 $\frac{rad}{s}$	4.45

Table 9.16: Accuracy metrics of the estimation shown Figure 9.15. The validation data was a nonlinear doublet with a main frequency of 4 Hz, a constant roll angle of 30° and a roll deflection of 15°. The estimation of the state derivatives was done using the state-space model shown in Equation 9.1.

The estimation of the state derivatives increases when a lower constant roll angle is used. This has been confirmed by analyzing a second nonlinear doublet maneuver. This nonlinear doublet had a main frequency of 4 Hz, a constant roll angle of 20°, and roll deflection of 15°. The estimation results are shown in Figure 9.16, and the accuracy metrics are shown in Table 9.17.

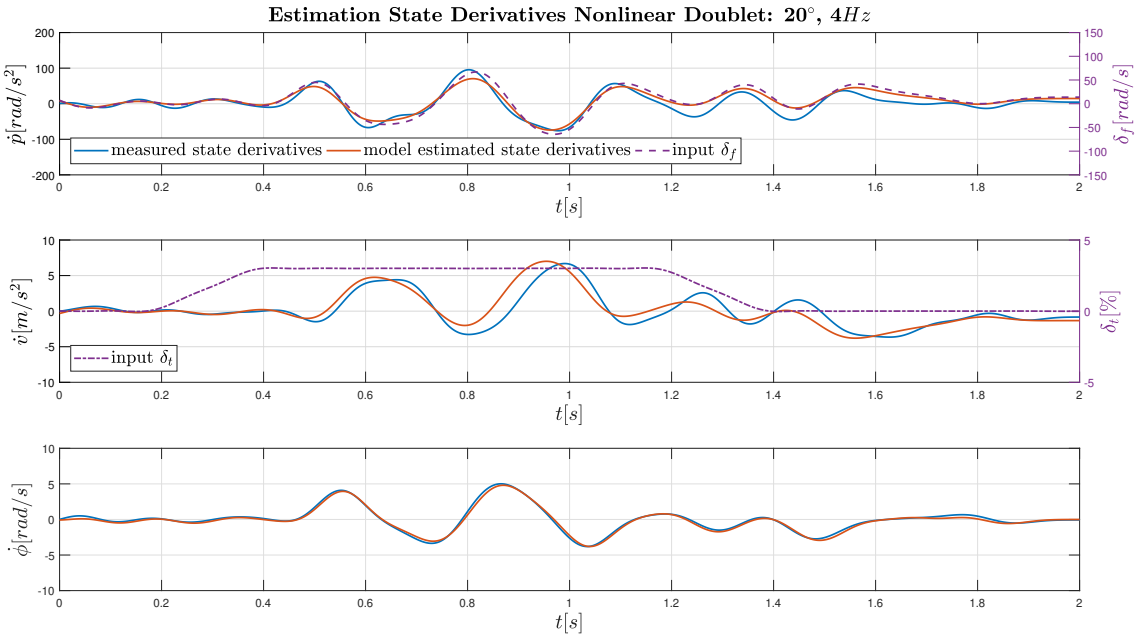

Figure 9.16: Estimation results of the state derivatives for a nonlinear doublet with a main frequency of 4 Hz, constant roll angle of 20° and a roll deflection of 15°. For the estimation the state-space model shown in Equation 9.1 was used.

Accuracy Metrics Validation Data Nonlinear Doublet: 20°, 4 Hz				
Output Variable	$\mathbf{r}_{xy}$	$\mathbf{R}^2$	**RMSE**	**RMSE** (% of meas. range)
$\dot{p}$	0.927	0.824	13.75 $\frac{rad}{s^2}$	8.02
$\dot{v}$	0.892	0.791	1.05 $\frac{m}{s^2}$	10.18
$\dot{\phi}$	0.994	0.985	0.21 $\frac{rad}{s}$	2.40

Table 9.17: Accuracy metrics of the estimation shown Figure 9.16. The validation data was a nonlinear doublet with a main frequency of 4 Hz, a constant roll angle of 30° and a roll deflection of 15°. The estimation of the state derivatives was done using the state-space model shown in Equation 9.1.

From Figure 9.16 it can be seen that the estimation of $\dot{v}$ improves with a lower constant roll angle. This is also visible in the accuracy metrics shown in Table 9.17, and also in the autocorrelation plots of the residuals,

which are shown in Figure G.11, where it can be seen that the residuals are less coloured then the residuals of the nonlinear doublet with a higher constant roll angle. The main reason for the improved estimation results is that the maximum lateral velocity v in this nonlinear doublet was $1.43\frac{m}{s}$, which is lower than the maximum v in the first nonlinear doublet. This indicates that the mathematical model is less accurate when a higher v is reached during the maneuver. This is in line with expectation, for when a higher v is reached during the maneuver, the Delfly moves away further from the initial condition of the identification data, which is the hover condition. The lower model accuracy can be due to the influence of lateral inflow, which can increase or decrease the lift generation due to the influence of the inflow on the LEV [18, 24, 82], as was described earlier in the validation results of the coupled maneuvers in Section 9.4.

10

Conclusion and recommendations

Flapping Wing Micro Air Vehicles (FWMAV) are a subcategory of Unmanned Air Vehicles which have favorable properties, such as being able to fly at low velocity, having high agility and maneuverability, and some of them are even capable to maintain hovering flight. A tailless FWMAV has been developed at the Delft University of Technology, the Delfly Nimble, a tailless member of the Delfly Family, a group of flapping robots. The Delfly Nimble requires an active controller to remain airborne. It controls the pitch attitude by changing the dihedral angle, the roll attitude by creating a difference in flapping frequency between both wings and the yaw attitude by changing the wing root angle. Mathematical models have been identified for the Delfly II, a tailed predecessor of the Delfly Nimble, while only models for the longitudinal dynamics of the Delfly Nimble have been identified.

The main goal of this thesis is to address the absence of a model for the lateral dynamics of the Delfly Nimble. Such a model could be used for stability analysis, the design of control systems, as well as to increase the knowledge about the lateral dynamics of the FWMAV. The mathematical model has been developed using the System Identification approach, which consists of three phases: the experiment phase, the model identification phase and the model validation phase. Identifying a mathematical model using this approach is an iterative process, for when it turns out that the model is not sufficiently accurate in the model validation phase, changes will have to be applied in either the experiment phase or the model identification phase. Based on the aim of this research and the system identification approach the following research objective has been formulated:*The research objective is to identify a mathematical model for the lateral body dynamics of the Delfly Nimble* ***by*** *using the System Identification Procedure for the development of a linear grey-box state-space model.*

One central question has been formulated in order to reach this objective: "Can the full envelope of the lateral body dynamics of the Delfly Nimble be modeled using a linear time-invariant state-space model, and what is the influence of the dynamic coupling and the non-linearities on the predictive power of this model?". This main question has been answered by identifying a mathematical model using the Systems Identification approach. Three subquestions were formulated to aid in answering the main central question, each covering a phase in the System Identification Cycle.

In the experiment phase measurement data was gathered by the use of various automated maneuvers. The flight experiments needed to be conducted in closed-loop, for the Delfly Nimble is inherently unstable due to its tailless design. For the system identification of this closed-loop system the direct approach was taken, where the controller is ignored in the model identification. One of the main difficulties encountered when using the direct approach is that the controller can dampen the natural response, reducing the information contained in the measurement data, leading to less accurate models. In order to cope with this, the gains of the controller were altered such that the influence of the controller was minimized, and large commands were given during the identification experiments. With these two measurements sufficient excitation was obtained. The identifiability was checked by analysis of the power spectral density plots of the measured states, which showed peaks around the expected frequencies. There were four categories of maneuvers used during the experiments: identification maneuvers, for which a train of doublets was used with hover as the initial condition, validation maneuvers, for which doublets and a 112-maneuver were used with hover as the

initial condition using both the adjusted and the original gains of the PD-controller, coupled maneuvers, for which a coupled doublet was used using the adjusted gains, and nonlinear maneuvers, for which the nonlinear doublets were used using the adjusted gains. During the coupled doublet the Delfly Nimble moves forward, and then does a doublet in the roll direction. When doing the nonlinear doublet, the Delfly is does a roll doublet while it is flying sideways. This maneuver is nonlinear in the sense that the Delfly Nimble moves away greatly from the hover condition. There were two sources of data used: the OptiTrack Motion tracking system and on-board measurements, which consisted of data logged on an inertial measurement unit and readings of the control mechanisms.

In the model identification phase, the first step is the state estimation, which in this research was done by use of an Extended Kalman Filter. The second step is the defining the model structure. Two types of model structures were used in this research, grey-box and black-box systems. For the development of the grey-box system the rigid-body approximation was used. Due to the focus on only the body dynamics, this approximation can be used, as has been done in previous research for the stability analysis of hovering insects and the modeling of flapping flight. The resulting equations of the aerodynamic forces, the aerodynamics moments, and the kinematic equations are nonlinear, and linearized using two techniques, the Taylor series expansion and the small perturbation theorem. This resulted in linear time-invariant state-space system with four states. Also, a reduced state-space system was used, omitting the yaw dynamics, which meant that this system only had three states. The black-box system was developed by using every element of the A and B matrices of the state-space, also using one system with four states and one with three states. This means that in total there were four different model structures used, a grey-box state-space system with four states, a a grey-box state-space system with three states, a black-box state-space system with four states, and a black-box state-space system with three states. The third step is the parameter estimation. The parameters of the grey-box models are the stability and control derivatives, while for the black-box model the parameters are all the elements of A and B matrix of the state-space system. The parameters were determined using the weighted least-squares approach. The final model structure chosen was the grey-box state-space system with three states. The yaw dynamics were omitted due to high frequency components in the measurement data, which was likely due to internal vibrations, and because of the little information contained in the measurement data. Two natural modes of the Delfly Nimble were identified using this three-state state-space model, a stable aperiodic mode and an unstable oscillatory mode.

In the model validation phase the accuracy of the identified model is analyzed. The identified state-space model was able to predict the state derivatives of the Delfly Nimble well for doublets and 112-maneuvers, having low values for the residuals and high values for the goodness of fit and the output correlation. The accuracy of the predicted state derivatives was over 90%. The identified model was also used in a closed-loop configuration using a Simulink model was used, in which a one to one copy of the PD-controller was implemented. The simulated states were close to the actual states and the simulation was stable, indicating that the developed model can be used in a closed-loop configuration. The accuracy of simulated state response exceeded 85%. However, there was oscillatory motion visible in the states when the Delfly Nimble was hovering which were not captured by he identified model. This could be due to time-varying dynamics, which were not considered in this research. The developed model can be used in a closed-loop configuration for the stability analysis of the body dynamics, which are time-averaged, and for the controller design. The justifiability of two assumptions which were used for the development of the state-space model: the longitudinal and lateral dynamics are decoupled, and that the body dynamics can be modeled using a linear model structure. The justifiability of the former was analyzed by conducting experiments using coupled maneuvers. The maneuver used in these experiments was the coupled doublet, where inputs are given to the roll control mechanism as well as the pitch control mechanism. The Delfly Nimble is then doing a roll doublet while flying forward. The justifiability of the latter was analyzed by conducting nonlinear maneuvers. The maneuver used in these experiments is the nonlinear doublet, where the Delfly Nimble is doing a roll doublet when flying sideways. This maneuver is nonlinear in the sense that the Delfly Nimble moves away greatly from the initial condition of the identification maneuvers, which was the Delfly Nimble hovering. The model accuracy for the coupled maneuver decreased the most for the lateral body acceleration $\dot{v}$, mainly due to the incoming airflow from the front, rather than the inputs of multiple control mechanism. This suggests that the assumption of uncoupled dynamics can be made. The model accuracy for the nonlinear maneuver also reduced the most for $\dot{v}$, now due to the incoming airflow from the side. It was shown that for lower sideways velocities the model accuracy significantly improved. This indicates that the linearity assumption is not a valid one.

There are still improvements possible for the development of a mathematical model of the lateral body dy-

namics of the Delfly Nimble, and thus recommendations are given for future research. The first recommendation is to give direct inputs to the control surfaces during the identification experiments. This can be done by giving a disturbance input to the roll control mechanism. The advantage of doing this is that the influence of the controller is then further minimized, leading to more excitation of the lateral body dynamics. The more excitation during the identification experiment, the more information is contained in the data, which leads to better identified models. The second recommendation is to use a different parameter estimation approach. This is mainly due to the high noise sensitivity of the stability derivatives L_p, L_v, and the control derivative L_{δ_t}. The parameter estimation approach which could be used to reduce the noise sensitivity is the maximum likelihood estimator. This estimation approach was also tried in this research, but due to the unstable nature of the identified state-space model the maximum likelihood estimator did not converge. When the maximum likelihood estimator is used, the controller must be included. The third recommendation is therefore is to use a different approach for the system identification of the closed-loop system, such as the indirect approach and the joint input-output approach. Using either one of these may help to ensure convergence of the maximum likelihood estimator. The fourth recommendation is to use foam between the IMU and the mounting point to the fuselage. In this research the IMU was mounted directly to the fuselage, which led to a lot of noise in the IMU data. This was especially the case for the yaw rate data, which had a very high frequency content around the 11 Hz. This peak was most likely due to internal vibration. Next to the issue of the high frequency components in the yaw rate data, there was also very little excitation seen in the PSD plot of the yaw rate. This was the main reason for the bad estimation of the yaw dynamics. The recommendation would then be to also use yaw inputs to increase the excitation of the yaw dynamics, improving the model identification of these dynamics. The fifth recommendation it to include the time-varying dynamics in the model, for it was seen that oscillations which occur during hover are not captured when using the identified model in closed-loop configuration. This can be done by modeling each wing of the Delfly Nimble as a separate body, which leads to a multi-body dynamic system with five bodies, or to model the time-varying components using a Fourier series. The last recommendation is to use a nonlinear model structure in order to expand the range of the identified model. The lateral body dynamics are very sensitive to incoming airflow. The range can be expanded using for example the linear parameter-varying model structure, similar to what was done for the model identification of the Delfly II, during which experiments were done with multiple trim conditions. For experiments with the Delfly Nimble, the Cyberzoo is too small to trim the Delfly Nimble properly when there is an initial velocity. For proper trimming, a larger area is required, or experiments have to be conducted in a wind tunnel.

Bibliography

[1] J.V. Aguiar Vieira Caetano. *Model identification of a flapping wing micro aerial vehicle*. PhD thesis, 2016. URL https://repository.tudelft.nl/islandora/object/uuid%3A5311a47f-267e-46b3-9131-5228e22fef8b?collection=research.

[2] R Wade Allen and Henry R Jex. An experimental investigation of compensatory and pursuit tracking displays with rate and acceleration control dynamics and a disturbance input. 1968.

[3] S. F. Armanini, C. C. de Visser, G. C. H. E. de Croon, and M. Mulder. Time-Varying Model Identification of Flapping-Wing Vehicle Dynamics Using Flight Data. *Journal of Guidance, Control, and Dynamics*, 39(3): 526–541, 2016. ISSN 0731-5090. doi: 10.2514/1.G001470. URL http://arc.aiaa.org/doi/10.2514/1.G001470.

[4] S. F. Armanini, M. Karasek, G. C.H.E. De Croon, and C. C. De Visser. Onboard/offboard sensor fusion for high-fidelity flapping-wing robot flight data. *Journal of Guidance, Control, and Dynamics*, 40(8): 2116–2127, 2017. ISSN 07315090. doi: 10.2514/1.G002527.

[5] S.F. Armanini. *Identification of time-varying models for flapping-wing micro aerial vehicles*. PhD thesis, 2018. URL https://repository.tudelft.nl/islandora/object/uuid%3A37be4591-3e02-4ad3-b800-30bf41a85f1c?collection=research.

[6] Sophie F. Armanini, Coen C. de Visser, and Guido de Croon. Black-box LTI modelling of flapping-wing micro aerial vehicle dynamics. *AIAA Atmospheric Flight Mechanics Conference*, (January), 2015. doi: 10.2514/6.2015-0234. URL http://arc.aiaa.org/doi/10.2514/6.2015-0234.

[7] Bassam Bamieh and Laura Giarré. Identification of linear parameter varying models. *International Journal of Robust and Nonlinear Control*, 12(9):841–853, 7 2002. ISSN 10498923. doi: 10.1002/rnc.706. URL http://doi.wiley.com/10.1002/rnc.706.

[8] Murat Bronz, Jean Marc Moschetta, Pascal Brisset, and Michel Gorraz. Towards a Long Endurance MAV. *International Journal of Micro Air Vehicles*, 1(4):241–254, 12 2009. ISSN 1756-8293. doi: 10.1260/175682909790291483.

[9] J. V. Caetano, M. Percin, B. W. Van Oudheusden, B. Remes, C. De Wagter, G. C.H.E. De Croon, and C. C. De Visser. Error analysis and assessment of unsteady forces acting on a flapping wing micro air vehicle: Free flight versus wind-tunnel experimental methods. *Bioinspiration and Biomimetics*, 10(5), 8 2015. ISSN 17483190. doi: 10.1088/1748-3190/10/5/056004.

[10] J.V. Caetano, C.C. de Visser, G.C.H.E. de Croon, B. Remes, C. de Wagter, J. Verboom, and M. Mulder. Linear Aerodynamic Model Identification of a Flapping Wing MAV Based on Flight Test Data. *International Journal of Micro Air Vehicles*, 5(4):273–286, 12 2013. ISSN 1756-8293. doi: 10.1260/1756-8293.5.4.273. URL http://journals.sagepub.com/doi/10.1260/1756-8293.5.4.273.

[11] Francois Caron, Emmanuel Duflos, Denis Pomorski, and Philippe Vanheeghe. GPS/IMU data fusion using multisensor Kalman filtering: Introduction of contextual aspects. *Information Fusion*, 7(2):221–230, 6 2006. ISSN 15662535. doi: 10.1016/j.inffus.2004.07.002.

[12] Bo Cheng and Xinyan Deng. Translational and rotational damping of flapping flight and its dynamics and stability at hovering. *IEEE Transactions on Robotics*, 27(5):849–864, 10 2011. ISSN 15523098. doi: 10.1109/TRO.2011.2156170.

[13] Cheng Cheng, Jianghao Wu, Yanlai Zhang, Han Li, and Chao Zhou. Aerodynamics and dynamic stability of micro-air-vehicle with four flapping wings in hovering flight. *Advances in Aerodynamics*, 2(1):5, 12 2020. ISSN 2524-6992. doi: 10.1186/s42774-020-0029-0. URL https://aia.springeropen.com/articles/10.1186/s42774-020-0029-0.

[14] Timothy Coffey and John A. Montgomery. The Emergence of Mini UAVs for Military Applications. *Defense Horizons*, (22):1, 12 2002.

[15] Fausto G. Costa, Jó Ueyama, Torsten Braun, Gustavo Pessin, Fernando S. Osorio, and Patricia A. Vargas. The use of unmanned aerial vehicles and wireless sensor network in agricultural applications. In *International Geoscience and Remote Sensing Symposium (IGARSS)*, pages 5045–5048, 2012. doi: 10.1109/IGARSS.2012.6352477.

[16] Coen C. de Visser, Daan M. Pool, and E. van Kampen. *"AE4320 - System Identification of Aerospace Vehicles", Lecture Slides*. Faculty of Aerospace Engineering, Delft University of Technology, Delft, Netherlands, 2017.

[17] G. C.H.E. Decroon, M. Perçin, B. D.W. Remes, R. Ruijsink, and C. De Wagter. *The delfly: Design, aerodynamics, and artificial intelligence of a flapping wing robot*. Springer Netherlands, 1 2015. ISBN 9789401792080. doi: 10.1007/978-94-017-9208-0.

[18] Charles P Ellington, Coen van den Berg, Alexander P Willmott, and Adrian L R Thomas. Leading-edge vortices in insect flight. *Nature*, 384(6610):626–630, 1996. ISSN 1476-4687. doi: 10.1038/384626a0. URL https://doi.org/10.1038/384626a0.

[19] Milan Erdelj, Enrico Natalizio, Kaushik R. Chowdhury, and Ian F. Akyildiz. Help from the Sky: Leveraging UAVs for Disaster Management, 1 2017. ISSN 15361268.

[20] J D Gibbons and S Chakraborti. *Nonparametric Statistical Inference, Fifth Edition*. Taylor & Francis, 2010. ISBN 9781420077612. URL https://books.google.nl/books?id=Xhm4IgAACAAJ.

[21] Hakseong Gim, Seungkeun Kim, Jinyoung Suk, and Sungbong Cho. Longitudinal System Identification of Ornithopter with Automated Flight Tests. *IFAC-PapersOnLine*, 49(17):194–199, 2016. ISSN 24058963. doi: 10.1016/j.ifacol.2016.09.034.

[22] Mohinder S Grewal and Angus P Andrews. *Kalman Filtering Kalman Filtering: Theory and Practice Using MATLAB, Second Edition*. John Wiley & Sons, Inc., 2nd editio edition, 2001. ISBN 0471392545. URL www.Wiley.com.

[23] M N Hammoudi and M H Lowenberg. Dynamic gain scheduled control of an F16 model. 2008. doi: 10.2514/6.2008-6487. URL http://arc.aiaa.org.

[24] Jong-Seob Han, Anh Tuan Nguyen, and Jae-Hung Han. Aerodynamic characteristics of flapping wings under steady lateral inflow. *J. Fluid Mech*, 870:735–759, 2020. doi: 10.1017/jfm.2019.255. URL https://doi.org/10.1017/jfm.2019.255.

[25] Lars Kai Hansen and Peter Salamon. Neural Network Ensembles. *IEEE Transactions on Pattern Analysis and Machine Intelligence*, 12(10):993–1001, 1990. ISSN 01628828. doi: 10.1109/34.58871.

[26] Simon Haykin. *Neural Networks: A Comprehensive Foundation*. Prentice Hall PTR, USA, 1st edition, 1994. ISBN 0023527617.

[27] R. C. Hibbeler, Kai Beng. Yap, S. C. Fan, and R. C. Hibbeler. *Mechanics for engineers : dynamics*. Pearson Education, 2012. ISBN 9810692617.

[28] R. C. Hibbeler, Kai Beng. Yap, Peter Schiavone, and S. C. Fan. *Mechanics for engineers : statics*. Pearson Education, 2013. ISBN 9810692862.

[29] Todd Hylton, Christopher Martin, Richmon Tun, and Vince Castelli. The DARPA nano air vehicle program. In *50th AIAA Aerospace Sciences Meeting Including the New Horizons Forum and Aerospace Exposition*, 2012. doi: 10.2514/6.2012-583.

[30] Ravindra V. Jategaonkar. *Flight Vehicle System Identification: A Time-Domain Methodology, Second Edition*. American Institute of Aeronautics and Astronautics, Inc., 1 2015. doi: 10.2514/4.102790.

[31] Zhong Jingyang, Song Bifeng, and Wang Jin. Flapping Wing Multi-body Dynamic Simulation. *Procedia Engineering*, 99:885–890, 2015. doi: 10.1016/j.proeng.2014.12.617. URL www.sciencedirect.com.

[32] K M Kajak, M Karásek, Q P Chu, and G C H E de Croon. A minimal longitudinal dynamic model of a tailless flapping wing robot for control design. *Bioinspiration & biomimetics*, 14(4):46008, 6 2019. ISSN 17483190. doi: 10.1088/1748-3190/ab1e0b.

[33] Karl Kajak. *A minimal longitudinal dynamic model of a tailless flapping wing robot.* PhD thesis, 2018. URL https://repository.tudelft.nl/islandora/object/uuid%3A717e7e15-94c3-47ac-a348-12f5c2275aa2?collection=education.

[34] Matej Karásek and André Preumont. Flapping Flight Stability in Hover: A Comparison of Various Aerodynamic Models. 4, 2012. URL https://journals-sagepub-com.tudelft.idm.oclc.org/doi/pdf/10.1260/1756-8293.4.3.203.

[35] Matěj Karásek. *Robotic hummingbird: Design of a control mechanism for a hovering flapping wing micro air vehicle.* PhD thesis, 2014.

[36] Matěj Karásek, Florian T. Muijres, Christophe De Wagter, Bart D. W. Remes, and Guido C. H. E. de Croon. A tailless aerial robotic flapper reveals that flies use torque coupling in rapid banked turns. *Science*, 361(6407):1089–1094, 9 2018. ISSN 0036-8075. doi: 10.1126/science.aat0350. URL http://www.sciencemag.org/lookup/doi/10.1126/science.aat0350.

[37] Matthew Keennon, Karl Klingebiel, Henry Won, and Alexander Andriukov. Development of the Nano Hummingbird: A Tailless Flapping Wing Micro Air Vehicle. 2012. doi: 10.2514/6.2012-588. URL http://arc.aiaa.org.

[38] Karel J. Keesman. *System identification: An introduction.* Number 9780857295217. Springer International Publishing, 2011. doi: 10.1007/978-0-85729-522-4.

[39] Qudrat Khan, Rini Akmeliawati, Hoang Vu Phan, and Hoon Cheol Park. Linear model identification of beetle-mimicking flapping wing micro-air vehicle in hovering flight. In *IRIS 2016 - 2016 IEEE 4th International Symposium on Robotics and Intelligent Sensors: Empowering Robots with Smart Sensors*, pages 46–51. Institute of Electrical and Electronics Engineers Inc., 10 2017. ISBN 9781509060849. doi: 10.1109/IRIS.2016.8066064.

[40] V Klein and E A Morelli. *Aircraft System Identification: Theory and Practice.* AIAA education series. American Institute of Aeronautics and Astronautics, 2006. ISBN 9781563478321. URL https://books.google.nl/books?id=SC90QgAACAAJ.

[41] Younsaeng Lee, Seungjoo Kim, Jinyoung Suk, Hueonjoon Koo, and Jongseong Kim. System Identification of an Unmanned Aerial Vehicle from Automated Flight Tests. In *1st UAV Conference*, Reston, Virigina, 5 2002. American Institute of Aeronautics and Astronautics. ISBN 978-1-62410-106-9. doi: 10.2514/6.2002-3493. URL http://arc.aiaa.org/doi/10.2514/6.2002-3493.

[42] L. Ljung. Black-box models from input-output measurements. In *Conference Record - IEEE Instrumentation and Measurement Technology Conference*, volume 1, pages 138–146, 2001. doi: 10.1109/imtc.2001.928802.

[43] Lennart. Ljung. *System identification : theory for the user.* Prentice Hall PTR, 1999. ISBN 9780136566953.

[44] Lennart Ljung. Prediction error estimation methods. *Circuits, Systems, and Signal Processing*, 21(1):11–21, 1 2002. ISSN 0278081X. doi: 10.1007/BF01211648.

[45] Kevin Y. Ma, Pakpong Chirarattananon, Sawyer B. Fuller, and Robert J. Wood. Controlled flight of a biologically inspired, insect-scale robot. *Science*, 340(6132):603–607, 5 2013. ISSN 10959203. doi: 10.1126/science.1231806.

[46] Henrik Madsen, Peder Bacher, Rune Juhl, and Jan Kloppenborg Møller. Grey-Box Modeling; An approach to combined physical and statistical model building. Technical report, 2015.

[47] Rachid Malti, Stéphane Victor, Alain Oustaloup, and Hugues Garnier. An optimal instrumental variable method for continuous-time fractional model identification. 2008.

[48] J A Mulder, W.H.J.J. van Staveren, J C van der Vaart, E de Weerdt, A C in 't Veld, and E Mooij. Flight Dynamics - Lecture Notes. Technical report, 2013. URL http://app.knovel.com/web/toc.v/cid:kpFD000016/viewerType:toc/root_slug:flight-dynamics/url_slug:kt00UQFX02?b-q=ailerons&b-within-title=true&b-group-by=false&b-search-type=tech-reference&b-sort-on=default.

[49] J A Mulder, J C Van Der Vaart, W H J J Van Staveren, Q P Chu, and M Mulder. Lecture Notes AE4304 Aircraft Responses to Atmospheric Turbulence. Technical report, 2016.

[50] Edward W. Ng. A general algorithm for the solution of Kepler's equation for elliptic orbits. *Celestial Mechanics*, 20(3):243–249, 10 1979. ISSN 00088714. doi: 10.1007/BF01371365.

[51] Jorgen Nijboer. *Longitudinal grey-box model identification of a tailless flapping-wing MAV based on free-flight data*. PhD thesis, 2019. URL https://repository.tudelft.nl/islandora/object/uuid%3Aa37b96b7-90de-4f22-99ce-87cc97d414d9?collection=education.

[52] Jorgen Nijboer, Sophie F. Armanini, Matej Karasek, and Coen C. de Visser. Longitudinal Grey-Box Model Identification of a Tailless Flapping-Wing MAV Based on Free-Flight Data. American Institute of Aeronautics and Astronautics (AIAA), 1 2020. doi: 10.2514/6.2020-1964.

[53] Jorge Niño, Flavius Mitrache, Peter Cosyn, and Robin De Keyser. Model Identification of a Micro Air Vehicle. *Journal of Bionic Engineering*, 4:227236, 2007.

[54] Norman S Nise. Control Systems Engineering, International Student Version, 2010.

[55] G J Olsder, J W Van Der Woude, J G Maks, and D Jeltsema. *Mathematical Systems Theory 4th edition*. VSSD, 2011.

[56] Christopher T Orlowski and Anouck R Girard. Modeling and Simulation of Nonlinear Dynamics of Flapping Wing Micro Air Vehicles. *AIAA JOURNAL*, 49(5), 2011. doi: 10.2514/1.J050649. URL http://arc.aiaa.org.

[57] George Papageorgiou, Keith Glover, Glenn D'Mello, and Yoge Patel. Taking robust LPV control into flight on the VAAC Harrier. *Proceedings of the IEEE Conference on Decision and Control*, 5:4558–4564, 2000. ISSN 01912216. doi: 10.1109/CDC.2001.914633.

[58] Hoang Vu Phan, Taesam Kang, and Hoon Cheol Park. Design and stable flight of a 21 g insect-like tailless flapping wing micro air vehicle with angular rates feedback control. *Bioinspiration and Biomimetics*, 12 (3):036006, 4 2017. ISSN 17483190. doi: 10.1088/1748-3190/aa65db.

[59] Alireza Ramezani, Xichen Shi, Soon Jo Chung, and Seth Hutchinson. Bat Bot (B2), a biologically inspired flying machine. In *Proceedings - IEEE International Conference on Robotics and Automation*, volume 2016-June, pages 3219–3226. Institute of Electrical and Electronics Engineers Inc., 6 2016. ISBN 9781467380263. doi: 10.1109/ICRA.2016.7487491.

[60] A Roshanbin, H Altartouri, M Karásek, and A Preumont. COLIBRI: A hovering flapping twin-wing robot. *International Journal of Micro Air Vehicles*, 9(4):270–282, 12 2017. ISSN 1756-8293. doi: 10.1177/1756829317695563. URL http://journals.sagepub.com/doi/10.1177/1756829317695563.

[61] Angelo M. Sabatini. Quaternion-based extended Kalman filter for determining orientation by inertial and magnetic sensing. *IEEE Transactions on Biomedical Engineering*, 53(7):1346–1356, 7 2006. ISSN 00189294. doi: 10.1109/TBME.2006.875664.

[62] Sanjay P. Sane and Michael H. Dickinson. The control of flight force by a flapping wing: Lift and drag production. *Journal of Experimental Biology*, 204(15):2607–2626, 4 2001. ISSN 00220949.

[63] Mordechai Shacham and Neima Brauner. Application of stepwise regression for dynamic parameter estimation. *Computers and Chemical Engineering*, 69:26–38, 10 2014. ISSN 00981354. doi: 10.1016/j.compchemeng.2014.06.013.

[64] Wei Shyy, Yongsheng Lian, Jian Tang, Dragos Viieru, and Hao Liu. *Aerodynamics of low Reynolds number flyers*, volume 10. Cambridge university press New York, 2008.

[65] Torsten Söderström and Petre Stoica. *System identification*. Prentice-Hall, Inc., 1988. ISBN 0138812365.

[66] Robert F Stengel. *Flight dynamics*. Princeton University Press, 2015.

[67] Brian L. Stevens, Frank L. Lewis, and Eric N. Johnson. *Aircraft control and simulation: Dynamics, controls design, and autonomous systems: Third edition*. wiley, 11 2015. ISBN 9781119174882. doi: 10.1002/9781119174882.

[68] Jinyoung Suk, Younsaeng Lee, Seungjoo Kim, Hueonjoon Koo, and Jongseong Kim. System identification and stability evaluation of an unmanned aerial vehicle from automated flight tests. *KSME International Journal*, 17(5):654–667, 2003. ISSN 12264865. doi: 10.1007/BF02983861.

[69] M. Sun. Dynamic flight stability of a hovering bumblebee. *Journal of Experimental Biology*, 208(3):447–459, 1 2005. ISSN 0022-0949. doi: 10.1242/jeb.01407.

[70] M. Sun and J. K. Wang. Flight stabilization control of a hovering model insect. *Journal of Experimental Biology*, 210(15):2714–2722, 7 2007. ISSN 0022-0949. doi: 10.1242/jeb.004507.

[71] Mao Sun. Insect flight dynamics: Stability and control. *Reviews of Modern Physics*, 86(2):615–646, 5 2014. ISSN 15390756. doi: 10.1103/RevModPhys.86.615. URL https://journals.aps.org/rmp/abstract/10.1103/RevModPhys.86.615.

[72] Mao Sun, Jikang Wang, Yan Xiong, M Sun, J Wang, and · Y Xiong. Dynamic flight stability of hovering insects. *Acta Mech Sin*, 23:231–246, 2007. doi: 10.1007/s10409-007-0068-3. URL https://link-springer-com.tudelft.idm.oclc.org/content/pdf/10.1007%2Fs10409-007-0068-3.pdf.

[73] Graham K. Taylor and Adrian L.R. Thomas. Dynamic flight stability in the desert locust Schistocerca gregaria. *Journal of Experimental Biology*, 206(16):2803–2829, 8 2003. ISSN 00220949. doi: 10.1242/jeb.00501.

[74] Frederick Tombe. Maxwell's Original Equations. 12 2011.

[75] Chiara Torresan, Andrea Berton, Federico Carotenuto, Salvatore Filippo Di Gennaro, Beniamino Gioli, Alessandro Matese, Franco Miglietta, Carolina Vagnoli, Alessandro Zaldei, and Luke Wallace. Forestry applications of UAVs in Europe: a review. *International Journal of Remote Sensing*, 38(8-10):2427–2447, 5 2017. ISSN 13665901. doi: 10.1080/01431161.2016.1252477.

[76] P. J. van Overloop, I. J. Miltenburg, X. Bombois, A. J. Clemmens, R. J. Strand, N. C. van de Giesen, and R. Hut. Identification of resonance waves in open water channels. *Control Engineering Practice*, 18(8):863–872, 8 2010. ISSN 09670661. doi: 10.1016/j.conengprac.2010.03.010.

[77] Joachim Vandekerckhove, Dora Matzke, and Eric-Jan Wagenmakers. Model Comparison and the Principle of Parsimony. 4 2015. doi: 10.1093/OXFORDHB/9780199957996.013.14.

[78] Piet Verschuren, H. (Hans) Doorewaard, and M. J. Mellion. *Designing a research project*. ISBN 9789059315723.

[79] Kwan Y. Wong and Elijah Polak. Identification of Linear Discrete Time Systems Using the Instrumental Variable Method. *IEEE Transactions on Automatic Control*, AC-12(6):707–718, 1967. ISSN 15582523. doi: 10.1109/TAC.1967.1098734.

[80] Jianghao Wu and Mao Sun. Control for going from hovering to small speed flight of a model insect. *Acta Mechanica Sinica/Lixue Xuebao*, 25(3):295–302, 6 2009. ISSN 05677718. doi: 10.1007/s10409-009-0241-y.

[81] Yan Xiong and Mao Sun. Dynamic flight stability of a bumblebee in forward flight. *Acta Mech Sin*, 24:25–36, 2008. doi: 10.1007/s10409-007-0121-2. URL https://link-springer-com.tudelft.idm.oclc.org/content/pdf/10.1007%2Fs10409-007-0121-2.pdf.

[82] Na Xu and Mao Sun. Lateral dynamic flight stability of a model bumblebee in hovering and forward flight. *Journal of Theoretical Biology*, 319:102–115, 2 2013. ISSN 00225193. doi: 10.1016/j.jtbi.2012.11.033.

[83] L. A. Zadeh. From Circuit Theory to System Theory. *Proceedings of the IRE*, 50(5):856–865, 1962. ISSN 00968390. doi: 10.1109/JRPROC.1962.288302.

[84] Lina Zeldovich. The drone and the honey. *Mechanical Engineering*, 141(5):32–37, 5 2019. ISSN 00256501. doi: 10.1115/1.2019-MAY2.

[85] Yan-Lai Zhang, Jiang-Hao Wu, Mao Sun, Y.-L Zhang, J.-H Wu, and · M Sun. Lateral dynamic flight stability of hovering insects: theory vs. numerical simulation. *Acta Mech. Sin*, 28(1):221–231, 2012. doi: 10.1007/s10409-012-0011-0. URL https://link-springer-com.tudelft.idm.oclc.org/content/pdf/10.1007%2Fs10409-012-0011-0.pdf.

[86] Yanlai Zhang, Mao Sun, Y Zhang, and · M Sun. Dynamic flight stability of a hovering model insect: lateral motion. *Acta Mech Sin*, 26:175–190, 2010. doi: 10.1007/s10409-009-0303-1. URL https://link-springer-com.tudelft.idm.oclc.org/content/pdf/10.1007%2Fs10409-009-0303-1.pdf.

A

Geometric properties of the Delfly Nimble

In this appendix an overview is given of the geometric properties of the Delfly Nimble. In Section A.1 the properties of the full vehicle, which were used for the set up of the grey-box state-space systems, are shown. In Section A.2 the properties of the wing, which were used for the non-dimensionalizing of the stability derivatives, are calculated.

A.1. Full vehicle properties

In this section an overview is given of the geometric properties of the full vehicle are shown. The axis system which was used to determine the location of the center of gravity of the Delfly Nimble is shown in Figure A.1.

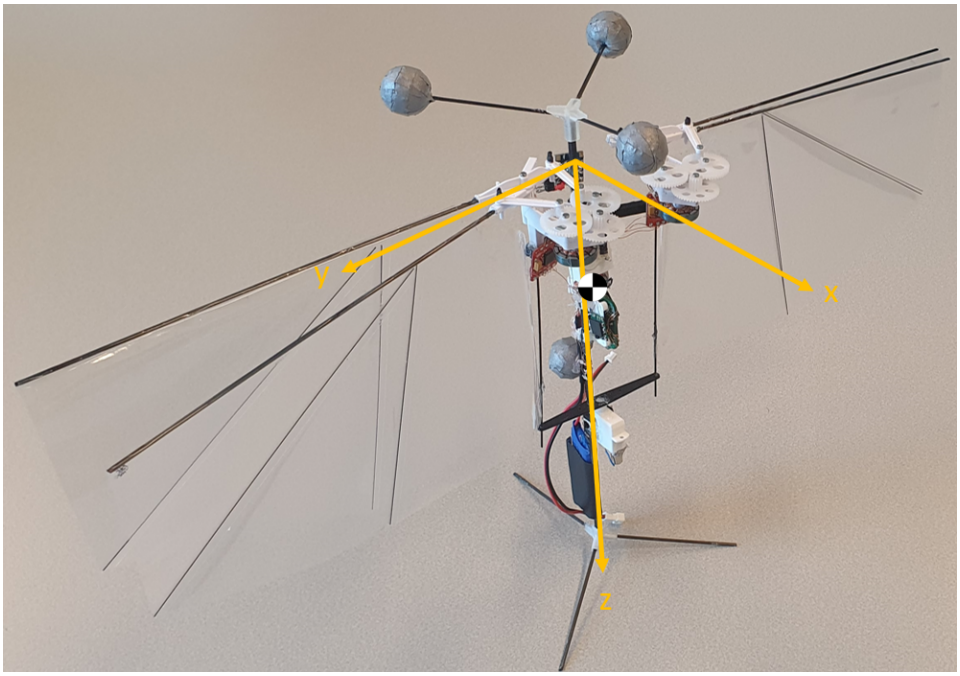

Figure A.1: Axis system used to determine the location of the center of gravity of the Delfly Nimble. The z-axis is pointed downward alongside the fuselage, the y-axis is pointed towards the right wing alongside the leading edge, and the x-axis is pointed towards the front, in the direction of the motors.

Where the z-axis is pointed downward alongside the fuselage, the y-axis is pointed towards the right wing alongside the leading edge, and the x-axis is pointed towards the front, in the direction of the motors. The properties of the full vehicle, which consist of the mass, the location of the center of gravity, and the inertia terms are shown in Table A.1.

Geometric properties of the Delfly Nimble		
Property	**With Wifi-Module**	**Without Wifi-Module**
Total mass $[g]$	29.47	28.76
Center of Gravity (x_{cg}) $[mm]$	0.43	0.44
Center of Gravity (y_{cg}) $[mm]$	-0.02	-0.02
Center of Gravity (z_{cg}) $[mm]$	51.93	52.74
Inertia I_{xx} $[kg \cdot m^2]$ (w.r.t c.g.)	9.76×10^{-5}	9.60×10^{-5}
Inertia I_{yy} $[kg \cdot m^2]$ (w.r.t c.g.)	7.35×10^{-5}	7.20×10^{-5}
Inertia I_{zz} $[kg \cdot m^2]$ (w.r.t c.g.)	3.34×10^{-5}	3.32×10^{-5}
Inertia I_{xy} $[kg \cdot m^2]$ (w.r.t c.g.)	2.66×10^{-8}	2.64×10^{-8}
Inertia I_{yz} $[kg \cdot m^2]$ (w.r.t c.g.)	7.51×10^{-9}	7.98×10^{-9}
Inertia I_{xz} $[kg \cdot m^2]$ (w.r.t c.g.)	-8.85×10^{-6}	-8.81×10^{-6}

Table A.1: Geometric properties of the Delfly Nimble. The inertia terms are given with respect to the center of gravity. Two configurations were used during the experiments: with and without the Wifi-Module.

A.2. Wing properties

In this section the calculations of the required wing properties for the non-dimensionalizing of the stability derivatives are shown. These calculations were done by use of the wing schematics of the Delfly Nimble, which uses the same wings as the Delfly II. The wing schematics are displayed in Figure A.2 [1].

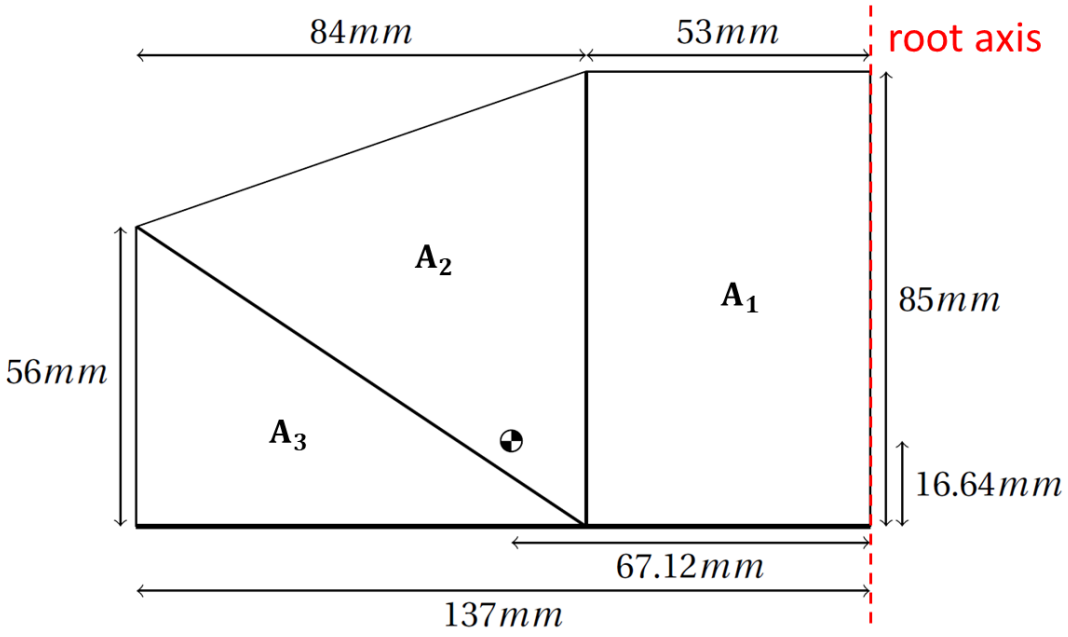

Figure A.2: Schematics of the wings of the Delfly Nimble [1]. The root axis is illustrated with the red dashed line.

In order to calculate the total area of the wing, it was divided into three subareas. These three areas are determined, as defined in Figure A.2. The calculated values are shown in Equation A.1.

$$\begin{aligned} A_1 &= 53 \cdot 84 &&= 4505 \ mm^2 \\ A_2 &= \frac{1}{2} \cdot 84 \cdot 85 &&= 3570 \ mm^2 \\ A_3 &= \frac{1}{2} \cdot 84 \cdot 56 &&= 2352 \ mm^2 \end{aligned} \tag{A.1}$$

The total area is determined by summing all the areas, as shown in Equation A.2.

$$A_w = A_1 + A_2 + A_3 = \quad 10427 \ \ mm^2 \tag{A.2}$$

The distances of the centroids of the three areas with respect to the root axis are determined, which is shown in Equation A.3.

$$\begin{aligned} r_1 = &\quad \frac{1}{2} \cdot 53 &&= \quad 26.5 \ \ mm \\ r_2 = &\quad \frac{1}{2} \cdot 84 + 53 &&= \quad 81 \ \ mm \\ r_3 = &\quad 137 - \frac{1}{3} \cdot 84 &&= \quad 109 \ \ mm \end{aligned} \tag{A.3}$$

The centroid of the wing can be then determined using the areas A_1, A_2, A_3 and the distances r_1, r_2, r_3, as shown in Equation A.4.

$$\hat{c} = \frac{\sum_{i=1}^{3} A_i \cdot r_i}{\sum_{i=1}^{3} A_i} = \frac{A_1 \cdot r_1 + A_2 \cdot r_2 + A_3 \cdot r_3}{A_w} = \quad 63.77 \ \ mm \tag{A.4}$$

In order to determine the radius of the second moment of inertia $\hat{r}$, the moment of inertia of the wing with respect to the root axis has to be computed. This is calculated using the parallel axis theorem, where the total moment of inertia is determined by determining the moment of inertia about an axis through the centroid and adding the Steiner term [28]. The moment of inertias of the areas A_1, A_2, A_3 about their centroids are determined in Equation A.5.

$$\begin{aligned} I_{1_c} = &\quad \frac{53^3 \cdot 84}{12} &&= \quad 1054545 \ \ mm^4 \\ I_{2_c} = &\quad \frac{84^3 \cdot 85}{36} &&= \quad 1399440 \ \ mm^4 \\ I_{3_c} = &\quad \frac{84^3 \cdot 56}{36} &&= \quad 921984 \ \ mm^4 \end{aligned} \tag{A.5}$$

The Steiner terms are determined in Equation A.6.

$$\begin{aligned} I_{1_s} = &\quad A_1 \cdot r_1 &&= \quad 3163636 \ \ mm^4 \\ I_{2_s} = &\quad A_2 \cdot r_2 &&= \quad 23422770 \ \ mm^4 \\ I_{3_s} = &\quad A_3 \cdot r_3 &&= \quad 24822210 \ \ mm^4 \end{aligned} \tag{A.6}$$

The total moment of inertia of the wing with respect to the root axis is shown in Equation A.7.

$$I_{tot} = I_{1_c} + I_{2_c} + I_{3_c} + I_{1_s} + I_{2_s} + I_{3_s} = \quad 57906487 \ \ mm^4 \tag{A.7}$$

With the total moment of inertia I_{tot} and the total wing area A_w the radius $\hat{r}$ can be determined using A.8.

$$\hat{r} = \quad \sqrt{\frac{I_{tot}}{A_w}} \quad = \quad 74.52 \ \ mm \tag{A.8}$$

The mean chord length $\bar{c}$ of the wing is determined using the wingspan b and the total wing area A_w, as shown in Equation A.9.

$$\bar{c} = \frac{A_w}{b} = \frac{10427}{137} = 76.11 mm \tag{A.9}$$

B

Derivation of EOM's

In this appendix the equations of motion are derived, which are used for the development of the mathematical model of the lateral dynamics of the Delfly Nimble. The axis system used on the Delfly Nimble is shown in Figure B.1.

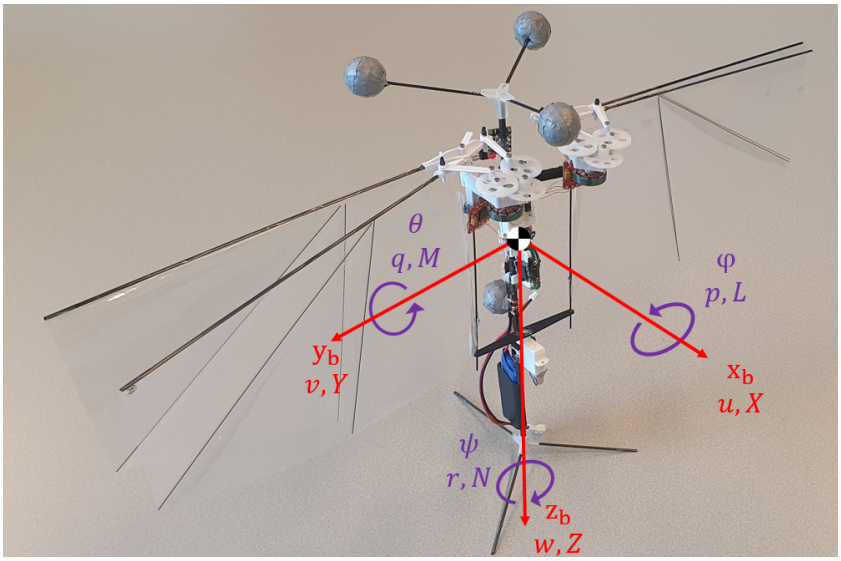

Figure B.1: Axis system used on the Delfly Nimble, where x_b, y_b and z_b are the body axes. The aerodynamic forces are indicated by X, Y and Z, while the aerodynamic moments are indicated by L, M and N. The body velocities are u, v and w. The angular rates are p, q and r and the attitude angles are ϕ, θ and ψ.

The following assumptions are used to determine the nonlinear equations of motion [48, 66, 67]:

- The body of the vehicle is rigid.
- The mass of the vehicle is constant.
- The Earth is flat and non-rotating.
- X_bZ_b is a symmetry plane, so I_{xy} and I_{yz} are assumed to be zero.

The rigid body assumption can be made if only the body dynamics of the Delfly Nimble are analysed, i.e. if the flapping dynamics and the body dynamics of the Delfly Nimble can be treated separately. Using these assumptions the nonlinear equations for the aerodynamic forces, moments, and the kinematic equations can be developed, resulting in Equations B.1, B.2 and B.3.

$$\begin{aligned} F_x &= X - mg\cdot\sin(\theta) &&= \overbrace{m\cdot(\dot{u}+qw-rv)}^{states} \\ F_y &= Y + mg\cdot\cos(\theta)\cdot\sin(\phi) &&= m\cdot(\dot{v}+ru-pw) \\ F_z &= \underbrace{Z + mg\cdot\cos(\theta)\cdot\cos(\phi)}_{forces} &&= m\cdot(\dot{w}+pv-qu) \end{aligned} \tag{B.1}$$

$$\begin{aligned} M_x = \quad L \quad &= \overbrace{I_{xx}\cdot\dot{p} + (I_{zz}-I_{yy})\cdot qr - I_{xz}\cdot(\dot{r}+pq)}^{states} \\ M_y = \quad M \quad &= I_{yy}\cdot\dot{q} + (I_{xx}-I_{zz})\cdot rp - I_{xz}\cdot(p^2+r^2) \\ M_z = \underbrace{\quad N \quad}_{moments} &= I_{zz}\cdot\dot{r} + (I_{yy}-I_{xx})\cdot pq - I_{xz}\cdot(\dot{p}-qr) \end{aligned} \tag{B.2}$$

$$\begin{aligned} \dot{\phi} &= p + q\cdot\sin(\phi)\cdot\tan(\theta) + r\cdot\cos(\phi)\cdot\tan(\theta) \\ \dot{\theta} &= q\cdot\cos(\phi) - r\cdot\sin(\phi) \\ \dot{\psi} &= q\cdot\frac{\sin(\phi)}{\cos(\theta)} + r\cdot\frac{\cos(\phi)}{\cos(\theta)} \end{aligned} \tag{B.3}$$

Here F_x, F_y, F_z are the forces, and M_x, M_y, M_z are the moment about the x, y, z axes. The m is the mass of the Delfly Nimble and the g is the gravitational constant. Furthermore, u, v, w are the body velocities, $\dot{u}$, $\dot{v}$, $\dot{w}$ are the body accelerations, p, q, r are the angular rates, $\dot{p}$, $\dot{q}$, $\dot{r}$ are the angular accelerations, X, Y, Z are the aerodynamic forces, L, M, N are the aerodynamic moments, I_{xx} etc. are the inertia terms, ϕ, θ, ψ are the attitude angles and $\dot{\phi}$, $\dot{\theta}$, $\dot{\psi}$ are the attitude angular rates.

The Force equations in Equation B.1 have two representations, one with the forces and one with the states. These equations are essentially an application of Newton's second law of motion [27]. Similar to the force equations, the moment equations shown in Equation B.2 also has two representations, the moments and the states. These equations are essentially an application of the Euler equations with non-zero products of inertia [27, 48, 66].

The nonlinear equations can be further simplified by linearization. Linearized equations of motion are often used for the analysis of the dynamic system[48, 66]. The linearization is done using two techniques, the Taylor series expansion and the small perturbation theorem[55, 66]. The Taylor series expansion is an approximation of a function using an initial value and its derivatives. An example of a Taylor series expansion is shown in Equation B.4.

$$\begin{aligned} g(a) &\approx g(a_0) + g'(a_0)\cdot(a-a_0) + \frac{g"(a_0)}{2}\cdot(a-a_0)^2 + h.o.t. \\ &\approx g(a_0) + g'(a_0)\cdot(\Delta a) + \frac{g"(a_0)}{2}\cdot(\Delta a)^2 + h.o.t. \end{aligned} \tag{B.4}$$

Where g is a function of the variable a, a_0 is the initial value and $h.o.t.$ indicates the higher order terms. If only the terms up to the first derivative are used the expansion which approximates the actual function is linear. If a function is dependent on more than one variable, the Taylor series expansion will be as shown in Equation B.5.

$$\begin{aligned} g(\mathbf{a}) &\approx g(\mathbf{a}_0) + \frac{\partial g}{\partial a_1}\cdot\Delta a_1 + \frac{\partial g}{\partial a_2}\cdot\Delta a_2 + \frac{\partial g}{\partial a_3}\cdot\Delta a_3 \\ \mathbf{a} &= \begin{bmatrix} a_1 \\ a_2 \\ a_3 \end{bmatrix} \end{aligned} \tag{B.5}$$

The Taylor series expansion can be used to linearize the equations of motion and the kinematic equations of Equations B.1 to B.3. The variables used for the linearization are the body velocities u, v, w, the body accelerations $\dot{u}, \dot{v}, \dot{w}$, the angular rates p, q, r, the angular accelerations $\dot{p}, \dot{q}, \dot{r}$, the attitude angles ϕ, θ, ψ and the

attitude angular rates $\dot{\phi},\dot{\theta},\dot{\psi}$. However, the aerodynamic forces X,Y,Z and moments L,M,N are still present in the equations. Since these are not constant terms they can't be omitted. In order to incorporate the forces and moments properly in the linearization an additional assumption is made, namely that the aerodynamic forces and moments can be modeled using a linear approximation. This can be done by applying the small perturbation theorem. In this theorem it is assumed that a variable can be rewritten by use of a nominal value and a perturbation term [66], as shown in Equation B.6.

$$\mathbf{b}(t) \triangleq \mathbf{b}_0(t) + \Delta\mathbf{b}(t) \tag{B.6}$$

Where $\mathbf{b}(t)$ is a variable, $\mathbf{b}_0(t)$ is the nominal value and $\Delta\mathbf{b}(t)$ is the perturbation term. When the aerodynamic forces and moments are modeled using this theorem, is essentially means that the forces and moments change due to a change in the states. Control inputs also have an influence on the aerodynamic forces and moments. For the Delfly Nimble there are three control inputs which have been defined, the dihedral angle δ_d, the difference in flapping frequency δ_f, the wing root angle δ_w, and the throttle input δ_t. This means that the aerodynamic forces and moments are a function of the states and the control inputs, presented in Equation B.7.

$$\begin{aligned}
X &= f(p,q,r,u,v,w,\delta_d,\delta_f,\delta_w,\delta_t)\\
Y &= f(p,q,r,u,v,w,\delta_d,\delta_f,\delta_w,\delta_t)\\
Z &= f(p,q,r,u,v,w,\delta_d,\delta_f,\delta_w,\delta_t)\\
L &= f(p,q,r,u,v,w,\delta_d,\delta_f,\delta_w,\delta_t)\\
M &= f(p,q,r,u,v,w,\delta_d,\delta_f,\delta_w,\delta_t)\\
N &= f(p,q,r,u,v,w,\delta_d,\delta_f,\delta_w,\delta_t)
\end{aligned} \tag{B.7}$$

The states chosen in Equation B.7 are not fixed. The number of states on which the aerodynamic forces and moments are dependent can be increased or decreased. The number of states can be decreased by use of another assumption, namely that there is no coupling between the longitudinal and lateral dynamics. This leads to the development of two dynamic subsystems, one for the longitudinal dynamics and one for the lateral dynamics. The state and input vectors for the longitudinal and lateral dynamic systems are defined in Equation B.8.

$$\underline{x}_{lon} = \begin{bmatrix} q \\ u \\ w \\ \theta \end{bmatrix}, \quad \underline{x}_{lat} = \begin{bmatrix} p \\ r \\ v \\ \phi \end{bmatrix}, \quad \underline{u}_{lon} = \underline{u}_{lat} = \begin{bmatrix} \delta_d \\ \delta_f \\ \delta_w \\ \delta_t \end{bmatrix} \tag{B.8}$$

It is then assumed that for the longitudinal dynamics the aerodynamic forces X, Z and the aerodynamic moment M is relevant, while for the lateral dynamics the aerodynamic force Y and the aerodynamic moments L, N are relevant, as done for the analysis of aircraft dynamics and flapping flight dynamics [34, 48, 66]. Therefore the equations for the aerodynamic forces can be reduced to Equation B.9.

$$\begin{aligned}
X &= f(q,u,w,\delta_d,\delta_f,\delta_w,\delta_t)\\
Y &= f(p,r,v,\delta_d,\delta_f,\delta_w,\delta_t)\\
Z &= f(q,u,w,\delta_d,\delta_f,\delta_w,\delta_t)\\
L &= f(p,r,v,\delta_d,\delta_f,\delta_w,\delta_t)\\
M &= f(q,u,w,\delta_d,\delta_f,\delta_w,\delta_t)\\
N &= f(p,r,v,\delta_d,\delta_f,\delta_w,\delta_t)
\end{aligned} \tag{B.9}$$

These equations can then be linearized using a Taylor series expansion, which leads to linear equations for the aerodynamic forces and moments shown in Equation B.10.

$$
\begin{aligned}
X_{lin} &= X_0 + X_q\Delta q + X_u\Delta u + X_w\Delta w + X_{\delta_d}\Delta\delta_d + X_{\delta_f}\Delta\delta_f + X_{\delta_w}\Delta\delta_w + X_{\delta_t}\Delta\delta_t \\
Y_{lin} &= Y_0 + Y_p\Delta p + Y_r\Delta r + Y_v\Delta v + Y_{\delta_d}\Delta\delta_d + Y_{\delta_f}\Delta\delta_f + Y_{\delta_w}\Delta\delta_w + Y_{\delta_t}\Delta\delta_t \\
Z_{lin} &= Z_0 + Z_q\Delta q + Z_u\Delta u + Z_w\Delta w + Z_{\delta_d}\Delta\delta_d + Z_{\delta_f}\Delta\delta_f + Z_{\delta_w}\Delta\delta_w + Z_{\delta_t}\Delta\delta_t \\
L_{lin} &= L_0 + L_p\Delta p + L_r\Delta r + L_v\Delta v + L_{\delta_d}\Delta\delta_d + L_{\delta_f}\Delta\delta_f + L_{\delta_w}\Delta\delta_w + L_{\delta_t}\Delta\delta_t \\
M_{lin} &= M_0 + M_q\Delta q + M_u\Delta u + M_w\Delta w + M_{\delta_d}\Delta\delta_d + M_{\delta_f}\Delta\delta_f + M_{\delta_w}\Delta\delta_w + M_{\delta_t}\Delta\delta_t \\
N_{lin} &= N_0 + N_p\Delta p + N_r\Delta r + N_v\Delta v + N_{\delta_d}\Delta\delta_d + N_{\delta_f}\Delta\delta_f + N_{\delta_w}\Delta\delta_w + N_{\delta_t}\Delta\delta_t
\end{aligned}
\tag{B.10}
$$

Where X_0, Y_0, Z_0, L_0, M_0, N_0 are the nominal forces and moment, and X_u is the partial derivative of X with respect to u, i.e. $\frac{\partial X}{\partial u}$. The partial derivative of an aerodynamic force or moment is known as a dimensional stability derivative. A partial derivative of a force or moment with respect to a control input, as is the case for X_{δ_d}, is known as a dimensional control derivative. With the aerodynamic forces now linearised, the nonlinear equations of motion and kinematic equations, shown in Equations B.1 to B.3, can be linearized. Further simplifications can be applied to the linearized equations of motion by assumptions on the nominal values for the states and forces, also called the initial conditions. The initial conditions are determined for the specific maneuvers which will be used during the experiments described in Chapter 3. The initial conditions are defined in Equation B.11.

$$
\begin{array}{ccccc}
u_0 \neq 0 & p_0 = 0 & \phi_0 \neq 0 & X_0 \neq 0 & L_0 = 0 \\
v_0 \neq 0 & q_0 = 0 & \theta_0 \neq 0 & Y_0 \neq 0 & M_0 = 0 \\
w_0 \neq 0 & r_0 = 0 & \psi_0 = 0 & Z_0 \neq 0 & N_0 = 0 \\
 & & & & \\
\dot{u}_0 = 0 & \dot{p}_0 = 0 & \dot{\phi}_0 = 0 & \dot{X}_0 = 0 & \dot{L}_0 = 0 \\
\dot{v}_0 = 0 & \dot{q}_0 = 0 & \dot{\theta}_0 = 0 & \dot{Y}_0 = 0 & \dot{M}_0 = 0 \\
\dot{w}_0 = 0 & \dot{r}_0 = 0 & \dot{\psi}_0 = 0 & \dot{Z}_0 = 0 & \dot{N}_0 = 0
\end{array}
\tag{B.11}
$$

When the Delfly Nimble is in hover or moving with a constant velocity, the resultant force is zero according to Newton's second law of motion [27, 28]. This means that the forces X_0, Y_0 and Z_0 are canceled out by the weight, further simplifying the equations of motion. The application of the Taylor series expansion, the small perturbation theorem and the initial conditions lead to the linearized force equations in Equation B.12, the linearized moment equations in Equation B.13 and the linearized kinematic equations in Equation B.14.

$$
\begin{aligned}
X_q\Delta q + X_u\Delta u + X_w\Delta w + X_{\delta_d}\Delta\delta_d + X_{\delta_f}\Delta\delta_f &= m\cdot(\Delta\dot{u} + w_0\cdot\Delta q - v_0\cdot\Delta r) \\
+ X_{\delta_w}\Delta\delta_w + X_{\delta_t}\Delta\delta_t - mg\cdot\cos(\theta)\cdot\Delta\theta & \\
Y_p\Delta p + Y_r\Delta r + Y_v\Delta v + Y_{\delta_d}\Delta\delta_d + Y_{\delta_f}\Delta\delta_f &= m\cdot(\Delta\dot{v} + u_0\cdot\Delta r - w_0\cdot\Delta p) \\
+ Y_{\delta_w}\Delta\delta_w + Y_{\delta_t}\Delta\delta_t + mg\cdot cos(\theta_0)\cdot cos(\phi_0)\cdot\Delta\phi & \\
Z_q\Delta q + z_u\Delta u + Z_w\Delta w + Z_{\delta_d}\Delta\delta_d + Z_{\delta_f}\Delta\delta_f &= m\cdot(\Delta\dot{w} + v_0\cdot\Delta p - u_0\cdot\Delta q) \\
+ Z_{\delta_w}\Delta\delta_w + Z_{\delta_t}\Delta\delta_t - mg\cdot\sin(\theta_0)\cdot cos(\phi_0)\cdot\Delta\theta &
\end{aligned}
\tag{B.12}
$$

$$
\begin{aligned}
L_p\Delta p + L_r\Delta r + L_v\Delta v + L_{\delta_d}\Delta\delta_d + L_{\delta_f}\Delta\delta_f + L_{\delta_w}\Delta\delta_w + L_{\delta_t}\Delta\delta_t &= I_{xx}\cdot\Delta\dot{p} - I_{xz}\cdot\Delta\dot{r} \\
M_q\Delta q + M_u\Delta u + M_w\Delta w + M_{\delta_d}\Delta\delta_d + M_{\delta_f}\Delta\delta_f + M_{\delta_w}\Delta\delta_w + M_{\delta_t}\Delta\delta_t &= I_{yy}\cdot\Delta\dot{q} \\
N_p\Delta p + N_r\Delta r + N_v\Delta v + N_{\delta_d}\Delta\delta_d + N_{\delta_f}\Delta\delta_f + N_{\delta_w}\Delta\delta_w + N_{\delta_t}\Delta\delta_t &= I_{zz}\cdot\Delta\dot{r} - I_{xz}\cdot\Delta\dot{p}
\end{aligned}
\tag{B.13}
$$

$$
\begin{aligned}
\Delta\dot{\phi} &= \Delta p + \Delta q\cdot\sin(\phi_0)\cdot\tan(\theta_0) + \Delta r\cdot\cos(\phi_0)\cdot\tan(\theta_0) \\
\Delta\dot{\theta} &= \Delta q\cdot\cos(\phi_0) - \Delta r\cdot\sin(\phi_0) \\
\Delta\dot{\psi} &= \Delta q\cdot\frac{\sin(\phi_0)}{\cos(\theta_0)} + \Delta r\cdot\frac{\cos(\phi_0)}{\cos(\theta_0)}
\end{aligned}
\tag{B.14}
$$

For the analysis of the stability of the flight the equation for the yaw angle ψ can be omitted [34], removing the third kinematic equation in Equation B.14. With the state and input vector defined in Equation B.8 the linearized equations of motion in Equations B.12 to B.14 can be written in two linear time-invariant state space systems, one for the longitudinal dynamics, defined in Equation B.15, and one for the lateral dynamics, presented in Equation B.16. For the longitudinal dynamics the additional assumption that v_0 is equal to zero was made. Furthermore, the Δ terms were removed in order to simplify the notations in the final equations of motion.

$$\begin{bmatrix} \dot{q} \\ \dot{u} \\ \dot{w} \\ \dot{\theta} \end{bmatrix} = \begin{bmatrix} \frac{M_q}{I_{yy}} & \frac{M_u}{I_{yy}} & \frac{M_w}{I_{yy}} & 0 \\ \frac{X_q}{m} - w_0 & \frac{X_u}{m} & \frac{X_w}{m} & -g \cdot \cos(\theta_0) \\ \frac{Z_q}{m} + u_0 & \frac{Z_u}{m} & \frac{Z_w}{m} & -g \cdot \sin(\theta_0) \cdot \cos(\phi_0) \\ \cos(\phi_0) & 0 & 0 & 0 \end{bmatrix} \cdot \begin{bmatrix} q \\ u \\ w \\ \theta \end{bmatrix} + \begin{bmatrix} \frac{M_{\delta_d}}{I_{yy}} & \frac{M_{\delta_f}}{I_{yy}} & \frac{M_{\delta_w}}{I_{yy}} & \frac{M_{\delta_t}}{I_{yy}} \\ \frac{X_{\delta_d}}{m} & \frac{X_{\delta_f}}{m} & \frac{X_{\delta_w}}{m} & \frac{X_{\delta_t}}{m} \\ \frac{Z_{\delta_d}}{m} & \frac{Z_{\delta_f}}{m} & \frac{Z_{\delta_w}}{m} & \frac{Z_{\delta_w}}{m} \\ 0 & 0 & 0 & 0 \end{bmatrix} \cdot \begin{bmatrix} \delta_d \\ \delta_f \\ \delta_w \\ \delta_t \end{bmatrix} \tag{B.15}$$

In Equation B.15 the M_q, M_u, M_w, X_q, X_u, X_w, Z_q, Z_u and Z_w are the stability derivatives, while the M_{δ_d}, M_{δ_f}, M_{δ_w}, M_{δ_t}, X_{δ_d}, X_{δ_f}, X_{δ_w}, X_{δ_t}, Z_{δ_d}, Z_{δ_f}, Z_{δ_w} and Z_{δ_t} are the control derivatives.

$$\begin{bmatrix} \dot{p} \\ \dot{r} \\ \dot{v} \\ \dot{\phi} \end{bmatrix} = \begin{bmatrix} \frac{I_{zz}}{I_c} \cdot L_p + \frac{I_{xz}}{I_c} \cdot N_p & \frac{I_{zz}}{I_c} \cdot L_r + \frac{I_{xz}}{I_c} \cdot N_r & \frac{I_{zz}}{I_c} \cdot L_v + \frac{I_{xz}}{I_c} \cdot N_v & 0 \\ \frac{I_{xz}}{I_c} \cdot L_p + \frac{I_{xx}}{I_c} \cdot N_p & \frac{I_{xz}}{I_c} \cdot L_r + \frac{I_{xx}}{I_c} \cdot N_r & \frac{I_{xz}}{I_c} \cdot L_v + \frac{I_{xx}}{I_c} \cdot N_v & 0 \\ \frac{Y_p}{m} + w_0 & \frac{Y_r}{m} - u_0 & \frac{Y_v}{m} & g \cdot \cos(\theta_0) \cdot \cos(\phi_0) \\ 1 & \tan(\theta_0) \cdot \cos(\phi_0) & 0 & 0 \end{bmatrix} \cdot \begin{bmatrix} p \\ r \\ v \\ \phi \end{bmatrix} + \begin{bmatrix} \frac{I_{zz}}{I_c} \cdot L_{\delta_d} + \frac{I_{xz}}{I_c} \cdot N_{\delta_d} & \frac{I_{zz}}{I_c} \cdot L_{\delta_f} + \frac{I_{xz}}{I_c} \cdot N_{\delta_f} & \frac{I_{zz}}{I_c} \cdot L_{\delta_w} + \frac{I_{xz}}{I_c} \cdot N_{\delta_w} & \frac{I_{zz}}{I_c} \cdot L_{\delta_t} + \frac{I_{xz}}{I_c} \cdot N_{\delta_t} \\ \frac{I_{xz}}{I_c} \cdot L_{\delta_d} + \frac{I_{xx}}{I_c} \cdot N_{\delta_d} & \frac{I_{xz}}{I_c} \cdot L_{\delta_f} + \frac{I_{xx}}{I_c} \cdot N_{\delta_f} & \frac{I_{xz}}{I_c} \cdot L_{\delta_w} + \frac{I_{xx}}{I_c} \cdot N_{\delta_w} & \frac{I_{xz}}{I_c} \cdot L_{\delta_t} + \frac{I_{xx}}{I_c} \\ \frac{Y_{\delta_d}}{m} & \frac{Y_{\delta_f}}{m} & \frac{Y_{\delta_w}}{m} & \frac{Y_{\delta_t}}{m} \\ 0 & 0 & 0 & 0 \end{bmatrix} \cdot \begin{bmatrix} \delta_d \\ \delta_f \\ \delta_w \\ \delta_t \end{bmatrix} \tag{B.16}$$

In Equation B.16 the L_p, L_r, L_v, N_p, N_r, N_v, Y_p, Y_r and Y_v are the stability derivatives, while the L_{δ_d}, L_{δ_f}, L_{δ_w}, L_{δ_t}, N_{δ_d}, N_{δ_f}, N_{δ_w}, N_{δ_t}, Y_{δ_d}, Y_{δ_f}, Y_{δ_w} and Y_{δ_t} are the control derivatives. What's more, $I_c = I_{xx} \cdot I_{zz} - I_{xz}^2$. In this research the linear time-invariant state space for the lateral dynamics, shown in Equation B.16, is used. This state space can be reduced by decoupling the roll and yaw dynamics. This leads to two systems, one for the roll dynamics, which is shown in Equation B.17, and one for the yaw dynamics, shown in Equation B.18.

$$\begin{bmatrix} \dot{p} \\ \dot{v} \\ \dot{\phi} \end{bmatrix} = \begin{bmatrix} \frac{I_{zz}}{I_c} \cdot L_p & \frac{I_{zz}}{I_c} \cdot L_v & 0 \\ \frac{Y_p}{m} + w_0 & \frac{Y_v}{m} & g \cdot \cos(\theta_0) \cdot \cos(\phi_0) \\ 1 & 0 & 0 \end{bmatrix} \cdot \begin{bmatrix} p \\ v \\ \phi \end{bmatrix} + \begin{bmatrix} \frac{I_{zz}}{I_c} \cdot L_{\delta_d} & \frac{I_{zz}}{I_c} \cdot L_{\delta_f} & \frac{I_{zz}}{I_c} \cdot L_{\delta_w} & \frac{I_{zz}}{I_c} \cdot L_{\delta_t} \\ \frac{Y_{\delta_d}}{m} & \frac{Y_{\delta_f}}{m} & \frac{Y_{\delta_w}}{m} & \frac{Y_{\delta_t}}{m} \\ 0 & 0 & 0 & 0 \end{bmatrix} \cdot \begin{bmatrix} \delta_d \\ \delta_f \\ \delta_w \\ \delta_t \end{bmatrix} \tag{B.17}$$

$$\dot{r} = \frac{I_{xz}}{I_c} \cdot N_r \cdot r + \begin{bmatrix} \frac{I_{xz}}{I_c} \cdot N_{\delta_d} & \frac{I_{xz}}{I_c} \cdot N_{\delta_f} & \frac{I_{xz}}{I_c} \cdot N_{\delta_w} & \frac{I_{xz}}{I_c} \cdot N_{\delta_t} \end{bmatrix} \cdot \begin{bmatrix} \delta_d \\ \delta_f \\ \delta_w \\ \delta_t \end{bmatrix} \tag{B.18}$$

C

Setup regression matrices

In this appendix the setup for the regression matrix is explained which are used for the ordinary least squares estimation. As was elaborated on in Section 4.3.2, for a state-space system Equations C.1 and C.2 are used in order to apply the equation-error approach.

$$Y(t) = \Theta \cdot \Phi(t) + E(t) \tag{C.1}$$

$$\begin{aligned} Y(t) &= \begin{bmatrix} \dot{x}(t) \\ y(t) \end{bmatrix}, \qquad \Theta = \begin{bmatrix} A & B \\ C & D \end{bmatrix} \\ \Phi(t) &= \begin{bmatrix} x(t) \\ u(t) \end{bmatrix}, \quad E(t) = \begin{bmatrix} w(t) \\ v(t) \end{bmatrix} \end{aligned} \tag{C.2}$$

Two different sets of state-space systems are used, a grey-box system which uses the state-space which was derived in Appendix B, and a black-box system which was shown in Section 4.2.2. The regression matrix for the former is shown in Section C.1, and for the latter in Section C.2.

C.1. Grey-box model regression matrix

For the grey-box model identification the state-space system defined in Equation C.3 is used.

$$\begin{bmatrix} \dot{p} \\ \dot{r} \\ \dot{v} \\ \dot{\phi} \end{bmatrix} = \begin{bmatrix} \frac{I_{zz}}{I_c} \cdot L_p + \frac{I_{xz}}{I_c} \cdot N_p & \frac{I_{zz}}{I_c} \cdot L_r + \frac{I_{xz}}{I_c} \cdot N_r & \frac{I_{zz}}{I_c} \cdot L_v + \frac{I_{xz}}{I_c} \cdot N_v & 0 \\ \frac{I_{xz}}{I_c} \cdot L_p + \frac{I_{xx}}{I_c} \cdot N_p & \frac{I_{xz}}{I_c} \cdot L_r + \frac{I_{xx}}{I_c} \cdot N_r & \frac{I_{xz}}{I_c} \cdot L_v + \frac{I_{xx}}{I_c} \cdot N_v & 0 \\ \frac{Y_p}{m} + w_0 & \frac{Y_r}{m} - u_0 & \frac{Y_v}{m} & g \cdot \cos(\theta_0) \cdot \cos(\phi_0) \\ 1 & \tan(\theta_0) \cdot \cos(\phi_0) & 0 & 0 \end{bmatrix} \cdot \begin{bmatrix} p \\ r \\ v \\ \phi \end{bmatrix} + \\ \begin{bmatrix} \frac{I_{zz}}{I_c} \cdot L_{\delta_d} + \frac{I_{xz}}{I_c} \cdot N_{\delta_d} & \frac{I_{zz}}{I_c} \cdot L_{\delta_f} + \frac{I_{xz}}{I_c} \cdot N_{\delta_f} & \frac{I_{zz}}{I_c} \cdot L_{\delta_w} + \frac{I_{xz}}{I_c} \cdot N_{\delta_w} & \frac{I_{zz}}{I_c} \cdot L_{\delta_t} + \frac{I_{xz}}{I_c} \cdot N_{\delta_t} \\ \frac{I_{xz}}{I_c} \cdot L_{\delta_d} + \frac{I_{xx}}{I_c} \cdot N_{\delta_d} & \frac{I_{xz}}{I_c} \cdot L_{\delta_f} + \frac{I_{xx}}{I_c} \cdot N_{\delta_f} & \frac{I_{xz}}{I_c} \cdot L_{\delta_w} + \frac{I_{xx}}{I_c} \cdot N_{\delta_w} & \frac{I_{xz}}{I_c} \cdot L_{\delta_t} + \frac{I_{xx}}{I_c} \\ \frac{Y_{\delta_d}}{m} & \frac{Y_{\delta_f}}{m} & \frac{Y_{\delta_w}}{m} & \frac{Y_{\delta_t}}{m} \\ 0 & 0 & 0 & 0 \end{bmatrix} \cdot \begin{bmatrix} \delta_d \\ \delta_f \\ \delta_w \\ \delta_t \end{bmatrix} \end{bmatrix} \tag{C.3}$$

The output of the systems $y(t)$ are states themselves, as in Equation C.4.

$$y(t) = \begin{bmatrix} p \\ r \\ v \\ \phi \end{bmatrix} \tag{C.4}$$

This means that the C matrix is an identity matrix which does not contain any parameters ans that the D matrix is a matrix full of zeros. This simplifies the terms in Equation C.2, resulting in Equation C.5.

$$\begin{aligned} Y(t) &= \begin{bmatrix} \dot{x}(t) \end{bmatrix}, \qquad \Theta = \begin{bmatrix} A & B \end{bmatrix} \\ \Phi(t) &= \begin{bmatrix} x(t) \\ u(t) \end{bmatrix}, \quad E(t) = \begin{bmatrix} w(t) \end{bmatrix} \end{aligned} \tag{C.5}$$

Before the A and B matrices can be used in order to form the Θ matrix, one issue needs to be resolved. Namely, that there are coupled parameters in the A matrix, i.e. there are two parameters which are present in a single entry of the matrix, for example L_p and N_p. There are two approaches for resolving this issue. The first one is to assume that the L and N parameters are decoupled, i.e. that the N parameters do not influence the roll acceleration $\dot{p}$ and that the L parameters do not influence the yaw acceleration $\dot{r}$. With this assumption the state-space system can be simplified, as presented in Equation C.6 [13].

$$\begin{bmatrix} \dot{p} \\ \dot{r} \\ \dot{v} \\ \dot{\phi} \end{bmatrix} = \begin{bmatrix} \frac{I_{zz}}{I_c} \cdot L_p & \frac{I_{zz}}{I_c} \cdot L_r & \frac{I_{zz}}{I_c} \cdot L_v & 0 \\ \frac{I_{xx}}{I_c} \cdot N_p & \frac{I_{xx}}{I_c} \cdot N_r & \frac{I_{xx}}{I_c} \cdot N_v & 0 \\ \frac{Y_p}{m} + w_0 & \frac{Y_r}{m} - u_0 & \frac{Y_v}{m} & g \cdot \cos(\theta_0) \cdot \cos(\phi_0) \\ 1 & \tan(\theta_0) \cdot \cos(\phi_0) & 0 & 0 \end{bmatrix} \cdot \begin{bmatrix} p \\ r \\ v \\ \phi \end{bmatrix} + \begin{bmatrix} \frac{I_{zz}}{I_c} \cdot L_{\delta_d} & \frac{I_{zz}}{I_c} \cdot L_{\delta_f} & \frac{I_{zz}}{I_c} \cdot L_{\delta_w} & \frac{I_{zz}}{I_c} \cdot L_{\delta_t} \\ \frac{I_{xx}}{I_c} \cdot N_{\delta_d} & \frac{I_{xx}}{I_c} \cdot N_{\delta_f} & \frac{I_{xx}}{I_c} \cdot N_{\delta_w} & \frac{I_{xx}}{I_c} \cdot N_{\delta_t} \\ \frac{Y_{\delta_d}}{m} & \frac{Y_{\delta_f}}{m} & \frac{Y_{\delta_w}}{m} & \frac{Y_{\delta_t}}{m} \\ 0 & 0 & 0 & 0 \end{bmatrix} \cdot \begin{bmatrix} \delta_d \\ \delta_f \\ \delta_w \\ \delta_t \end{bmatrix} \tag{C.6}$$

The state-space system shown in C.6 can then be used in order to get to the form shown in Equation C.1, resulting in Equation C.7.

$$\begin{bmatrix} \dot{p} \\ \dot{r} \\ \dot{v} \\ \dot{\phi} \end{bmatrix} = \begin{bmatrix} \frac{I_{zz}}{I_c} \cdot L_p & \frac{I_{zz}}{I_c} \cdot L_r & \frac{I_{zz}}{I_c} \cdot L_v & 0 & \frac{I_{zz}}{I_c} \cdot L_{\delta_d} & \frac{I_{zz}}{I_c} \cdot L_{\delta_f} & \frac{I_{zz}}{I_c} \cdot L_{\delta_w} & \frac{I_{zz}}{I_c} \cdot L_{\delta_t} \\ \frac{I_{xx}}{I_c} \cdot N_p & \frac{I_{xx}}{I_c} \cdot N_r & \frac{I_{xx}}{I_c} \cdot N_v & 0 & \frac{I_{xx}}{I_c} \cdot N_{\delta_d} & \frac{I_{xx}}{I_c} \cdot N_{\delta_f} & \frac{I_{xx}}{I_c} \cdot N_{\delta_w} & \frac{I_{xx}}{I_c} \cdot N_{\delta_t} \\ \frac{Y_p}{m} + w_0 & \frac{Y_r}{m} - u_0 & \frac{Y_v}{m} & g \cdot \cos(\theta_0) \cdot \cos(\phi_0) & \frac{Y_{\delta_d}}{m} & \frac{Y_{\delta_f}}{m} & \frac{Y_{\delta_w}}{m} & \frac{Y_{\delta_t}}{m} \\ 1 & \tan(\theta_0) \cdot \cos(\phi_0) & 0 & 0 & 0 & 0 & 0 & 0 \end{bmatrix} \cdot \begin{bmatrix} p \\ r \\ v \\ \phi \\ \delta_d \\ \delta_f \\ \delta_w \\ \delta_t \end{bmatrix} \tag{C.7}$$

The constant terms should be removed form the regression matrix, which can be done by moving them to the left hand side of Equation C.7, resulting in Equation C.8.

$$\begin{bmatrix} \dot{p} \\ \dot{r} \\ \dot{v} - w_0 \cdot p + u_0 \cdot r - g \cdot \cos(\theta_0) \cdot \cos(\phi_0) \cdot \phi \\ \dot{\phi} - p - \tan(\theta_0) \cdot \cos(\phi_0) \cdot r \end{bmatrix} = \begin{bmatrix} \frac{I_{zz}}{I_c} \cdot L_p & \frac{I_{zz}}{I_c} \cdot L_r & \frac{I_{zz}}{I_c} \cdot L_v & 0 & \frac{I_{zz}}{I_c} \cdot L_{\delta_d} & \frac{I_{zz}}{I_c} \cdot L_{\delta_f} & \frac{I_{zz}}{I_c} \cdot L_{\delta_w} & \frac{I_{zz}}{I_c} \cdot L_{\delta_t} \\ \frac{I_{xx}}{I_c} \cdot N_p & \frac{I_{xx}}{I_c} \cdot N_r & \frac{I_{xx}}{I_c} \cdot N_v & 0 & \frac{I_{xx}}{I_c} \cdot N_{\delta_d} & \frac{I_{xx}}{I_c} \cdot N_{\delta_f} & \frac{I_{xx}}{I_c} \cdot N_{\delta_w} & \frac{I_{xx}}{I_c} \cdot N_{\delta_t} \\ \frac{Y_p}{m} & \frac{Y_r}{m} & \frac{Y_v}{m} & 0 & \frac{Y_{\delta_d}}{m} & \frac{Y_{\delta_f}}{m} & \frac{Y_{\delta_w}}{m} & \frac{Y_{\delta_t}}{m} \\ 0 & 0 & 0 & 0 & 0 & 0 & 0 & 0 \end{bmatrix} \cdot \begin{bmatrix} p \\ r \\ v \\ \phi \\ \delta_d \\ \delta_f \\ \delta_w \\ \delta_t \end{bmatrix} \tag{C.8}$$

It can be seen that there is a column and row full of zeroes in the matrix at the right hand side of Equation C.8. These can be omitted in order to reduce the size of the matrix, taking the form of Equation C.9.

$$\begin{bmatrix} \dot{p} \\ \dot{r} \\ \dot{v} - w_0 \cdot p + u_0 \cdot r - g \cdot \cos(\theta_0) \cdot \cos(\phi_0) \cdot \phi \end{bmatrix} =$$

$$\begin{bmatrix} \frac{I_{zz}}{I_c} \cdot L_p & \frac{I_{zz}}{I_c} \cdot L_r & \frac{I_{zz}}{I_c} \cdot L_v & \frac{I_{zz}}{I_c} \cdot L_{\delta_d} & \frac{I_{zz}}{I_c} \cdot L_{\delta_f} & \frac{I_{zz}}{I_c} \cdot L_{\delta_w} & \frac{I_{zz}}{I_c} \cdot L_{\delta_t} \\ \frac{I_{xx}}{I_c} \cdot N_p & \frac{I_{xx}}{I_c} \cdot N_r & \frac{I_{xx}}{I_c} \cdot N_v & \frac{I_{xx}}{I_c} \cdot N_{\delta_d} & \frac{I_{xx}}{I_c} \cdot N_{\delta_f} & \frac{I_{xx}}{I_c} \cdot N_{\delta_w} & \frac{I_{xx}}{I_c} \cdot N_{\delta_t} \\ \frac{Y_p}{m} & \frac{Y_r}{m} & \frac{Y_v}{m} & \frac{Y_{\delta_d}}{m} & \frac{Y_{\delta_f}}{m} & \frac{Y_{\delta_w}}{m} & \frac{Y_{\delta_t}}{m} \end{bmatrix} \cdot \begin{bmatrix} p \\ r \\ v \\ \delta_d \\ \delta_f \\ \delta_w \\ \delta_t \end{bmatrix} \tag{C.9}$$

The third terms in the vector in the left-hand side of Equation C.9 can be simplified by substituting Equation C.10.

$$\dot{v}^*_{full} = \dot{v} - w_0 \cdot p + u_0 \cdot r - g \cdot \cos(\theta_0) \cdot \cos(\phi_0) \cdot \phi \tag{C.10}$$

There are still constant terms which are multiplied with the parameters. These can be omitted by moving them to the left hand side as well, resulting in Equation C.11.

$$\begin{bmatrix} \frac{I_c}{I_{zz}} \cdot \dot{p} \\ \frac{I_c}{I_{xx}} \cdot \dot{r} \\ m \cdot \dot{v}^*_{full} \end{bmatrix} = \begin{bmatrix} L_p & L_r & L_v & L_{\delta_d} & L_{\delta_f} & L_{\delta_w} & L_{\delta_t} \\ N_p & N_r & N_v & N_{\delta_d} & N_{\delta_f} & N_{\delta_w} & N_{\delta_t} \\ Y_p & Y_r & Y_v & Y_{\delta_d} & Y_{\delta_f} & Y_{\delta_w} & Y_{\delta_t} \end{bmatrix} \cdot \begin{bmatrix} p \\ r \\ v \\ \delta_d \\ \delta_f \\ \delta_w \\ \delta_t \end{bmatrix} \tag{C.11}$$

Using Equation C.11 an OLS estimator can be setup for each output on the left hand side of the equation. The three output equations are shown in Equations C.12 to C.14

$$\begin{aligned} \frac{I_c}{I_{zz}} \cdot \dot{p} &= \begin{bmatrix} p & r & v & \delta_d & \delta_f & \delta_w & \delta_t \end{bmatrix} \cdot \begin{bmatrix} L_p \\ L_r \\ L_v \\ L_{\delta_d} \\ L_{\delta_f} \\ L_{\delta_w} \\ L_{\delta_t} \end{bmatrix} \\ &= A_{grey} \cdot \theta_L \end{aligned} \tag{C.12}$$

$$\begin{aligned} \frac{I_c}{I_{xx}} \cdot \dot{r} &= \begin{bmatrix} p & r & v & \delta_d & \delta_f & \delta_w & \delta_t \end{bmatrix} \cdot \begin{bmatrix} N_p \\ N_r \\ N_v \\ N_{\delta_d} \\ N_{\delta_f} \\ N_{\delta_w} \\ N_{\delta_t} \end{bmatrix} \\ &= A_{grey} \cdot \theta_N \end{aligned} \tag{C.13}$$

$$
\begin{aligned}
m \cdot \dot{v}^*_{full} &= \begin{bmatrix} p & r & v & \delta_d & \delta_f & \delta_w & \delta_t \end{bmatrix} \cdot \begin{bmatrix} Y_p \\ Y_r \\ Y_v \\ Y_{\delta_d} \\ Y_{\delta_f} \\ Y_{\delta_w} \\ Y_{\delta_t} \end{bmatrix} \\
&= A_{grey} \cdot \theta_Y
\end{aligned} \tag{C.14}
$$

Where A_{grey} is the regression matrix and $\theta_L, \theta_N, \theta_Y$ are the parameter vectors for the $L-$, $N-$ and $Y-$parameters. The parameters can the be determined using the OLS estimator, resulting in Equation C.20.

$$
\begin{aligned}
\hat{\theta}_L &= \left(A^T_{grey} \cdot A_{grey} \right)^{-1} \cdot A^T_{grey} \cdot \frac{I_c}{I_{zz}} \cdot \dot{p} \\
\hat{\theta}_N &= \left(A^T_{grey} \cdot A_{grey} \right)^{-1} \cdot A^T_{grey} \cdot \frac{I_c}{I_{xx}} \cdot \dot{r} \\
\hat{\theta}_Y &= \left(A^T_{grey} \cdot A_{grey} \right)^{-1} \cdot A^T_{grey} \cdot m \cdot \dot{v}^*_{full}
\end{aligned} \tag{C.15}
$$

The second approach to solve the coupling of the L and N parameters is to use the aerodynamics forces and moments. As was explained in Appendix B, a linear model structure was used for the forces and moments, shown in Equation C.16.

$$
\begin{aligned}
Y &= Y_0 + Y_p \Delta p + Y_r \Delta r + Y_v \Delta v + Y_{\delta_d} \Delta \delta_d + Y_{\delta_f} \Delta \delta_f + Y_{\delta_w} \Delta \delta_w + Y_{\delta_t} \Delta \delta_t \\
L &= L_0 + L_p \Delta p + L_r \Delta r + L_v \Delta v + L_{\delta_d} \Delta \delta_d + L_{\delta_f} \Delta \delta_f + L_{\delta_w} \Delta \delta_w + L_{\delta_t} \Delta \delta_t \\
N &= N_0 + N_p \Delta p + N_r \Delta r + N_v \Delta v + N_{\delta_d} \Delta \delta_d + N_{\delta_f} \Delta \delta_f + N_{\delta_w} \Delta \delta_w + N_{\delta_t} \Delta \delta_t
\end{aligned} \tag{C.16}
$$

Equation C.16 can be written in vector from, which results in Equations C.17 to C.19.

$$
\begin{aligned}
Y &= \begin{bmatrix} 1 & p & r & v & \delta_d & \delta_f & \delta_w & \delta_t \end{bmatrix} \cdot \begin{bmatrix} Y_0 \\ Y_p \\ Y_r \\ Y_v \\ Y_{\delta_d} \\ Y_{\delta_f} \\ Y_{\delta_w} \\ Y_{\delta_t} \end{bmatrix} \\
&= A_{aero} \cdot \theta_Y
\end{aligned} \tag{C.17}
$$

$$
\begin{aligned}
L &= \begin{bmatrix} 1 & p & r & v & \delta_d & \delta_f & \delta_w & \delta_t \end{bmatrix} \cdot \begin{bmatrix} L_0 \\ L_p \\ L_r \\ L_v \\ L_{\delta_d} \\ L_{\delta_f} \\ L_{\delta_w} \\ L_{\delta_t} \end{bmatrix} \\
&= A_{aero} \cdot \theta_L
\end{aligned} \tag{C.18}
$$

$$
\begin{aligned}
N &= \begin{bmatrix} 1 & p & r & v & \delta_d & \delta_f & \delta_w & \delta_t \end{bmatrix} \cdot \begin{bmatrix} N_0 \\ N_p \\ N_r \\ N_v \\ N_{\delta_d} \\ N_{\delta_f} \\ N_{\delta_w} \\ N_{\delta_t} \end{bmatrix} \\
&= A_{aero} \cdot \theta_N
\end{aligned} \tag{C.19}
$$

Where A_{aero} is the regression matrix and $\theta_L, \theta_N, \theta_Y$ are the parameter vectors for the $L-$, $N-$ and $Y-$parameters. The parameters can then be determined using the OLS estimator, which results in Equation C.20.

$$
\begin{aligned}
\hat{\theta}_Y &= \left(A_{aero}^T \cdot A_{aero}\right)^{-1} \cdot A_{aero}^T \cdot \frac{I_c}{I_{zz}} \cdot Y \\
\hat{\theta}_L &= \left(A_{aero}^T \cdot A_{aero}\right)^{-1} \cdot A_{aero}^T \cdot \frac{I_c}{I_{xx}} \cdot L \\
\hat{\theta}_N &= \left(A_{aero}^T \cdot A_{aero}\right)^{-1} \cdot A_{aero}^T \cdot \frac{I_c}{I_{xx}} \cdot N
\end{aligned} \tag{C.20}
$$

If the reduced state-space system derived in Appendix B is used, the regression matrices can be determined in a similar way as was done when using the first approach to decouple the L and N parameters. The reduced state-pace system will take the form of Equation C.21.

$$
\begin{bmatrix} \dot{p} \\ \dot{v} \\ \dot{\phi} \end{bmatrix} = \begin{bmatrix} \frac{I_{zz}}{I_c} \cdot L_p & \frac{I_{zz}}{I_c} \cdot L_v & 0 \\ \frac{Y_p}{m} + w_o & \frac{Y_v}{m} & g \cdot \cos(\theta_0) \cdot \cos(\phi_0) \\ 1 & 0 & 0 \end{bmatrix} \cdot \begin{bmatrix} p \\ v \\ \phi \end{bmatrix} + \begin{bmatrix} \frac{I_{zz}}{I_c} \cdot L_{\delta_d} & \frac{I_{zz}}{I_c} \cdot L_{\delta_f} & \frac{I_{zz}}{I_c} \cdot L_{\delta_w} & \frac{I_{zz}}{I_c} \cdot L_{\delta_t} \\ \frac{Y_{\delta_d}}{m} & \frac{Y_{\delta_f}}{m} & \frac{Y_{\delta_w}}{m} & \frac{Y_{\delta_t}}{m} \\ 0 & 0 & 0 & 0 \end{bmatrix} \cdot \begin{bmatrix} \delta_d \\ \delta_f \\ \delta_w \\ \delta_t \end{bmatrix} \tag{C.21}
$$

Equation C.21 can be rewritten to Equation C.22.

$$
\begin{bmatrix} \dot{p} \\ \dot{v} \\ \dot{\phi} \end{bmatrix} = \begin{bmatrix} \frac{I_{zz}}{I_c} \cdot L_p & \frac{I_{zz}}{I_c} \cdot L_v & 0 & \frac{I_{zz}}{I_c} \cdot L_{\delta_d} & \frac{I_{zz}}{I_c} \cdot L_{\delta_f} & \frac{I_{zz}}{I_c} \cdot L_{\delta_w} & \frac{I_{zz}}{I_c} \cdot L_{\delta_t} \\ \frac{Y_p}{m} + w_0 & \frac{Y_v}{m} & g \cdot \cos(\theta_0) \cdot \cos(\phi_0) & \frac{Y_{\delta_d}}{m} & \frac{Y_{\delta_f}}{m} & \frac{Y_{\delta_w}}{m} & \frac{Y_{\delta_t}}{m} \\ 1 & 0 & 0 & 0 & 0 & 0 & 0 \end{bmatrix} \cdot \begin{bmatrix} p \\ v \\ \phi \\ \delta_d \\ \delta_f \\ \delta_w \\ \delta_t \end{bmatrix} \tag{C.22}
$$

The constants in Equation C.22 can then be brought to the left hand side of the equation, which results in Equation C.23

$$
\begin{bmatrix} \dot{p} \\ \dot{v} - w_0 \cdot p - g \cdot \cos(\theta_0) \cdot \cos(\phi_0) \cdot \phi \\ \dot{\phi} - p \end{bmatrix} = \begin{bmatrix} \frac{I_{zz}}{I_c} \cdot L_p & \frac{I_{zz}}{I_c} \cdot L_v & 0 & \frac{I_{zz}}{I_c} \cdot L_{\delta_d} & \frac{I_{zz}}{I_c} \cdot L_{\delta_f} & \frac{I_{zz}}{I_c} \cdot L_{\delta_w} & \frac{I_{zz}}{I_c} \cdot L_{\delta_t} \\ \frac{Y_p}{m} & \frac{Y_v}{m} & 0 & \frac{Y_{\delta_d}}{m} & \frac{Y_{\delta_f}}{m} & \frac{Y_{\delta_w}}{m} & \frac{Y_{\delta_t}}{m} \\ 0 & 0 & 0 & 0 & 0 & 0 & 0 \end{bmatrix} \cdot \begin{bmatrix} p \\ v \\ \phi \\ \delta_d \\ \delta_f \\ \delta_w \\ \delta_t \end{bmatrix} \tag{C.23}
$$

The column and row with only zeros in the matrix on the right hand side of Equation C.23 can be omitted, resulting in Equation C.24.

$$\begin{bmatrix} \dot{p} \\ \dot{v} - w_0 \cdot p - g \cdot \cos(\theta_0) \cdot \cos(\phi_0) \cdot \phi \end{bmatrix} = \begin{bmatrix} \frac{I_{zz}}{I_c} \cdot L_p & \frac{I_{zz}}{I_c} \cdot L_v & \frac{I_{zz}}{I_c} \cdot L_{\delta_d} & \frac{I_{zz}}{I_c} \cdot L_{\delta_f} & \frac{I_{zz}}{I_c} \cdot L_{\delta_w} & \frac{I_{zz}}{I_c} \cdot L_{\delta_t} \\ \frac{Y_p}{m} & \frac{Y_v}{m} & \frac{Y_{\delta_d}}{m} & \frac{Y_{\delta_f}}{m} & \frac{Y_{\delta_w}}{m} & \frac{Y_{\delta_t}}{m} \end{bmatrix} \cdot \begin{bmatrix} p \\ v \\ \delta_d \\ \delta_f \\ \delta_w \\ \delta_t \end{bmatrix} \tag{C.24}$$

Similar to as it was done for the full grey-box model, the second term in the vector in the left-hand side of Equation C.24 can be simplified by substitution of Equation C.25.

$$\dot{v}^*_{red} = \dot{v} - w_0 \cdot p - g \cdot \cos(\theta_0) \cdot \cos(\phi_0) \cdot \phi \tag{C.25}$$

The constant terms which are multiplied with the parameters in Equation C.24 can be brought to the left hand side, which results in Equation C.26.

$$\begin{bmatrix} \frac{I_c}{I_{zz}} \dot{p} \\ m \cdot \dot{v}^*_{red} \end{bmatrix} = \begin{bmatrix} L_p & L_v & L_{\delta_d} & L_{\delta_f} & L_{\delta_w} & L_{\delta_t} \\ Y_p & Y_v & Y_{\delta_d} & Y_{\delta_f} & Y_{\delta_w} & Y_{\delta_t} \end{bmatrix} \cdot \begin{bmatrix} p \\ v \\ \delta_d \\ \delta_f \\ \delta_w \\ \delta_t \end{bmatrix} \tag{C.26}$$

Two output equations are then formulated using Equation C.26, which are shown in Equation C.27 and C.28.

$$\begin{aligned} \frac{I_c}{I_{zz}} \cdot \dot{p} &= \begin{bmatrix} p & v & \delta_d & \delta_f & \delta_w & \delta_t \end{bmatrix} \cdot \begin{bmatrix} L_p \\ L_v \\ L_{\delta_d} \\ L_{\delta_f} \\ L_{\delta_w} \\ L_{\delta_t} \end{bmatrix} \\ &= A_{red} \cdot \theta_L \end{aligned} \tag{C.27}$$

$$\begin{aligned} m \cdot \dot{v}^*_{red} &= \begin{bmatrix} p & v & \delta_d & \delta_f & \delta_w & \delta_t \end{bmatrix} \cdot \begin{bmatrix} Y_p \\ Y_v \\ Y_{\delta_d} \\ Y_{\delta_f} \\ Y_{\delta_w} \\ Y_{\delta_t} \end{bmatrix} \\ &= A_{red} \cdot \theta_Y \end{aligned} \tag{C.28}$$

Where A_{red} is the regression matrix and θ_L and θ_Y are the parameter vectors for the L and Y parameters. The parameters can then be estimated using Equation C.29.

$$\begin{aligned} \hat{\theta}_L &= \left(A^T_{red} \cdot A_{red}\right)^{-1} \cdot A^T_{red} \cdot \frac{I_c}{I_{zz}} \cdot \dot{p} \\ \hat{\theta}_Y &= \left(A^T_{red} \cdot A_{red}\right)^{-1} \cdot A^T_{red} \cdot m \cdot \dot{v}^*_{red} \end{aligned} \tag{C.29}$$

C.2. Black-box model regression matrix

The OLS estimation for the black-box state-space system is done in a similar way as was done for the grey-box state-space system in Section C.1. The black-box state-space system is shown in Equation C.30.

$$\begin{bmatrix} \dot{p} \\ \dot{r} \\ \dot{v} \\ \dot{\phi} \end{bmatrix} = \begin{bmatrix} a_{11} & a_{12} & a_{13} & a_{14} \\ a_{21} & a_{22} & a_{23} & a_{24} \\ a_{31} & a_{32} & a_{33} & a_{34} \\ a_{41} & a_{42} & a_{43} & a_{44} \end{bmatrix} \cdot \begin{bmatrix} p \\ r \\ v \\ \phi \end{bmatrix} + \begin{bmatrix} b_{11} & b_{12} & b_{13} & b_{14} \\ b_{21} & b_{22} & b_{23} & b_{24} \\ b_{31} & b_{32} & b_{33} & b_{34} \\ b_{41} & b_{42} & b_{43} & b_{44} \end{bmatrix} \cdot \begin{bmatrix} \delta_d \\ \delta_f \\ \delta_w \\ \delta_t \end{bmatrix} \tag{C.30}$$

Equation C.30 can be written in the form of Equation C.5, which results in Equation C.31.

$$\begin{bmatrix} \dot{p} \\ \dot{r} \\ \dot{v} \\ \dot{\phi} \end{bmatrix} = \begin{bmatrix} a_{11} & a_{12} & a_{13} & a_{14} & b_{11} & b_{12} & b_{13} & b_{14} \\ a_{21} & a_{22} & a_{23} & a_{24} & b_{21} & b_{22} & b_{23} & b_{24} \\ a_{31} & a_{32} & a_{33} & a_{34} & b_{31} & b_{32} & b_{33} & b_{34} \\ a_{41} & a_{42} & a_{43} & a_{44} & b_{41} & b_{42} & b_{43} & b_{44} \end{bmatrix} \cdot \begin{bmatrix} p \\ r \\ v \\ \phi \\ \delta_d \\ \delta_f \\ \delta_w \\ \delta_t \end{bmatrix} \tag{C.31}$$

With Equation C.31 four output equations can be formulated, defined in Equations C.32 to C.35.

$$\begin{aligned} \dot{p} &= \begin{bmatrix} p & r & v & \phi & \delta_d & \delta_f & \delta_w & \delta_t \end{bmatrix} \cdot \begin{bmatrix} a_{11} \\ a_{12} \\ a_{13} \\ a_{14} \\ b_{11} \\ b_{12} \\ b_{13} \\ b_{14} \end{bmatrix} \\ &= A_{black} \cdot \theta_p \end{aligned} \tag{C.32}$$

$$\begin{aligned} \dot{r} &= \begin{bmatrix} p & r & v & \phi & \delta_d & \delta_f & \delta_w & \delta_t \end{bmatrix} \cdot \begin{bmatrix} a_{21} \\ a_{22} \\ a_{23} \\ a_{24} \\ b_{21} \\ b_{22} \\ b_{23} \\ b_{24} \end{bmatrix} \\ &= A_{black} \cdot \theta_r \end{aligned} \tag{C.33}$$

$$\begin{aligned} \dot{r} &= \begin{bmatrix} p & r & v & \phi & \delta_d & \delta_f & \delta_w & \delta_t \end{bmatrix} \cdot \begin{bmatrix} a_{31} \\ a_{32} \\ a_{33} \\ a_{34} \\ b_{31} \\ b_{32} \\ b_{33} \\ b_{34} \end{bmatrix} \\ &= A_{black} \cdot \theta_v \end{aligned} \tag{C.34}$$

$$\begin{aligned}\dot{\phi} &= \begin{bmatrix} p & r & v & \phi & \delta_d & \delta_f & \delta_w & \delta_t \end{bmatrix} \cdot \begin{bmatrix} a_{41} \\ a_{42} \\ a_{43} \\ a_{44} \\ b_{41} \\ b_{42} \\ b_{43} \\ b_{44} \end{bmatrix} \\ &= A_{black} \cdot \theta_\phi \end{aligned} \tag{C.35}$$

Where A_{black} is the regression matrix and $\theta_p, \theta_r, \theta_v, \theta_\phi$ are the parameter vectors. The parameter vectors can be determined using Equation C.36.

$$\begin{aligned} \hat{\theta}_p &= \left(A_{black}^T \cdot A_{black}\right)^{-1} \cdot A_{black}^T \cdot \dot{p} \\ \hat{\theta}_r &= \left(A_{black}^T \cdot A_{black}\right)^{-1} \cdot A_{black}^T \cdot \dot{r} \\ \hat{\theta}_v &= \left(A_{black}^T \cdot A_{black}\right)^{-1} \cdot A_{black}^T \cdot \dot{v} \\ \hat{\theta}_\phi &= \left(A_{black}^T \cdot A_{black}\right)^{-1} \cdot A_{black}^T \cdot \dot{\phi} \end{aligned} \tag{C.36}$$

The black-box state-space system can also be reduced in a similar way as the grey-box one. The reduced black-box state-space system is shown in Equation C.37.

$$\begin{bmatrix} \dot{p} \\ \dot{v} \\ \dot{\phi} \end{bmatrix} = \begin{bmatrix} a_{11} & a_{12} & a_{13} \\ a_{21} & a_{22} & a_{23} \\ a_{31} & a_{32} & a_{33} \end{bmatrix} \cdot \begin{bmatrix} p \\ v \\ \phi \end{bmatrix} + \begin{bmatrix} b_{11} & b_{12} & b_{13} & b_{14} \\ b_{21} & b_{22} & b_{23} & b_{24} \\ b_{31} & b_{32} & b_{33} & b_{34} \end{bmatrix} \cdot \begin{bmatrix} \delta_d \\ \delta_f \\ \delta_w \\ \delta_t \end{bmatrix} \tag{C.37}$$

Then, following the same approach as was done for the full black-box system, output equations can be formulated, shown in Equations C.38 to C.40.

$$\begin{aligned}\dot{p} &= \begin{bmatrix} p & v & \phi & \delta_d & \delta_f & \delta_w & \delta_t \end{bmatrix} \cdot \begin{bmatrix} a_{11} \\ a_{12} \\ a_{13} \\ b_{11} \\ b_{12} \\ b_{13} \\ b_{14} \end{bmatrix} \\ &= A_{black_{red}} \cdot \theta_p \end{aligned} \tag{C.38}$$

$$\begin{aligned}\dot{r} &= \begin{bmatrix} p & v & \phi & \delta_d & \delta_f & \delta_w & \delta_t \end{bmatrix} \cdot \begin{bmatrix} a_{21} \\ a_{22} \\ a_{23} \\ b_{21} \\ b_{22} \\ b_{23} \\ b_{24} \end{bmatrix} \\ &= A_{black_{red}} \cdot \theta_v \end{aligned} \tag{C.39}$$

$$\begin{aligned}\dot{\phi} &= \begin{bmatrix} p & v & \phi & \delta_d & \delta_f & \delta_w & \delta_t \end{bmatrix} \cdot \begin{bmatrix} a_{31} \\ a_{32} \\ a_{33} \\ b_{31} \\ b_{32} \\ b_{33} \\ b_{34} \end{bmatrix} \\ &= A_{black_{red}} \cdot \theta_\phi \end{aligned} \tag{C.40}$$

Where $A_{black_{red}}$ is the regression matrix and $\theta_p, \theta_v, \theta_\phi$ are the parameter vectors. The parameter vectors can be determined using Equation C.41.

$$\begin{aligned} \hat{\theta}_p &= \left(A^T_{black_{red}} \cdot A_{black_{red}} \right)^{-1} \cdot A^T_{black_{red}} \cdot \dot{p} \\ \hat{\theta}_v &= \left(A^T_{black_{red}} \cdot A_{black_{red}} \right)^{-1} \cdot A^T_{black_{red}} \cdot \dot{v} \\ \hat{\theta}_\phi &= \left(A^T_{black_{red}} \cdot A_{black_{red}} \right)^{-1} \cdot A^T_{black_{red}} \cdot \dot{\phi} \end{aligned} \tag{C.41}$$

D

Comparison parameter estimation methods

In this Appendix comparisons are made between different parameter estimation methods. The results of the OLS and WLS results are shown in Section D.1, while the results of the grey-box and black-box models are compared in Section D.2.

D.1. OLS vs. WLS

In this section the parameter estimation results of the OLS estimation are compared to the WLS estimation of the full grey-box models. The OLS and WLS estimation results are shown in Table D.1.

	OLS Estimation Results			**WLS Estimation Results**		
Stability Derivative	$\hat{\boldsymbol{\Theta}}$	$\lvert\hat{\sigma}\rvert$	$100\lvert\hat{\sigma}/\hat{\boldsymbol{\Theta}}\rvert$	$\hat{\boldsymbol{\Theta}}$	$\lvert\hat{\sigma}\rvert$	$100\lvert\hat{\sigma}/\hat{\boldsymbol{\Theta}}\rvert$
L_p	-3.79×10^{-4}	2.08×10^{-5}	5.49×10^{0}	-3.80×10^{-4}	1.00×10^{-4}	2.64×10^{1}
L_r	-2.79×10^{-4}	4.23×10^{-5}	1.52×10^{1}	-2.81×10^{-4}	3.25×10^{-4}	1.16×10^{2}
L_v	-2.72×10^{-3}	1.76×10^{-4}	6.46×10^{0}	-2.72×10^{-3}	1.01×10^{-3}	3.70×10^{1}
N_p	5.42×10^{-5}	1.56×10^{-5}	2.88×10^{1}	5.55×10^{-5}	7.58×10^{-4}	1.36×10^{3}
N_r	9.93×10^{-5}	3.17×10^{-5}	3.20×10^{1}	1.01×10^{-4}	1.16×10^{-3}	1.15×10^{3}
N_v	1.17×10^{-4}	1.32×10^{-4}	1.13×10^{2}	1.34×10^{-4}	5.51×10^{-3}	4.10×10^{3}
Y_p	-1.29×10^{-3}	3.50×10^{-4}	2.72×10^{1}	-1.23×10^{-3}	9.55×10^{-6}	7.72×10^{-1}
Y_r	8.54×10^{-3}	7.11×10^{-4}	8.33×10^{0}	8.37×10^{-3}	1.66×10^{-5}	1.98×10^{-1}
Y_v	-2.42×10^{-2}	2.95×10^{-3}	1.22×10^{1}	-2.38×10^{-2}	8.41×10^{-5}	3.53×10^{-1}
Control Derivative	$\hat{\boldsymbol{\Theta}}$	$\lvert\hat{\sigma}\rvert$	$100\lvert\hat{\sigma}/\hat{\boldsymbol{\Theta}}\rvert$	$\hat{\boldsymbol{\Theta}}$	$\lvert\hat{\sigma}\rvert$	$100\lvert\hat{\sigma}/\hat{\boldsymbol{\Theta}}\rvert$
L_{δ_d}	1.44×10^{-3}	1.47×10^{-3}	1.02×10^{2}	1.41×10^{-3}	6.96×10^{-3}	4.93×10^{2}
L_{δ_f}	1.11×10^{-4}	1.14×10^{-6}	1.02×10^{0}	1.11×10^{-4}	7.46×10^{-6}	6.72×10^{0}
L_{δ_w}	7.26×10^{-3}	5.19×10^{-4}	7.15×10^{0}	7.28×10^{-3}	2.29×10^{-3}	3.14×10^{1}
L_{δ_t}	-3.09×10^{-5}	5.34×10^{-6}	1.73×10^{1}	-3.09×10^{-5}	2.64×10^{-5}	8.56×10^{1}
N_{δ_d}	1.83×10^{-3}	1.11×10^{-3}	6.06×10^{1}	1.89×10^{-3}	4.23×10^{-2}	2.24×10^{3}
N_{δ_f}	-5.53×10^{-8}	8.52×10^{-7}	1.54×10^{3}	-1.44×10^{-7}	3.83×10^{-5}	2.67×10^{4}
N_{δ_w}	-7.18×10^{-4}	3.90×10^{-4}	5.43×10^{1}	-7.09×10^{-4}	1.21×10^{-2}	1.70×10^{3}
N_{δ_t}	8.04×10^{-6}	4.01×10^{-6}	4.98×10^{1}	8.19×10^{-6}	9.08×10^{-5}	1.11×10^{3}
Y_{δ_d}	-6.69×10^{-2}	2.48×10^{-2}	3.70×10^{1}	-6.06×10^{-2}	8.43×10^{-4}	1.39×10^{0}
Y_{δ_f}	-9.26×10^{-4}	1.91×10^{-5}	2.06×10^{0}	-9.25×10^{-4}	5.44×10^{-7}	5.88×10^{-2}
Y_{δ_w}	-9.14×10^{-2}	8.73×10^{-3}	9.56×10^{0}	-9.16×10^{-2}	1.74×10^{-4}	1.90×10^{-1}
Y_{δ_t}	6.38×10^{-4}	8.99×10^{-5}	1.41×10^{1}	6.44×10^{-4}	1.01×10^{-6}	1.57×10^{-1}

Table D.1: Estimated parameters for the four-state state-space system shown in Equation 8.7 as a result of the OLS and WLS estimator, using the maneuver data shown in Figure 7.7. $\hat{\boldsymbol{\Theta}}$ indicates the estimated parameter, while $\lvert\hat{\sigma}\rvert$ indicates the parameter standard deviation. The fourth column shows the relative parameter standard deviation in percent.

From Table D.1 it can be seen that the values $\hat{\boldsymbol{\Theta}}$ are very similar. The main difference is seen in the standard deviation $|\hat{\sigma}|$. For both estimators, it can be seen that the $|\hat{\sigma}|$ is the largest for the N-parameters. When using the WLS estimator, the $|\hat{\sigma}|$ of the L- and N-parameters is larger, with some values increasing with two orders of magnitude. In contrast, the $|\hat{\sigma}|$ of the Y-parameters is lower when using the WLS estimator, with some values decreasing with two orders of magnitude. Similar results were found when using the reduced grey-box model, as is shown in Table D.2.

	OLS Estimation Results			**WLS Estimation Results**		
Stability Derivative	$\hat{\boldsymbol{\Theta}}$	$\lvert\hat{\sigma}\rvert$	$100\lvert\hat{\sigma}/\hat{\boldsymbol{\Theta}}\rvert$	$\hat{\boldsymbol{\Theta}}$	$\lvert\hat{\sigma}\rvert$	$100\lvert\hat{\sigma}/\hat{\boldsymbol{\Theta}}\rvert$
L_p	-2.45×10^{-4}	1.93×10^{-5}	7.87×10^{0}	-2.43×10^{-4}	1.69×10^{-4}	6.96×10^{1}
L_v	-4.01×10^{-4}	1.72×10^{-4}	4.30×10^{1}	-3.74×10^{-4}	1.52×10^{-3}	4.07×10^{2}
Y_p	2.76×10^{-3}	2.27×10^{-4}	8.23×10^{0}	2.75×10^{-3}	3.31×10^{-6}	1.20×10^{-1}
Y_v	-5.57×10^{-2}	2.03×10^{-3}	3.65×10^{0}	-5.61×10^{-2}	3.32×10^{-5}	5.92×10^{-2}
Control Derivative	$\hat{\boldsymbol{\Theta}}$	$\lvert\hat{\sigma}\rvert$	$100\lvert\hat{\sigma}/\hat{\boldsymbol{\Theta}}\rvert$	$\hat{\boldsymbol{\Theta}}$	$\lvert\hat{\sigma}\rvert$	$100\lvert\hat{\sigma}/\hat{\boldsymbol{\Theta}}\rvert$
L_{δ_f}	1.05×10^{-4}	9.32×10^{-7}	8.84×10^{-1}	1.06×10^{-4}	8.47×10^{-6}	8.02×10^{0}
L_{δ_t}	-4.19×10^{-5}	4.86×10^{-6}	1.16×10^{1}	4.19×10^{-5}	5.48×10^{-5}	1.31×10^{2}
Y_{δ_f}	-8.62×10^{-4}	1.10×10^{-5}	1.27×10^{0}	-8.63×10^{-4}	1.22×10^{-7}	1.41×10^{-2}
Y_{δ_t}	-4.05×10^{-4}	5.72×10^{-5}	1.41×10^{1}	-4.05×10^{-4}	4.55×10^{-7}	1.12×10^{-1}

Table D.2: Estimated parameters for the four-state state-space system shown in Equation 8.4 as a result of the OLS and WLS estimator, using two doublets of the maneuver data shown in Figure 7.7, and setting the inputs δ_d and δ_w to zero.. $\hat{\boldsymbol{\Theta}}$ indicates the estimated parameter, while $|\hat{\sigma}|$ indicates the parameter standard deviation. The fourth column shows the relative parameter standard deviation in percent.

D.2. Grey-Box vs. Black-Box modeling

In this section the identified grey-box and black-box models are compared. The main difference between the two model structures is the prior knowledge which have been used. The grey-box model has been developed by deriving the equations of motion using the rigid-body approach, while the black-box model is a blind fit, the only assumption being about which states are included. The comparison between the grey-box and black-box model for the four-state state-space system is shown in Subsection D.2.1, and for the three-state state-space system is shown in Subsection D.2.2.

D.2.1. Four-State State-Space Models

For the comparison of the the identified grey-box and black-box four-state state-space systems, the A and B-matrices are compared. The matrices A_{grey} and A_{black} are shown in Equation D.1.

$$A_{grey} = \begin{bmatrix} -4.058 & -3.004 & -29.102 & 0 \\ 1.713 & 3.122 & 4.140 & 0 \\ -0.156 & -0.090 & -0.823 & 9.743 \\ 1 & -0.079 & 0 & 0 \end{bmatrix}, \quad A_{black} = \begin{bmatrix} -3.771 & -2.865 & -26.445 & -5.044 \\ 1.740 & 3.121 & 4.384 & -0.632 \\ -0.097 & -0.074 & -0.272 & 8.658 \\ 1.002 & -0.023 & 0.064 & 0.238 \end{bmatrix} \tag{D.1}$$

The main difference between the two A-matrices can be seen in the fourth column. In A_{grey} most of the elements have been set to zero, while this is not the case for A_{black}. However such differences are expected since the black-box model is a blind fit of the data. The matrices B_{grey} and B_{black} are shown in Equation D.2.

$$B_{grey} = \begin{bmatrix} 15.091 & 1.185 & 77.761 & -0.330 \\ 58.230 & -0.004 & -21.858 & 0.252 \\ -2.106 & -0.032 & -3.186 & 0.022 \\ 0 & 0 & 0 & 0 \end{bmatrix}, \quad B_{black} = \begin{bmatrix} 25.616 & 1.170 & 79.393 & -0.333 \\ 59.311 & -0.006 & -21.695 & 0.251 \\ -0.125 & -0.036 & -2.768 & 0.022 \\ 1.315 & 0.008 & 0.320 & 0.006 \end{bmatrix} \tag{D.2}$$

The major differences between the two matrices are seen in the first column, which correspond to the values multiplied with the input δ_d. There are no direct commands given to the dihedral servo, the controller is fully

responsible for the commands to these servos during the identification maneuver. The parameter variance for the elements in these columns was also very high compared tot the variances of the other parameters in B_{black}, which could explain the variations compared to B_{grey}.

D.2.2. Three-State State-Space Models

For the comparison of the the identified grey-box and black-box three-state state-space systems, the A and B-matrices are compared. The matrices A_{grey} and A_{black} are shown in Equation D.3.

$$A_{grey} = \begin{bmatrix} -2.592 & -4.000 & 0 \\ -0.201 & -1.951 & 9.744 \\ 1 & 0 & 0 \end{bmatrix}, \qquad A_{black} = \begin{bmatrix} -3.411 & -11.149 & 19.013 \\ -0.088 & -0.959 & 7.063 \\ 0.937 & -0.310 & 1.468 \end{bmatrix} \tag{D.3}$$

The largest differences between the two matrices can be seen in the first row. This corresponds to the equation for $\dot{p}$. What is noteworthy is that the second element of this row is lower value in A_{black}, while the third element is has a higher value in A_{black}. This could indicate that these two values are compensating for one another. This is possible in a black-box model structure, since there is a blind fit of the data. The third element in the first row does not have a physical meaning, therefore it has been set to zero in A_{grey}. The variances of the second and third elements in the first row of A_{black} also had very large values, which could explain why these values are very different compared to A_{grey}. The matrices B_{grey} and B_{black} are shown in Equation D.4.

$$B_{grey} = \begin{bmatrix} 1.128 & 0.447 \\ -0.030 & -0.014 \\ 0 & 0 \end{bmatrix}, \qquad B_{black} = \begin{bmatrix} 1.212 & 0.486 \\ -0.042 & -0.019 \\ 0.013 & 0.035 \end{bmatrix} \tag{D.4}$$

Very little differences are shown in both columns. The first column is multiplied with δ_f, while the second column is multiplied with δ_d. Also in the four-state state-space systems it was seen that there is little difference between the values of the B-matrices of the grey-box and black-box model which are multiplied with these two inputs.

E

Numeric State-Space Models

In this appendix, the numeric versions of the state-space models are included which have been used in the model validation presented in Chapter 9. All models are three-state state-space grey box models. The numeric version of the state-space models have been set up by using the estimated stability and control derivatives and the geometric properties of the Delfly Nimble **without** the Wifi-module of Table A.1. The models which includes the inputs δ_f and δ_t are defined in Section E.1, the model which includes only the input δ_f is shown in Section E.2, and the model which includes the inputs δ_f and δ_d is presented in Section E.3. The numerical state-space system for the longitudinal model, as determined in the research of Jorgen et al. [51, 52], is shown in Section E.4.

E.1. Models including inputs δ_f and δ_t

The symbolic equation for the state-space model which includes the inputs δ_f and δ_t is shown in Equation E.1, and the estimated stability and control derivatives using five different data-sets are indicated in Table E.1.

$$\begin{bmatrix} \dot{p} \\ \dot{v} \\ \dot{\phi} \end{bmatrix} = \begin{bmatrix} \frac{I_{zz}}{I_c} \cdot L_p & \frac{I_{zz}}{I_c} \cdot L_v & 0 \\ \frac{Y_p}{m} + w_0 & \frac{Y_v}{m} & g \cdot \cos(\theta_0) \cdot \cos(\phi_0) \\ 1 & 0 & 0 \end{bmatrix} \cdot \begin{bmatrix} p \\ v \\ \phi \end{bmatrix} + \begin{bmatrix} \frac{I_{zz}}{I_c} \cdot L_{\delta_f} & \frac{I_{zz}}{I_c} \cdot L_{\delta_t} \\ \frac{Y_{\delta_f}}{m} & \frac{Y_{\delta_t}}{m} \\ 0 & 0 \end{bmatrix} \cdot \begin{bmatrix} \delta_f \\ \delta_t \end{bmatrix} \tag{E.1}$$

Estimated Parameters Reduced Grey-Box Model: inputs δ_f and δ_t					
Stability Derivative	$\hat{\Theta}_1$	$\hat{\Theta}_2$	$\hat{\Theta}_3$	$\hat{\Theta}_4$	$\hat{\Theta}_5$
L_p	-2.43×10^{-4}	-3.16×10^{-4}	-4.23×10^{-4}	-5.23×10^{-4}	-2.89×10^{-4}
L_v	-3.74×10^{-4}	-9.34×10^{-4}	-1.38×10^{-3}	-3.42×10^{-3}	-1.01×10^{-3}
Y_p	2.75×10^{-3}	-2.64×10^{-3}	7.01×10^{-3}	-1.82×10^{-3}	-2.31×10^{-3}
Y_v	-5.61×10^{-2}	-7.74×10^{-2}	-2.15×10^{-2}	-4.43×10^{-2}	-1.08×10^{-1}
Control Derivative	$\hat{\Theta}_1$	$\hat{\Theta}_2$	$\hat{\Theta}_3$	$\hat{\Theta}_4$	$\hat{\Theta}_5$
L_{δ_f}	1.06×10^{-4}	9.79×10^{-5}	1.01×10^{-4}	8.85×10^{-5}	9.58×10^{-5}
L_{δ_t}	4.19×10^{-5}	5.40×10^{-5}	7.68×10^{-6}	4.66×10^{-5}	4.54×10^{-5}
Y_{δ_f}	-8.63×10^{-4}	-8.46×10^{-4}	-8.33×10^{-4}	-7.98×10^{-4}	-9.87×10^{-4}
Y_{δ_t}	-4.05×10^{-4}	-7.60×10^{-4}	1.85×10^{-4}	-3.88×10^{-4}	-1.22×10^{-3}

Table E.1: Estimated parameters for the three-state state-space system shown in Equation E.1 as a result of the WLS estimator, using various datasets. $\hat{\Theta}$ indicates the value of the estimated parameter. The subscript indicates the number of the dataset.

The numeric state-space using the values of the stability and control derivatives $\hat{\mathbf{\Theta}}_1$ is shown in Equation E.2.

$$\begin{bmatrix} \dot{p} \\ \dot{v} \\ \dot{\phi} \end{bmatrix} = \begin{bmatrix} -2.59 & -4.00 & 0 \\ 0.10 + w_0 & -1.95 & 9.81 \cdot \cos(\theta_0) \cdot \cos(\phi_0) \\ 1 & 0 & 0 \end{bmatrix} \cdot \begin{bmatrix} p \\ v \\ \phi \end{bmatrix} + \begin{bmatrix} 1.13 & 0.45 \\ -0.03 & -0.01 \\ 0 & 0 \end{bmatrix} \cdot \begin{bmatrix} \delta_f \\ \delta_t \end{bmatrix} \tag{E.2}$$

The numeric state-space using the values of the stability and control derivatives $\hat{\mathbf{\Theta}}_2$ is shown in Equation E.3.

$$\begin{bmatrix} \dot{p} \\ \dot{v} \\ \dot{\phi} \end{bmatrix} = \begin{bmatrix} -3.37 & -9.97 & 0 \\ -0.09 + w_0 & -2.69 & 9.81 \cdot \cos(\theta_0) \cdot \cos(\phi_0) \\ 1 & 0 & 0 \end{bmatrix} \cdot \begin{bmatrix} p \\ v \\ \phi \end{bmatrix} + \begin{bmatrix} 1.05 & 0.58 \\ -0.03 & -0.01 \\ 0 & 0 \end{bmatrix} \cdot \begin{bmatrix} \delta_f \\ \delta_t \end{bmatrix} \tag{E.3}$$

The numeric state-space using the values of the stability and control derivatives $\hat{\mathbf{\Theta}}_3$ is shown in Equation E.4.

$$\begin{bmatrix} \dot{p} \\ \dot{v} \\ \dot{\phi} \end{bmatrix} = \begin{bmatrix} -4.52 & -14.69 & 0 \\ 0.24 + w_0 & -0.75 & 9.81 \cdot \cos(\theta_0) \cdot \cos(\phi_0) \\ 1 & 0 & 0 \end{bmatrix} \cdot \begin{bmatrix} p \\ v \\ \phi \end{bmatrix} + \begin{bmatrix} 1.08 & 0.08 \\ -0.03 & -0.01 \\ 0 & 0 \end{bmatrix} \cdot \begin{bmatrix} \delta_f \\ \delta_t \end{bmatrix} \tag{E.4}$$

The numeric state-space using the values of the stability and control derivatives $\hat{\mathbf{\Theta}}_4$ is shown in Equation E.5.

$$\begin{bmatrix} \dot{p} \\ \dot{v} \\ \dot{\phi} \end{bmatrix} = \begin{bmatrix} -5.59 & -36.56 & 0 \\ -0.06 + w_0 & -1.54 & 9.81 \cdot \cos(\theta_0) \cdot \cos(\phi_0) \\ 1 & 0 & 0 \end{bmatrix} \cdot \begin{bmatrix} p \\ v \\ \phi \end{bmatrix} + \begin{bmatrix} 0.94 & 0.50 \\ -0.03 & -0.01 \\ 0 & 0 \end{bmatrix} \cdot \begin{bmatrix} \delta_f \\ \delta_t \end{bmatrix} \tag{E.5}$$

The numeric state-space using the values of the stability and control derivatives $\hat{\mathbf{\Theta}}_5$ is shown in Equation E.6.

$$\begin{bmatrix} \dot{p} \\ \dot{v} \\ \dot{\phi} \end{bmatrix} = \begin{bmatrix} -3.09 & -10.81 & 0 \\ -0.08 + w_0 & -3.77 & 9.81 \cdot \cos(\theta_0) \cdot \cos(\phi_0) \\ 1 & 0 & 0 \end{bmatrix} \cdot \begin{bmatrix} p \\ v \\ \phi \end{bmatrix} + \begin{bmatrix} 1.02 & 0.48 \\ -0.03 & -0.04 \\ 0 & 0 \end{bmatrix} \cdot \begin{bmatrix} \delta_f \\ \delta_t \end{bmatrix} \tag{E.6}$$

E.2. Model including input δ_f only

The symbolic equation for the state-space model which includes only the input δ_f is shown in Equation E.7, and the estimated stability and control derivatives are shown in Table E.2. For this model, only the first data-set, which is the doublet train maneuver used in Section 8.3.2, was used to was used to estimate the stability and control derivatives.

$$\begin{bmatrix} \dot{p} \\ \dot{v} \\ \dot{\phi} \end{bmatrix} = \begin{bmatrix} \frac{I_{zz}}{I_c} \cdot L_p & \frac{I_{zz}}{I_c} \cdot L_v & 0 \\ \frac{Y_p}{m} + w_0 & \frac{Y_v}{m} & g \cdot \cos(\theta_0) \cdot \cos(\phi_0) \\ 1 & 0 & 0 \end{bmatrix} \cdot \begin{bmatrix} p \\ v \\ \phi \end{bmatrix} + \begin{bmatrix} \frac{I_{zz}}{I_c} \cdot L_{\delta_f} \\ \frac{Y_{\delta_f}}{m} \\ 0 \end{bmatrix} \cdot \begin{bmatrix} \delta_f \end{bmatrix} \tag{E.7}$$

Estimated Parameters Reduced Grey-Box Model: input δ_f			
L-parameters:	L_p -2.68×10^{-4}	L_v -6.69×10^{-4}	L_{δ_f} 1.06×10^{-4}
Y-parameters:	Y_p 2.96×10^{-3}	Y_v -5.33×10^{-2}	Y_{δ_f} -8.66×10^{-4}

Table E.2: Estimated parameters for the three-state state-space system shown in Equation E.7 as a result of the WLS estimator, using the first identification data-set.

The numeric state-space using the values of the stability and control derivatives of Table E.2 is shown in Equation E.8.

$$\begin{bmatrix} \dot{p} \\ \dot{v} \\ \dot{\phi} \end{bmatrix} = \begin{bmatrix} -2.86 & -7.14 & 0 \\ 0.10 + w_0 & -1.85 & 9.81 \cdot \cos(\theta_0) \cdot \cos(\phi_0) \\ 1 & 0 & 0 \end{bmatrix} \cdot \begin{bmatrix} p \\ v \\ \phi \end{bmatrix} + \begin{bmatrix} 1.13 \\ -0.03 \\ 0 \end{bmatrix} \cdot \begin{bmatrix} \delta_f \\ \delta_t \end{bmatrix} \tag{E.8}$$

E.3. Model including inputs δ_f and δ_d

The symbolic equation for the state-space model which includes only the input δ_f is shown in Equation E.9, and the estimated stability and control derivatives are presented in Table E.3. For this model, only the first data-set, which is the doublet train maneuver used in Section 8.3.2, was used to was used to estimate the stability and control derivatives.

$$\begin{bmatrix} \dot{p} \\ \dot{v} \\ \dot{\phi} \end{bmatrix} = \begin{bmatrix} \frac{I_{zz}}{I_c} \cdot L_p & \frac{I_{zz}}{I_c} \cdot L_v & 0 \\ \frac{Y_p}{m} + w_0 & \frac{Y_v}{m} & g \cdot \cos(\theta_0) \cdot \cos(\phi_0) \\ 1 & 0 & 0 \end{bmatrix} \cdot \begin{bmatrix} p \\ v \\ \phi \end{bmatrix} + \begin{bmatrix} \frac{I_{zz}}{I_c} \cdot L_{\delta_f} & \frac{I_{zz}}{I_c} \cdot L_{\delta_d} \\ \frac{Y_{\delta_f}}{m} & \frac{Y_{\delta_d}}{m} \\ 0 & 0 \end{bmatrix} \cdot \begin{bmatrix} \delta_f \\ \delta_d \end{bmatrix} \tag{E.9}$$

Estimated Parameters Reduced Grey-Box Model: inputs δ_f and δ_d				
L-parameters:	L_p -2.57×10^{-4}	L_v -4.91×10^{-4}	L_{δ_f} 1.06×10^{-4}	L_{δ_d} 1.20×10^{-3}
Y-parameters:	Y_p 2.42×10^{-3}	Y_v -6.00×10^{-2}	Y_{δ_f} -8.86×10^{-4}	Y_{δ_d} -5.41×10^{-2}

Table E.3: Estimated parameters for the three-state state-space system shown in Equation E.9 as a result of the WLS estimator, using the first identification data-set (TableX).

The numeric state-space using the values of the stability and control derivatives from Table E.3 is shown in Equation E.10.

$$\begin{bmatrix} \dot{p} \\ \dot{v} \\ \dot{\phi} \end{bmatrix} = \begin{bmatrix} -2.74 & -5.24 & 0 \\ 0.08 + w_0 & -2.09 & 9.81 \cdot \cos(\theta_0) \cdot \cos(\phi_0) \\ 1 & 0 & 0 \end{bmatrix} \cdot \begin{bmatrix} p \\ v \\ \phi \end{bmatrix} + \begin{bmatrix} 1.14 & 12.77 \\ -0.03 & -1.88 \\ 0 & 0 \end{bmatrix} \cdot \begin{bmatrix} \delta_f \\ \delta_d \end{bmatrix} \tag{E.10}$$

E.4. Model for the longitudinal dynamics

The lateral state-space model can be combined with the longitudinal state-space system which was developed in the research of Nijboer et al.[51, 52]. The symbolic state-space system is shown in Equation (E.11).

$$\begin{bmatrix} \dot{q} \\ \dot{u} \\ \dot{w} \\ \dot{\theta} \end{bmatrix} = \begin{bmatrix} \frac{M_q}{I_{yy}} & \frac{M_u}{I_{yy}} & \frac{M_w}{I_{yy}} & 0 \\ \frac{X_q}{m} - w_0 & \frac{X_u}{m} & \frac{X_w}{m} & -g \cdot \cos(\theta_0) \\ \frac{Z_q}{m} + u_0 & \frac{Z_u}{m} & \frac{Z_w}{m} & -g \cdot \sin(\theta_0) \\ 1 & 0 & 0 & 0 \end{bmatrix} \cdot \begin{bmatrix} q \\ u \\ w \\ \theta \end{bmatrix} + \begin{bmatrix} \frac{M_{\delta_d}}{I_{yy}} \\ \frac{X_{\delta_d}}{m} \\ \frac{Z_{\delta_d}}{m} \\ 0 \end{bmatrix} \cdot \begin{bmatrix} \delta_d \end{bmatrix} \tag{E.11}$$

The estimated stability and control derivatives for this state-space system are shown in Table E.4, and the resuting numeric state-space system using these values of the stability and control derivatives is shown in Equation (E.11).

$$\begin{bmatrix} \dot{q} \\ \dot{u} \\ \dot{w} \\ \dot{\theta} \end{bmatrix} = \begin{bmatrix} -2.64 & 26.94 & -2.64 & 0 \\ 0.14 - w_0 & -3.52 & 0.31 & -9.81 \cdot \cos(\theta_0) \\ -0.19 + u_0 & 0.68 & -0.21 & -9.81 \cdot \sin(\theta_0) \\ 1 & 0 & 0 & 0 \end{bmatrix} \cdot \begin{bmatrix} q \\ u \\ w \\ \theta \end{bmatrix} + \begin{bmatrix} 3862.82 \\ 25.10 \\ 10.37 \\ 0 \end{bmatrix} \cdot \begin{bmatrix} \delta_d \end{bmatrix} \tag{E.12}$$

Estimated Parameters Reduced Grey-Box Model: inputs δ_f and δ_d				
M-parameters:	M_q -1.90×10^{-3}	M_u 1.94×10^{-2}	M_w -1.90×10^{-3}	M_{δ_d} 2.78×10^{-1}
X-parameters:	X_q 4.10×10^{-3}	X_u -1.01×10^{-1}	X_w 8.90×10^{-3}	X_{δ_d} 7.22×10^{-1}
Z-parameters:	Z_q -5.60×10^{-3}	Z_u 1.96×10^{-2}	Z_w -5.90×10^{-3}	Z_{δ_d} 2.98×10^{-2}

Table E.4: Estimated parameters for a grey-box state-space system for the longitudinal dynamics, determined in the work of Nijboer et al. [52].

F

Estimated Aerodynamic Forces and Moments

In this appendix the estimation of the aerodynamic forces and moments is discussed . The reduced grey-box stat-space system is defined in Equation F.1.

$$\begin{bmatrix} \dot{p} \\ \dot{v} \\ \dot{\phi} \end{bmatrix} = \begin{bmatrix} \frac{I_{zz}}{I_c} \cdot L_p & \frac{I_{zz}}{I_c} \cdot L_v & 0 \\ \frac{Y_p}{m} + w_0 & \frac{Y_v}{m} & g \cdot \cos(\theta_0) \cdot \cos(\phi_0) \\ 1 & 0 & 0 \end{bmatrix} \cdot \begin{bmatrix} p \\ v \\ \phi \end{bmatrix} + \begin{bmatrix} \frac{I_{zz}}{I_c} \cdot L_{\delta_f} & \frac{I_{zz}}{I_c} \cdot L_{\delta_t} \\ \frac{Y_{\delta_f}}{m} & \frac{Y_{\delta_t}}{m} \\ 0 & 0 \end{bmatrix} \cdot \begin{bmatrix} \delta_f \\ \delta_t \end{bmatrix} \tag{F.1}$$

The stability and control derivatives in this state-space system are used to estimate the moment L and the force Y. The equations are shown in Equation F.2.

$$\begin{aligned} Y &= Y_p \Delta p + Y_r \Delta r + Y_v \Delta v + Y_{\delta_f} \Delta \delta_f + Y_{\delta_t} \Delta \delta_t \\ L &= L_p \Delta p + L_r \Delta r + L_v \Delta v + L_{\delta_f} \Delta \delta_f + L_{\delta_t} \Delta \delta_t \end{aligned} \tag{F.2}$$

The estimated forced and moments for the identification data, which consisted of a doublet train with two doublets, which had main frequencies of 7 and 4 Hz, is illustrated in Figure F.1, and the accuracy metrics are indicated in Table F.1.

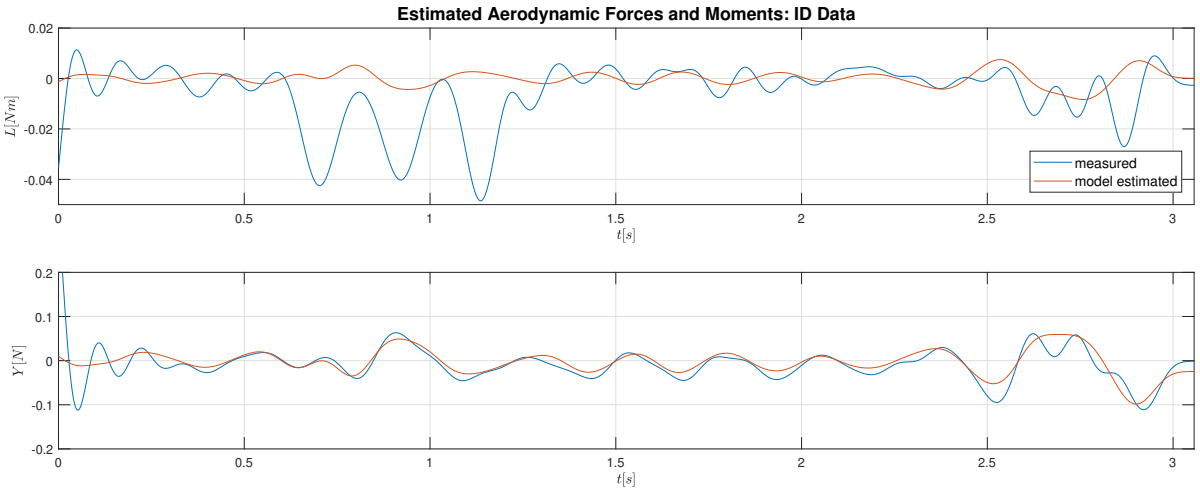

Figure F.1: Estimation of the aerodynamic moment L and the aerodynamics force Y during the doublet train, which had main frequencies of 7 and 4 Hz

Accuracy Metrics Aerodynamic Forces and Moments: ID Data				
Output Variable	$\mathbf{r}_{xy}$	$\mathbf{R}^2$	**RMSE**	**RMSE** (% of meas. range)
L	0.079	-0.217	0.013 Nm	22.12
Y	0.744	0.490	0.027 N	6.03

Table F.1: Accuracy metrics for the estimated aerodynamics forces and moments during the doublet train maneuver, which had main frequencies of 7 and 4 Hz.

It can be seen that the moment L is poorly estimated with the stability and control derivatives. What is noteworthy, is that the estimation is worse during the doublet with the higher main frequency, as can be seen in Figure F.2.

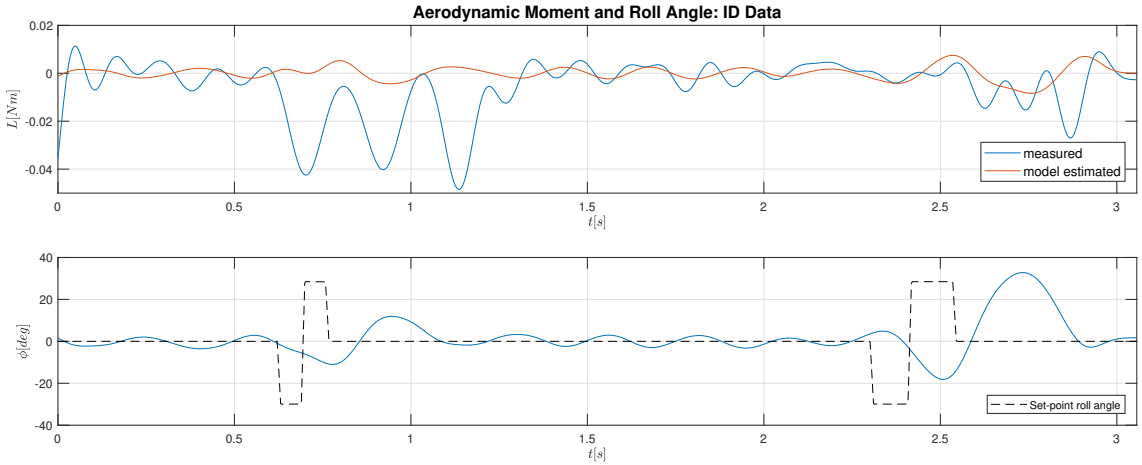

Figure F.2: Aerodynamic moment L and the roll angle ϕ during the doublet train, which had main frequencies of 7 and 4 Hz.

The measured forces and moments were determine using OptiTrack. What could be the cause of the poor estimation of L are vibrations of the markers during flight. The marker setup used in the experiments is presented in Figure F.3.

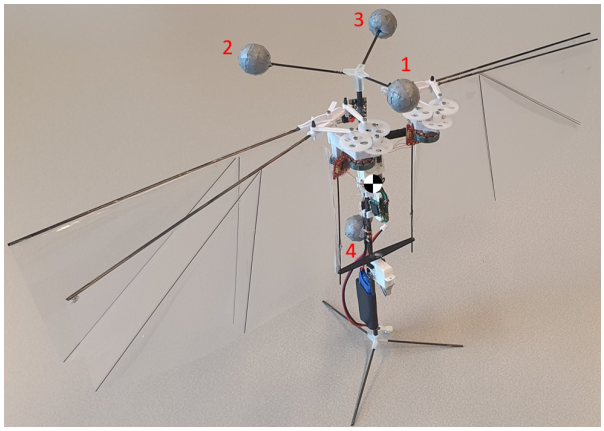

Figure F.3: Marker setup of the Delfly Nimble used during the experiments.

The markers on the 'crown' of the Delfly Nimble, which are indicated by the numbers '1', '2' and '3' are connected using a flat carbon rod. In flight, these rods can bend due to the vibrations, leading to displacement of the markers which can influence the accuracy of the OptiTrack data. For more rapid maneuvers, such as the 112-maneuver, the accuracy reduces even more. For slower maneuvers, the accuracy of the of L does im-

prove, as can be seen in the estimation for a doublet with a main frequency of 4 Hz, as can be seen in Figure F.4 and Table F.2.

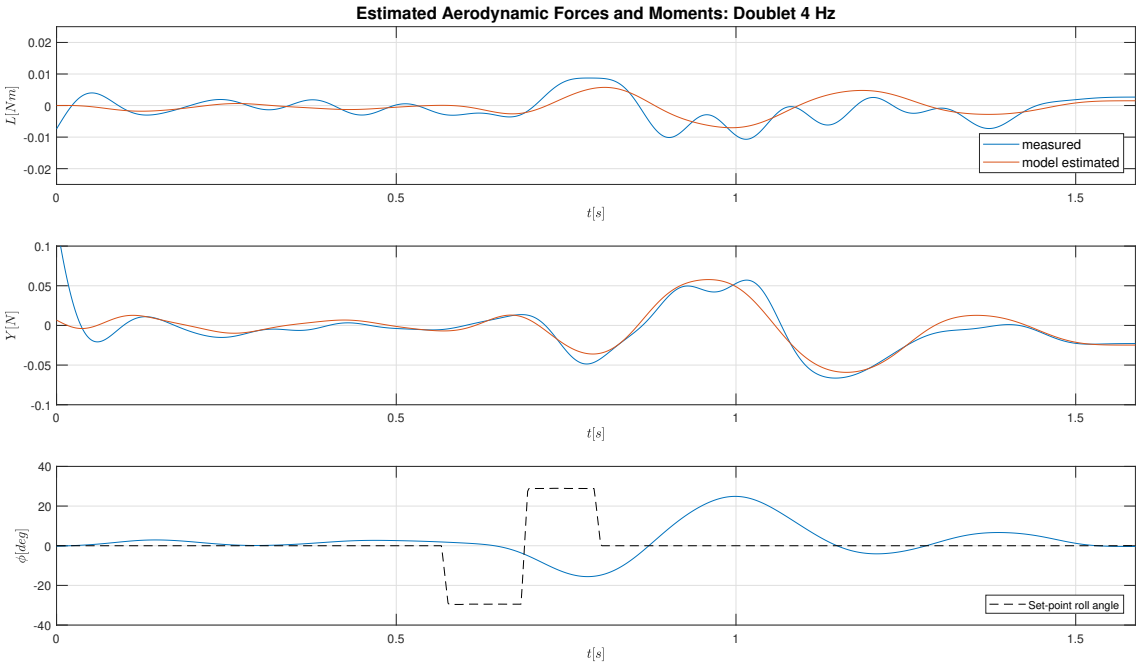

Figure F.4: Aerodynamic moment L, force Y and the roll angle ϕ during the doublet train, which had main frequencies of 7 and 4 Hz.

Accuracy Metrics Aerodynamic Forces and Moments: Doublet 4 Hz				
Output Variable	$\mathbf{r}_{xy}$	$\mathbf{R}^2$	**RMSE**	**RMSE** (% of meas. range)
L	0.670	0.484	0.003 Nm	14.80
Y	0.889	0.766	0.014 N	6.92

Table F.2: Accuracy metrics for the estimated aerodynamics forces and moments during a doublet which had a main frequency 4 Hz.

During slower maneuvers there would be less vibrations, which would increase the accuracy of the measured L. The improved accuracy of the estimated L suggests that indeed there might be some issue with the method that the moment L is measured in OptiTrack. In both Figures F.1 and F.4 the range of the model estimated L are similar, while the ranges of the measured L differ greatly. To fully verify that the accuracy of the measured moment L form OptiTrack is decreased due to vibrations of the markers on the crown, stiffer rods can be used. If the rods are more stiff, there would be less displacement of the markers due to vibrations.

G

Autocorrelation plots

In this Appendix autocorrelation plots of the residuals of the simulated state response, the coupled maneuvers and the nonlinear maneuvers are shown. Section G.1 shows the plots of the residuals of states and the difference in flapping frequency input δ_f. Section G.2 presents the plots of the residuals of the coupled maneuvers. In section G.3 the plots of the residuals of the nonlinear maneuvers are illustrated.

G.1. Closed-loop Validation Autocorrelation Plots

This section presents the plots of the residuals of states and the difference in flapping frequency input δ_f.The states are determined using the the state-space model shown in Equation E.2, and a Simulink model in which a one to one copy of the PD-controller is implemented. The dynamics of the flapping mechanism is models using Equation 9.4. The autocorrelation plots of the states of the doublet train, which used the fast gains shown in Table 7.1 during the maneuver, are presented in Figure G.1. The autocorrelation plots of the input δ_f during this maneuver are shown in Figure G.2.

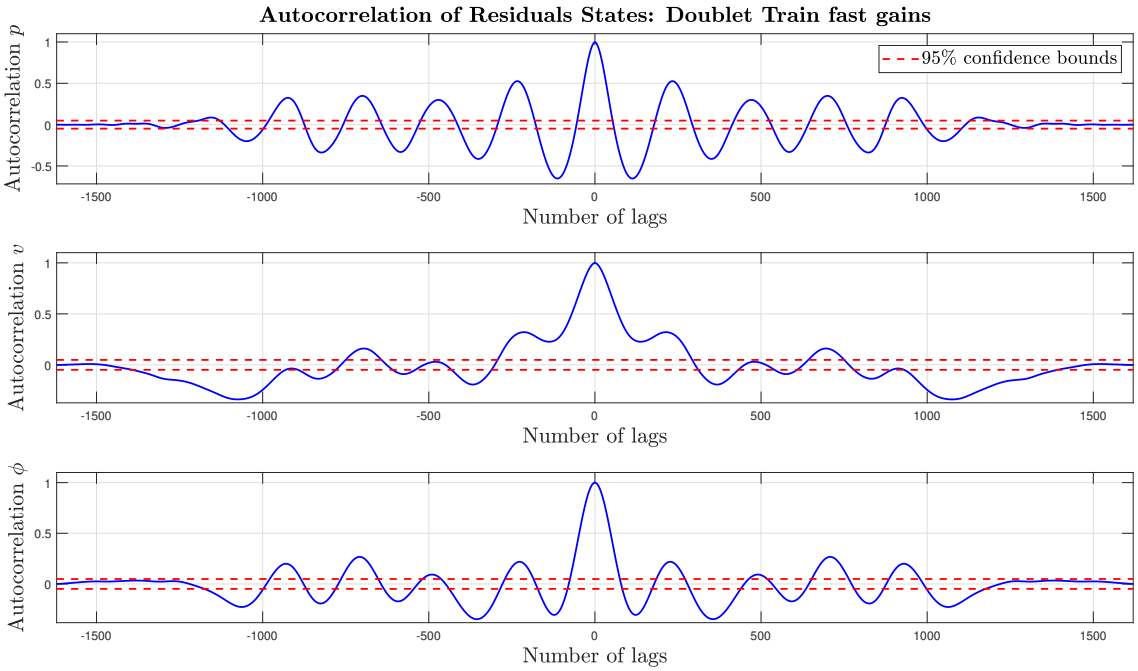

Figure G.1: Autocorrelation plot of the residuals of the states of a doublet train. The states are determined using the the state-space model shown in Equation E.2, and a Simulink model in which a one to one copy of the PD-controller is implemented. The dynamics of the flapping mechanism is models using Equation 9.4. For this simulation the fast gains shown in Table 7.1 were used. Additionally, the 95% confidence bounds are shown.

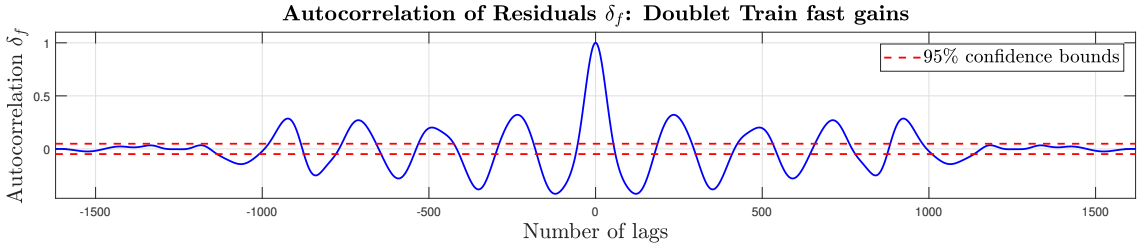

Figure G.2: Autocorrelation plot of the residuals of the input δ_f of a doublet train. The states are determined using the the state-space model shown in Equation E.2, and a Simulink model in which a one to one copy of the PD-controller is implemented. The dynamics of the flapping mechanism is models using Equation 9.4. For this simulation the fast gains shown in Table 7.1 were used. Additionally, the 95% confidence bounds are shown.

The residuals in Figures G.1 and G.2 are more coloured when compared to the residuals of the identification data, as can be seen in Figure 8.10. The autocorrelation plots of the states of the doublet train, which used the CL gains shown in Table 7.1 during the maneuver, is shown in Figure G.3. The autocorrelation plots of the input δ_f during this maneuver are illustrated in Figure G.4.

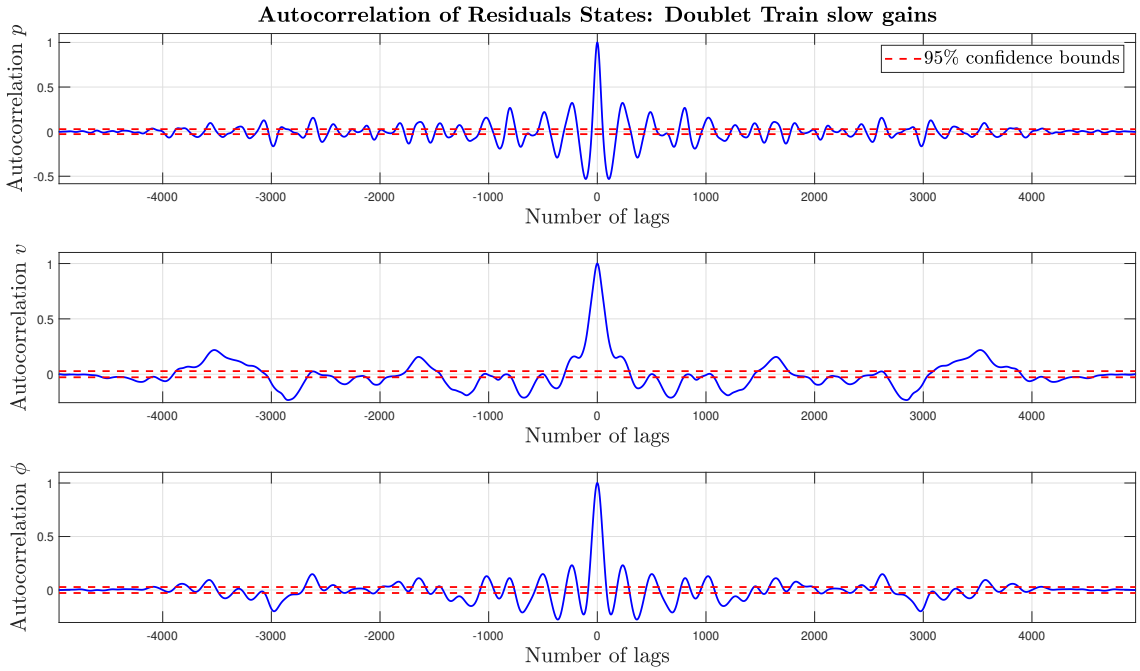

Figure G.3: Autocorrelation plot of the residuals of the states of a doublet train. The states are determined using the the state-space model shown in Equation E.2, and a Simulink model in which a one to one copy of the PD-controller is implemented. The dynamics of the flapping mechanism is models using Equation 9.4. For this simulation the slow gains shown in Table 7.1 were used. Additionally, the 95% confidence bounds are shown.

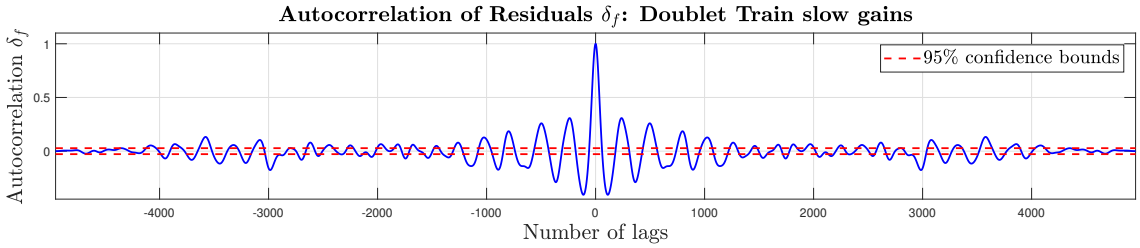

Figure G.4: Autocorrelation plot of the residuals of the input δ_f of a doublet train. The states are determined using the the state-space model shown in Equation E.2, and a Simulink model in which a one to one copy of the PD-controller is implemented. The dynamics of the flapping mechanism is models using Equation 9.4. For this simulation the slow gains shown in Table 7.1 were used. Additionally, the 95% confidence bounds are shown.

The residuals in Figures G.3 and G.4 are more coloured when compared to the residuals of the identification data, as can be seen in Figure 8.10. The autocorrelation plots of the states of the 112-manauvers, which used the slow gains shown in Table 7.1 during the maneuver, are shown in Figure G.5. The autocorrelation plots of the input δ_f during this maneuver are presented in Figure G.6.

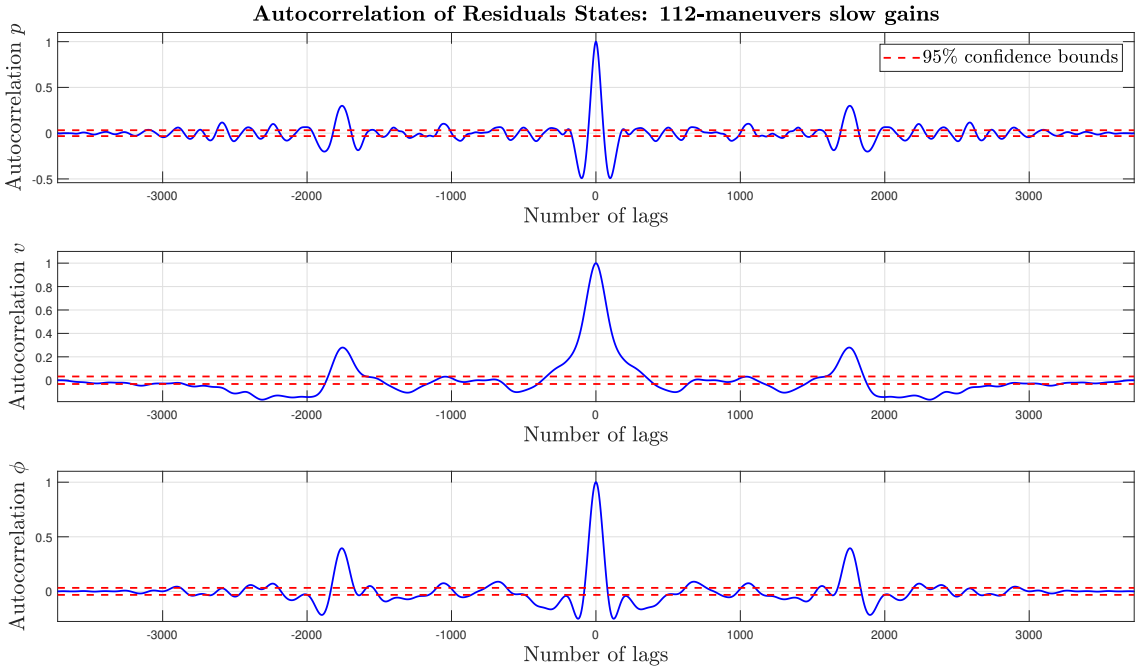

Figure G.5: Autocorrelation plot of the residuals of the states of multiple 112-maneuvers. The states are determined using the the state-space model shown in Equation E.2, and a Simulink model in which a one to one copy of the PD-controller is implemented. The dynamics of the flapping mechanism is models using Equation 9.4. For this simulation the slow gains shown in Table 7.1 were used. Additionally, the 95% confidence bounds are shown.

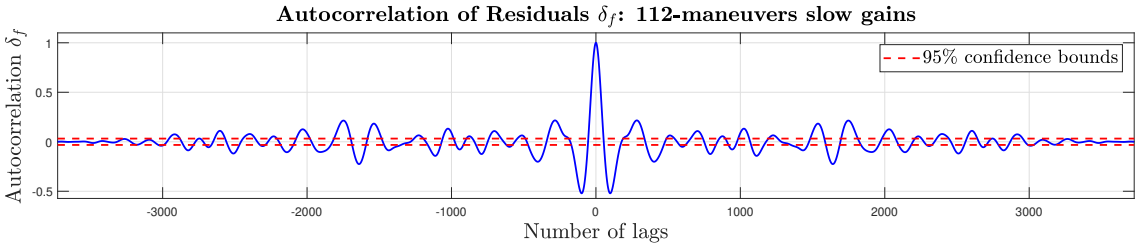

Figure G.6: Autocorrelation plot of the residuals of the input δ_f of multiple 112-maneuvers. The states are determined using the the state-space model shown in Equation E.2, and a Simulink model in which a one to one copy of the PD-controller is implemented. The dynamics of the flapping mechanism is models using Equation 9.4. For this simulation the slow gains shown in Table 7.1 were used. Additionally, the 95% confidence bounds are shown.

The residuals in Figures G.5 and G.6 are more coloured when compared to the residuals of the identification data, as can be seen in Figure 8.10.

G.2. Coupled Maneuvers Autocorrelation Plots

In this section the autocorrelation plots of the residuals of the state derivatives of a coupled doublet with a main frequency of 6 Hz are shown. During the coupled doublet, the Delfly Nimble is doing a doublet in the roll direction when it is flying forward. For the coupled doublet, the state derivatives were determined using three different state-space models, each with a different combination of inputs. The first combination includes the inputs δ_f and δ_t, resulting in the state-space of Equation E.2. The autocorrelation plots of the residuals of the state derivatives when using this state-space are shown in Figure G.7. The second combination only includes the input δ_f, resulting in the state-space of Equation E.8. The autocorrelation plots of the

residuals of the state derivatives when using this state-space are presented in Figure G.8. The third combination includes the inputs δ_f and δ_d, resulting in the state-space shown in Equation E.10. The autocorrelation plots of the residuals of the state derivatives when using this state-space are illustrated in Figure G.9.

All autocorrelation plots in Figures G.7, G.8, and G.9 are very similar to one another. The residuals are more coloured compared to the residuals of the state derivatives of the identification data, as can be seen in Figure 8.10.

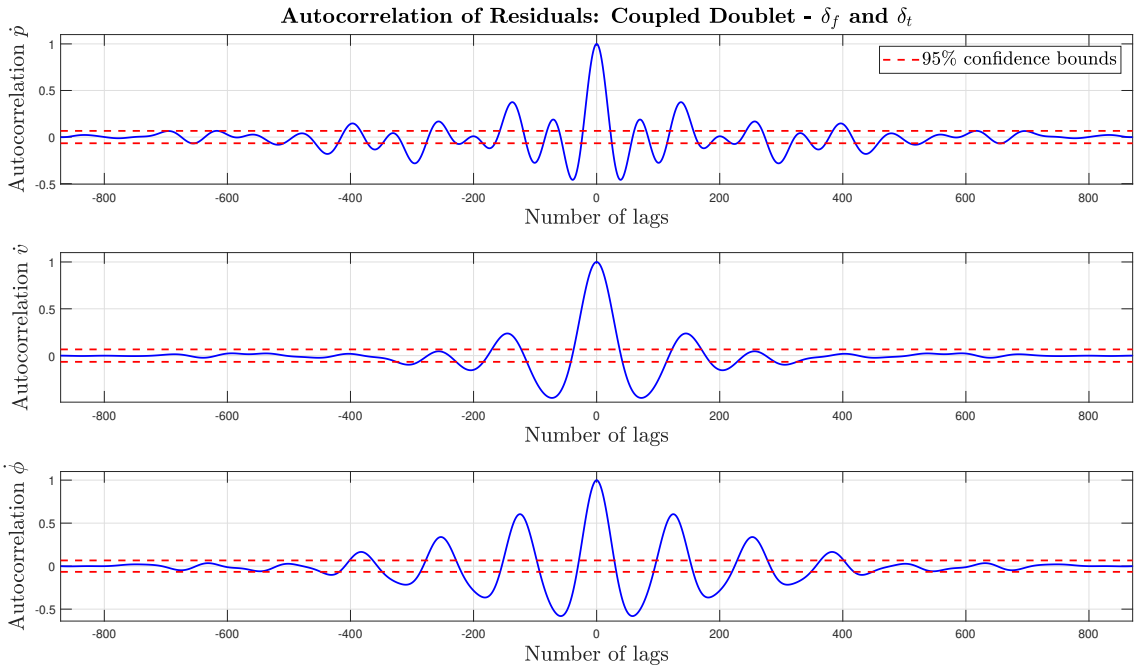

Figure G.7: Autocorrelation plot of the residuals of the state derivatives of a coupled doublet with a main frequency of 6 Hz. The states derivatives are determined using the the state-space model shown in Equation E.2. Additionally, the 95% confidence bounds are shown.

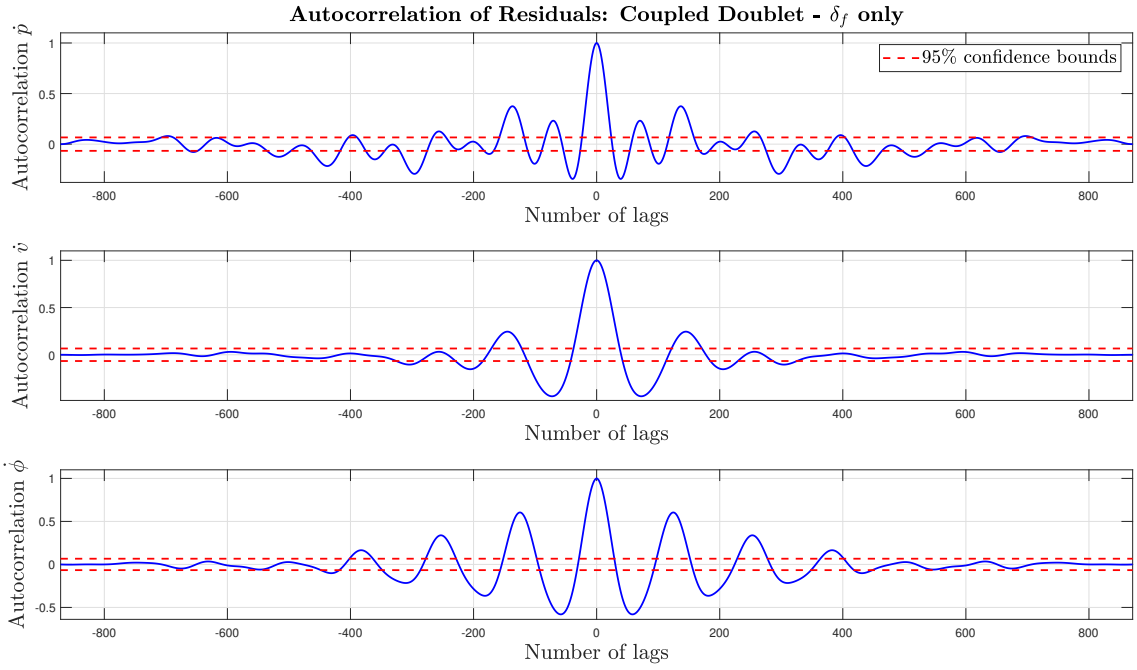

Figure G.8: Autocorrelation plot of the residuals of the state derivatives of a coupled doublet with a main frequency of 6 Hz. The states derivatives are determined using the the state-space model shown in Equation E.8. Additionally, the 95% confidence bounds are shown.

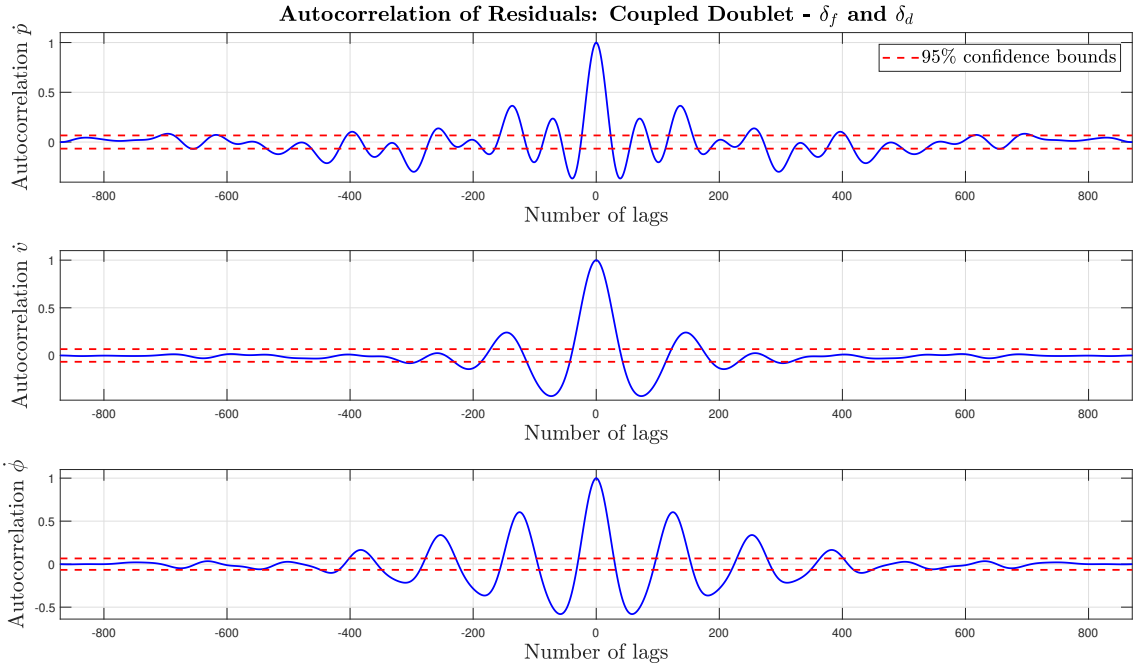

Figure G.9: Autocorrelation plot of the residuals of the state derivatives of a coupled doublet with a main frequency of 6 Hz. The states derivatives are determined using the the state-space model shown in Equation E.10. Additionally, the 95% confidence bounds are shown.

G.3. Nonlinear Maneuvers Autocorrelation Plots

This section shows the autocorrelation plots of the residuals of the state derivatives during the nonlinear doublet maneuver, where the Delfly Nimble is doing a doublet in the roll direction while flying sideways. Two different nonlinear doublets were used. The autocorrelation plots of the first one, which had a roll angle of 30°, a main frequency of 4 Hz, and a roll deflection angle of 15°, are presented in Figure G.10.

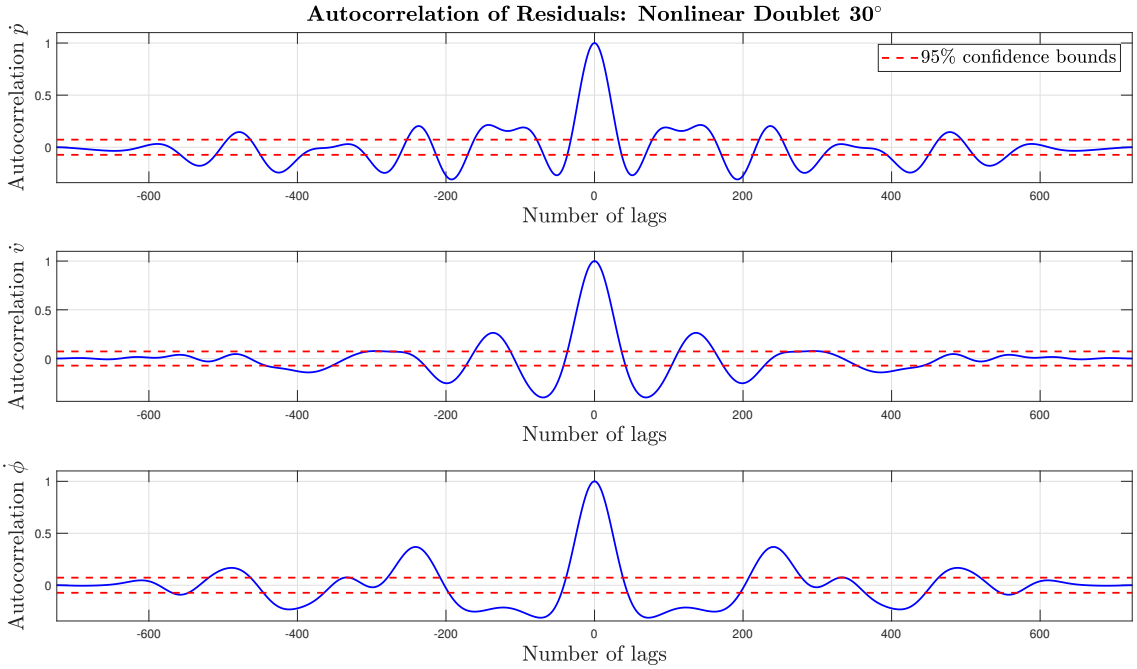

Figure G.10: Autocorrelation plot of the residuals of the state derivatives of a nonlinear doublet with a main frequency of 4 Hz, a constant roll angle of 30° and a roll deflection angle of 15°. The states derivatives are determined using the the state-space model shown in Equation E.2. Additionally, the 95% confidence bounds are shown.

The state derivatives were deteremined using the state-space model of Equation E.2. The second nonlinear doublet had a constant roll angle of 20°, a main frequency of 4 Hz, and a roll deflection angle of 15°. The autocorrelation plots of this maneuver are illustrated in Figure G.11.

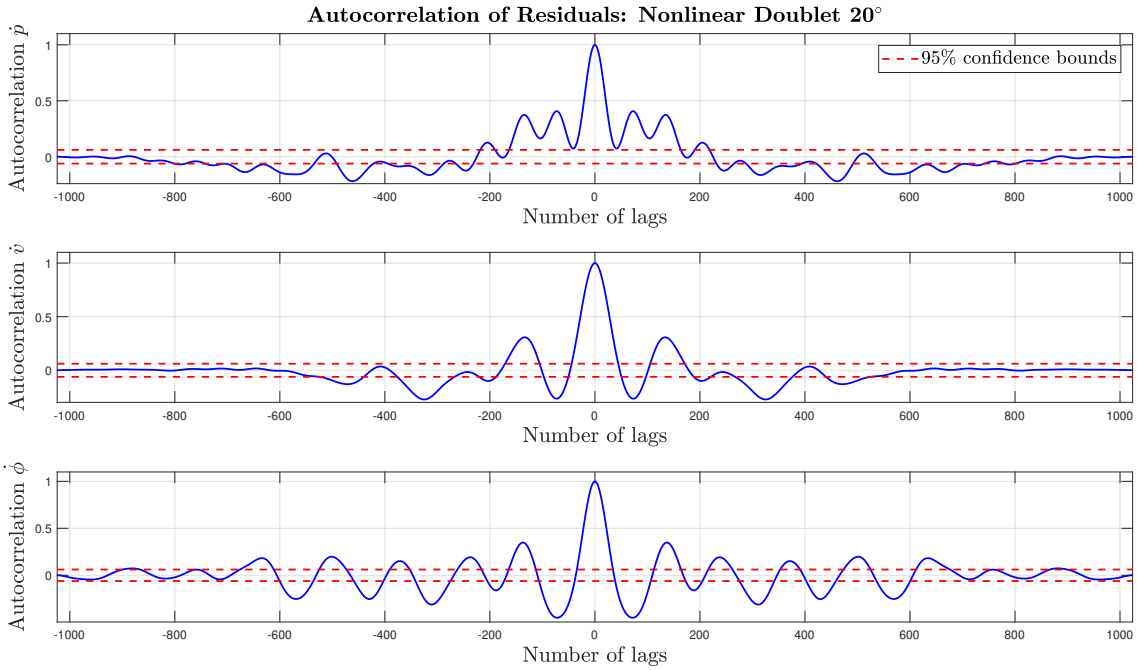

Figure G.11: Autocorrelation plot of the residuals of the state derivatives of a nonlinear doublet with a main frequency of 4 Hz, a constant roll angle of 20° and a roll deflection angle of 15°. The states derivatives are determined using the the state-space model shown in Equation E.2. Additionally, the 95% confidence bounds are shown.

The residuals of both maneuvers are more coloured compared to the residuals of the identification data, shown in Figure 8.10. The residuals of the nonlinear doublet which uses a constant roll angle of 20° are more white compared to when using a constant roll angle of 30°.

H

Parameter Correlations

In this appendix the correlation between parameters is analyzed. This is done by determining the correlation coefficients between parameters, which should not exceed the critical value of 0.9 [40]. This analysis is only done for the grey-box systems. In Section H.1, the correlation of the parameters of the four-state grey-box state-space system are discussed. Section H.2 elaborates on the correlation of the parameters of the three-state grey-box state-space system.

H.1. Correlations Four-state Grey-box State-space system

The correlation matrix for the L-parameters is shown in Table H.1. All the correlation coefficients are below the critical value of 0.9. The highest correlation is found between the parameters L_v and L_{δ_d}.

	L_p	L_r	L_v	L_{δ_f}	L_{δ_w}	L_{δ_d}	L_{δ_t}
L_p	1.0000	0.5140	0.6387	0.0253	0.0855	0.5387	0.2950
L_r	-	1.0000	0.1234	0.3535	0.1187	0.2179	0.1614
L_v	-	-	1.0000	0.5831	0.3493	0.8534	0.6002
L_{δ_f}	-	-	-	1.0000	0.0647	0.5762	0.6608
L_{δ_w}	-	-	-	-	1.0000	0.2377	0.0092
L_{δ_d}	-	-	-	-	-	1.0000	0.4633
L_{δ_t}	-	-	-	-	-	-	1.0000

Table H.1: Correlation matrix for the L-parameters of the four-state grey-box state-space system. The identification data was a doublet train with main frequencies of 7 and 4 Hz.

The correlation matrix for the N-parameters is shown in Table H.2. The highest correlation coefficient is just under 0.9, which indicates the correlation between the parameters N_v and N_{δ_d}.

	N_p	N_r	N_v	N_{δ_f}	N_{δ_w}	N_{δ_d}	N_{δ_t}
N_p	1.0000	0.4061	0.8541	0.0135	0.5296	0.7321	0.7283
N_r	-	1.0000	0.5562	0.6065	0.2152	0.5749	0.3681
N_v	-	-	1.0000	0.0272	0.2459	0.8946	0.5587
N_{δ_f}	-	-	-	1.0000	0.0988	0.2356	0.1459
N_{δ_w}	-	-	-	-	1.0000	0.1176	0.5953
N_{δ_d}	-	-	-	-	-	1.0000	0.5660
N_{δ_t}	-	-	-	-	-		1.0000

Table H.2: Correlation matrix for the N-parameters of the four-state grey-box state-space system. The identification data was a doublet train with main frequencies of 7 and 4 Hz.

The correlation matrix for the Y-parameters is shown in Table H.3. Here the critical value of 0.9 is exceeded.

This is the case for the correlation between the parameters Y_v and Y_{δ_d}.

	Y_p	Y_r	Y_v	Y_{δ_f}	Y_{δ_w}	Y_{δ_d}	Y_{δ_t}
Y_p	1.0000	0.4427	0.7705	0.6439	0.4167	0.7958	0.6022
Y_r	-	1.0000	0.4588	0.0888	0.0776	0.5722	0.5999
Y_v	-	-	1.0000	0.3596	0.8013	0.9026	0.4946
Y_{δ_f}	-	-	-	1.0000	0.1250	0.4696	0.0604
Y_{δ_w}	-	-	-	-	1.0000	0.4997	0.0841
Y_{δ_d}	-	-	-	-	-	1.0000	0.6687
Y_{δ_t}	-	-	-	-	-	-	1.0000

Table H.3: Correlation matrix for the Y-parameters of the four-state grey-box state-space system. The identification data was a doublet train with main frequencies of 7 and 4 Hz.

H.2. Correlations Three-state Grey-box State-space system

The correlation matrix for the L-parameters is shown in Table H.4. All the correlation coefficients are below the critical value of 0.9. The highest correlation is found between the parameters L_p and L_{δ_f}.

	L_p	L_v	L_{δ_f}	L_{δ_t}
L_p	1.0000	0.6516	0.8047	0.3521
L_v	-	1.0000	0.1803	0.0965
L_{δ_f}	-	-	1.0000	0.1657
L_{δ_t}	-	-	-	1.0000

Table H.4: Correlation matrix for the L-parameters of the three-state grey-box state-space system. The identification data was a doublet train with main frequencies of 7 and 4 Hz.

The correlation matrix for the Y-parameters is shown in Table H.5. All the correlation coefficients are below the critical value of 0.9. The highest correlation is found between the parameters Y_p and Y_v.

	Y_p	Y_v	Y_{δ_f}	Y_{δ_t}
Y_p	1.0000	0.5877	0.0892	0.4318
Y_v	-	1.0000	0.2379	0.0197
Y_{δ_f}	-	-	1.0000	0.1244
Y_{δ_t}	-	-	-	1.0000

Table H.5: Correlation matrix for the Y-parameters of the three-state grey-box state-space system. The identification data was a doublet train with main frequencies of 7 and 4 Hz.